

Università degli Studi di Padova

Dipartimento di Fisica e Astronomia “Galileo Galilei”

DOTTORATO DI RICERCA IN FISICA

Search for new physics with two-neutrino double-beta decay in GERDA data

Candidato
LUIGI PERTOLDI

Supervisore
PROF. RICCARDO BRUGNERA

Coordinatore della Scuola di Dottorato
PROF. FRANCO SIMONETTO

Sommario

La ricerca del decadimento doppio beta senza neutrini viene spesso indicata come l'unica maniera pratica per stabilire la natura della massa del neutrino, una delle particelle elementari più sfuggenti e intriganti del Modello Standard. La rilevazione di questo raro decadimento nucleare attribuirebbe al neutrino delle caratteristiche descritte per la prima volta da Ettore Majorana all'inizio del secolo scorso, mettendo in chiara luce l'inadeguatezza delle attuali teorie sulla fisica fondamentale. Secondo alcune teorie, potrebbe anche contribuire a risolvere il mistero dell'asimmetria tra materia e anti-materia nel nostro universo. Da oltre cinquant'anni, il decadimento doppio-beta senza neutrini viene ricercato, senza successo, nell'isotopo del germanio formato da 76 nucleoni. L'esperimento GERDA, conclusosi a novembre del 2019, è stato un pioniere del campo, avendo dimostrato la maturità di questa tecnica sperimentale per la realizzazione di un esperimento su larga scala, in grado di arrivare a mettere limiti dell'ordine di 10^{27} anni sulla vita media del decadimento. Questo lavoro di tesi vuole mettere in luce gli eccellenti risultati raggiunti in termini di livello di eventi di fondo, elaborando un modello statistico di questi ultimi. In particolare, verrà presentata per la prima volta una simulazione Monte Carlo del taglio dell'argon liquido, basato sulla luce di scintillazione in esso prodotta al passaggio di radiazione ionizzante. I risultati di questo modello verranno impiegati nello studio della distribuzione in energia del decadimento doppio beta a due neutrini, allo scopo di misurarne la vita media e ricercare segnali di nuova fisica provenienti da una eventuale emissione di Majoroni. La stima della vita media del decadimento doppio beta a due neutrini estratta è di $(2.050 \pm 0.011_{\text{stat}} \pm 0.042_{\text{sys}}) \cdot 10^{21}$ anni, mentre il limite inferiore sulla vita media del decadimento doppio-beta senza neutrini ma con emissione di un Majorone (indice spettrale $n = 1$) ottenuto al 90% C.L. è di $6.8 \cdot 10^{23}$ anni. I risultati superano notevolmente in precisione stime precedenti con ${}^{76}\text{Ge}$.

Abstract

The search for neutrinoless double-beta decay is generally quoted as the only practical way to establish the nature of the mass of neutrino, one of the most elusive and intriguing elementary particles in the Standard Model. The detection of this rare nuclear decay would attribute to neutrino special properties, described for the first time by Ettore Majorana at the beginning of the last century. A discovery would decisively prove the inadequacy of current fundamental physics theories, in favour of more general formulations. According to some of these novel theories, it might even contribute to solve the mystery of the asymmetry between matter and anti-matter in our universe. For more than fifty years, neutrinoless double-beta decay has been unsuccessfully searched for in the isotope of germanium with 76 nucleons. The GERDA experiment, officially concluded in November 2019, has been a pioneer of the field. It demonstrated the maturity of the germanium experimental technology to realize a tonne-scale experiment, capable of setting limits on the order of 10^{27} yr on the decay half-life. This thesis project aims to attest the excellent GERDA results in terms of background event level, developing a statistical model of the latter. In particular, a Monte Carlo simulation of the liquid argon veto cut, based on the scintillation light emitted at the passage of ionizing particles, will be presented for the first time. The results of this model will be employed in the study of the two-neutrino double-beta decay energy distribution, to measure the process half-life and to search for new-physics signals, originating from a hypothetical Majoron emission. The estimated two-neutrino double-beta decay half-life is $(2.050 \pm 0.011_{\text{stat}} \pm 0.042_{\text{sys}}) \cdot 10^{21}$ yr, while a lower limit at 90% C.L. on the neutrinoless double-beta decay with Majoron emission (spectral index $n = 1$) is set at $6.8 \cdot 10^{23}$ yr. These results substantially improve previous estimates with ^{76}Ge in terms of precision and sensitivity.

Contents

INTRODUCTION	i	
1	THE PHYSICS OF DOUBLE-BETA DECAY	1
1.1	Standard two-neutrino double-beta decay	
1.2	Neutrinoless double-beta decay, neutrino mass and baryogenesis	
1.3	Neutrinoless double-beta decay with Majoron emission	
1.4	From theory to the experimental practice	
2	THE GERDA EXPERIMENT	21
2.1	Overview of the Phase II experimental setup	
2.2	Background reduction techniques	
2.3	Final GERDA results on the search for $0\nu\beta\beta$ decay	
3	THE BACKGROUND BEFORE ANALYSIS CUTS	45
3.1	Analysis data sets	
3.2	Monte Carlo simulations and probability density functions	
3.3	Background expectations	
3.4	Statistical analysis	
3.5	α -events analysis	
3.6	Potassium tracking analysis	
3.7	Full-range analysis	
3.8	Discussion	
3.9	Full Phase II data analysis	
4	THE BACKGROUND AFTER THE LAr VETO CUT	83
4.1	Analysis data sets	
4.2	Monte Carlo simulations and probability density functions	
4.3	Full-range analysis	
4.4	Discussion	
5	PRECISION $2\nu\beta\beta$ DISTRIBUTION ANALYSIS	103

- 5.1 Statistical analysis
- 5.2 Systematic uncertainties
- 5.3 Results and discussion

CONCLUSIONS AND OUTLOOK 119

- A GERMANIUM DETECTOR MODELS 123
 - A.1 Recommended model from characterization data
 - A.2 Tuning the BEGe model on calibration data
 - A.3 Insights from low-energy data
- B ASSAY MEASUREMENTS 139
- C MONTE CARLO SIMULATIONS AND PROBABILITY DENSITY FUNCTIONS 143
 - C.1 Optical physics in MAGE
- D TIME DISTRIBUTION OF α EVENTS 155
- E POTASSIUM TRACKING ANALYSIS PLOTS 159
- F BAYESIAN BLOCKS 165

*Mibi crede, verum gaudium res
severa est.*

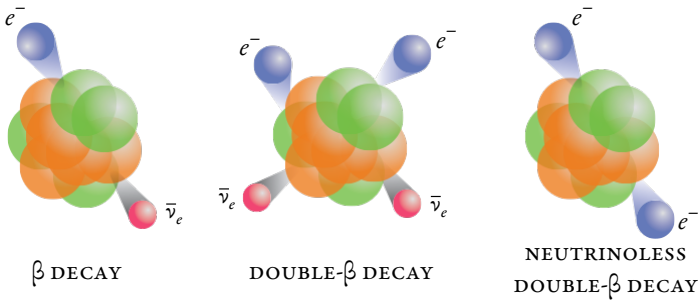
—SENECA

Introduction

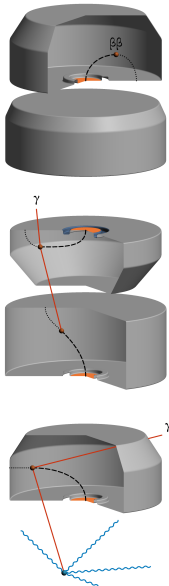
Since the first direct neutrino detection in 1956 [1], physicists have shed light on many mysteries involving one of the most elusive elementary particles ever observed. From the discovery of neutrino oscillations, an unambiguous signature of its tiny but non-zero mass, the field has been progressively acquiring importance in the scientific community as it provides a way to test the most fundamental physics laws. The fact that neutrino is a massive particle represents a crack in the minimal formulation of the Standard Model of particle physics, in which the neutrino, just as the photon, is massless. The unrevealed fundamental nature of its mass, however, might lead physicists to a more revolutionary discovery: our Standard Model, which has proven to be incredibly successful in describing the Nature we know, could be just part of a broader scheme.

What could such a tiny mass be possibly hiding? Physicists have always been puzzled by the arbitrarily diverging mass scales of the Standard Model. The electron neutrino is more than one million times lighter than the electron itself, and we believe that it is not by chance: a more general theory must exist to explain it. Theorists have formulated a plethora of models, which usually foresee the existence of new fundamental particles, in attempt to unveil the underlying picture. No conclusive experimental evidence, however, has been reported in favor of any of these theories. In perhaps the simplest model explaining the neutrino mass scale, heavy neutrino counterparts provide the suppression factor necessary to give the neutrino such a small mass. Unfortunately, the energies at which these hypothetical heavy particles can be directly detected is far from being reachable with current experimental technologies. The mass the neutrino acquires through this mechanism is called *Majorana* mass, named in honor of the Italian physicist who first proposed this type of particles, Ettore Majorana [2]. The reason why Majorana neutrinos are so popular is now evident: small masses probe higher energy scale physics.

How can we experimentally test if the neutrino is a Majorana particle? An extremely rare nuclear process, the so-called neutrinoless double-beta decay, has been identified by physicists as the most promising discovery channel. Certain atomic nuclei have been observed to undergo a double-beta decay, i.e. the occurrence of two simultaneous beta decays, in which two electrons and two electron anti-neutrinos are emitted. The rate of this process is extremely low: the probability for one of these nuclei to decay in a time equal to the age of the universe is less than one over one billionth or less, depending on the nucleus. Theoreticians have demonstrated that, if neutrino is a Majorana particle, another double-beta decay mode can take place, in which no neutrinos are produced at all. The experimental signature of this hypothesized neutrinoless double-beta decay mode is the emission of two electrons, at the maximum energy available in the process.



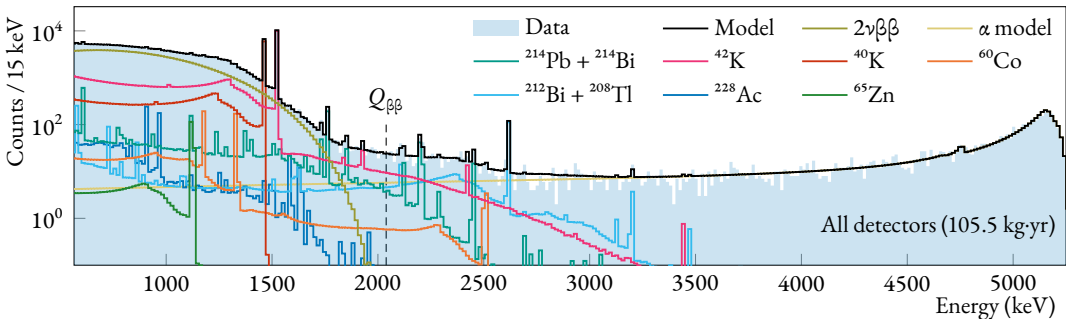
In addition to being inevitably tied to the origins of the neutrino mass, neutrinoless double-beta decay has a second critical consequence related to the fundamental laws of Nature. One of the crucial conserved symmetries in the Standard Model concerns matter and anti-matter: in all processes they must be produced, or destroyed, in the same amount. The world we know, however, is evidently made of matter — and cosmological observations seem to confirm that the rest of the universe looks very similar. How can it be that all the balancing anti-matter predicted by the Standard Model is gone? The reader might have realized now, after this preamble, that only matter (the two electrons) is produced in neutrinoless double-beta decay. According to many theories, the existence of this process might be enough to explain the asymmetry between matter and anti-matter produced in the very early moments after the Big Bang. At this point, it is clear that the search for neutrinoless double-beta decay is much more than a mere investigation of the properties of a tiny fundamental particle. Its discovery would prove the existence of Majorana neutrinos, physics beyond the Standard Model and perhaps shed light on the origins of our universe.



One of the candidate atomic nuclei for a discovery is the germanium isotope with mass number 76. The experimental quest to discover neutrinoless double-beta decay in ^{76}Ge began more than fifty years ago, with the proposal by a group of researchers in Milano [3]. Germanium was already being used to build high-purity particle detectors with excellent energy resolution, and the concept of incorporating the source in the detector medium made the potential of this discovery channel immediately evident. Since then, many experimental projects succeeded each other in developing the detector technology and pushing forward the discovery sensitivity. None of them reported unambiguous evidence for the existence of neutrinoless double-beta decay, and, in absence of a signal, increasing lower limits on its half-life have been set. The 10^{26} yr threshold has been recently surpassed by the GERDA experiment, which is the subject of this thesis work. GERDA was a ^{76}Ge experiment operating between 2008 and 2019 at the Laboratori Nazionali del Gran Sasso, Italy. The core of the project was an array of forty detectors submerged bare in liquid argon, which provided a passive and active shield against external background, thanks to its scintillation properties. Thanks to this and various other background mitigation techniques, GERDA has been operating in background-free conditions (namely, less than a background count in the neutrinoless double-beta decay search region in the entire measurement time) for the largest part of its collected exposure. This achievement has successfully demonstrated the maturity of the germanium technology as the base of a next-generation, tonne-scale experiment, which is currently being prepared by the LEGEND collaboration.

Searching for a signal in presence of a background is a common circumstance in a physics experiment. Since the signal is hypothetical and possibly faint, the search for a signal inevitably becomes a quest to reduce the background event rate in the search region as much as possible. Several strategies

are set up in GERDA both at the hardware level, during design and construction, and at the software level, with data analysis routines. Care is taken during the design phase not to expose the detectors to background sources and to eventually mitigate their impact with passive or active shields. Materials for setup items deployed in the vicinity of the detectors have been screened for the presence of radioactive contaminants before deployment. Despite all these precautions, residual backgrounds have to be expected and are indeed observed in the data. The task of the background model is to identify the origin of these events by comparing the data collected by the experiment to Monte Carlo simulations of radioactive contaminations in the setup. The results are crucial to select the appropriate mitigation strategy when designing future hardware upgrades or next-generation projects, and enhance the signal sensitivity. Data selection algorithms can also benefit from an accurate knowledge of the expected backgrounds. Below in light blue is the energy spectrum of all events collected by GERDA, together with the result of the background decomposition analysis, which is one of the main subjects of this thesis.



The signature of neutrinoless double-beta decay is an event excess at the maximum energy available in the process, indicated with a dashed line. The background model aims to give an answer to the following questions: what kind of events dominate the background in the region of interest? How many events from β , γ and α events are expected? What is their interaction topology in the detectors? What are the sources and where are they located? Is the background uniform in the region, or peak-like structures have to be expected? What is the correct background model to be used in the neutrinoless double-beta decay signal search? As it is evident from the picture above, an accurate description of the full-energy spectrum is mandatory to extract solid predictions in the region of interest. The present thesis work aims to present and discuss the methodology developed by the GERDA collaboration over the years and tries to give an answer to the questions above.

The development of a background model in double-beta decay experiments is, nonetheless, not only devoted to the neutrinoless double-beta decay signal search. Along with that, the potential of the two-neutrino decay as a precision test bench for the Standard Model and theories beyond it must not be overlooked. An example of new-physics signal that can be searched among the two-neutrino double-beta decay events is the so-called neutrinoless double-beta decay with Majoron emission. In this hypothesized decay mode, two electrons are emitted together with one or more additional bosonic particles that do not interact with the detector medium. These processes would produce a deformation of the two-neutrino double-beta decay energy spectrum (the olive green distribution in the figure above) with respect to the Standard Model prediction. One of the goals of the work presented in the

following chapters is to constrain the presence of the distortions that could be associated with new-physics phenomena. Since backgrounds contribute to this energy region as well, an accurate model is mandatory to extract the signal distribution and precisely study the shape of the standard double-beta decay distribution. Data after the liquid argon veto cut, which exploits the scintillation light emitted in liquid argon in presence of background events, is analyzed for the first time. To obtain theoretical predictions on the background and signal distribution after the cut, a complete Monte Carlo simulation of the veto system has been developed and tuned on calibration data.

The present thesis work is structured as follows. In chap. 1, an overview of the double-beta decay field is given, from the theoretical framework to the experimental endeavors. The reader should then be equipped with a basic understanding of the theory behind the standard two-neutrino mode as well as the new-physics modes and an overview of the projects devoted to this search. In chap. 2, **GERDA**, the experiment on which this work is based, is introduced with a description of the experimental apparatus and the background reduction technologies that allow it to reach an unprecedentedly low background in the region of interest for neutrinoless double-beta decay. At the end of the chapter the final full-data set results on the search for the decay are presented and discussed. The reader is introduced to the background model in chap. 3, starting from data before the high-level analysis cuts. The chapter starts with a description of the analysis data set and continues with an overview of the Monte Carlo methods that are used to generate the probability density functions for background sources. It follows an illustration of the statistical framework in which the background decomposition is performed and, finally, the results are discussed. The background model after the event selection based on the scintillation light detected by the liquid argon veto system is presented in chap. 4. The Monte Carlo framework which has been developed to simulate the propagation of optical photons in the experimental setup and obtain the veto condition for synthetic events is described. The chapter flows straight to the final chap. 5, which presents the analysis of the two-neutrino double-beta decay distribution after the liquid argon veto cut, an improved estimate of the decay half-life and constraints on new-physics processes. A final outlook on the work and appendices close out the thesis.



The physics of double-beta decay

Studying the properties and interactions of neutrinos has been one of the most exciting and vigorous activities in particle physics and astrophysics ever since Wolfgang Pauli suggested their existence in 1930 [4]. Despite their weakly interacting nature, which let them elude direct detection until 1965 [1], we have so far accumulated an enormous amount of knowledge about neutrinos. No experiments that have been performed so far have reported conclusive evidence of deviations from the Standard Model of Particle Physics, except neutrino oscillation experiments, which have shown that neutrinos are massive and mixed [5–9]. This discovery, however, is far from being the last word on the fundamental properties of neutrino. The mechanism through which the neutrino acquires mass and why it is so tiny with respect to all the other elementary particles remains a mystery. How can such a rare nuclear process like double-beta decay help shading some light on these enigmas?

The mass-generation mechanism is strongly connected to the nature of these extremely light particles, which could be either of *Dirac* or *Majorana* type (i.e. neutrino and anti-neutrino are distinct particles or the same particle). An attempt to address this problem is pursued by experiments looking for the neutrinoless mode of double-beta decay. Double-beta decay, in its two-neutrino Standard Model mode ($2\nu\beta\beta$), consists in a nucleus decaying into a daughter nucleus with two electrons and two electron anti-neutrinos as a byproduct. If neutrino is a Majorana particle then another mode may occur ($0\nu\beta\beta$), in which neutrinos are not produced at all [10]. Neutrinoless double-beta decay experiments are considered the most promising way to solve the neutrino mass puzzle, although these events are very rare processes controlled by weak interactions.

From its definition it is also clear that neutrinoless double-beta decay violates lepton number conservation, an accidental symmetry of the Standard Model, by two units. The existence of such a process beyond the Standard Model would be crucial to support baryogenesis ideas, that aim to explain why we live in matter-dominated Universe. Many theories, as a matter of fact, predict that the asymmetry is eventually produced by a violation of lepton number via leptogenesis. Neutrino Majorana masses and lepton-number violation can be therefore verified at the same time by observing neutrinoless double-beta decay.

Neutrinoless double-beta decay is not the only hypothetical process that can be searched in a dedicated physics experiment. Other exotic processes have been conjectured by theorists that have different theoretical signatures and are usually searched by studying the distribution of two-neutrino double-beta decay events. In this work, neutrinoless double-beta decay with Majoron emission, a variant of neutrinoless double beta decay in which massless Goldstone bosons connected to the symmetry breaking are emitted together with the two electrons, has been considered.

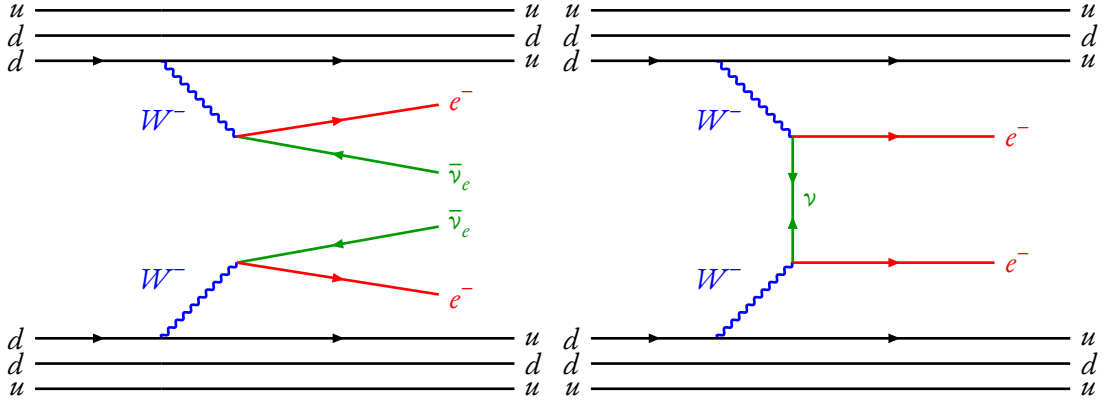


Figure 1.1: Feynman graphs for two-neutrino (left) and neutrinoless (right) double-beta decay. In the neutrinoless mode, the two interaction vertices are connected by a Majorana propagator, such that no neutrinos are present in the final state.

In the following, the theory of double-beta decay is briefly reviewed, focusing on the core concepts and formulas which will be used in this work. First, the decay scheme of the standard two-neutrino double-beta decay mode is discussed in §1.1. The ingredients to calculate its differential decay rate are presented, including a brief discussion of the long-standing nuclear matrix element issue. The theoretical implications of the hypothesized neutrinoless double-beta decay mode on the nature of the neutrino mass and the baryogenesis puzzle are discussed in §1.2. In §1.3 other exotic double-beta decay modes that contemplate the emission of additional particles (i.e. the Majorons) are considered. Finally, aspects concerning the detection of double-beta decay events in real experimental settings will be examined in §1.4.

1.1 Standard two-neutrino double-beta decay

Two-neutrino double-beta decay ($2\nu\beta\beta$) processes, first suggested by M. Goeppert-Mayer in 1935 [11], can be schematically represented as:

$$\begin{aligned} 2\nu\beta^-\beta^- : \quad & \mathcal{N}(A, Z) \longrightarrow \mathcal{N}(A, Z+2) + 2e^- + 2\bar{\nu}_e \\ 2\nu\beta^+\beta^+ : \quad & \mathcal{N}(A, Z) \longrightarrow \mathcal{N}(A, Z-2) + 2e^+ + 2\nu_e \end{aligned},$$

where $\mathcal{N}(A, Z)$ represents a nucleus with mass number A and atomic number Z . The $2\nu\beta^-\beta^-$ ($2\nu\beta^+\beta^+$) process consists of the simultaneous β^- (β^+) decay of two neutrons (protons) in the same nucleus. The processes are generated at second-order in the perturbative expansion of weak interactions in the Standard Model. The Feynman graph for $2\nu\beta^-\beta^-$ is shown in fig. 1.1, left.

Since $2\nu\beta\beta$ decays have a four-body leptonic final state, the sum of the kinetic energies of the two decay electrons follows a continuous distribution from zero to the Q-value of the decay process (the recoil energy of the final nucleus is negligible), which is given by

$$Q_{\beta\beta} = M_i - M_f - 2m_e,$$

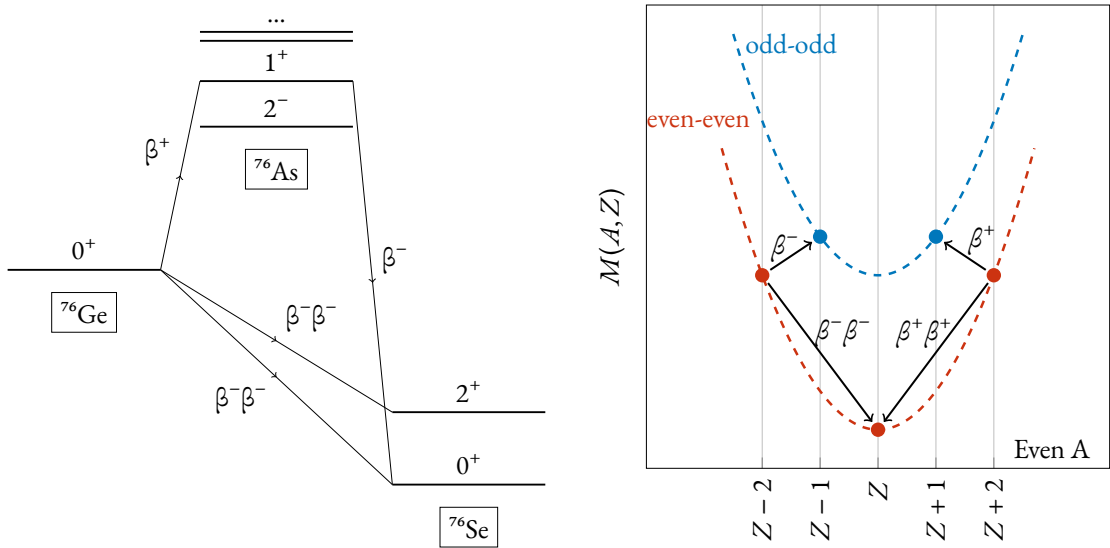


Figure 1.2: On the left: schematic illustration of the energy level structure of the $2\nu\beta^-\beta^-$ decay of ^{76}Ge into ^{76}Se . On the right: general energy level configuration for double-beta decay emitters. The situation for a nucleus with even mass number A is presented: the mass parabola, representing the dependence of the binding energy $M(A, Z)$ on the atomic number Z , is plotted for even-even (even number of protons and neutrons) and odd-odd nuclei with the relevant β and $\beta\beta$ decays among them.

where M_i and M_f are, respectively, the masses of the initial and final nuclei (i.e. the energy levels of their ground states; if the transition occurs into an excited energy level of the final nucleus, M_f must be replaced with the appropriate energy).

A nucleus $\mathcal{N}(A, Z)$ can decay through a $2\nu\beta\beta$ process if its ground state has an energy which is larger than the ground-state energy of the nucleus $\mathcal{N}(A, Z \pm 2)$ plus twice the electron mass. Moreover, if a nucleus can decay through both the β and $2\nu\beta\beta$ processes, the latter, in practice, is not observable, because its β -decay lifetime is much shorter than its $2\nu\beta\beta$ -decay lifetime (the $2\nu\beta\beta$ half-life is typically around 10^{19} – 10^{24} yr). Therefore, in practice, the $2\nu\beta\beta$ decay of a nucleus is observable only if its β decay is energetically forbidden or strongly suppressed because of a large change of spin. The β^- decay of a nucleus $\mathcal{N}(A, Z)$ is energetically forbidden if its ground-state energy is lower than the ground-state energy of the nucleus $\mathcal{N}(A, Z + 1)$ plus the electron mass ($Q_{\beta^-} < 0$). Typically, in $2\nu\beta^-\beta^-$ decays the energy levels of the three nuclei $\mathcal{N}(A, Z)$, $\mathcal{N}(A, Z + 1)$, and $\mathcal{N}(A, Z + 2)$ are of the type depicted in fig. 1.2, left, where the specific case of ^{76}Ge , ^{76}As , and ^{76}Se nuclei is considered.

The naturally occurring isotopes which can decay through the $2\nu\beta^-\beta^-$ process, with forbidden or suppressed β^- decay are 35, and they are listed in [12]. All of the initial and final nuclei in the $2\nu\beta^-\beta^-$ process are even-even, i.e. they have an even number of protons and neutrons. Their binding energy is larger than the intermediate odd-odd nuclei one because of the pairing force acting between identical nucleons (see fig. 1.2, right). For the same reason, all of the initial and final nuclei have a 0^+ ground state. Therefore, all ground-state to ground-state transitions are $0^+ \rightarrow 0^+$. Ground-state transitions to an excited state of the final nucleus may be energetically allowed, as in the case of the $^{76}\text{Ge} \rightarrow ^{76}\text{Se}$ decay in fig. 1.2, left, in which there is an accessible 2^+ excited state of ^{76}Se . However, due to a cancellation

occurring in the phase space integral and the lower Q-value [13], the $0^+ \rightarrow 2^+$ double-beta decay is suppressed with respect to $0^+ \rightarrow 0^+$.

$2\nu\beta^+\beta^+$ There are only six naturally occurring isotopes which can decay through the $2\nu\beta^+\beta^+$ process [14].
DECAY These isotopes have small Q-values and half-lives which are much longer than $2\nu\beta^-\beta^-$ half-lives. The reason for the rarity of $2\nu\beta^+\beta^+$ -decaying isotopes and their small Q-values can be understood considering that the decay $\mathcal{N}(A, Z) \rightarrow \mathcal{N}(A, Z - 1)$ can occur in two ways:

$$\begin{aligned} \beta^+ : & \quad \mathcal{N}(A, Z) \rightarrow \mathcal{N}(A, Z - 1) + e^+ + \nu_e \\ \text{EC} : & \quad e^- + \mathcal{N}(A, Z) \rightarrow \mathcal{N}(A, Z - 1) + \nu_e \quad . \end{aligned}$$

Since $Q_{\text{EC}} = Q_{\beta^+} + 2m_e$, the electron-capture process (EC) can occur even if the β^+ process is energetically forbidden ($Q_{\beta^+} < 0$). Thus, in order to have an energetically forbidden $\mathcal{N}(A, Z) \rightarrow \mathcal{N}(A, Z - 1)$ transitions, the ground-state energy of $\mathcal{N}(A, Z)$ must be smaller than the ground-state energy of the nucleus $\mathcal{N}(A, Z - 1)$ minus the electron mass ($Q_{\text{EC}} < 0$). Considering as a reference the energy of the ground-state energy of the intermediate nucleus, the ground-state energy of the initial nucleus in a $2\nu\beta^+\beta^+$ decay must be at least $2m_e$ lower than in the case of a $2\nu\beta^-\beta^-$ decay. This implies that $2\nu\beta^+\beta^+$ -decaying isotopes are more rare than $2\nu\beta^-\beta^-$ -decaying isotopes. Moreover, for the same energy difference between the ground states of the intermediate and final nuclei, the energy difference between the ground states of the initial and final nucleus in a $2\nu\beta^+\beta^+$ decay is at least $2m_e$ lower than in the case of a $2\nu\beta^-\beta^-$ decay, leading to a correspondingly smaller Q-value. For these reasons, $2\nu\beta^+\beta^+$ decay has been less studied than the $2\nu\beta^-\beta^-$ decay, and in the following we will consider only $2\nu\beta^-\beta^-$ decays (from now on we will simply refer to them with $2\nu\beta\beta$). Let us only mention that $\mathcal{N}(A, Z) \rightarrow \mathcal{N}(A, Z - 2)$ transitions can occur not only through $2\nu\beta^+\beta^+$ processes, but also through processes involving single- and double-electron capture:

$$\begin{aligned} \text{EC}\beta_{2\nu}^+ : & \quad e^- + \mathcal{N}(A, Z) \rightarrow \mathcal{N}(A, Z - 2) + e^+ + 2\nu_e \\ 2\text{EC}_{2\nu} : & \quad 2e^- + \mathcal{N}(A, Z) \rightarrow \mathcal{N}(A, Z - 2) + 2\nu_e \quad . \end{aligned}$$

DECAY RATE The $2\nu\beta\beta$ rate can be calculated by invoking the recipe of the Fermi golden rule for simple β decay. To a good approximation, the decay rate can be factorized as a kinematic part, or phase space factor, times the matrix element describing the transition probability between the initial and final nuclear states:

$$I^{2\nu} = G^{2\nu}(Q_{\beta\beta}, Z) |\mathcal{M}^{2\nu}|^2.$$

The phase space factor $G^{2\nu}$ is obtained by integration over the phase space of the four leptons emitted in the decay and can be calculated to a high degree of accuracy [15, 16]. Its value for $2\nu\beta\beta$ varies between 10^{-21} and 10^{-17} yr $^{-1}$ depending on the double-beta emitter. The nuclear matrix element (NME) $\mathcal{M}^{2\nu}$ deals with the nuclear structure of the transition and is notoriously much more difficult to evaluate. Its value for $2\nu\beta\beta$ depends on the isotope and is on the order of 10^{-1} .

NUCLEAR MATRIX ELEMENTS Denoting the 4-momentum of the two electrons and the two anti-neutrinos by $p_i^\alpha = (E_i, \mathbf{p}_i)$ and $q_i^\alpha = (\omega_i, \mathbf{q}_i)$, respectively ($i = 1, 2$), the relevant matrix element for $2\nu\beta\beta$ is given by

$$i\mathcal{M} = iG_F^2 V_{ud}^2 [\bar{e}(p_1)\gamma^\mu(1 - \gamma_5)\nu(q_1)][\bar{e}(p_2)\gamma^\nu(1 - \gamma_5)\nu(q_2)]J_{\mu\nu} - (p_1 \leftrightarrow p_2) ,$$

where the last expression in brackets represents the first term with p_1 and p_2 interchanged. The hadronic tensor $J_{\mu\nu}$ is the troublesome part, as it encodes all the details of the interaction with the atomic nucleus. While the Lagrangian for double-beta decay is written at the quark level, in fact, the atomic nucleus contains hadrons. Therefore, operators need to be run from their fundamental high scale down to the lower nuclear scale, and then matched to the hadronic operators built from the hadronic (effective) degrees of freedom. A problem is that the hadronic operators are phenomenologically expressed in terms of the form factors, when this transition is made. As an example, the nucleon matrix element $J^\mu = \langle p | \bar{u} \gamma^\mu (1 - \gamma_5) d | n \rangle$, which is relevant for double-beta decay, can be expressed as:

$$\bar{u}(p) [F_V(q^2)\gamma^\mu - iF_W(q^2)/(2m_p)\sigma^{\mu\nu}q_\nu - F_A\gamma^\mu\gamma_5 + F_P(q^2)/(2m_p)\gamma_5q_\mu] u(p') e^{iqx},$$

where $u(p)$ and $u(p')$ are the spinors for the initial and final-state nucleons, $p' - p = q$ and the normalization factors $F_i(q^2 = 0)$ are the coupling constants. The q^2 -dependence and the normalization of several form factors is, unfortunately, poorly known. To proceed with the calculations, most authors apply three approximations: *a*) the impulse approximation for the nuclear current J^μ , which sums over the individual free-nucleon matrix elements; *b*) the non-relativistic expansion for the form factors; *c*) the closure approximation, which averages on the energies of all intermediate odd-odd nuclear states (1^+ for $2\nu\beta\beta$) that must be considered when calculating the amplitude of a second-order process. In this setting, the un-polarized transition probability reads:

$$\sum_{\text{spin}} |\mathcal{M}|^2 = 64G_F^4|V_{ud}|^4 g_A^4(p_1 \cdot p_2)(q_1 \cdot q_2) |\mathcal{M}^{2\nu}|^2, \quad (1.1)$$

where $\mathcal{M}^{2\nu}$ involves vector and axial couplings $g_V^2 \equiv F_V(q^2 = 0)$ and $g_A^2 \equiv F_A(q^2 = 0)$ for Fermi and Gamow-Teller transitions in the form¹

$$\mathcal{M}^{2\nu} = \mathcal{M}_{GT}^{2\nu} - \frac{g_V^2}{g_A^2} \mathcal{M}_F^{2\nu}.$$

In particular, \mathcal{M}_F depends on the integral over q of $F_V(q^2)$, whereas \mathcal{M}_{GT} depends on the corresponding integrals over linear combinations of $F_{A,P,W}(q^2)$.

The difficulty of NME calculations is to know the initial- and final-state nuclear wave functions, a many-body problem that has no exact solution. A consistent treatment of both the strong and weak interactions and a precise modeling of nuclear many-body systems is needed. Several numerical approaches to the problem exist; the reader is referred to [17] and references therein for a complete review. In summary, all approaches miss certain features, and are therefore expected to be affected by systematic biases². This seems to be confirmed by comparisons between results from different methods (see fig. 1.5 for $0\nu\beta\beta$). The evaluation of $2\nu\beta\beta$ NMEs presents a formidable challenge and could help improve the reliability of $\mathcal{M}^{0\nu}$ calculations, that present the same difficulties. $2\nu\beta\beta$, in fact, gives

¹The most general formula includes also the tensor matrix element \mathcal{M}_T , which can be safely neglected [17].

²Thanks to the development in high-performance computing and the introduction of new computational methods into low-energy nuclear physics in the past decade, significant progress has been made in the *ab initio* modeling of atomic nuclei. Recently, the first *ab initio* calculation for the NME of lightest $0\nu\beta\beta$ candidate ^{48}Ca has been reported in the literature [18]. These studies open the door to *ab initio* calculations of the matrix elements for the decays of heavier nuclei such as ^{76}Ge , ^{130}Te , and ^{136}Xe .

only indirect information on $0\nu\beta\beta$, as the set of intermediate states considered in the calculations is different³, but can be used to verify the accuracy of the various techniques. Under this perspective, the greatest advantage of the two-neutrino mode is that the calculations can be directly verified in an experiment by measuring the half-life of the process.

QUENCHING

With the Gamow-Teller matrix element \mathcal{M}_{GT} being the leading one, the nuclear matrix element is to a good approximation proportional to g_A^2 , and $T_{1/2}^{2\nu}$ is proportional to g_A^{-4} . Quenching denotes the reduction of g_A with respect to its free nucleon value of 1.27 that is necessary to reproduce the observable quantities of nuclear decays, particularly β and $2\nu\beta\beta$ decays. Possible origins of quenching are nuclear-medium effects, many-body currents or the inherent shortcomings of the nuclear many-body models (see [19] and references therein). The latter usually fix g_A first and then adjust the nuclear interaction to reproduce the measured $2\nu\beta\beta$ rates. Another common approach is to take g_A from Gamow-Teller β decay and electron capture rates, assuming a common quenching for all weak processes. In this way, one can reproduce $2\nu\beta\beta$ rates and predict non-measured ones. A possibly important observation is that β and $2\nu\beta\beta$ decays have energy scales of order MeV, i.e. much smaller than the $0\nu\beta\beta$ scale of order 100 MeV. Recent studies suggest that low-energy processes may require more quenching and thus, less or no quenching might be needed in $0\nu\beta\beta$ decay (not more than 20–30%) [20–22]. However, there is not yet consensus in the literature on this issue, and further studies are needed. The dependence of quenching on the nuclear calculations can be demonstrated by analyzing the $2\nu\beta\beta$ electron-energy spectra, which allows the extraction of the sub-leading higher-order contributions to the matrix elements [23].

ENERGY SPECTRUM

Having found in eq. (1.1) an expression for the transition probability in which the kinematic variables of the decay products are factored out, it is possible to proceed and calculate the decay rate, which is obtained by integrating over all possible energies and angles of the leptons emitted in the decay. The differential decay amplitude reads:

$$\begin{aligned} dI^{2\nu} = & \frac{1}{4} \int \frac{d^3 p_1}{(2\pi)^3 2E_1} \frac{d^3 p_2}{(2\pi)^3 2E_2} \frac{d^3 q_1}{(2\pi)^3 2\omega_1} \frac{d^3 q_2}{(2\pi)^3 2\omega_2} \\ & \times F(Z, E_1) F(Z, E_2) \sum |\mathcal{M}|^2 \\ & \times 2\pi \delta(E_1 + E_2 + \omega_1 + \omega_2 - E_F + E_I), \end{aligned}$$

where $F(Z, E)$ is the Fermi function that describes the Coulomb effect on the outgoing electrons and E_I, E_F are the energies of the parent and the daughter nucleus, respectively.

In the Primakoff–Rosen approximation [24] for the non-relativistic Coulomb correction, the sum spectrum of the electrons energies can be analytically calculated. After a suitable change of integration variables and defining the sum of kinetic energies $K = T_1 + T_2$ for the two electrons and integrating over the remaining variables, one obtains

$$\frac{dI^{2\nu}}{dK} = A \cdot (K^5 + 10K^4 + 40K^3 + 60K^2 + 30K)(Q_{\beta\beta} - K)^5, \quad (1.2)$$

³In $0\nu\beta\beta$ all intermediate states up to 100 MeV contribute; in contrast, $2\nu\beta\beta$ has only 1^+ states (as two real neutrinos are emitted) with energies up to $Q_{\beta\beta}$ of a few MeV.

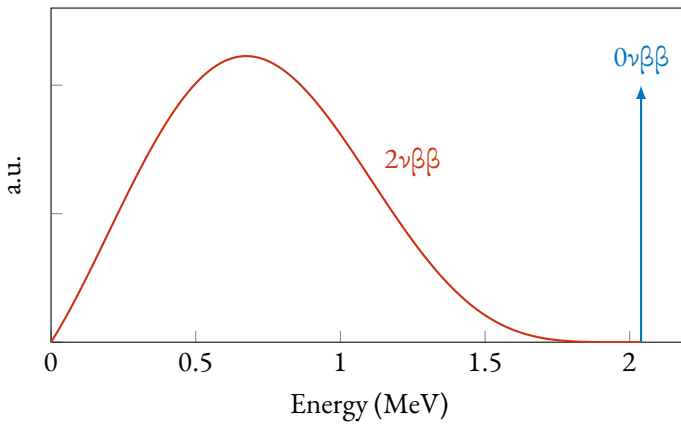


Figure 1.3: Two-electron energy spectra for the two-neutrino and the neutrinoless double-beta decay modes of ^{76}Ge . Analytic formulas, obtained with the Primakoff-Rosen approximation for the Fermi function, are taken from [25, 26].

Table 1.1: A compilation of the most precise measurements of the two-neutrino double-beta decay half-life for a selection of double-beta emitters.

Experiment	Isotope	Exposure (kg·yr)	$T_{1/2}^{2\nu}$ (yr)
GERDA [27]	^{76}Ge	17.9	$(1.926_{-0.022}^{\text{stat}} \pm 0.092_{\text{sys}}) \cdot 10^{21}$
CUPID-Mo [28]	^{100}Mo	0.12	$(7.12_{-0.14}^{\text{stat}} \pm 0.10_{\text{sys}}) \cdot 10^{18}$
CUPID-0 [29]	^{82}Se	9.95	$(8.60 \pm 0.03_{\text{stat}}_{-0.13}^{\text{sys}}) \cdot 10^{19}$
CUORE [30]	^{130}Te	86.34	$(7.9 \pm 0.1_{\text{stat}} \pm 0.2_{\text{sys}}) \cdot 10^{20}$
KAMLAND-ZEN [23]	^{136}Xe	504	$(2.23 \pm 0.03_{\text{stat}} \pm 0.07_{\text{sys}}) \cdot 10^{21}$
EXO-200 [31]		23.14	$(2.165 \pm 0.016_{\text{stat}} \pm 0.059_{\text{sys}}) \cdot 10^{21}$

where K and $Q_{\beta\beta}$ are expressed in units of the electron mass. The overall constant factor is given by

$$A = \frac{G_F^4 g_A^4 |V_{ud}|^4 F_{\text{PR}}^2(Z) m_e^{11}}{7200 \pi^7} |\mathcal{M}^{2\nu}|^2 ,$$

with $F_{\text{PR}}(Z) = 2\pi\alpha/Z(e^{-2\pi\alpha Z})$, where α is the fine structure constant. The distribution in eq. (1.2) for ^{76}Ge is shown in fig. 1.3, in red.

Since double-beta decay experiments are starting to collect high-statistics $2\nu\beta\beta$ data sets, experimental determinations of the process half-life are becoming very precise. A compilation of the most accurate measurements, with relative uncertainties of few percents, performed in recent years is presented in tab. 1.1.

EXPERIMENTAL MEASURES

1.2 Neutrinoless double-beta decay, neutrino mass and baryogenesis

Neutrinoless double-beta decay processes ($0\nu\beta\beta$) of the types⁴

$$\begin{aligned} 0\nu\beta^-\beta^- : \quad & \mathcal{N}(A, Z) \longrightarrow \mathcal{N}(A, Z+2) + 2e^- \\ 0\nu\beta^+\beta^+ : \quad & \mathcal{N}(A, Z) \longrightarrow \mathcal{N}(A, Z-2) + 2e^+ \end{aligned},$$

which have been first proposed by W. H. Furry in 1939 [32], are forbidden in the minimal Standard Model, where the neutrinos are massless, because the conservation of the total lepton number is violated by two units. Interestingly, lepton number L (as well as baryon number B) is only an accidentally-conserved global symmetry in the Standard Model, and its conservation in extended theories seems very unlikely. Moreover, to support the idea that L and B conservation laws are nothing sacred and lack of a deep justification even in the Standard Model, one should note that they are only valid at the classical level⁵. In the effective field theory framework, one can easily realize that the (unique) lowest higher-dimensional $d = 5$ operator one can write down,

$$\mathcal{L}_{\text{eff}} = \frac{1}{2} \frac{h_{\alpha\beta}}{\Lambda} (\bar{L}_\alpha^c \tilde{\Phi})(\tilde{\Phi}^T L_\beta) + \text{h.c.},$$

often referred to as *Weinberg operator* [33], immediately violates lepton number. Superscript c denotes the charge conjugation operation, $L_\alpha = (\nu_\alpha, \alpha)^T$ are the lepton doublets of flavor $\alpha = \{e, \mu, \tau\}$, Φ is the Higgs doublet and Λ denotes the energy scale of the complete theory. Therefore, it is natural to suspect that the validity of B and L conservation laws is just approximate or circumstantial, since it is related to the range of energies that we can explore in laboratories.

LEPTON VIOLATION

Why searching for lepton violation is so important? Apart from the just discussed naturalness issue, the connection with baryon number in most Grand Unified Theories (GUTs), i.e. gauge theories with a single gauge coupling at a certain high-energy scale, might help solving the long-standing problem of explaining why we live in a matter-dominated universe, often referred as the *baryogenesis* problem, despite the equal importance of matter and anti-matter in the Standard Model. In 1967, A. Sakharov proposed a set of necessary conditions to generate the cosmic baryon asymmetry [34]. These conditions are satisfied in the Standard Model [35], but they do not generate the required amount of baryonic asymmetry observed by current experiments [36, 37]. One viable and attractive way to match theoretical predictions to experimental data is to assume that lepton number violating processes had a major role in the early history of the Universe. This is referred as the *leptogenesis* mechanism, which was first proposed by Fukugita and Yanigada in 1986 [38]. In this model (*unflavored* leptogenesis), heavy

⁴The additional double-beta decay modes mentioned in §1.1 which involve single- or double-electron capture also have their neutrinoless analog:

$$\begin{aligned} \text{EC}\beta_{0\nu}^+ : \quad & e^- + \mathcal{N}(A, Z) \rightarrow \mathcal{N}(A, Z-2) + e^+ \\ 2\text{EC}_{0\nu} : \quad & 2e^- + \mathcal{N}(A, Z) \rightarrow \mathcal{N}(A, Z-2) \end{aligned}.$$

⁵Chiral anomalies actually violate this conservation law. It can be shown that the currents associated with baryon and lepton number have non-vanishing divergences: $\partial^\mu J_\mu^{B,L} = c G_{\mu\nu} \tilde{G}^{\mu\nu} \neq 0$, where $G_{\mu\nu}$ is the electroweak gauge field strength and $J_\mu^B = \sum \bar{q}_i \gamma_\mu q_i$, $J_\mu^L = \sum \bar{l}_i \gamma_\mu l_i$.

particles present in many GUTs would have been produced during the Big Bang and then quickly decayed through CP -violating processes, producing a leptonic asymmetry. Note however that, since its first formulation, a large number of alternative theoretical possibilities for leptogenesis have also been formulated [35]. How can leptogenesis convert to baryogenesis? As already mentioned, quarks and leptons live together in GUT multiplets, and hence both B and L are not expected to be conserved quantities. By the way, the combination $B - L$, which is conserved in the Standard Model both at the classical and quantum level (by *sphaleron* processes), often plays an important role in GUTs, and is broken at some stage. In the spirit of baryogenesis, one needs to require that baryon number is violated, and hence lepton number should be violated too. In this sense, lepton violation should be treated on the same level as baryon number violation, and its observation would be far more fundamental than a simple measurement of neutrino properties, which is often quoted as the main goal of $0\nu\beta\beta$ searches. For the sake of completeness, it should be mentioned that the link between $0\nu\beta\beta$ and the baryon asymmetry is not guaranteed, as remarked in [39]. The often-made and popular statement that $0\nu\beta\beta$ experiments probe the origin of matter in the Universe is not true in all cases. There might be scenarios in which new physics processes that allow for $0\nu\beta\beta$ do not generate baryon asymmetry, yet the decay is very well possible.

Besides lepton number violation, $0\nu\beta\beta$, if observed, would be of great importance for establishing the mechanism through which the neutrino acquires its mass. As a starting point, it's interesting to note that the aforementioned Weinberg operator, upon electroweak symmetry breaking, leads to mass terms in the Lagrangian which are not of the usual *Dirac* type.

NEUTRINO
MASS

$$\mathcal{L}_{\text{eff}} \xrightarrow{\text{EWSB}} \frac{1}{2} (m_\nu)_{\alpha\beta} \bar{\nu}_\alpha^\ell \nu_\beta^\ell \quad (1.3)$$

where $m_\nu = \hbar v^2/\Lambda$ is the Majorana neutrino mass matrix and $v = 174$ GeV is the vacuum expectation value. As a brief reminder, we recall that there are two ways to characterize massive fermions: they could be particles of the Dirac type (as all the other fundamental fermions) or the *Majorana* type. Such a distinction arises from different representation choices of neutral fermionic fields in quantum field theory [12]. Majorana particles were first proposed by E. Majorana [2], who showed a peculiar consequence of such an alternative representation: in contrast to Dirac particles, Majorana particles and anti-particles are the same entity. With the proper phase convention, in fact, $\nu_i^c = C\bar{\nu}_i^T = \nu_i$. At the typical mass scale of $m_\nu \simeq 0.05$ eV, it follows that $\Lambda \simeq 10^{15}$ GeV, which is tantalizingly close to the GUT scale. This is why Majorana neutrinos are so popular: small neutrino masses probe higher energy scale physics.

It has been shown that within the minimal standard electroweak model there are only three tree-level realizations of the Weinberg operator [40]. One is the canonical *type-I seesaw* mechanism with right-handed neutrinos. Another approach is introducing a scalar Higgs triplet (*type-II*, or *triplet seesaw*), and the third one involves hypercharge-less fermion triplets (*type-III seesaw*). In the simplest type-I mechanism, as an example, one introduces three Majorana neutrinos, which are Standard Model singlets, and therefore can be arbitrarily heavy with mass matrix M_R [41]. Integrating out the heavy states gives a Majorana mass term for the light neutrinos, which is suppressed by the mass of the heavy degrees of freedom. The Weinberg operator is realized with $\Lambda \simeq M_R$.

Many Standard Model extensions predict neutrinoless double-beta decay, most often through the introduction of a $\Delta L = 2$ Majorana mass term (as the Weinberg operator) for standard or new neu-

trinos. It should be noted that, via the black-box or Schechter-Valle theorem [10], all realizations of neutrinoless double-beta decay in gauge theories are connected to a Majorana neutrino mass. This, nevertheless, generates a tiny mass at the 4-loop level, too small to account for the mass scale as identified in oscillation experiments. Therefore, as discussed in [39], it is possible to classify the possible interpretations of $0\nu\beta\beta$ into the *standard interpretation*, in which the decay is mediated by light and massive Majorana neutrinos (the same that oscillate, see Feynman diagram in fig. 1.1), and the *non-standard interpretations*, in which the decay is mediated by some other lepton-number-violating physics. Most experimental searches focus on the standard interpretation, which is arguably the best motivated possibility for the decay. The discussion that follows will be focused on this standard mechanism. Considerable experimental efforts are being dedicated to the detection of $0\nu\beta\beta$, as such experiments still represent the only practical way of establishing the nature of neutrino mass.

In the standard interpretation, searches for $0\nu\beta\beta$ are searches for neutrino mass, complementing the other approaches to determine it. We recall that in the *3-Majorana neutrino paradigm* the neutrino mass matrix m_ν is diagonalized by the Pontecorvo-Maki-Nakagawa-Sakata (PMNS) unitary mixing matrix U :

$$m_\nu = U \text{diag}(m_1, m_2, m_3) U^T ,$$

where m_i are the (real and positive) masses of neutrino mass eigenstates. The PMNS matrix, in its standard parametrization, contains three mixing angles θ_{12} , θ_{13} and θ_{23} , one Dirac phase δ and two Majorana phases α and β . It is important to know that among the open problems in neutrino physics there is the *hierarchy problem*, i.e. whether $m_1 < m_2 < m_3$ (normal ordering) or $m_3 < m_1 < m_2$ (inverted ordering). In recent years the normal ordering hypothesis has progressively gained support against the inverted ordering. In 2019, frequentist global fits of neutrino oscillation data were favoring the normal ordering hypothesis over the inverted ordering by more than 3σ [42]. Results of Bayesian analyses, however, showed how the normal ordering preference was strongly dependent on the choices of the prior and the parameter space [43, 44]. Normal ordering was most strongly preferred when the sampling was performed for the three neutrino masses with logarithmic priors [45]. After the publication of new oscillation data at the NEUTRINO2020 conference⁶, a significant reduction of the preference for normal ordering has been reported [46, 47]

In the standard interpretation of $0\nu\beta\beta$, the decay width can be expressed as:

$$\Gamma^{0\nu} = G^{0\nu}(Q_{\beta\beta}, Z) |\mathcal{M}^{0\nu}|^2 \langle m_{\beta\beta} \rangle^2 , \quad (1.4)$$

where $\langle m_{\beta\beta} \rangle$ is the so-called *effective Majorana mass*:

$$\langle m_{ee} \rangle = \left| \sum U_{ei}^2 m_i \right| = |c_{12}^2 c_{13}^2 m_1 + s_{12}^2 c_{13}^2 m_2 e^{i\alpha} + s_{13}^2 m_3 e^{i\beta}| .$$

where $c_{ij} \equiv \cos \theta_{ij}$ and $s_{ij} \equiv \sin \theta_{ij}$. The effective mass depends thus on 7 out of the 9 physical neutrino parameters. This is the observable connected with the neutrino mass tested by $0\nu\beta\beta$ experiments. The neutrino mass can also be probed by cosmological observations [48] and direct kinematic (Kurie-plot) searches, such as the KATRIN [49], ECHo [50] and HOLMES [51] experiments. The observables tested by these two methods are the sum of the neutrino masses and the *incoherent sum*:

$$\Sigma = \sum m_i \quad \text{and} \quad m_\beta = \sqrt{\sum |U_{ei}^2 m_i|^2} ,$$

⁶<https://conferences.fnal.gov/nu2020/>

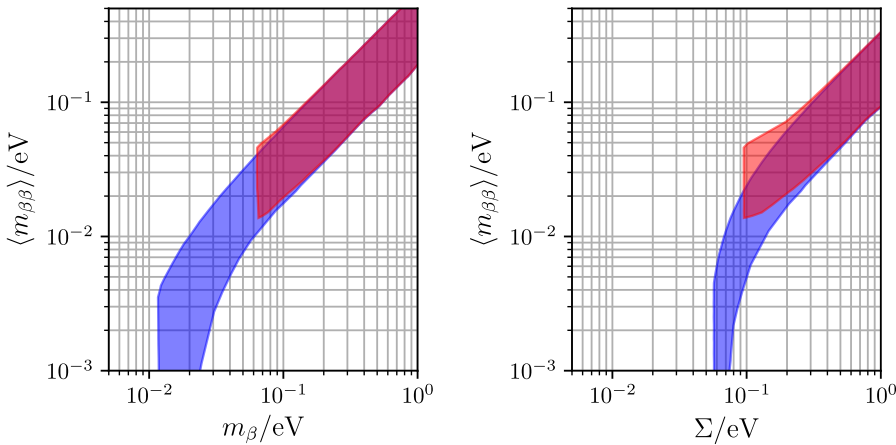


Figure 1.4: The effective mass $\langle m_{\beta\beta} \rangle$ versus the kinematic neutrino mass observable m_β , and the cosmological observable Σ . The uncertainty bands are mainly due to the unknown values of Majorana phases. The neutrino oscillation parameters are varied within their 3σ ranges. The blue (red) area is for the normal (inverted) mass ordering. Taken from [55].

respectively. While the direct kinematic searches provide the most model-independent approach to test the neutrino mass, they give the weakest limits; the projected m_β sensitivity in the KATRIN experiment is 0.2 eV. Cosmology gives the strongest mass limits in the sum of the neutrino masses Σ , but they depend on the data sets and on the cosmological model. The current conservative limits on Σ are about 0.3 eV [37].

Varying the neutrino oscillation parameters within their 3σ ranges it is possible to plot $\langle m_{\beta\beta} \rangle$, m_β and Σ one against each other in fig. 1.4. In the normal ordering hypothesis, $\langle m_{\beta\beta} \rangle$ can even vanish, while in the inverted ordering scenario there is a minimum value of about 0.013 eV. This value represents a physics goal for the current and upcoming $0\nu\beta\beta$ experiments. The normal ordering scenario, however, does not strictly imply a small $\langle m_{\beta\beta} \rangle$, as the smallest neutrino mass can be still sizable. Moreover, $0\nu\beta\beta$ would still be a probe lepton violation, as extensively discussed above.

Considering the cosmological and neutrino oscillation constraints imposed on the available data it is possible to obtain the probability distribution for $\langle m_{\beta\beta} \rangle$, from which the discovery potential of future experiments can be inferred [52–54]. An optimistic picture can be drawn from these studies, since there is better than a 50% $0\nu\beta\beta$ discovery probability for normal ordering and almost unity for inverted ordering for some of the future experiments.

As we have seen in eq. (1.4), the $0\nu\beta\beta$ decay rate can be still factorized to a good approximation into a phase space factor and a nuclear part, times a factor encoding the new-physics effects generated beyond the Standard Model (the effective mass, in the case of standard interpretation). Considerations about the theoretical evaluation of $G^{2\nu}$ and $\mathcal{M}^{2\nu}$ in §1.1 are still largely valid for $0\nu\beta\beta$. The phase space factor $G^{0\nu}$ is of the order of 10^{-25} yr^{-1} and can be calculated to a satisfying degree of accuracy [15, 16] (for ${}^{76}\text{Ge}$ it is $\sim 2.3 \cdot 10^{-15} \text{ yr}^{-1}$), while nuclear term $\mathcal{M}^{0\nu}$ estimations are in the 1–10 range, and remain terribly affected by large systematic biases. The situation for the latter is depicted in fig. 1.5. As already mentioned in §1.1, the quenching problem affects also $0\nu\beta\beta$. Recent studies suggest that there might be less quenching needed (not more than 20–30%) in processes with large momentum

DECAY
RATE

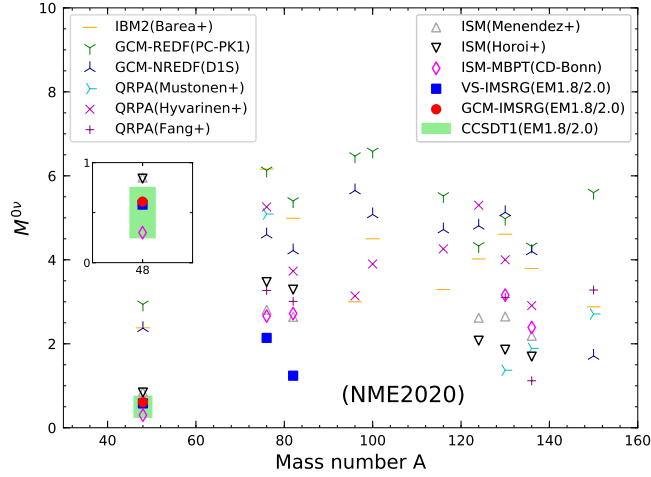


Figure 1.5: A representative compilation of nuclear matrix element calculations with an unquenched $g_A = 1.27$ for different isotopes. Taken from [56].

transfer such as $0\nu\beta\beta$, but there is not yet consensus in the literature. A reduced g_A implies a longer $T_{1/2}^{0\nu}$, which is undesirable for experimental searches. Since no neutrinos are emitted during the process, the experimental signature of $0\nu\beta\beta$ is a Dirac-delta function at $Q_{\beta\beta}$ in the summed energy spectrum of the decay products (fig. 1.3).

EXPERIMENTAL LIMITS

A compilation of the current most stringent experimental bounds on $T_{1/2}^{0\nu}$ and $\langle m_{\beta\beta} \rangle$ from ^{76}Ge , ^{130}Te and ^{136}Xe is given in tab. 1.2. The GERDA, KAMLAND-ZEN and CUORE experiments are competing in setting the best half-life lower limits and corresponding $\langle m_{\beta\beta} \rangle$ upper limits. The experimental program to search for $0\nu\beta\beta$ decay will be presented more in detail in §1.4.

1.3 Neutrinoless double-beta decay with Majoron emission

As mentioned in §1.2, the Majorana nature of the neutrino leads to the violation of the baryon-lepton number $U(1)_{B-L}$ by two units. Assuming that the symmetry is global and its breaking occurs spontaneously, a massless Nambu-Goldstone boson, called the *Majoron* (denoted χ), must exist in the theory [65–69]. Models with massless Majorons where the Majoron is either a singlet [65] or part of a doublet or a triplet [67, 68] have been studied extensively in the ‘80. However, the last two possibilities can be ruled out by measurements of the Z_0 invisible width at particle colliders, because of the coupling of the Z_0 to the Majoron [70]. All the mentioned models predict neutrinoless double-beta decay with Majoron emission:

$$0\nu\beta\beta\chi : \quad \mathcal{N}(A, Z) \longrightarrow \mathcal{N}(A, Z+2) + 2e^- + \chi .$$

The Feynman diagram is shown in fig. 1.6, left. Since the coupling strength of the singlet “seesaw” Majoron is proportional to m_ν/Λ , where Λ is the lepton-number-breaking energy scale (i.e. the heavy right-handed neutrino mass in the seesaw mechanism), obtaining observable decay rates for $0\nu\beta\beta\chi$ and

Table 1.2: Compilation of current most stringent 90% C.L. experimental bounds on $T_{1/2}^{0\nu}$ and $\langle m_{\beta\beta} \rangle$ from ${}^{76}\text{Ge}$, ${}^{130}\text{Te}$ and ${}^{136}\text{Xe}$ experiments. The spread in the $\langle m_{\beta\beta} \rangle$ limits accounts for the uncertainty in the NME values. An unquenched value of axial coupling constant $g_A \simeq 1.27$ is assumed.

Experiment	Isotope	Exposure (kg·yr)	$T_{1/2}^{0\nu} (10^{25} \text{ yr})$	$\langle m_{\beta\beta} \rangle (\text{meV})$
GERDA [57, 58]	${}^{76}\text{Ge}$	127.2	18	79–182
MAJORANA [59]		26	2.7	200–430
CUORICINO [60]		19.8	0.28	300–710
CUORE-0 [61]	${}^{130}\text{Te}$	9.8	0.24	270–760
CUORE [62]		372.5	3.2	75–350
EXO-200 [63]	${}^{136}\text{Xe}$	234.1	3.5	93–286
KAMLAND-ZEN [64]		504	10.7	61–165

preserving existing bounds on neutrino masses would require a severe fine-tuning in the theory [71, 72].

Another possibility for neutrinoless double-beta decay with Majoron emission arises in supersymmetric models with R-parity violation [69, 73], in which the emission of two Majorons is also allowed [74]:

$$0\nu\beta\beta\chi\chi : \quad \mathcal{N}(A, Z) \longrightarrow \mathcal{N}(A, Z + 2) + 2e^- + 2\chi .$$

See fig. 1.6 (right) for the Feynman diagram of the process.

To overcome the fine-tuning problem, many alternative models have been developed starting from the ‘90. In this class of models, the term *Majoron* refers more generically to a light or massless boson, not necessarily a Goldstone scalar boson, that couples to the neutrino. There are models which foresee Majorons carrying leptonic charge, thus assuring lepton-number conservation and forbidding $0\nu\beta\beta$. For the case of Majorons with $L = -2$, $0\nu\beta\beta\chi$ is expected [71], while $L = -1$ leads to $0\nu\beta\beta\chi\chi$ [72]. Other models make use of a vector Majoron which becomes the longitudinal component of a massive gauge boson emitted in double-beta decay [75], which we will also refer to as Majoron in the latter. A decay process that involves the emission of two Majorons is also possible [76]. In [77], the model of a “bulk” Majoron has been proposed within models featuring extra dimensionalities (*brane-bulk* scenario for elementary-particle physics).

For the sake of completeness, it has to be mentioned that models with massive Majorons ([78] and references therein) have progressively gained popularity in recent years, being this kind of Majoron an appealing dark matter particle candidate. This hypothesis remains however largely untested from the experimental point of view, because of the additional level of complexity added to the double-beta event analysis.

Independently on the model, the decay rate for double-beta decay with Majoron emission can be factorized as:

$$\begin{aligned} I^{0\nu\chi} &= g_\alpha^2 \cdot G_\alpha^{0\nu\chi}(Q_{\beta\beta}, Z) \cdot |M_\alpha^{0\nu\chi}|^2 \\ I^{0\nu\chi\chi} &= g_\alpha^4 \cdot G_\alpha^{0\nu\chi\chi}(Q_{\beta\beta}, Z) \cdot |M_\alpha^{0\nu\chi\chi}|^2 , \end{aligned}$$

DECAY
RATE

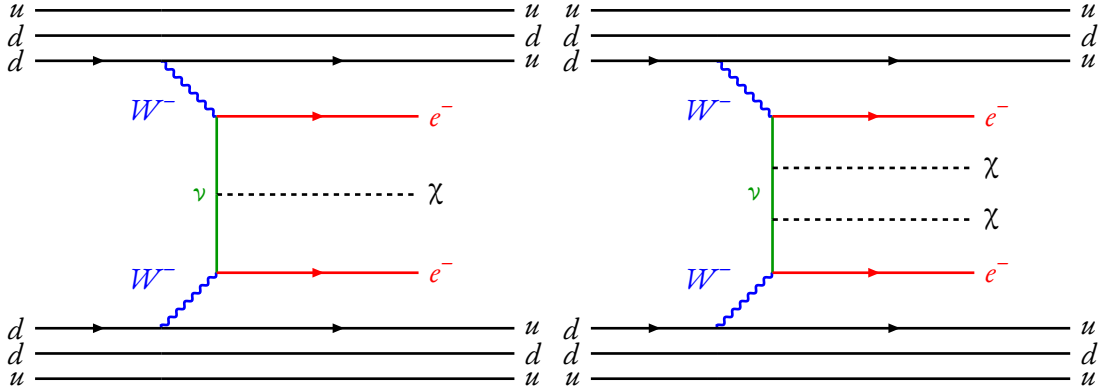


Figure 1.6: Feynman graphs for neutrinoless double-beta decay with single (right) and double (left) Majoron emission.

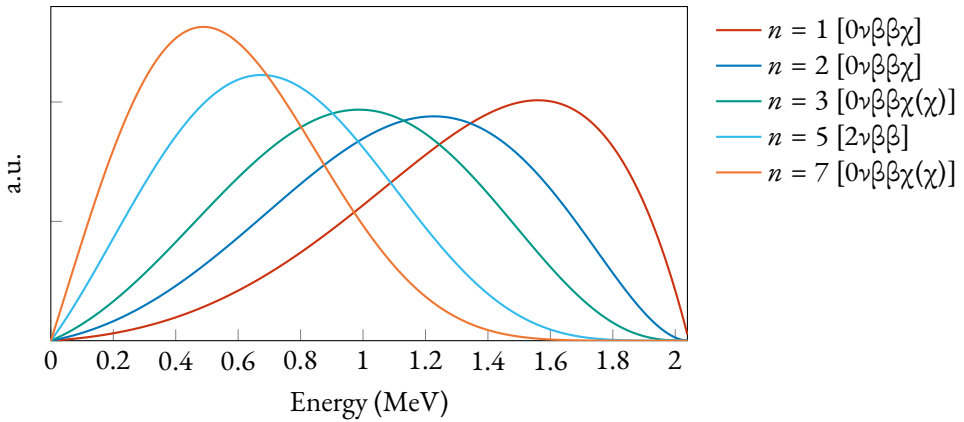


Figure 1.7: Two-electron energy spectra from different models (labeled by the spectral index n , see text) of double-beta decay of ^{76}Ge , including the standard $2\nu\beta\beta$ and the Majoron emitting modes. Analytic formulas, obtained with the Primakoff-Rosen approximation for the Fermi function, are taken from [25, 26].

where g_α is the effective coupling constant and α denotes the considered model. The phase space factors can be parametrized as a function of $Q_{\beta\beta}$, the sum kinetic energy of the two electrons emitted in the decay K and the spectral index n :

$$G_\alpha^{0\nu\chi(\chi)}(Q_{\beta\beta}, Z) \sim (Q_{\beta\beta} - K)^n.$$

$n = 5$ corresponds to the standard $2\nu\beta\beta$ (i.e. eq. (1.2)) whereas $0\nu\beta\beta\chi$ can have $n = 1, 2, 3$ and $0\nu\beta\beta\chi\chi$ can have $n = 3, 7$, depending on the model. As a consequence, the energy spectrum of the two emitted electrons allows to distinguish between the different models. The energy spectra for all modes of the Majoron-emitting double-beta decay are shown in fig. 1.7.

Table 1.3: A compilation of the current 90% C.L. lower limits on Majoron-emitting $0\nu\beta\beta$ modes as set by the GERDA, EXO-200, KamLAND-Zen and NEMO-3 experiments for different isotopes. The limit on the coupling constant g_α for $n = 1$ is reported, as calculated with phase-space factors from [79] and most up-to-date nuclear matrix elements [17]. g_α limits for the other indices and different models can be found in the references. Note that the limits on g_α reported here might differ from those found in the original publications.

Experiment	Isotope	Exposure (kg·yr)	$T_{1/2}^{0\nu\chi(\chi)} (10^{21} \text{ yr})$				$g_\alpha/10^{-5}$
			$n = 1$	$n = 2$	$n = 3$	$n = 7$	
GERDA [27]	^{76}Ge	20.3	420	180	80	30	2.3–5.1
EXO-200 [80]	^{136}Xe	100	1200	250	27	6.1	0.6–1.8
KAMLAND-ZEN [81]	^{136}Xe	36.8	2600	1000	250	11	0.4–1.2
NEMO-3 [82, 83]	^{100}Mo	34.3	44	9.9	4.4	1.2	1.8–3.1
NEMO-3 [84]	^{82}Se	4.9	37	—	—	—	3.1–6.4
NEMO-3 [85]	^{116}Cd	2.16	8.5	—	—	—	5.3–9.1
NEMO-3 [86]	^{48}Ca	0.037	4.6	—	—	—	7.9–40
NEMO-3 [87]	^{150}Nd	0.19	30	—	—	—	1.2–2.9
NEMO-3 [88]	^{130}Te	2.31	16	—	—	—	4.2–17
NEMO-3 [89]	^{96}Zr	0.031	1.9	0.99	0.58	0.11	7.2–16

upper limit on g_α is calculated for the spectral index $n = 1$, for which the half-life limit is usually higher. Phase space factors $G^{0\nu\chi(\chi)}$ are taken from [79], nuclear matrix elements $\mathcal{M}^{0\nu\chi(\chi)}$ from [17]. The most stringent limits at the moment are for ^{136}Xe from EXO-200 and KAMLAND-ZEN.

I.4 From theory to the experimental practice

The primary focus of experiments that involve double-beta decay is the search for the neutrinoless decay mode, by far the most important compared to other processes. The observables in direct searches of $0\nu\beta\beta$ are the kinematic parameters of the two emitted electrons. A typical experiment measures the total energy of the two electrons (the only observable that is both necessary and sufficient for discovery) and may have the capability to reconstruct the electron tracks in order to reject background events with different event topologies. Since $Q_{\beta\beta}$ is usually known to a high degree of accuracy and the $0\nu\beta\beta$ signature is a mono-energetic peak at $Q_{\beta\beta}$, the signal search is performed in a narrow energy window defined by the energy resolution of the detector.

The number of signal counts in this region of interest (ROI) depends linearly on the detector signal efficiency ϵ , the active mass M , the measurement time t and the isotopic fraction α of the double-beta emitter. These are the quantities that usually play a fundamental role when designing an experiment. The sensitivity to the half-life $T_{1/2}^{0\nu}$ scales linearly with the number of candidate signal counts in the ROI, but the dependence is weaker if some of them are background counts. Two experimental regimes can be defined:

$$T_{1/2}^{0\nu} = \begin{cases} \alpha M \epsilon t & \text{background-free} \\ \alpha \epsilon \sqrt{\frac{Mt}{B\Delta E}} & \text{with background ,} \end{cases} \quad (1.5)$$

BACKGROUND
LEVEL

where B is the *background index*, namely the number of background events normalized to the width of the ROI, source mass and measurement time. This expression clearly shows the advantage of a background-free experiment, since the $T_{1/2}^{0\nu}$ scales linearly with t as opposed to \sqrt{t} in the presence of backgrounds. The background-free condition is effectively realized when the expected number of background events in the ROI in the measurement time t is less than one:

$$M \cdot T \cdot B \cdot \Delta E < 1 .$$

ISOTOPE CHOICE Not all the double-beta emitters that exist in Nature can be effectively employed to search for $0\nu\beta\beta$. As it can be clearly understood from eq. (1.5), an ideal isotope should have high isotopic abundance a , should be available in large quantities M as high-resolution ΔE detectors under low background conditions B . Other relevant isotope features are a low $2\nu\beta\beta$ decay rate to mitigate the occurrence of background events in the ROI, and a high $Q_{\beta\beta}$ to avoid backgrounds from primordial radioisotopes, which are naturally present in construction materials. Moreover, the detection efficiency ϵ can be drastically enhanced if the source material is integrated in the detector medium. A good double-beta emitter should also be readily available in its natural form and have a high natural abundance, to reduce the cost of the experiment. If natural abundance is high enough, isotope enrichment might also be unnecessary, as demonstrated in the case of ^{130}Te [90].

BACKGROUNDS To achieve the ambitious goal of operating in a background-free regime, next-generation experiments need to fight against many different background sources. Here a short summary of the main experimental issues concerning this topic is given. The only irreducible background to $0\nu\beta\beta$ signal searches is given by $2\nu\beta\beta$ events. A careful isotope and detector technology choice can mitigate the impact of such a contribution, since the number of $2\nu\beta\beta$ events that can leak in the ROI reduces with increasing energy resolution. Solar neutrino interactions are also expected to be relevant in tonne-scale detectors, and the respective background contribution can be mitigated by a high mass loading of the decaying isotope in the target medium. As already mentioned, radioisotopes from the uranium and thorium decay chains are ubiquitous in construction materials and their presence must be kept to a minimum. Material radio-purity must be kept high during production and later on before installation, to avoid, among the others, contamination by exposure to ^{222}Rn . Natural radioactivity from components far away from the active source, e.g. rock walls of an underground laboratory, can be passively screened with clean lead or copper, water or cryogenic liquid. The latter two options allow the shielding medium to serve also as an active shield vetoing background events. Cosmic rays can also induce several type of backgrounds. Prompt muon interactions typically deposit a large amount of energy in detectors and can be easily vetoed. Backgrounds from secondary neutrons and cosmogenically-activated isotopes are the main worries. The latter can be avoided by minimizing the exposure of the active material to cosmic rays on the Earth’s surface and rapidly deploying them underground.

EXPERIMENTAL APPROACHES Neutrinoless double-beta decay has a characteristic event topology, in which two $\sim\text{MeV}$ electrons are emitted. Low-density-gas tracking detectors can in principle resolve the two electron tracks, leaving only the irreducible background from $2\nu\beta\beta$ decay. For higher density detectors, such as discrete detectors or liquid scintillator detectors, these electrons deposit their energy within a few millimeters, allowing a less powerful but still useful discrimination between “compact” signal-like events and γ rays, which are likely to scatter and deposit energy at multiple sites. The difference may be resolved through discriminating between the *single-site* and *multi-site* events by pulse-shape discrimination or

reconstructed event topology, depending on the spatial resolution, as well as the size and type of a given detector. Some detectors are capable of particle discrimination through multiple detection channels, e.g. scintillation and ionization. This could allow for the identification of α backgrounds. Other discrimination techniques exploit the spatial distribution of background events, if consistently different from that of the signal events. If background events coming from mechanical support materials are concentrated close around them they might be rejected by an optimized fiducial volume cut, if a monolithic detector is used. In presence of a discrete detector, instead, multi-detector event cuts can be used to isolate double-beta point-like events.

Semiconductors. One of the most promising approaches for scaling to tonne-scale experiments is using ^{76}Ge -enriched High-Purity Germanium (HPGe) detectors, which serve as active source and target for $0\nu\beta\beta$ at the same time. The main advantages of using HPGe detectors are the maturity of the industrial production technologies, their intrinsic purity and the superior energy resolution (per-mill level at $Q_{\beta\beta}$). A clear disadvantage of these detectors is their production cost and the low $Q_{\beta\beta}$ of ~ 2 MeV. The current generation of ^{76}Ge experiments is constituted by GERDA [91] and the MAJORANA DEMONSTRATOR [92], whose collaborations are currently joining their efforts into the next-generation LEGEND experimental program [93]. Its first phase, LEGEND-200, is expected to start data taking in 2021 while its planned tonne-scale phase LEGEND-1000, aims at $T_{1/2}^{0\nu} \sim 10^{28}$ yr sensitivity.

Bolometers. Bolometers are cryogenic calorimeters that operate at temperatures of ~ 10 mK. An absorber is connected to the thermal bath via a weak thermal link, and the temperature is read out by a sensitive thermometer. Crystal absorbers can be grown from many materials that include double-beta decay isotopes, e.g. TeO_2 , $^{116}\text{CdWO}_4$, Zn^{82}Se , $^{40}\text{Ca}^{100}\text{MoO}_4$, $\text{Zn}^{100}\text{MoO}_4$ and $\text{Li}_2^{100}\text{MoO}_4$. Advantages of this detector technology are the possibility to deploy various different double-beta isotopes, the intrinsically-low crystal radioactivity and the high energy resolution. The challenge is to operate a large-scale detector at these ultra-low temperatures. Existing projects that exploit the bolometric technique are CUORE [94, 95], that takes advantage of the large natural abundance of ^{130}Te , CUPID [96], which explores the possibility to improve the background rejection in CUORE through active particle discrimination, and AMoRE, a ^{100}Mo -based experiment [97]. The ultimate sensitivity goal of the CUPID and AMoRE tonne-scale program is $T_{1/2}^{0\nu} > 10^{27}$ yr and $T_{1/2}^{0\nu} \sim 5 \cdot 10^{26}$ yr, respectively.

Time Projection Chambers. The time projection chamber (TPC) is an attractive detector technology for $0\nu\beta\beta$ -decay searches because of the combination of mass scalability and access to multiple background discrimination variables. A TPC takes advantage of a detection medium that produces two energy channels: ionization and scintillation. The combination of these two signals allows the reconstruction of event topology, position, energy and particle type. ^{136}Xe is a convenient source and detector medium for both liquid- and gas-phase TPCs. By operating high-pressure gas-phase xenon TPCs in electroluminescent mode, an energy resolution of better than 0.5% FWHM at $Q_{\beta\beta}$ can be achieved. Liquid-phase xenon TPCs, instead, offer maximum source density. Since $0\nu\beta\beta$ searches focus on low background and good energy resolution, single-phase detectors are usually chosen for liquid-phase TPCs. The achievable energy resolution is somewhat worse than that of the gas-phase detectors, but multi-site background and spatial distribution discrimination work well, with position resolution achievable at the few-mm level. Notable projects focusing on the liquid-xenon single-phase TPC technology to search for $0\nu\beta\beta$ are EXO-200 [98] and its proposed tonne-scale suc-

cessor, nEXO [99], which aims at $T_{1/2}^{0\nu} \sim 10^{28}$ yr sensitivity. Planned high-pressure xenon gas-phase TPC projects are NEXT [100] ($T_{1/2}^{0\nu}$ sensitivity goal of $2.8 \cdot 10^{25}$ yr with NEXT-100) and PANDAX-III [101] (10^{27} yr sensitivity goal within its tonne-scale program). Two-phase liquid-xenon detectors, popular for dark matter searches, such as LUX-ZEPLIN [102], XENON-nT [103] and the future DARWIN [104] might also have the capability to search for $0\nu\beta\beta$ decay.

Scintillators. The main appeal of organic scintillators for $0\nu\beta\beta$ searches is their mass scalability, despite their poor energy resolution. Another advantage of liquid target masses is the possibility to remove contaminants online. A notable experiment exploiting this detection approach is KAMLAND-ZEN, which loaded nearly 400 kg of enriched xenon (KAMLAND-ZEN-400, Phase II). The collaboration is currently starting the new KAMLAND-ZEN-800 phase, that will load 750 kg of enriched xenon. In the longer term, the KAMLAND-ZEN collaboration plans to deploy over a tonne of enriched xenon and to reduce the $2\nu\beta\beta$ -decay background in the signal region of interest by improving the detector resolution within the KAMLAND2-ZEN experiment. The projected $T_{1/2}^{0\nu}$ sensitivity is $\sim 2 \cdot 10^{27}$ yr. Searching $0\nu\beta\beta$ decay with ^{130}Te is the main goal of another liquid scintillator experiment, SNO+ [105], which is currently loading its target medium with the source isotope [106]. Also inorganic CaF_2 scintillators have been always receiving interest, because of the high ^{48}Ca $Q_{\beta\beta}$ of 4.27 MeV. However, finding a cost-effective process to enrich the isotope, whose natural abundance is only $\sim 0.2\%$, is still a challenge. The CANDLES series [107] of $0\nu\beta\beta$ searches at the Kamioka Observatory is actively exploring this experimental approach.

Tracking Calorimeters. The SUPERNEMO [108] unique experimental program, based on the technology demonstrated by NEMO-3 [109], uses a thin foil of source material in the center of a sandwich configuration, surrounded first by a low-pressure gas-tracking layer to track the two β particles and then a calorimetric layer to measure the energy. This type of detectors provides superior topological information and is the only detector technology capable of measuring the opening angle between the two β s — one observable that can distinguish certain underlying mechanisms for $0\nu\beta\beta$ decay. In addition, many different isotopes can be formed into foils and studied in the same detector configuration. The advantage of this detection approach is the excellent background discrimination, which allows to easily reach a zero-background condition. However, the low energy resolution does not permit to efficiently discriminate between $2\nu\beta\beta$ and $0\nu\beta\beta$ events around $Q_{\beta\beta}$. Moreover, the detection efficiency is low (around 30%) and the thin source foils are difficult to scale up to large exposures. The projected sensitivity with ^{82}Se for a full SUPERNEMO is $1.2 \cdot 10^{26}$ yr.

A comparison of the discovery sensitivity of current and planned neutrinoless double-beta decay projects is shown in fig. 1.8, taken from [110]. The experimental program is rich and determined to improve the sensitivity beyond the inverted mass ordering (see fig. 1.4) for at least a decade with multiple isotopes. A discovery of neutrinoless double-beta decay in the next years could come at any time.



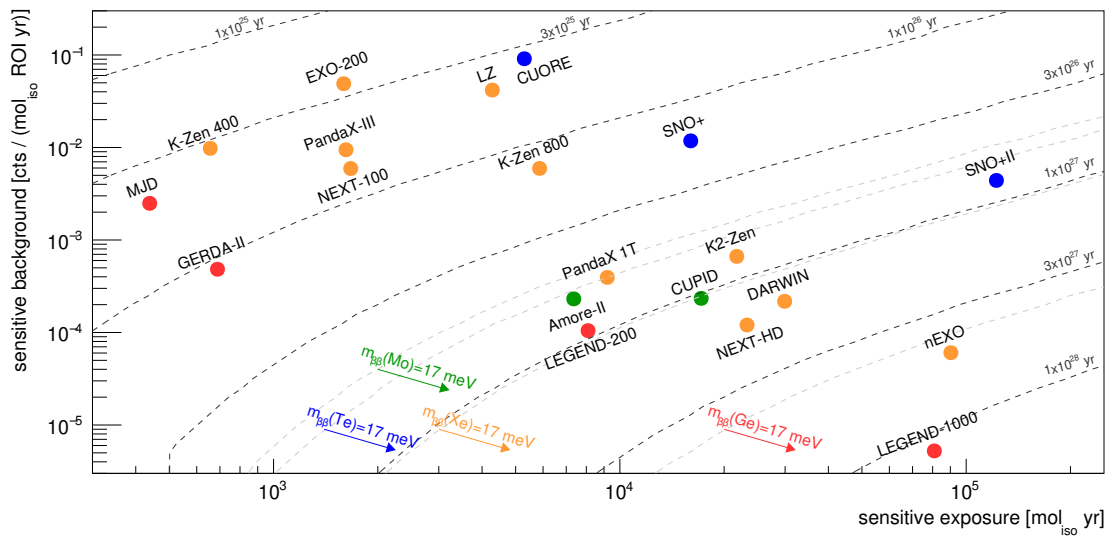


Figure 1.8: Discovery sensitivity comparison between completed or running (top-left side) and future neutrinoless double-beta decay experiments. Taken from [110]. ^{100}Mo (green), ^{130}Te (blue), ^{136}Xe (yellow) and ^{76}Ge (red) projects are considered. Contours of $0\nu\beta\beta$ half-life are shown.

IN SHORT

- Double-beta decay is a rare nuclear decay process in which two electrons and two electron anti-neutrinos are emitted. The decay rate can be factorized in a phase space factor, that can be calculated to a high degree of accuracy, and a nuclear matrix element, which is notoriously much more difficult to evaluate. Several numerical approaches to the problem have been proposed, which give inconsistent results. The energy spectrum of the two emitted electrons is a continuous distribution between zero and the Q-value of the reaction.
- Neutrinoless double-beta decay is an hypothetical decay mode in which no neutrinos are present in the final state. The occurrence of such a process is connected to the fundamental properties of the neutrino and the origin of the our matter-dominated universe. The observation of neutrinoless double-beta decay would establish the Majorana nature of the neutrino and imply the existence of physics beyond the Standard Model. The observable connected to the neutrino mass tested by neutrinoless double-beta decay is the so-called effective Majorana mass. The experimental signature of the decay is a mono-energetic peak in the summed energy spectrum at the process Q-value. No experiments have reported unambiguous evidence of the existence of the decay so far.
- Since neutrinoless double-beta decay requires a symmetry breaking in the model, a massless bosonic particle, the so-called Majoron, must exist in the theory. Many theories predict the presence of Majorons in the final state of the decay process. The experimental signature of these exotic decay modes is a distortion of the standard two-neutrino double-beta decay spectrum, regulated by the coupling constant g_α .
- Several experimental aspects are of paramount importance when searching for neutrinoless double-beta decay in laboratories. The so-called background-free condition, in which the sensitivity to the signal scales linearly with exposure time, is realized when the expected number of background events at the double-beta decay Q-value is less than one. The current and planned experimental program is rich and vast. Science collaborations that deploy semiconductors, bolometers, time projection chambers, scintillators and tracking calorimeters are challenging each other in setting the most stringent limit on the neutrinoless double-beta decay half life, if not finding a signal.

The GERDA experiment

The GERmanium Detector Array (GERDA) has been proposed in 2004 [111] to search for neutrinoless double-beta decay with High-Purity Germanium detectors (HPGe) enriched in the ^{76}Ge double-beta emitter. The proposal lies in the path opened by the Heidelberg-Moscow (HDM) [112] and IGEX [113] experiments, aiming to develop the germanium technology towards large-scale, background-free experimental conditions that could tackle the scale of $\mathcal{O}(10^{26})$ yr sensitivity on the neutrinoless double-beta decay half-life. The history of ^{76}Ge experimental achievements is presented in fig. 2.1¹. The evolution of half-life lower limits and background indices is reported in the top panel, $\langle m_{\beta\beta} \rangle$ ranges and ^{76}Ge exposure at the bottom. Different markers for the exposure data series are used to indicate the type of experiment (natural or enriched germanium, above or under ground). The technological advance and the physics achievements over more than 50 years are impressive. In fig. 2.2 the evolution of sensitivity and limits set by GERDA as a function of accumulated exposure are shown. The linear sensitivity gain demonstrates the background-free conditions in which GERDA has been operating for most of its run time. The GERDA data taking officially ended in November 2019, after hitting the total background-free target exposure of 100 kg·yr and establishing itself as a leading experiment in the field, in terms of lowest background level ever achieved around $Q_{\beta\beta}$ [57, 58].

Since the start of data taking in 2008, the experiment, located in hall A of the Laboratori Nazionali del Gran Sasso (LNGS) in Italy, has been running through two distinct experimental phases (Phase I and Phase II). Detectors from the former HDM and IGEX experiments (of semi-coaxial geometry) along with newly produced diodes (of BEGe geometry type, shorthand for Broad Energy Germanium detectors) were deployed bare into liquid argon (LAr) during Phase I, as suggested in [114], for a total amount of 21.3 kg of germanium. Phase I ended in June 2013 with a total exposure of 21.6 kg·yr and a background index in the region of interest of $1.2 \cdot 10^{-2}$ cts/(keV·kg·yr) [115]. Shortly after, the upgrade works for GERDA Phase II started: a new event veto system based on the LAr scintillation light was installed along with additional 20 kg of BEGe-type detectors. The new detector types together with the re-designed veto system set the stage for a significant reduction of the background index down to the 10^{-4} cts/(keV·kg·yr) scale, allowing GERDA to seamlessly run in background-free conditions for its full second experimental phase and surpass the 10^{26} yr sensitivity threshold in April 2018 [116]. Data taking was then stopped again to permit a third hardware upgrade, during which another 9.6 kg of

GERDA
PHASES

¹The plotted data can be downloaded in JSON format at <https://github.com/gipert/phd-thesis/src/img/plots/history/data/ge76-history.json>.

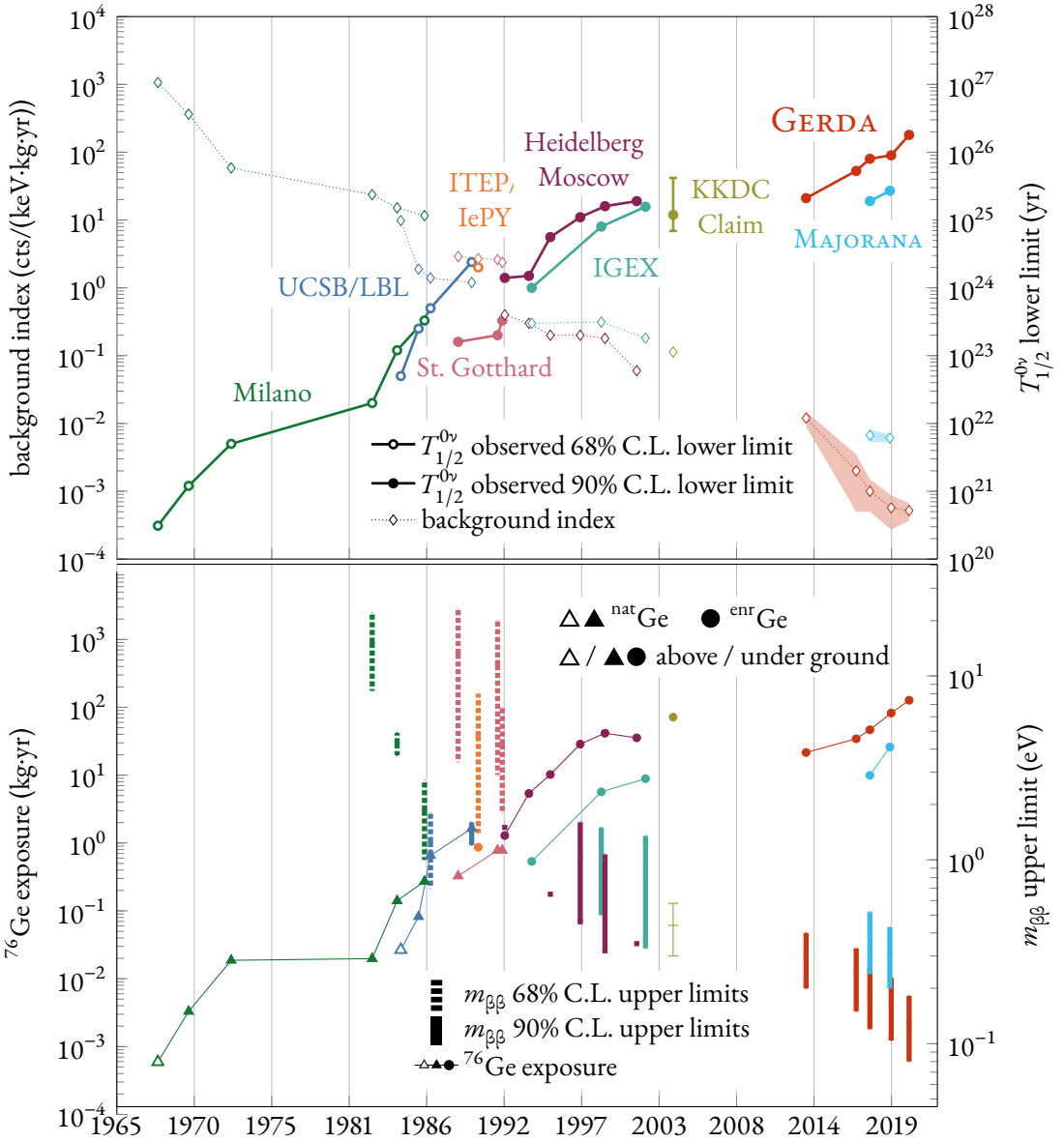


Figure 2.1: History of ${}^{76}\text{Ge}$ neutrinoless double-beta decay experiments with. Each data point corresponds to a specific journal publication. Top panel: evolution of $T_{1/2}^{0\nu}$ lower limits and background indices. Bottom panel: evolution of the accumulated ${}^{76}\text{Ge}$ exposure and $\langle m_{\beta\beta} \rangle$ upper limits, if reported in the publication. Note that these $\langle m_{\beta\beta} \rangle$ constrains include the theoretical uncertainty on matrix elements as known at the time of publication. Some HDM publications report a single $\langle m_{\beta\beta} \rangle$ value. 90% C.L. limits, if available, are preferred to 68% C.L. limits. Different markers are used in the bottom panel to distinguish between experiments above or under ground, experiments using natural or isotopically-enriched germanium¹.

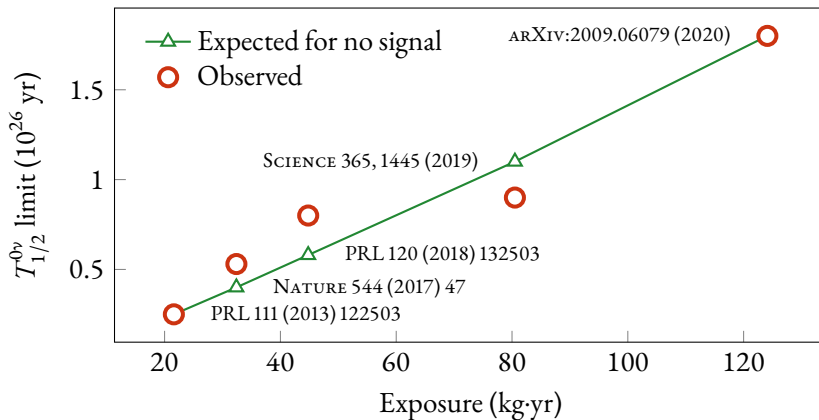


Figure 2.2: Sensitivity (i.e. the median expectation in the assumption of no signal) and $T_{1/2}^{0\nu}$ 90% C.L. lower limits set by GERDA as a function of accumulated exposure. The almost perfect linear increase of the sensitivity for limit setting demonstrates the background-free conditions in which the experiment has been operating in its second phase. Deviations of the observed limit from expectations for no signal are due to the particular statistical realization.

enriched germanium in the form of 5 inverted-coaxial geometry detectors was deployed². Moreover, the LAr veto system was exchanged with a more efficient one featuring a denser fiber curtain and an additional shroud enclosing the central string, now consisting of inverted-coaxial detectors only. This last part of Phase II, which will be referred as Phase II⁺ in the following, ended in November 2019 after collecting the total exposure of 103.7 kg·yr and setting the final GERDA lower limit at 90% C.L. on the neutrinoless double-beta decay half-life of $1.8 \cdot 10^{26}$ yr. In the following, when generally referring to the Phase II period, Phase II⁺ is considered as implicitly included.

The Phase II⁺ upgrade has partly been also a test bench for the next-generation successor of GERDA in the field of double-beta decay physics with ^{76}Ge , the LEGEND experiment. The collaboration, born in October 2016 as a fusion of GERDA and MAJORANA³ [92], pursues the goal of building a tonne-scale ^{76}Ge experiment and reaching the $\mathcal{O}(10^{28})$ yr sensitivity scale. The first phase of the experiment, LEGEND-200, will deploy 200 kg of germanium in the existing GERDA infrastructure at LNGS and it is currently in commissioning phase.

As the present thesis work is based on GERDA Phase II data, the description of the experimental setup and the main analysis techniques given in the following will be limited to that data taking time period. The chapter is structured as follows. In §2.1 a general overview of the GERDA Phase II (and Phase II⁺) apparatus is given. In §2.2 the working principles of the main background reduction techniques that allow GERDA to operate in a background-free regime are outlined. The application of these event-selection criteria to the Phase II data, the statistical analysis of the events at $Q_{\beta\beta}$ and the final results with the full data set are presented in §2.3.

²Note, however, that a semi-coaxial detector (ANG1) and the natural GTF detectors were removed.

³The MAJORANA collaboration is operating an array of high-purity and isotopically-enriched germanium detectors to search for $0\nu\beta\beta$ at the Sanford Underground Research Facility in Lead, South Dakota (USA). Being the MAJORANA DEMONSTRATOR and the GERDA experiments similar from the technological point of view, the two collaborations have intensively shared expertise during the years, converging to the joint next-generation LEGEND effort.

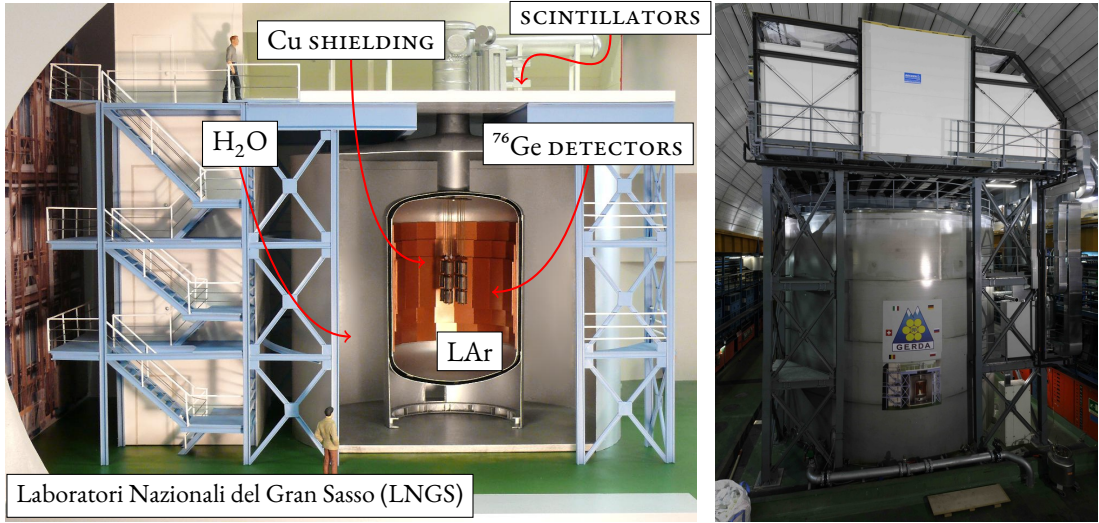


Figure 2.3: On the right: artist view of the GERDA experimental setup. On the left: a picture taken during inauguration in November 2010. The experiment, installed in hall A of the Laboratori Nazionali del Gran Sasso in Italy, deploys an array of germanium detectors enriched in ^{76}Ge bare in liquid argon, together with a liquid argon scintillation light veto system. The cryostat is submerged in a water tank to provide additional shielding from external background sources. A plastic scintillating panel system is installed on the top of the whole structure as an active muon veto, together with the water tank.

2.1 Overview of the Phase II experimental setup

The GERDA experiment is located in hall A of the LNGS laboratories, at a depth of about 3500 m water equivalent, to suppress cosmogenically-induced background sources [117]. The germanium detectors are arranged into strings within a cryostat filled with 64 m^3 of liquid argon (LAr), which acts as a shielding and cooling medium at the same time. The cryostat itself is enclosed by a large tank containing 590 m^3 of ultra-pure water. Besides the additional shielding effect, this water layer act as a medium for a Čerenkov veto system with 66 photomultiplier tubes (PMTs) against muons. An array of scintillating panels is installed at the top of the clean room and completes the muon veto system [118] (see fig. 2.6a). A simplified representation of the experimental setup is given in fig. 2.3, together with a picture taken from the outside.

DETECTORS

The GERDA Phase II detector array is organized in 7 vertical strings, holding 40 detectors in total. The detectors can be divided in three groups: the BEGe detectors, the semi-coaxial ANG and RG, and the semi-coaxial GTF detectors. The detectors of the first two groups are made of germanium enriched in ^{76}Ge , the third group includes detectors with natural isotopic germanium abundance. During the upgrade works for Phase II⁺ in 2018 four enriched inverted-coaxial IC detectors were introduced to replace the three GTF detectors in the central string, for a total of 41 detectors deployed.

All GERDA HPGe detectors are made of high-purity⁴ p-type germanium, which is initially used

⁴The net impurity concentration, defined as the difference between the acceptor and donor concentrations, must be as low as $10^{10}\text{ atoms}/\text{cm}^3$.

to pull crystals, typically fuse-shaped (see for example fig. 4.1a in [119]). Crystals are then cut in slices, and each of them is further processed to obtain the final detector geometry. The electrodes for signal read-out and voltage biasing are then fabricated on the detector surface. The n^+ contact, where the external voltage is applied, “wraps around” the detector. It is obtained by deposition of a lithium layer on the surface, which diffuses below the surface until a depth of ~1 mm during the subsequent thermal annealing cycles. The presence of lithium impurities effectively creates a region with decreased charge collection efficiency (CCE), or “dead-layer”, even when biased at full-depletion voltages. In this region, the CCE is zero at the surface and reaches its maximal value at the full charge collection depth (FCCD). The p^+ electrode, where the signal is read out, is instead fabricated by boron implantation, and the associated dead layer is typically smaller, at the level of hundreds of microns. The two conductive surfaces are separated by an insulating region, which is typically produced by excavating a “groove”. In some cases the groove is passivated by deposition of a germanium-oxide layer.

The GERDA Phase II detectors before the 2018 upgrade can be classified according to two different geometry types: semi-coaxial (SEMI⁺COAX) and BEGE. In the semi-coaxial design, a bore-hole is excavated along the central axis to accomodate the p^+ electrode. With such a configuration, relatively large detector masses can be achieved, on the order of 2–3 kg. The ANG (5), RG (2) and GTF (3) detectors, inherited from the HDM and IGEX experiments and already used in Phase I, are of semi-coaxial type. Their total mass amounts to 23.2 kg of germanium, while the enrichment fractions are in the 85.5–88.3% range. For Phase II, 20 kg of germanium enriched at 87.8% was procured by the GERDA collaboration for the production of 30 new diodes of BEGE type (visible in fig. 2.6d). The Broad Energy Germanium detector design does not include a bore-hole, therefore the p^+ contact is a small, dot-shaped surface at the center of one of the two detector sides. The absence of a bore-hole makes this kind of detectors harder to electrically deplete, requiring lower impurity level and smaller masses, generally less than 1 kg. A detailed description of the BEGE detectors characteristics, from germanium procurement to diode production can be found in [120–122]. For Phase II⁺, 4 new enriched IC detectors of inverted-coaxial (INV⁺COAX) type were fabricated and deployed in place of the natural GTF detectors. This new inverted-coaxial geometry design includes a dot-shaped p^+ contact, to enable BEGE-like pulse-shape discrimination features, and a bore-hole on the other side, to make it possible to achieve large detector masses. Details about the production and characterization of the 4 inverted-coaxial detectors deployed in GERDA Phase II⁺ can be found in [123, 124].

As already mentioned, the GERDA Phase II detectors are arranged into 7 strings, packed closely together as depicted in fig. 2.4⁵, to maximize the multi-detector event rejection efficiency. Since the main background sources in Phase I were located close to the detectors, the design of the mounting and cabling system has been carefully chosen to minimize the exposed mass. The detector holder unit consists of a low-mass, intrinsically radio-pure silicon plate and three vertical copper bars, which hold the detector and connect the modules together into a string. The silicon plate provides the substrate onto which signal and high voltage cables are attached (fig. 2.6d). The germanium detectors are read out with custom-produced, cryogenic and low radioactivity preamplifiers called CC3 [125] (fig. 2.6g). The germanium readout electrode is connected to the JFET-PCB by a flexible flat cable. Two different cable types are adopted for the signal and HV contact: the HV cables are made of 10 mils Cuflon® or



ARRAY
INSTRUMENTATION

⁵The gedet-plots drawing library is based on the Asymptote (<https://asymptote.sourceforge.io/>) vector graphics language and is freely available on GitHub at <https://github.com/gipert/gedet-plots>.

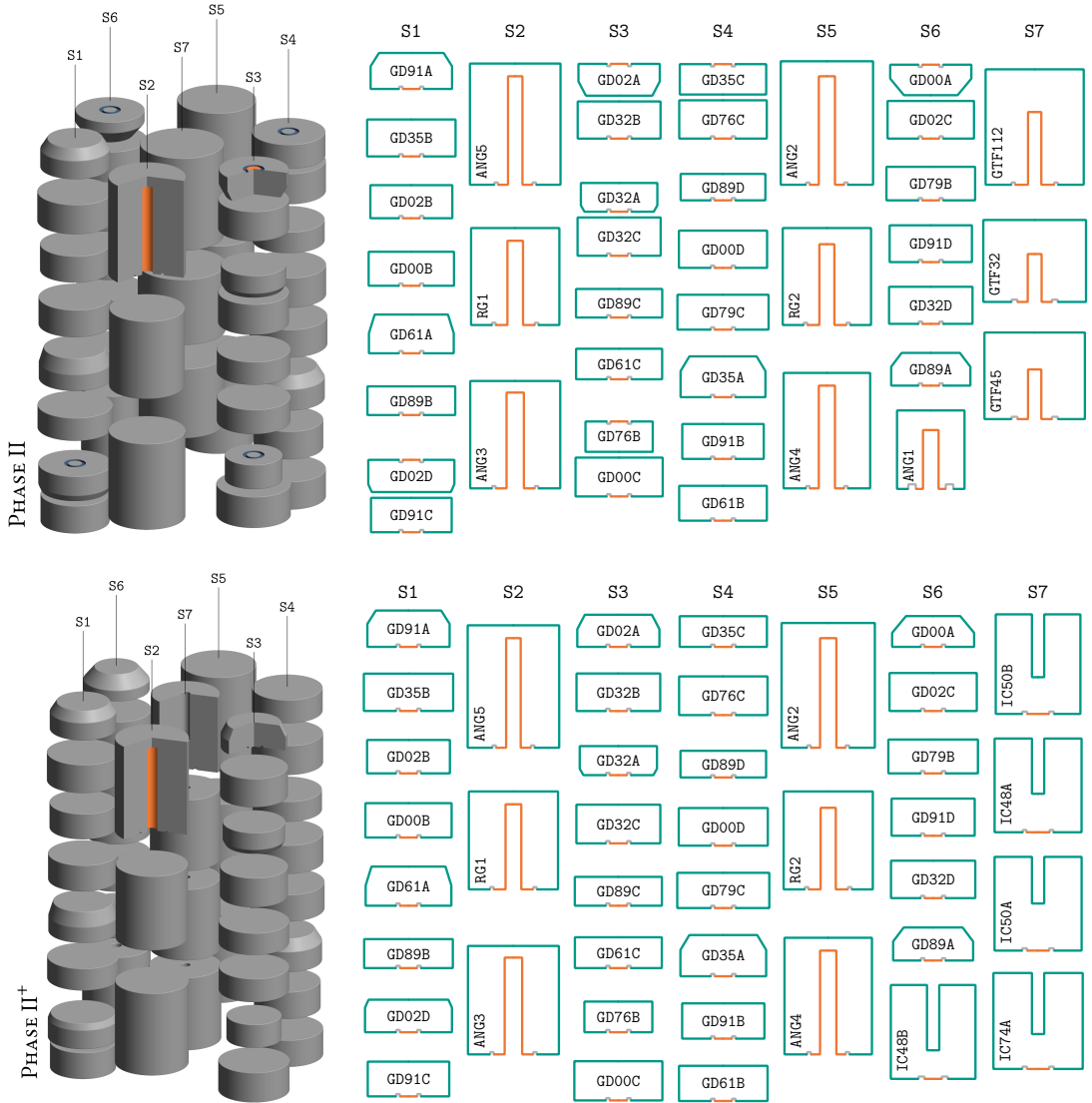


Figure 2.4: The GERDA Phase II detector array. On top: setup from the start of Phase II (December 2015). On bottom: Phase II⁺ setup after the 2018 upgrade works. The main difference between the two configurations is the presence of upside-down detectors in the first configuration and the inverted-coaxial detectors in place of the natural detectors (central string) in the Phase II⁺ configuration. Drawings have been created through the `gedet-plots` library⁵.

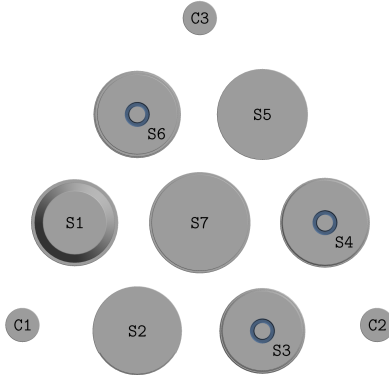


Figure 2.5: Top view of the Phase II array, with the three calibration sources C1, C2 and C3. Drawings have been created through the gedet-plots library⁵.

3 mils Pyralux[®], the signal cables from 3 mils Cuflon[®] or Pyralux[®] (see fig. 2.7a). During the Phase II⁺ upgrade all cables have been exchanged, using only the 3 mils Pyralux[®] cable type.

To improve the sensitivity on the $0\nu\beta\beta$ half-life and operate in the background-free regime, an additional active veto system to collect the LAr scintillation light produced by background events was designed and installed during the upgrade works for Phase II. A cylindrical hybrid design was chosen to detect light: a curtain made of light-guiding plastic fibers coupled to a ring of silicon photomultipliers (SiPMs) to surround the array (fig. 2.6b) and 9 PMTs on the top (fig. 2.6h) plus 7 on the bottom (fig. 2.6i). To enhance the light collection efficiency two copper shrouds (visible in fig. 2.7b and fig. 2.6i) coated with a reflective Tetratex[®] layer were added between the fiber shroud and the PMT holder plates. The latter were coated with a reflective VM2000 layer. Another light collection improvement introduced by the Phase II upgrade is the installation of nylon (mini-)shrouds enclosing each detector string (fig. 2.6d and fig. 2.7f). The presence of these shrouds provides an essential mechanical barrier to reduce the background from ^{42}K ions naturally present in LAr, which undergo β -decay and can mimic the $0\nu\beta\beta$ signature at $Q_{\beta\beta}$ [126]. Being made of transparent nylon material, in contrast to the ones from Phase I made of copper, the mini-shrouds let the light propagate more efficiently to a close-by light-collecting surface. To match the fibers, the SiPMs and PMTs spectral response many surfaces in the close vicinity of the array were coated with tetraphenyl-butadiene (TPB), a wavelength-shifting material. Coating has been applied on mini-shrouds, fiber-shroud, copper shroud, PMTs as well as their holder plates. The reader is referred to ref. [121] for the detailed technical LAr veto specifications, as implemented for the first part of Phase II.

The LAr veto system was upgraded in 2018 for Phase II⁺ to achieve a higher vetoing efficiency. The fiber shroud was exchanged and fiber density increased by 50%. A new fiber curtain was fabricated to wrap the central string around and enhance the detection probability in volumes close to detectors (fig. 2.6c, fig. 2.6f and fig. 2.7c). The light collected by the inner fibers is read out by two SiPM arrays at the top end (visible in fig. 2.6b).

The GERDA weekly calibrations are performed by lowering (through holes in the top PMT plate, visible in fig. 2.6h) three ^{228}Th sources in the close vicinity of the array, at the same radial distance from the central instrumentation axis and evenly spaced (see fig. 2.5). The sources were produced and

LAr VETO

CALIBRATION
SYSTEM

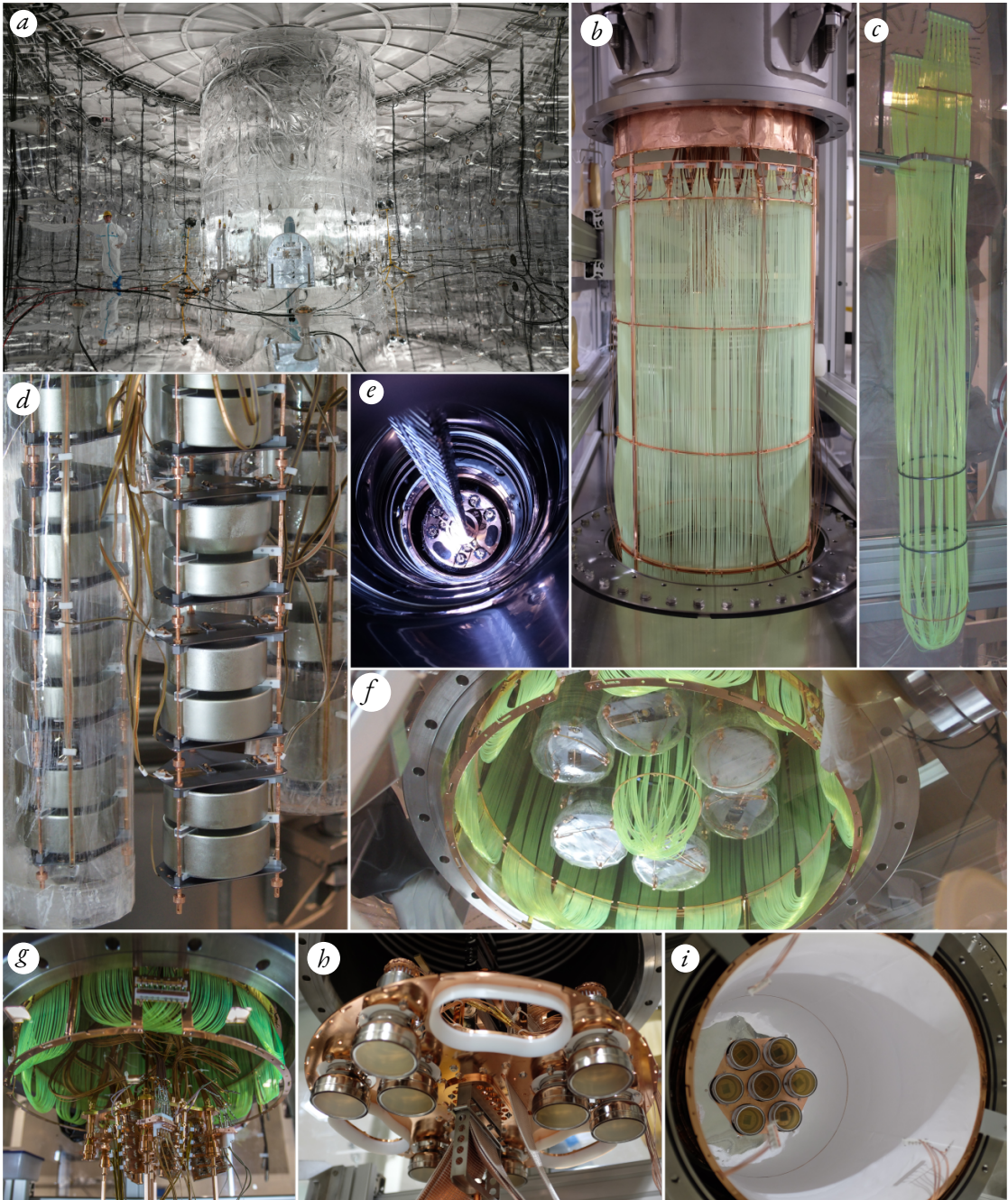


Figure 2.6: Various pictures of the GERDA Phase II setup, taken during the upgrade works. *a)* the muon veto instrumentation inside the water tank; *b)* the light guiding outer fiber shroud; *c)* the central fiber shroud; *d)* Phase II array closeup, BEGe detector strings with their holder mounting and WLS mini-shroud are visible; *e)* the array being lowered into LAr; *f)* the end cap of the central fiber shroud is visible from below the assembled array; *g)* the electronics front-end; *h)* the top PMTs and holes for calibration sources; *i)* the bottom PMTs inside the Tetratex®-coated copper shroud.

characterized for the first part of Phase II [127] and then again for Phase II⁺. A typical energy spectrum of ^{228}Th calibration events is shown in fig. 2.11. The position and the width of the known γ peaks is extracted to calibrate the germanium detectors in terms of energy scale and resolution. The LAr veto instrumentation is usually switched off during calibration runs because of the too high source activity of $\mathcal{O}(10)$ kBq. However, less intense ^{226}Ra sources are also available and can be easily exchanged with the standard ones. Special calibration data has been acquired with these sources and the LAr light instrumentation turned on, to study the performance of the LAr veto system. The reader is referred to [123, 128, 129] for an extensive description of the GERDA calibration system.

A FADC system (SIS 3301 Struck) records traces from germanium detectors (40), PMTs (16) and SiPMs (15) of the LAr veto, PMTs and scintillating panels of the muon veto, when an energy deposition greater than about 100 keV occurs in at least one of the germanium detectors⁶. In addition to real physical triggers, two special artificial events are recorded by the DAQ: test signals injected with a pulser in each germanium detector and baseline events with no physical trigger to study the electronic noise. These events are recorded at fixed time intervals during data taking. Since the outset, GERDA has adopted a rigorous blind analysis strategy to ensure an unbiased search for $0\nu\beta\beta$ decays. Events with a reconstructed energy of $Q_{\beta\beta} \pm 25$ keV are blinded (i.e., removed from the data stream) until the data selection is fixed.

DATA
ACQUISITION

The energy deposition associated to each germanium detector signal is determined via a Zero Area Cusp (ZAC) filter which is optimized offline for each detector and each calibration run [130]. PMT and SiPM hits are reconstructed in the offline analysis following the procedure documented in [121]. Each event has to pass a series of quality cuts tailored to discard unphysical events with very high efficiency (see §2.2). The reconstructed trigger positions are converted into time differences relative to the first trigger found in the germanium detector traces. Trigger positions and amplitudes are subsequently used together with hits from the SiPMs and PMTs to test the LAr veto condition. Software algorithms were implemented in the GELATIO framework [131] which is used to process GERDA data. Each event is characterized by the calibrated energy deposited in the germanium diode, a data quality flag, the classification as signal or background event from the pulse shape analysis, and veto flags from the muon veto and LAr veto systems.

2.2 Background reduction techniques

Various background mitigation techniques are adopted in GERDA, both at the data acquisition level (online) and the analysis level (offline), to reduce the background index to the background-free level of 10^{-3} cts/(keV·kg·yr) and lower. The techniques outlined in the following have been gradually developed and refined during several years of research and publications, and have been employed for the Phase II final analysis in [57, 58]. Documentation about past partial analyses of GERDA Phase II data can be found in publications [27, 116, 132, 133] and references therein.

Muons may pose a substantial background to rare event searches like GERDA by generating counts at $Q_{\beta\beta}$, either through direct energy deposition in the detectors or through e.g. decay radiation of spallation products. The cosmic muon flux at LNGS is reduced by a factor of $\sim 10^6$ to a rate of

MUON VETO

⁶The exact trigger threshold is detector- and run-dependent and varies between 20 keV and 200 keV.

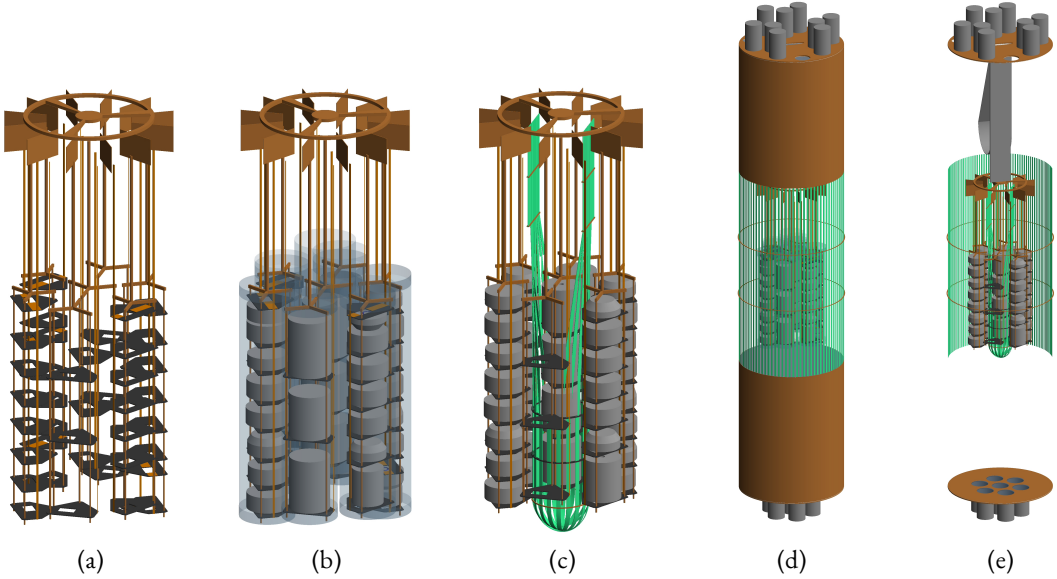


Figure 2.7: Implementation of the GERDA array in MAGe, displayed using the GEANT4 visualization drivers. From left to right: *a)* the Phase II holder mounting, composed of silicon plates and copper bars, and the high-voltage and signal cables. Front-end electronics are on the top end, *b)* the full Phase II array instrumentation, including the transparent nylon mini-shrouds, *c)* the full Phase II⁺ array instrumentation, including the central fiber shroud (in green), *d)* the full Phase II LAr veto system, including the outer fiber shroud, the Tetrapex®-coated copper shrouds (above and below the fibers) and the two PMT arrays, *e)* the Phase II⁺ LAr veto system without the copper shrouds.

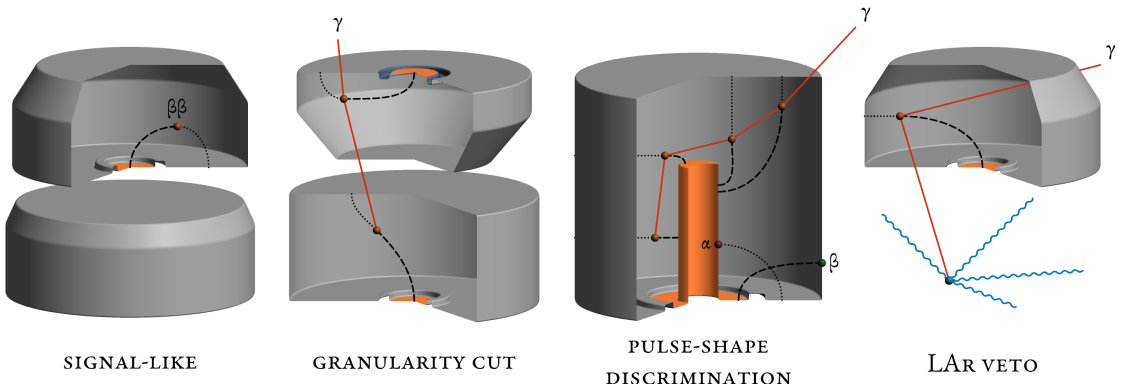


Figure 2.8: Signal, background events in GERDA and working principles of the main background reduction techniques. From left to right: *signal-like events*: the point-like topology in dense detectors of double-beta decays generates distinct single-detector pulse shapes. *granularity cut*: external, background γ s can deposit energy in multiple detectors. *pulse-shape discrimination*: insights on the event topology can be obtained by analyzing its waveform. Single-site events, multi-site events, β s and α s on the surface can be discriminated with offline algorithms depending on the specific detector geometry. *LAr veto*: background events that deposit energy in germanium and LAr at the same time can be efficiently vetoed by the GERDA LAr veto. Drawings have been created through the gedet-plots library⁵.

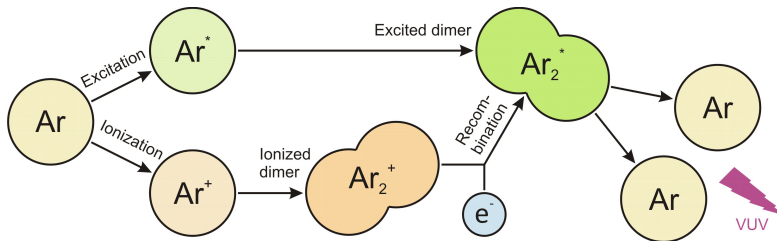


Figure 2.9: Scintillation mechanism of liquid argon (or gaseous argon) via excited dimers decay. The excited dimer can be either formed directly from an excited argon atom or from an ionized atom. The latter forms an ionized dimer before its recombination in molecular form. Courtesy of Christoph Wiesinger.

$\sim 3.4 \cdot 10^{-4} \text{ s}^{-1} \text{ m}^{-2}$, which is still sufficient to generate a non-negligible background of the order of $10^{-3} \text{ cts}/(\text{keV}\cdot\text{kg}\cdot\text{yr})$. As already described in §2.1, a muon veto comprising of a water Čerenkov veto and a scintillator veto was implemented in GERDA to reduce this background contribution. An event with energy deposition in germanium is flagged as muon-induced background if a coincidence with the muon veto signal occurs in a $\pm 10 \mu\text{s}$ window around the germanium trigger. The efficiency of the muon veto system has been estimated to be of $\sim 99\%$, leading to a residual background index of $\sim 10^{-5} \text{ cts}/(\text{keV}\cdot\text{kg}\cdot\text{yr})$ [118].

The primary role of liquid argon in GERDA is to keep the germanium detectors at a cryogenic operational temperature and provide a passive shielding medium against external backgrounds. Moreover, the LAr can be employed as a detector medium in an active veto system, thanks to its scintillation properties. The production mechanism of scintillation light in LAr and its energy spectrum is well known and described in detail in literature. The incident particles deposit their energy mainly by interactions with the electron shell of argon atoms which lead to either an excitation or an ionization of argon atoms. Excited argon atoms are frequently called *excited dimers* or *excimers* in the literature. Their decay is accompanied by the emission of scintillation light in the vacuum ultraviolet region, at the typical wavelength of 128 nm [134]. The ratio between excitation and ionization processes is strongly dependent on the pressure and density of the argon as well as on the type of radiation itself. In the case of excitation, the excited argon atom can directly form an excimer via the collision with neighboring argon atoms. The process is sketched in fig. 2.9. The excimer itself is meta-stable and appears in two different states: the *singlet* and the *triplet* state [135, 136]. The decay of the triplet state is forbidden due to angular momentum conservation, while the decay of the singlet state is allowed. Consequently, the lifetime of the triplet state ($1.59 \mu\text{s}$) is significantly higher than the singlet state (6 ns). The scintillation light yield (combined for both components) is roughly 40 photons/keV, measured in ultra-pure LAr [137]. This value is dependent on different factors, e.g. the presence of contaminants, the pressure and density of the argon as well as the ionization density of the incident particle [137].

LAr VETO

The goal of the GERDA LAr veto is to reject those types of background events in germanium detectors that simultaneously deposit energy in the surrounding LAr, and hence trigger the scintillation process. These background types mainly include γ -rays from ^{226}Ra and ^{228}Th decays in solid materials inside and around the detectors. Also other types of background can successfully be rejected, such as muons or decays from ^{42}Ar or ^{42}K . An event depositing energy in germanium detectors is classified as background if a coincidence with the LAr veto signal is found in the time window spanned by the

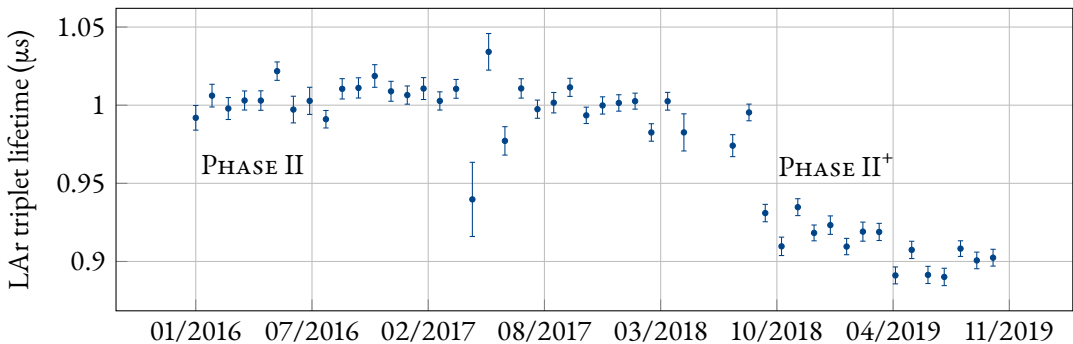


Figure 2.10: LAr triplet lifetime regularly measured during Phase II. The decrease of the LAr purity in 2018 might be attributed to maintenance works of the cryogenic infrastructure.

germanium traces. Since LAr triplet state lifetime significantly depends on the argon purity [138], it is possible to monitor the purity of LAr over time. fig. 2.10 shows the lifetime values, measured about every month, since the start of Phase II. The average measured lifetime dropped after the Phase II⁺ upgrade works from $\sim 1 \mu\text{s}$ to $\sim 0.9 \mu\text{s}$, as a probable consequence of maintenance works of the cryogenic system. The veto condition is realized when the signal in at least one channel (SiPM array or PMT) exceeds a certain threshold (around one photo-electron or less) within a certain time window around the germanium trigger (usually few microseconds). The $0\nu\beta\beta$ -signal efficiency of the LAr veto cut can be estimated by evaluating the number of test pulses and baseline events that are randomly flagged as background events. This fraction has been evaluated to $(97.7 \pm 0.1)\%$ and $(98.2 \pm 0.1)\%$ for the first part of Phase II and Phase II⁺, respectively. Combining these two estimates for the whole Phase II results in an efficiency for $0\nu\beta\beta$ events of

$$\epsilon_{0\nu\beta\beta}^{\text{LAr-veto}} = (97.92 \pm 0.07)\% .$$

GRANULARITY

Since the topology of $0\nu\beta\beta$ -decay events in germanium is, to a good approximation, point-like, all events in which some energy is simultaneously deposited in more than one detector (or, with *multiplicity* higher than one) can be classified as background. In the offline analysis of a physical event, a trigger algorithm is applied over all the germanium traces to determine the presence of other signals above the threshold other than the main trigger. This *offline* trigger threshold can be as low as the electronic noise and accounts for possible electronic crosstalk effects between channels. Triggers from all detectors, independently on the status of the energy calibration⁷, are used to determine the event multiplicity.

CUT

Each event has to pass a series of quality cuts tailored to discard unphysical events such as discharges, pile-up, overflowed events and other problematic traces with very high efficiency. The $0\nu\beta\beta$ -signal efficiency of data quality cuts has been estimated by building an artificial signal-like data sample and

⁷During data taking, the status of a detector can be either *on* (fully operational), *off* (high-voltage switched off because of significant hardware instabilities e.g. leakage current, etc.) or *anti-coincidence*. The latter is set when the detector is functional but unstable from the point of view of the performance, e.g. when significant drifts are noticed in the energy of the test pulser events. The detector can be therefore reliably used only for anti-coincidence studies.

applying data quality cuts to it. The base of this data sample consists of special pure-baseline events without physical triggers, which are regularly recorded in GERDA. Since these events are artificially triggered, no signal is expected in any detector with very high probability, and they can therefore be used to characterize background noise at a given time during data taking. On top of these baseline events, special averaged waveforms from ^{228}Th double-escape peak events are added as a proxy for single-site events to produce the signal-like sample. An estimation of the acceptance of these events after quality cuts yields

$$\epsilon_{0\nu\beta\beta}^{\text{QC}} = (99.922 \pm 0.002)\%.$$

The drift of charges created by a ionizing particle in a voltage-biased germanium detector, which determines the shape of recorded event waveforms, depends on the electric field in the diode. The latter, in particular, depends on the geometry and crystal parameters like impurity concentration and gradient. Therefore, analysis techniques can be developed to discriminate between various event types in germanium detectors. Distinguishing between single-site (SSE) and multi-site (MSE) events is of primary interest for GERDA, since $0\nu\beta\beta$ decays pertain to the SSE class. The two electrons, in fact, deposit their energy within $\sim 1 \text{ mm}^3$ in germanium, and can be considered as point-like events. On the other hand, background events due to e.g. multiple Compton scattering of external γ rays are mostly of the multi-site type. Besides MSEs, surface events are another prominent source of background. Energetic β rays created at the n^+ electrode surface can penetrate the dead-layer and deposit energy in the active volume. In particular, the β decay of ^{42}K , a daughter of ^{42}Ar , naturally present in LAr, is a dangerous background in the ROI because of its high Q-value. These β decays at the n^+ surface can create “slow” pulses with incomplete charge collection because of the low electric field in the lithium-diffused region. The p^+ electrode and the insulating groove can be trespassed also by α particles. The shallowness of the p^+ boron implantation (hundreds of nanometers) and the absence of a dead layer in the groove⁸ let external β and α particles deposit energy in the detector active volume. The intense electric field causes energy depositions in this region to generate pulses with short rise times. α events on the p^+ electrode are mainly produced by ^{210}Po accumulated on its surface, most probably during detector handling. These 5.3 MeV α particles may lose part of their energy before reaching the active volume and contribute to the background in the ROI.

To mitigate all these background sources, pulse-shape discrimination (PSD) techniques were developed for BEGE and inverted-coaxial (InvCoax) detectors from one side, and semi-coaxial (SEMICoax) detectors from the other, to be applied after the LAr veto cut. For the first class a simple univariate cut was sufficient, while for the latter two techniques were worked out: one based on neural networks and one on the analysis of the rise time of the pulses. In order to avoid systematic effects, calibration, training and evaluation of the PSD methods should be performed on pulses with energies close to those of the expected signal at $Q_{\beta\beta}$. In practice, appropriate event samples are extracted from the weekly ^{228}Th calibration spectra. The PSD methods applied to the GERDA data are briefly outlined in the following. The reader is referred to [139] for a detailed treatment of the topic.

PSD for point-contact detectors (BEGE and InvCoax) is based on the A/E ratio, where A is the maximum amplitude of the current signal and E is the event energy. This technique has been extensively studied in the past in the context of GERDA [140–145]. The motivation in employing such

⁸The passivation layer, if present, is usually hundreds of nanometers thick and can be penetrated by α particles.

a relatively simple, univariate cut lies in the observation that in BEGe and InvCoax detectors, thanks to their small p⁺ contact, the electric field has a peculiar distribution. As a result, pulses induced by holes drifting along paths near the p⁺ electrode have similar shapes [141]. Moreover, multiple energy depositions in the detector can be treated as a superposition of several single interactions. It follows that a MSE will have a lower A compared to an SSE with the same E . A two-sided cut on A/E to reject MSE (slow) pulses and p⁺ (fast) events is introduced and adjusted separately for each detector. Energy and time stability corrections to A/E are discussed in detail in [139]. As mentioned before, the A/E cut values are determined with representative data samples from ²²⁸Th calibration runs⁹. The low cut position (rejection of MSEs and slow pulses) is adjusted to achieve a 90% survival fraction of the ²⁰⁸Tl double-escape peak (DEP), a SSE sample. The threshold on the high A/E side (rejection of fast pulses) has been fixed to 3 standard deviations away from the SSE distribution. The survival fraction for the 0νββ-decay signal has been calculated assuming that it is the same as for the DEP events. A full analysis of the statistical and systematic uncertainties yields

$$\epsilon_{0\nu\beta\beta}^{A/E} = (88.7 \pm 2.3)\% .$$

for the combined BEGe and InvCoax data sets.

PSD FOR SEMI COAXS

In semi-coaxial detectors the length of the holes drift path depends on the location of the energy deposition and it induces different types of pulse shapes. Because of this reason, a simple A/E cut would not be as effective as for the BEGe detectors, and therefore alternative methods have been worked out.

The primary method to reject MSE, called here ANN_{MSE}, consists in a TMVA-based artificial neural network¹⁰ and requires appropriate selection of input variables (from the rising part of the preamplifier charge pulse) and training on independent data samples. Several of these samples are available for training in calibration data (see fig. 2.11, top) and also in physics data (⁴²K full-energy peak, 2νββ events, α-induced events). The ANN_{MSE} is specifically trained on ²²⁸Th calibration data, selecting the ²⁰⁸Tl DEP as a SSE sample and the ²¹²Bi FEP at 1621 keV as a MSE sample. The classifier cut threshold is then fixed to a 90% survival probability for the ²²⁸Th DEP, and the cut signal efficiency is calculated from Monte Carlo simulations of 0νββ-decay events. The obtained ANN_{MSE} signal survival fraction is (82.2 ± 3.7)%.

α-induced events on the p⁺ electrode surface are not completely rejected by the ANN_{MSE} method. Therefore, a new method based on the analysis of the pulses rise time (RT) was developed. These events are generally characterized by a fast collection time, and their charge collection might be delayed or partial, if originated in the proximity of the groove. The RT cut exploits the fast rise time of these α events and is therefore equivalent to a volume cut, which excludes the surfaces vulnerable to the α-induced events. The rise time is defined as the time the waveform needs to reach from 10% to 90% of its amplitude. The RT-cut threshold is defined to maximize the 0νββ survival fraction and the signal-to-noise

⁹The ²²⁸Th calibration data constitutes a high-statistic and rich set of events with different interaction topologies in germanium detectors. Full-energy peaks (FEP) (e.g. at 2615 keV from ²⁰⁸Tl or 1621 keV from ²¹²Bi in fig. 2.11) are composed by γ events releasing all their energy in germanium. Other interaction topologies occur when 511 keV photons from pair-production processes “escape” the active volume, reducing the total collected event energy. These events form the *single-escape* peak (SEP) or the *double-escape* peak (DEP), depending on the number of escaped photons. The ²⁰⁸Tl SEP and DEP are clearly visible in regular calibration spectra (see fig. 2.11). Because of their interaction topology, FEP and DEP events are mainly multi-site and single-site events, respectively, and can be exploited as a test sample for 0νββ pulse-shape discrimination techniques.

¹⁰The TMVA library is part of the ROOT data analysis toolkit [146]

ratio at the same time through the definition of a figure of merit. The latter is defined as the product of the $2\nu\beta\beta$ -signal survival square-probability and the α -events rejection probability. The $2\nu\beta\beta$ and α -event test samples are obtained from physics data by selecting data in the [1.0, 1.3] MeV and > 3.5 MeV energy regions, respectively, after ANN_{MSE} and LAr veto cuts. The $0\nu\beta\beta$ -signal efficiency of the RT cut is assumed to be the same as for $2\nu\beta\beta$ decays and hence estimated to 82.3%, with an uncertainty on the order of 1% [147].

Events featuring slow charge collection might suffer from ballistic deficit in the ZAC energy reconstruction [130] and survive the PSD cuts, especially in semi-coaxial detectors. Therefore, an additional rejection criteria is applied based on the energy reconstructed with different integration times. The figure of merit for such a cut is the ratio between the energy of an event reconstructed with a short (4 μ s) integration time E_s and the energy reconstructed with a long (10 μ s) integration time E_l . The energy here is reconstructed using a gaussian-shaping filter, which has been the default GERDA energy reconstruction method for Phase I. Since ballistic deficit is observed to reduce this ratio, the δE classifier is defined as $\delta E = E \cdot ([E_s/E_l]_{\text{norm}} - 1)$, where the energy ratio is normalized to values assumed by the ^{228}Th FEP events. The normalization is applied in a certain calibration-validity period and for each detector separately. The cut value is defined as 3 negative standard deviations away from the mean of the FEP δE distribution. The survival fraction of $2\nu\beta\beta$ events, which provides an estimate of the $0\nu\beta\beta$ efficiency, is higher than 98% for all detector types. It has been estimated, after all the other PSD cuts, to $(99.449 \pm 0.006)\%$ for SEMICOAX, $(99.9572 \pm 0.0003)\%$ for BEGE and 100% for INVCOAX detectors separately. A weighted combination yields:

$$\epsilon_{0\nu\beta\beta}^{\delta E} = (99.769 \pm 0.002)\%.$$

The ANN_{MSE}, RT, A/E and δE cut efficiencies can be combined to obtain an overall survival fraction for $0\nu\beta\beta$ -decay events after the PSD cut:

Before upgrade (%)		After upgrade (%)		
SEMICOAX	BEGE	SEMICOAX	BEGE	INVCOAX
69.1 ± 5.6	88.2 ± 3.4	68.8 ± 4.1	89.0 ± 4.1	90.0 ± 1.8

Combining all data together one gets

$$\epsilon_{0\nu\beta\beta}^{\text{PSD}} = (80.8 \pm 2.1)\%$$

as total $0\nu\beta\beta$ PSD signal efficiency for the full Phase II data set.

2.3 Final GERDA results on the search for $0\nu\beta\beta$ decay

The full Phase II single-detector data is presented in this section together with LAr veto and PSD data. The statistical analysis used to extract a lower limit for the $0\nu\beta\beta$ half-life in ^{76}Ge is finally presented, and the results for the combined GERDA data are given.

As already emphasized in §1.4, a good energy resolution is a key ingredient to achieve a high $0\nu\beta\beta$ -decay sensitivity. The main goal of the calibration analysis is therefore to define and maintain a stable

ENERGY
SCALE AND
RESOLUTION

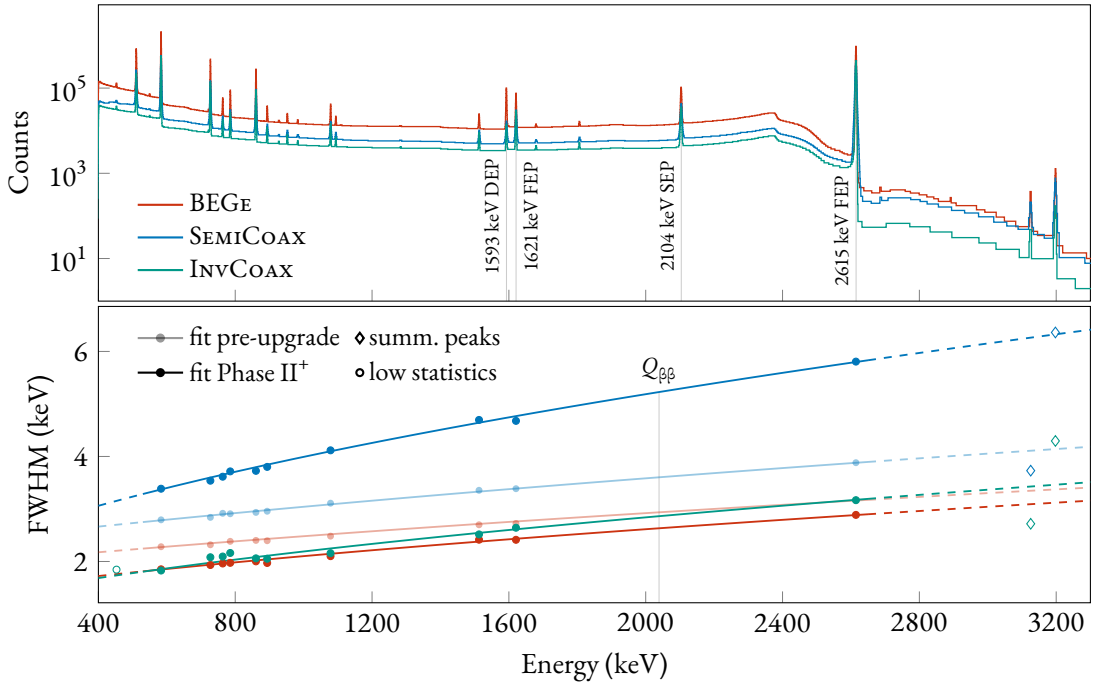


Figure 2.11: Top panel: summed ^{228}Th calibration spectra of BEGE, semi-coaxial and inverted-coaxial detectors as used to determine the energy resolution curves. Bayesian blocks are used to display the histograms (see app. F). Three prominent ^{208}Tl high-energy peaks (full-energy, single-escape and double-escape) and the ^{212}Bi full-energy peak at 1621 keV are highlighted. Bottom panel: extracted peak widths (FWHM) and fitted calibration curves for pre- and post-upgrade data separately. Points represented by empty markers are excluded from the fit because of additional effects that contribute to the width. Diamonds label summation peaks.

energy scale over years of data taking. It is necessary to identify the peak region (and reject all background events with different energy), combine data from different detectors over extended periods of time, and efficiently exploit the excellent energy resolution of germanium detectors.

As already mentioned in §2.1, germanium detectors are calibrated by exposing them to ^{228}Th sources with an activity of about 10 kBq. A typical calibration spectrum is shown in fig. 2.11. The pattern of γ lines in the spectrum can be exploited to identify selected peaks and calibrate the energy scale of a detector with their known position in terms of energy. Additionally, the detector resolution can be determined from the γ lines width. Once the positions and the widths are determined by modeling the peaks with a suitable analytical function, a function interpolation is performed to obtain the energy calibration and resolution at other energies. Once these two curves are determined for a given calibration, they are assumed to be valid until the next one. This validity is constantly monitored by evaluating the shift of the pulser event energy over time with respect to its value right after a calibration. Time periods in which a detector shows deviations from its calibration above a certain threshold are removed from the final analysis in order to meet the stringent requirements for the $0\nu\beta\beta$ analysis in terms of uncertainties on the energy scale and resolution. Fluctuations below this threshold are taken into account when estimating the systematic contribution to the uncertainty on the energy resolution. The stability of the energy scale and resolution is also monitored on a calibration basis, and time periods for which detectors show a degraded performance are excluded from combined analysis data sets. The calibration spectra that refer to these combined data sets are obtained by summing together spectra from all the calibration runs of the relative time period weighted by their actual validity in time. Gaussian mixtures are usually not needed to model peaks in these combined spectra, as the variance of the single centroids and widths is usually small enough to enable the use of single gaussian distributions with effective parameters. The effective data set energy resolution as a function of energy is then determined by fitting the square root of a linear function to the reconstructed γ -line widths. The uncertainty on this effective resolution includes systematic contributions from the choice of the peak model, the resolution function and time stability of the experimental setup. The resolution curves for BEGE, semi-coaxial and inverted-coaxial Phase II⁺ data sets are reported in fig. 2.11 as an example. The energy resolution at $Q_{\beta\beta}$ (FWHM) for Phase II is the following:

Before upgrade (keV)		After upgrade (keV)		
SEMI COAX	BEGE	SEMI COAX	BEGE	INV COAX
3.6 ± 0.3	2.9 ± 0.3	5.2 ± 1.9	2.6 ± 0.2	2.9 ± 0.1

The calibrated energy spectrum of the GERDA Phase II data after granularity cut is shown in fig. 2.12, empty histogram.

The first cut applied to Phase II data (after the quality cuts and the multiplicity cut) is the LAr veto cut. Event energy histograms before and after this event selection are shown in fig. 2.12. The cut clearly suppresses background events from the ^{228}Th and ^{238}U decay chains, as well as ^{42}K events. The ^{42}K FEP event reduction to 20% and 18% in Phase II and Phase II⁺ data, respectively, demonstrates the effectiveness of the improved fiber instrumentation installed for Phase II⁺. ^{40}K events, which are characterized by a single γ emission at 1461 keV and typically do not deposit energy in LAr, show a high survival fraction of about 98%, but cannot enter the ROI at 2039 keV and are therefore of minor concern. α events that dominate the energy spectrum at higher energies cannot be vetoed by the LAr

LAR VETO AND
PSD CUTS ON
DATA

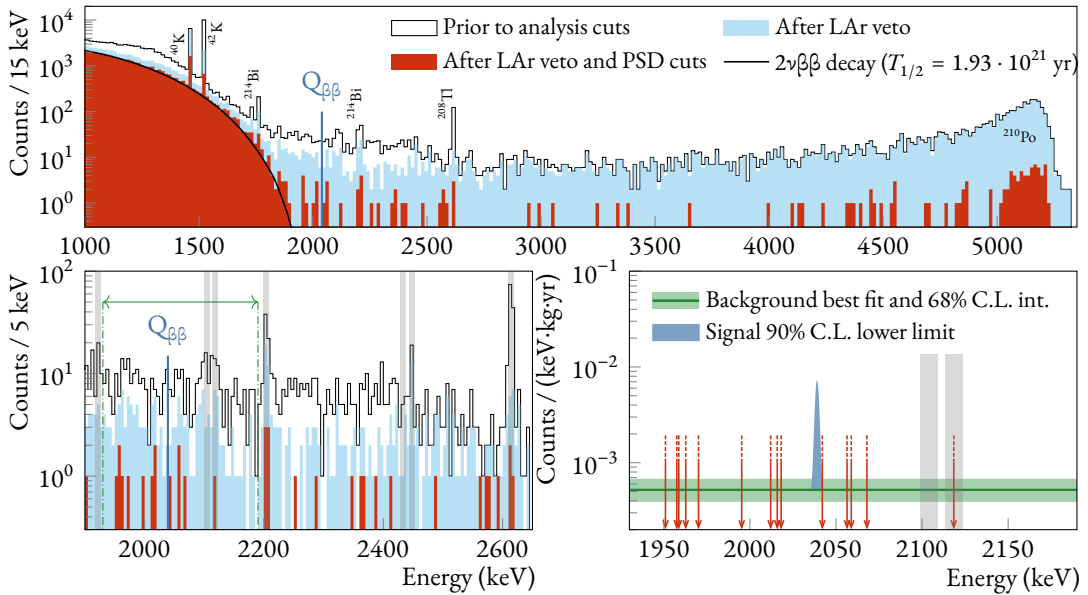


Figure 2.12: Single-detector data from the enriched detectors is displayed in a combined spectrum after indicated cuts. Main contributions to the spectra are labeled in the top panel. The bottom-left panel shows data in the $Q_{\beta\beta}$ region. Known γ peaks and the $0\nu\beta\beta$ analysis window are highlighted in gray and green, respectively. The bottom-right panel shows unbinned data after all cuts in the analysis window and the fit results.

instrumentation and still constitute a major background at $Q_{\beta\beta}$.

PSD data versus energy is showed in fig. 2.13 subdivided according to the PSD method. Data from BEGE and inverted-coaxial detectors, for which the A/E cut is used, is shown in the top-left plot. Data from semi-coaxial detectors, for which the ANN_{MSE} and the rise-time cuts are implemented, is shown in the remaining plots. Colored data points correspond to events that survive the PSD cut.

The energy range considered for the $0\nu\beta\beta$ statistical analysis goes from 1930 keV to 2190 keV, excluding the two regions 2014 ± 5 keV and 2119 ± 5 keV in which two known γ lines from ^{214}Bi and ^{208}Tl lie. No other non-flat background structure is expected from the background studies that will be presented in the following chapters. The analysis window is shown in fig. 2.12: in green in the bottom left panel and in the bottom right panel. After the unblinding, 13 events are found in this analysis window after all cuts (5 in SEMICOAX, 7 in BEGE and 1 in INVCOAXdetectors). These events are likely due to α decays, ^{42}K β decays or γ decays from ^{238}U and ^{232}Th series. Data which were unblinded in [132], when less effective PSD techniques against surface events were available, have been re-analyzed according to the new methods described in this work: as a consequence, three events (at energies 1967, 2061 and 2064 keV) that were previously included in the analysis window in past data releases [116, 132, 133] are now discarded.

STATISTICAL ANALYSIS

The energy distribution of the events in this window is fitted to search for a $0\nu\beta\beta$ -decay signal. The baseline fit model includes a Gaussian distribution for the signal, centered at $Q_{\beta\beta}$ with a width corresponding to the energy resolution, and a uniform distribution for the background. The free parameters of the fit are the signal strength $S = 1/T$ and the background index B . The number of signal

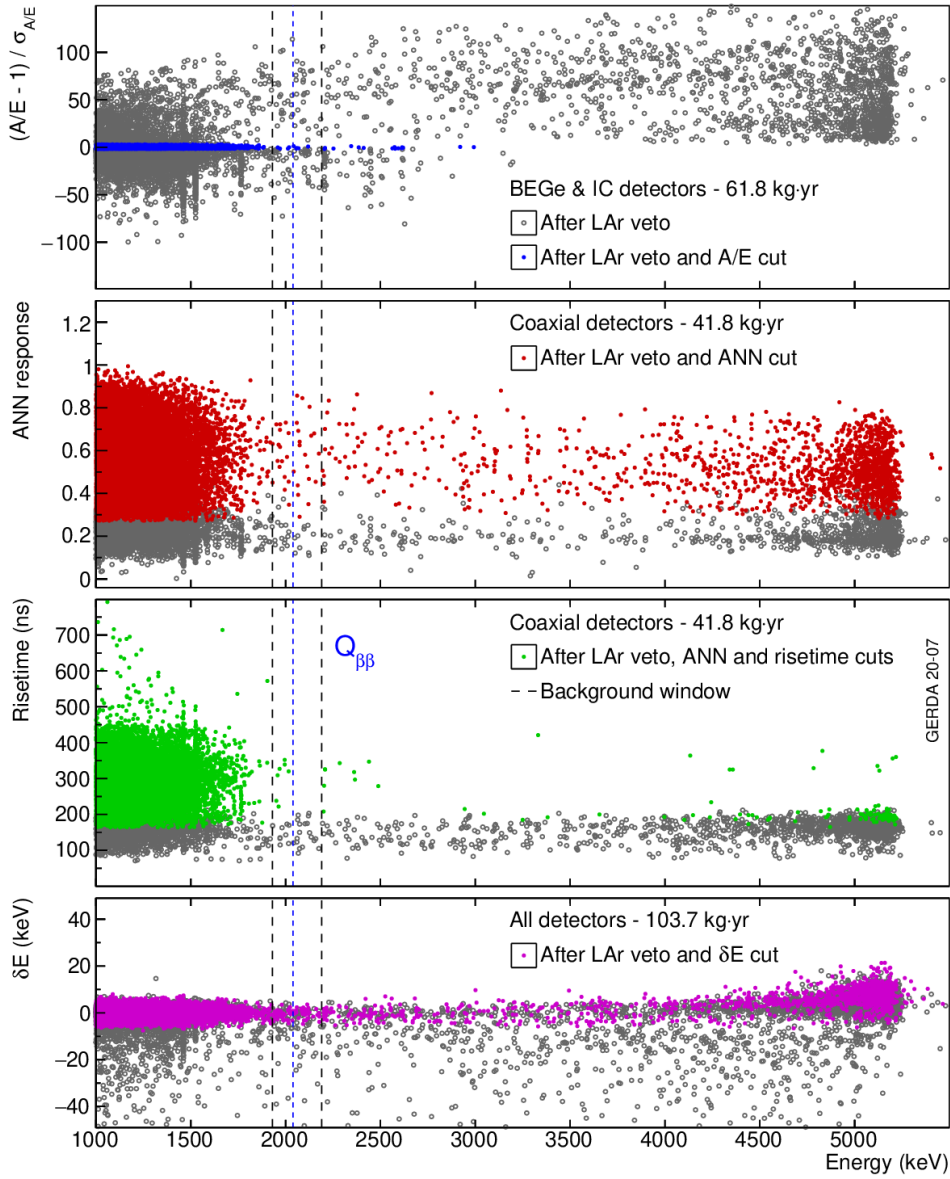


Figure 2.13: The four pulse shape discrimination techniques applied on the final GERDA Phase II data set. From top to bottom: the A/E cut, the ANN_{MSE} cut, the rise-time cut and the δE cut. Note that, being the δE cut highly-correlated with A/E in BEGe and InvCoax detectors, its direct application on data after the LAr veto cut results in a high cut efficiency. If applied after all others PSD cuts, the event survival fraction is >99%.

Table 2.1: Summary of the parameters of interest for GERDA Phase II for different detector types and before/after the upgrade. The components of the total efficiency ϵ for $0\nu\beta\beta$ decays are also reported individually. The efficiency factors due to muon veto and quality cuts are above 99.9% and are not shown explicitly. Energy resolution and all $0\nu\beta\beta$ decay efficiencies are reported as exposure-weighted average for each detector type and their uncertainties are given as standard deviation.

	Dec 2015 – May 2018		July 2018 – Nov 2019		
	SEMI-Coax	BEGE	SEMI-Coax	BEGE	InvCoax
Number of detectors	7	30	6	30	5
Total mass	15.6 kg	20 kg	14.6 kg	20 kg	9.6 kg
Exposure \mathcal{E}	28.6 kg·yr	31.5 kg·yr	13.2 kg·yr	21.9 kg·yr	8.5 kg·yr
Energy resolution at $Q_{\beta\beta}$ (FWHM)	(3.6 ± 0.2) keV	(2.9 ± 0.3) keV	(4.9 ± 1.4) keV	(2.6 ± 0.2) keV	(2.9 ± 0.1) keV
$0\nu\beta\beta$ decay detection efficiency ϵ :	$(46.2 \pm 5.2)\%$	$(60.5 \pm 3.3)\%$	$(47.2 \pm 5.1)\%$	$(61.1 \pm 3.9)\%$	$(66.0 \pm 1.8)\%$
<i>Electron Containment</i>	$(91.4 \pm 1.9)\%$	$(89.7 \pm 0.5)\%$	$(92.0 \pm 0.3)\%$	$(89.3 \pm 0.6)\%$	$(91.8 \pm 0.5)\%$
<i>^{76}Ge enrichment</i>	$(86.6 \pm 2.1)\%$	$(88.0 \pm 1.3)\%$	$(86.8 \pm 2.1)\%$	$(88.0 \pm 1.3)\%$	$(87.8 \pm 0.4)\%$
<i>Active volume</i>	$(86.1 \pm 5.8)\%$	$(88.7 \pm 2.2)\%$	$(87.1 \pm 5.8)\%$	$(88.7 \pm 2.1)\%$	$(92.7 \pm 1.2)\%$
<i>Liquid Argon veto</i>	$(97.7 \pm 0.1)\%$	$(98.2 \pm 0.1)\%$	$(98.2 \pm 0.1)\%$	$(98.2 \pm 0.1)\%$	$(90.0 \pm 1.8)\%$
<i>Pulse shape discrimination</i>	$(69.1 \pm 5.6)\%$	$(88.2 \pm 3.4)\%$	$(68.8 \pm 4.1)\%$	$(89.0 \pm 4.1)\%$	$(90.0 \pm 1.8)\%$

events scales with S as

$$\mu_s = \frac{\mathcal{N}_A \log 2}{M_{76}} \cdot \epsilon \cdot \mathcal{E} \cdot S , \quad (2.1)$$

where \mathcal{N}_A is the Avogadro number, M_{76} is the ^{76}Ge molar mass, \mathcal{E} is the total exposure scrutinized and ϵ is the total $0\nu\beta\beta$ detection efficiency. The efficiency ϵ accounts for the enrichment fraction in ^{76}Ge , the active volume fraction of the germanium detectors, the electron containment efficiency and the analysis cuts. The latter include the quality cuts, the muon veto cut, the LAr veto cut and the PSD cut. The efficiency ϵ is evaluated on the full Phase II dataset to be $(47.0 \pm 3.9)\%$ for the SEMICOAX detectors $(60.7 \pm 2.5)\%$ for the BEGE detectors and $(66.0 \pm 1.8)\%$ for the INVCOAX detectors. The average total efficiency ϵ and the breakdown in the individual components are listed in tab. 2.1 The number of background events in the analysis window is given by

$$\mu_b = B \cdot \Delta E \cdot \mathcal{E} , \quad (2.2)$$

where $\Delta E = 240$ keV is the effective width of the window after removing the two aforementioned γ -line regions.

Data from each detector is divided in partitions, i.e. periods of time in which parameters such as the resolution and efficiency are stable. The parameters of each of the 408 partitions are indicated by the index k . The signal strength S and the background index B instead are common parameters to all partitions. This construction constitutes a significant improvement over the previous data releases [116, 132, 133] as it allows a precise tracing of the performance of each detector at a given moment. Another difference compared to the previous analyses is that the background index is now assumed to be the same for all detectors, while independent parameters were used in the past for each detector type. There is no statistical evidence indeed that the background is different between the three detector types, or detector position within the array, or time.

The statistical analysis is based on an unbinned extended likelihood function and it is performed in both frequentist and Bayesian frameworks, following the procedure described in [132]. The likelihood function is given by the product of likelihoods of each partition:

$$\mathcal{L} = \prod_k \left[\frac{(\mu_s + \mu_b)^{N_k} e^{-(\mu_s + \mu_b)}}{N_k!} \times \frac{1}{\mu_s + \mu_b} \times \prod_{i=1}^{N_k} \left(\frac{\mu_b}{\Delta E} + \frac{\mu_s}{\sqrt{2\pi\sigma_k^2}} e^{-\frac{(E_i - Q_{\beta\beta})^2}{2\sigma_k^2}} \right) \right] ,$$

where E_i is the energy of the N_k events in the k -th partition and $\sigma_k = \text{FWHM}/2.35$ is the energy resolution of the partition. The parameters μ_s and μ_b are calculated from eqs. (2.1) and (2.2) respectively and are a function of the efficiency ϵ_k and the exposure \mathcal{E}_k of each partition. Phase I data sets are included in the analysis as individual partitions with independent background indices.

The frequentist analysis is performed using a two-sided test statistics based on the profile likelihood, as described in [132]. The probability distributions of the test statistic have been computed using Monte Carlo techniques, as they are found to significantly deviate from χ^2 distributions. The analysis of the $N = 13$ events of Phase II returns no indication for a signal and a lower limit is set to $T_{1/2}^{0\nu} > 1.5 \cdot 10^{26}$ yr at 90% C.L. Phase I and Phase II data together give a total exposure of 127.2 kg·yr. The combined analysis has also a best fit for null signal strength, and provides a half-life limit of

$$T_{1/2}^{0\nu} > 1.8 \cdot 10^{26} \text{ yr at 90\% C.L.}$$

The limit coincides with the median expectation under the no-signal hypothesis (i.e. the sensitivity): $1.8 \cdot 10^{26}$ yr at 90% C.L. GERDA achieved an unprecedentedly low background in Phase II, as derived from the fit, of $B = 5.2_{-1.3}^{+1.6} \cdot 10^{-4}$ cts/(keV·kg·yr), and met the design goal to run the entire Phase I data taking in the background-free regime: the number of background events expected in the signal region ($Q_{\beta\beta} \pm 2\sigma$) is in fact 0.3.

The statistical analysis is carried out also within a Bayesian framework. The one-dimensional posterior probability density function $P(S|\text{data})$ of the signal strength is derived by marginalizing over the other free parameters. The calculation is performed via a Markov chain Monte Carlo (MCMC) numerical integration using the Bayesian analysis toolkit BAT [148]. The prior distribution for S is assumed to be constant between 0 and 10^{-24} yr $^{-1}$, as in the previous GERDA releases. The limit on the half-life is $T_{1/2}^{0\nu} > 1.4 \cdot 10^{26}$ yr (90% C.I.). Other choices for the prior are also possible: as instance, equiprobable Majorana neutrino masses (prior $\propto 1/\sqrt{S}$). The limit derived in this case is significantly stronger, $T_{1/2}^{0\nu} > 2.3 \cdot 10^{26}$ yr (90% C.I.), as the prior gives a higher probability for low values of S .

Uncertainties on the energy reconstruction, energy resolution, and efficiencies are folded into the analysis through additional nuisance parameters, each constrained by a Gaussian probability distribution in the likelihood. Their overall effect on the limit is at the percent level. Potential systematic uncertainties related to the fit model have been studied and found to marginally impact the results. In particular, different background energy distribution were investigated and it was found that in all cases the limit is stable within a few percent.

OUTLOOK

GERDA was the first experiment to have reached a $0\nu\beta\beta$ half-life sensitivity above 10^{26} yr. At the time of writing, GERDA is providing the best sensitivity and the most stringent half-life constraint of the entire field.

The $T_{1/2}^{0\nu}$ limit can be converted into an upper limit on the effective Majorana mass ($m_{\beta\beta}$) under the assumption that the decay dominated by the exchange of light Majorana neutrinos. Assuming an unquenched value of the axial coupling constant $g_A = 1.27$, the phase space factors and the set of most recent nuclear matrix elements, an upper limit of $m_{\beta\beta} = 79\text{--}182$ meV is obtained, which is comparable to the most stringent constraints from other isotopes [62–64]. GERDA has been a pioneering experiment in the search for $0\nu\beta\beta$ decay. In about a decade, GERDA improved the experimental sensitivity by one order of magnitude with respect to previous ${}^{76}\text{Ge}$ experiments and proved that a background-free experiment with ${}^{76}\text{Ge}$ is feasible. This paves the way for the next generation experiment that is currently being prepared by the LEGEND collaboration.



IN SHORT

- The GERDA experiment is searching for neutrinoless double-beta decay with high-purity germanium detectors enriched in the ^{76}Ge double-beta emitter at the Laboratori Nazionali del Gran Sasso in Italy. In its second experimental phase, GERDA deployed 35 kg of enriched detectors into liquid argon, to provide an active and passive shield to background events. The data taking stopped in 2019 after collecting more than 100 kg·yr of data and surpassing the 10^{26} yr signal sensitivity in the background-free regime. GERDA adopts a rigorous data blinding scheme by removing events in the region of interest from the primary data stream. These events are analyzed after the analysis procedures are fixed.
- Several background reduction techniques have been worked out to achieve a background index on the order of 10^{-3} cts/(keV·kg·yr) in the $0\nu\beta\beta$ region of interest. A liquid argon veto system is constructed to tag background events that deposit energy in the LAr by collecting its scintillation light. The instrumentation includes light-guiding fiber curtains, PMTs and several wavelength-shifting surfaces. Algorithms to determine the event topology from pulse-shape data and reject multiple-site events have been developed, with an overall 80% efficiency on the $0\nu\beta\beta$ signal.
- The full GERDA data set is analyzed in frequentist and Bayesian frameworks. Data from each detector is divided in partitions in which parameters such as the resolution and efficiency are stable, a significant improvement over previous data releases. The extracted final lower limit on the neutrinoless double-beta decay half-life at 90% C.L. is $1.8 \cdot 10^{26}$ yr, with a background index of $5.2_{-1.3}^{+1.6} 10^{-4}$ cts/(keV·kg·yr) achieved in the region of interest. GERDA is the experiment providing the best sensitivity, the most stringent half-life constraint and the lowest background at the $Q_{\beta\beta}$ of the entire field. The pioneering effort of GERDA paves the way for the next-generation, tonne-scale experiment that is currently being prepared by the LEGEND collaboration.

The background before analysis cuts

A precise knowledge of background intensity and distribution is essential to searches for faint signals. One main assumption of the $0\nu\beta\beta$ -decay signal analysis is the distribution of background events in the analysis window around $Q_{\beta\beta}$ being uniform, except for known ^{208}Tl and ^{212}Bi γ lines. The primary role of the background model is to verify this assumption by exploiting data outside this energy region or filtered with a different event selection. The background model is also complementary to assay measurements in determining the location of the most dangerous background sources and learn how to improve experimental design and material selection in similar future projects. Lastly, a good background model allows to statistically isolate $2\nu\beta\beta$ -decay events, estimate the half-life of the process and study their distribution as a source of potential new-physics effects (see chap. 1).

A first background model has been built for the GERDA Phase I data and published in [149]. Later, a new and advanced model has been constructed to describe the first 60 kg·yr of Phase II data before the LAr veto and PSD cuts, which has been published in [150] and is described in detail in this chapter. In §3.1 the selected data is presented and characterized, while the procedure to compute the theoretical expectations used in the statistical analysis is outlined in §3.2 (the topic is addressed in more detail in app. C). The prior knowledge about the presence of contaminants in the GERDA setup that contribute to the germanium background spectrum is summarized in §3.3. The statistical framework and the analysis strategy is presented in §3.4. As it will be shown, the high-statistic ^{40}K , ^{42}K and α event data samples deserve dedicated studies and are thus treated separately. These potassium and α event analyses are presented in §3.6 and §3.5 respectively. Finally, the results of the background decomposition in the full energy range of data from the first part of Phase II will be given in §3.7 and discussed in §3.8. To complete the survey of background contributions to the complete GERDA Phase II energy spectrum before analysis cuts, the background model of data from the second part of Phase II (Phase II⁺) is presented in §3.9.

3.1 Analysis data sets

As already mentioned, the background model before cuts has been developed using data from the first part of Phase II, namely, for data acquired starting from December 2015 to March 2018. Single-detector (or multiplicity-one, abbreviated M1) events and two-detector (multiplicity-two, abbreviated M2) events are considered for this analysis. Events from the semi-coaxial detectors with natural isotope composition, located in the central detector string, are not used in this analysis due to large uncertainties on their n^+ contact thickness and detection efficiency. The M1 events are split in two data sets based on

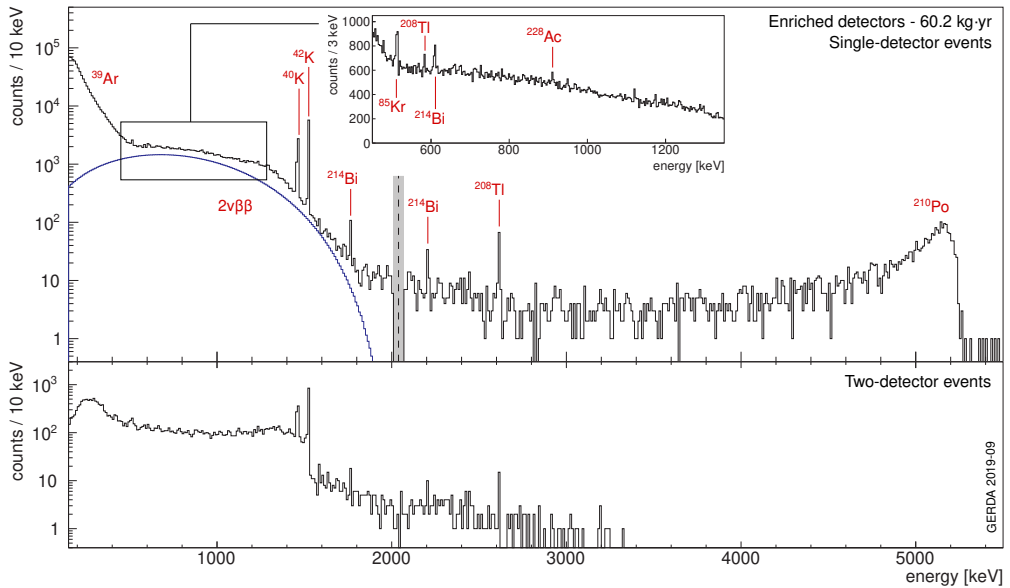


Figure 3.1: Summed energy spectra of single-detector events (M1-BEGe and M1-SemiCoax, top panel) and two-detector events (M2-AllEnr, bottom panel) collected in GERDA Phase II. The prominent features due to detector intrinsic $2\nu\beta\beta$ events, ^{39}Ar and ^{85}Kr in the LAr, ^{40}K , the ^{232}Th and ^{238}U decay chains are highlighted. The window blinded for the $0\nu\beta\beta$ analysis is marked in grey.

the two enriched detector geometries which we call M1-BEGe and M1-SemiCoax in the following. The M2 data form a third data set which is named M2-AllEnr. The energy we associate to an M2 event is the sum of the energies reconstructed in the two detectors. The data sets, their exposure and respective detector mass are listed in tab. 3.1.

The event energy distribution of the three data sets is displayed in fig. 3.1: the sum spectrum of M1-BEGe and M1-SemiCoax in the top panel and M2-AllEnr in the bottom panel. For the single-detector data, in the top panel, the following features are most noticeable: the β decay of ^{39}Ar dominates the spectrum up to 565 keV while between 600 and 1500 keV the most prominent component is the continuous spectrum of $2\nu\beta\beta$ decay of ^{76}Ge . Two γ lines at 1461 and 1525 keV can be attributed to ^{40}K and ^{42}K ; further visible γ lines belonging to ^{85}Kr , ^{208}Tl , ^{214}Bi and ^{228}Ac are indicated in the figure. The highest energies displayed are dominated by a peak-like structure emerging at 5.3 MeV with a pronounced low energy tail. This is a typical spectral feature of α particles and can, here, be attributed to ^{210}Po decay on the thin detector p^+ surfaces [149]. Events above the ^{210}Po peak belong to α decays emerging from the ^{226}Ra sub-chain on the detector p^+ surfaces. All these components contribute also to M2-AllEnr except for ^{39}Ar , $2\nu\beta\beta$ and high energy α -components. This is due to the short range of α (tens of μm) and β particles (typically smaller than 1.5 cm) in LAr and germanium with respect to the distance between detectors which is of the order of several cm.

¹The BEGe detector GD02D is the only detector that does not fully deplete [121]. Hence, events triggered by this detector are not considered in either data set and it is omitted from the mass computation.

Table 3.1: Properties of the data sets considered in this analysis. Further details about the GERDA detectors can be found in past publications [121, 149]. Note that the BEGe exposure of $31.1 \text{ kg}\cdot\text{yr}$ is higher than the one reported in [116] because additional data for which PSD methods are not applicable is here included.

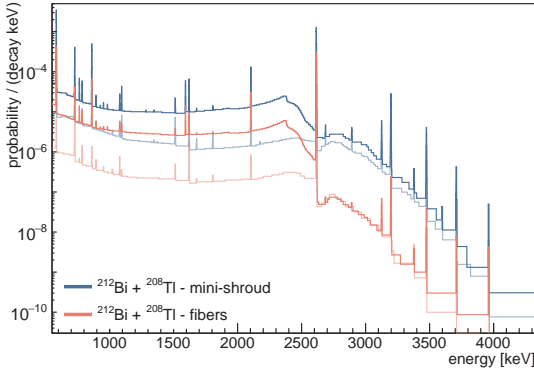
data set	composition	total Ge mass (kg)	active ^{76}Ge mass (kg)	total Ge exposure (kg·yr)	active ^{76}Ge exposure (kg·yr)
M1-BEGe	29 BEGe ¹	19.362 ± 0.029	15.06 ± 0.40	32.124 ± 0.048	25.08 ± 0.45
M1-SemiCoax	7 SEMICOAX	15.576 ± 0.007	11.61 ± 0.54	28.088 ± 0.013	21.0 ± 1.0
M2-AllEnr	all enriched	34.938 ± 0.030	26.67 ± 0.67	60.212 ± 0.050	46.1 ± 1.1

3.2 Monte Carlo simulations and probability density functions

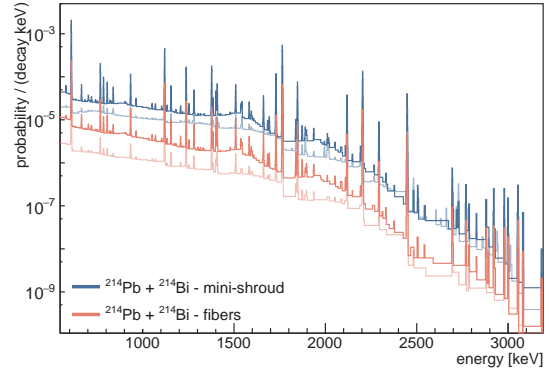
The probability density functions (PDFs) used to model contributions to the energy spectra are obtained from Monte Carlo simulations. The latter are performed using the MAGE simulation framework [151], based on GEANT4 v10.4 [152–154]. MAGE contains a software implementation of the GERDA Phase II detectors as well as the assembly and all other surrounding hardware components. A visualization of this implementation is presented in fig. 2.7. Detector intrinsic $2\nu\beta\beta$ decays of ^{76}Ge and background events originating from radioactive contaminations in and around the detector assembly are simulated. The energy spectrum of the two electrons emitted in the $2\nu\beta\beta$ decay is sampled according to the distribution given in [25] and implemented in DECAY0 [155]. The PDFs are obtained from the Monte Carlo simulations, taking into account the finite energy resolution and individual exposure acquired with each detector during the considered data taking periods. Special care is taken not to statistically bias the PDFs by assuring that each simulated decay is taken into account only once in the production of a PDF. For more details see app. C. The germanium detector active volume model is also applied to the simulations during this post-processing step. A simplified step-like function that defines the charge-collection efficiency (CCE) value depending on the depth from the detector surface is used to produce the PDFs for the analysis of Phase II data before the upgrade. The CCE is set to a null value through all the transition region between the surface and the full charge-collection efficiency region. From the full charge-collection depth (FCCD) and below, the CCE is set to unity. The recommended FCCD values obtained from dedicated characterization data (the same used in the $0\nu\beta\beta$ detection efficiency calculation) are documented and discussed in app. A. The PDFs for the background model of GERDA Phase II data before cuts are displayed in figs. 3.2, 3.3, C.1 and C.2 and will be presented in more detail in the following.

3.3 Background expectations

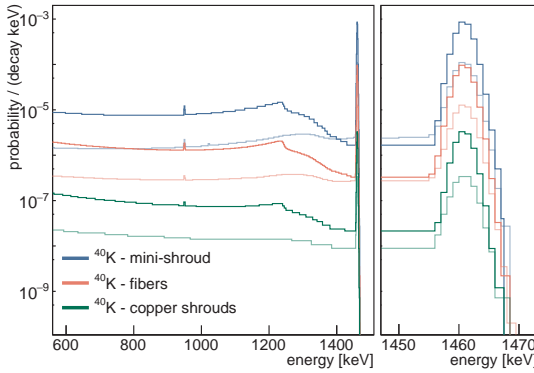
The structural components of the setup have been screened for their radio-purity before deployment. Two measurement methods were used depending on the screened isotope: γ -ray spectroscopy ($\text{Ge}-\gamma$) with high-purity germanium (in four underground laboratories, for details see reference [156]) and mass spectrometry with Inductively Coupled Plasma Mass Spectrometers (ICP-MS) [157]. Especially materials close to the detectors have been screened for radioactive contaminations originating from the ^{238}U and ^{232}Th decay chains, ^{40}K and ^{60}Co . For measured activities and upper limits see app. B and



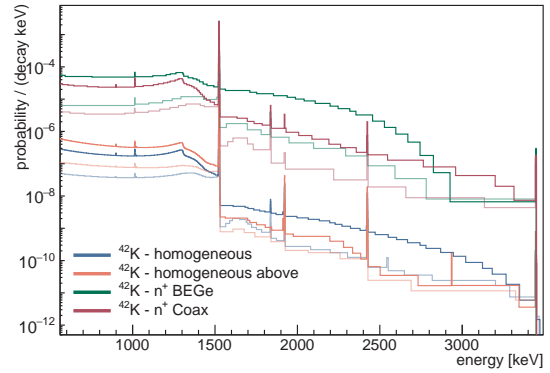
(a) ^{212}Bi and ^{208}Tl (^{232}Th chain) contaminations far from (fiber shroud) and close to (mini-shrouds) the detectors.



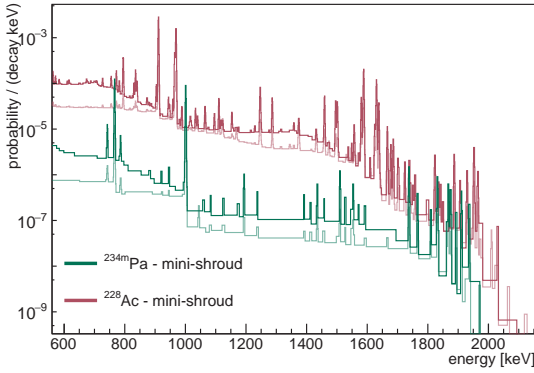
(b) ^{214}Bi and ^{214}Pb (^{238}U chain) contaminations far from (fiber shroud) and close to (mini-shrouds) the detectors.



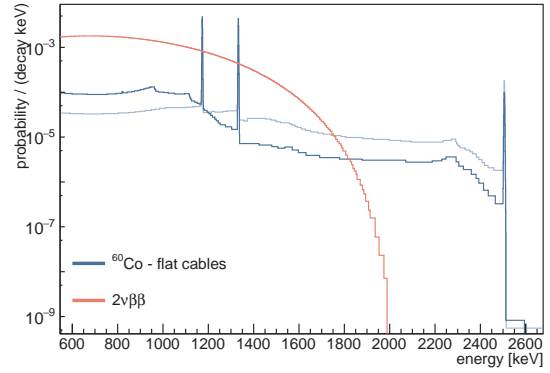
(c) ^{40}K contamination close to the detectors (mini-shrouds), at a higher radial distance (fiber shroud) and higher vertical distance (copper shrouds).



(d) ^{42}K contamination in different locations inside the LAr.



(e) $^{234\text{m}}\text{Pa}$ and ^{228}Ac contaminations in the close vicinity of the detectors (mini-shrouds).



(f) ^{60}Co contamination in the signal and high-voltage cables and detector intrinsic ^{76}Ge $2\nu\beta\beta$ decay.

Figure 3.2: The PDFs for the M1-AllEnr (M1-BEGe+M1-SemiCoax) (in fully opaque colors) and the M2-AllEnr (in shaded colors) data sets in the full energy domain and relative to different background sources. Bayesian blocks are used to visualize histograms (see app. F for details). All PDFs are normalized to the number of simulated events.

sec. 5 in [121]. All possible background sources taken into consideration in this analysis are described in detail below.

The only isotopes simulated are ^{234m}Pa , ^{214}Pb and ^{214}Bi from the ^{238}U decay chain and ^{228}Ac , ^{212}Bi and ^{208}Tl from the ^{232}Th decay chain. The following groups of isotopes are assumed to be in secular equilibrium:

$$^{238}\text{U} > ^{234m}\text{Pa} \parallel ^{226}\text{Ra} > ^{214}\text{Pb} > ^{214}\text{Bi} \parallel ^{228}\text{Ra} > ^{228}\text{Ac} \parallel ^{228}\text{Th} > ^{212}\text{Bi} > ^{208}\text{Tl}.$$

Their decay products consist of γ or β particles with an energy higher than 520 keV (figs. 3.2a, 3.2b and 3.2e). Less energetic particles from the remaining constituents in the chain do not enter the energy window which is considered in the presented analysis. The α emitters from the decay chains contaminating the thin p^+ electrodes are described in a separate paragraph below.

A significant fraction of components in the GERDA setup is made of copper [121], which can be produced with high radio-purity but is potentially activated by cosmic rays and contaminated by the long-lived isotope ^{60}Co (fig. 3.2f). The latter decays with a half-life of 5.2711(8) yr; from material screening it is also expected to be found in some of the detector high-voltage flexible flat cables.

This isotope is found in all screened materials. Construction materials were not optimized for ultra-low ^{40}K content because the Q-value of its decay is well below $Q_{\beta\beta}$ and hence does not contribute to the background in the ROI. The ^{40}K decay spectrum exhibits a γ line at 1460.822(6) keV (see fig. 3.2c) with an accumulated statistics on the order of 100 cts/detector. In fig. C.1 the expected counts per detector channel for ^{40}K simulated in different locations are shown. Using the ratio of events detected in different detectors, information about the spatial distribution of ^{40}K can be extracted. This spatial information is used to resolve degeneracies of ^{40}K in the energy spectra (for details see §3.6).

A cosmogenically-produced isotope in LAr is ^{42}Ar ($T_{1/2} = 32.9(11)$ yr) which decays to ^{42}K . The distribution of ^{42}K inside the LAr is likely to be inhomogeneous due to drift of the ionized decay products induced by the electric field (generated by high-voltage cables and detectors) and convection [158]. ^{42}K decays to ^{42}Ca via β decay with a half-life of 12.355(7) h and a Q-value of 3525.22(18) keV, well above $Q_{\beta\beta}$ (see fig. 3.2d). For the β particle to be detected the decay needs to happen within a distance of a few centimeters² to the detector surface. As the detectors are in direct contact with the LAr, the β component of ^{42}K potentially gives one of the most significant contributions to the background in the ROI. Therefore, we separate decays originating inside and outside the mini-shrouds in the following analysis. The full-range fit has little sensitivity to any potassium inhomogeneity outside the mini-shrouds. ^{42}K is hence assumed to be distributed homogeneously in this region. Based on detector-wise observations, however, a surplus of ^{42}K above the detector array in the vicinity of the front-end electronics is deduced (see §3.6). Inside the mini-shrouds the β spectrum becomes potentially important. Some scenarios are possible: the closer ^{42}K decays to the detector surface, namely to the n^+ and p^+ contacts, the more β particles enter the germanium. A fraction of events around $Q_{\beta\beta}$ coming from ^{42}K is potentially due to γ particles with higher energy and sub-percent level branching ratio or simultaneous energy deposition of multiple γ particles. This γ component could become important for large quantities of ^{42}K not located directly on the detector surfaces with the β particle being absorbed in

²The path length of ^{42}K β particles in LAr is less than 1.6 cm, but bremsstrahlung photons from the interaction with LAr can travel as far as ~ 10 cm.

the LAr. As for ^{40}K also the γ line at 1525 keV of ^{42}K contains valuable information about the spatial decay distribution of this isotope. In contrast to ^{40}K no additional information, e.g. from radio-purity screening measurements, is available. For more detailed information about ^{40}K and ^{42}K see §3.6.

α EMITTERS

The lithium-diffused n⁺ detector surfaces act as a barrier for α particles. The latter can only penetrate the very thin boron-implanted p⁺-contact or the contact separating groove. α particles have to be emitted directly at the surface or from a thin adjacent layer of LAr. Since α particles have to cross the $\sim 0.5 \mu\text{m}$ thick p⁺ dead layer and therefore only part of their initial energy is deposited in the active volume, this background component leads to peaks with characteristic low-energy tails in the HPGe energy spectra (see fig. 3.3). Some α events, presumably originating from the detector groove, are reconstructed with degraded energy and lead to an additional, continuous spectral component. We find mainly ^{210}Po but also traces of isotopes from the ^{226}Ra decay chain.

DETECTOR BULK IMPURITIES

Cosmogenically produced long-lived isotopes can also be found in germanium [159–161]. In particular, ^{68}Ge and ^{60}Co can occur as detector intrinsic impurities with half-lives of $270.93(13)$ d and $5.2711(8)$ yr. The BEGe detectors were kept underground during major parts of the fabrication and characterization operations. Periods when these detectors were above ground have been tracked in a database [120]. Thus, for the well-monitored BEGe detectors we expect impurities of 5 nuclei/kg of ^{68}Ge and 21 nuclei/kg of ^{60}Co as of September 2014 [120]. Extrapolating the expected impurities to the whole Phase II data taking period we expect on average 0.03 cts/day from ^{68}Ge and 0.1 cts/day due to ^{60}Co . From background modeling in Phase I [149] the contribution for the coaxial detectors formerly used in the Heidelberg-Moscow (HDM) [112] and IGEX [113] experiments is expected to be even smaller due to their long storage underground. Simulating the expected detector bulk impurities we find background contributions around $Q_{\beta\beta}$ of less than 10^{-4} cts/(keV·kg·yr) in both cases. Hence, we conclude that ^{68}Ge as well as ^{60}Co can be neglected in the following analysis. Potential bulk contaminations with ^{238}U and ^{232}Th were studied in reference [162]. Only upper limits were found, establishing germanium crystals as material of outstanding radio-purity. Hence, only the decay of ^{76}Ge via $2\nu\beta\beta$ as detector intrinsic background component is considered while all other intrinsic impurities are considered to be negligible.

OTHER SOURCES

Prompt cosmic muon induced background events are efficiently vetoed by the identification of Čerenkov light emitted by muons when they pass the water tank [149]. The expected background indices, due to the direct muon and neutron fluxes at the LNGS underground laboratory, have been estimated to be of the order $3 \cdot 10^{-5}$ cts/(keV·kg·yr) [163] and 10^{-5} cts/(keV·kg·yr) [161] in earlier works, respectively. Background contributions coming from delayed decays of ^{77}Ge and ^{77m}Ge , also induced by cosmic muons, are estimated to be 0.21 ± 0.01 nuclei/(kg·yr) [117] corresponding to a background index prior to the active background suppression techniques of about 10^{-5} cts/(keV·kg·yr). Also, the water tank and LAr cryostat contaminations are expected to contribute to the GERDA background index with less than 10^{-4} cts/(keV·kg·yr) [156, 164]. All above mentioned contributions are considered negligible in this work. Other potential sources of background from interactions of ^{76}Ge [161, 165] and ^{206}Pb [166] with neutrons and ^{56}Co for which no evidence was found are not taken into consideration. The cosmogenically-produced isotope ^{39}Ar and the anthropogenic isotope ^{85}Kr [167], which are dissolved in LAr, emit particles which are dominantly less energetic than the energy window which is considered in the presented analysis.

3.4 Statistical analysis

The multivariate statistical analysis, which is used to model and disentangle the background in its components, runs on the three binned data sets M1-BEGe, M1-SemiCoax and M2-AllEnr. The single-detector data sets M1-BEGe and M1-SemiCoax contain the reconstructed energy of all M1 events whereas for the two-detector events the sum of the two reconstructed energies is put in the M2-AllEnr data set. Moreover, the count rate per detector is used for the two potassium γ lines. The spatial event distribution is a collection of the number of events per detector for M1 events and expressed in a matrix of pairs of detectors for all M2 events.

Assuming that the number of events in each bin follows the Poisson probability distribution $\mathcal{P}(n; \nu)$, where ν is the expected mean and n is the experimentally measured number of counts, the likelihood function for a binned data set reads $\prod_{i=1}^{N_{\text{bins}}} \mathcal{P}(n_i; \nu_i)$. Here $\nu_i = \sum_{k=1}^{N_{\text{com}}} \nu_i^{(k)}$ is the expected number of events in the i -th bin, calculated as the sum of the contributions from each background component k ; $\nu_i(\lambda_1, \dots, \lambda_{N_{\text{com}}})$ is a function of the parameters of interests λ_j (isotope activities, $2\nu\beta\beta$ half-life, etc.). The complete likelihood function adopted for the present analysis combines the $N_{\text{dat}} = 3$ data sets M1-BEGe, M1-SemiCoax and M2-AllEnr:

$$\mathcal{L}(\lambda_1, \dots, \lambda_m | \text{data}) = \prod_{d=1}^{N_{\text{dat}}} \prod_{i=1}^{N_{\text{bins}}} \mathcal{P}(n_{d,i}; \nu_{d,i}) . \quad (3.1)$$

The statistical inference is made within a Bayesian framework. Hence, to obtain posterior probabilities for the free parameters of interest λ_j , the likelihood defined in eq. (3.1) is multiplied according to the Bayes theorem by a factor modeling the prior knowledge of each background component as presented in §3.3. The computation is performed using a Markov Chain Monte Carlo (MCMC) methods and is implemented using the BAT software package [148, 168]. Posterior probability distributions of any observable that is not a free parameter of the likelihood function, like background index estimates, are obtained by sampling the desired parameter from the MCMC. A p -value estimate is provided as a goodness-of-fit measure by adopting the algorithm suggested in [169] for Poisson-distributed data. It has to be kept in mind that this p -value estimate, however, is not as well suited for model comparison as is for instance a Bayes factor; e.g. the number of free parameters is not taken into account while a Bayes factor always penalizes models that add extra complexity without being required by the data.

The fit range and data bins are chosen such as to exploit as much information from spectral features as possible brought by data without introducing undesired bias. The chosen fit range in energy space for the single-detector data sets (M1-BEGe and M1-SemiCoax) starts from just above the end-point of the ${}^{39}\text{Ar}$ β^- -spectrum at 565 keV and ends just above the ${}^{210}\text{Po}$ peak at 5260 keV, where the event rate drops to almost zero values. For the two-detector events (M2-AllEnr data set) the fit range starts at 520 keV and extends up to 3500 keV. Possible additional components outside of this range (e.g. ${}^{39}\text{Ar}$) do neither add information to the background decomposition in the ROI around $Q_{\beta\beta}$ nor to the analysis of $2\nu\beta\beta$ decay. Furthermore, at energies lower than ~ 100 keV the shape of the PDFs is dominated by uncertainties on the detector transition layer model, which describes the charge-carrier collection at the interface between the n^+ contact and the detector active volume. The exact nature of this transition region is different for each detector and prone to systematic uncertainties (see app. A

LIKELIHOOD

STATISTICAL
INFERENCEANALYSIS
WINDOW
AND BINNING

for a detailed discussion).

With an energy resolution which is typically 3–4 keV at $Q_{\beta\beta}$ (FWHM) [116, 133] and better at lower energies, a fixed bin size of 1 keV was chosen for all data sets. The only exceptions are the two γ lines from ^{40}K and ^{42}K each of which is combined in a single bin from 1455 keV to 1465 keV and from 1520 keV to 1530 keV, respectively. This is done in order to suppress any systematic uncertainties of the energy calibration and resolution model that affect the position and shape of the γ lines [122].

LIKELIHOOD FACTORIZATION

A feature of the selected data is that the likelihood in eq. (3.1) can be factorized in uncorrelated parts which can be studied individually and in detail. In the following we shortly outline the parts of the data which were studied in depth based on the approach of factorizing the likelihood into uncorrelated parts. Finally, the results of these analyses are incorporated into a full-range fit. This procedure is equivalent to a simultaneous analysis of all data but increases the input knowledge for the fit and breaks down the computational complexity in smaller steps.

POTASSIUM TRACKING ANALYSIS

As can be noted from fig. 3.2c and fig. 3.2d the PDFs of ^{40}K and ^{42}K in energy from different locations are prone to degeneracies and hence parameter correlation. Their most prominent γ lines at 1461 and 1525 keV, respectively, contain information on the spatial distribution while the two-detector events contain information about the angular distribution of Compton scattered events. Their combination is beneficial in order to pin down the potential location of the two potassium isotopes. In total the M1 data contains 4472 cts in 1461 ± 4 keV and 6718 cts in 1525 ± 4 keV while the M2 events contain 554 cts in 1461 ± 6 keV and 865 cts in 1525 ± 6 keV, respectively. An analysis of the number of events in the two potassium γ lines in each detector (and detector pair) is used to exploit mainly top-down and rotational asymmetries in the ^{40}K and ^{42}K distributions. The events in the two energy windows are classified according to the detectors in which an energy deposition was registered, so to exploit the available information about the event location. In the following this classification procedure will be referred to as “projection in detector space”. The treatment of the likelihood in eq. (3.1) is outlined in detail in §3.6. The number of events in all other γ lines is too low in order to adopt a useful detector-wise analysis. The spatial analysis of ^{40}K and ^{42}K is incorporated in the full-range fit by directly employing the posterior parameter distributions as prior information.³

α EVENTS BACKGROUND ANALYSIS

The single-detector energy spectra above 3.5 MeV (the Q-value of ^{42}K β decay) are strongly dominated by α events. They are not present in two-detector data due to the short range of α particles in LAr and germanium. Also, this component is not correlated to other backgrounds considered here because it peaks at energies well above the highest γ emission energies and β decay Q-values. A careful study was carried out considering various p^+ contact thickness and event rates to reproduce the ^{210}Po peak. In order to reproduce α events with degraded energy an empirical model is fit to the data. A linear function with free slope and offset and a cut-off below the maximum of the ^{210}Po peak fits the data well. The agreement of the α background model with the data is demonstrated in §3.5 and app. D. Information from the detailed analysis of the high-energy α region is incorporated in the full-range fit using a combined PDF that summarizes the ^{210}Po peak plus the ^{226}Ra decay chain and a linear floating component for energy-degraded α events.

³By adopting this approach, a part of the data in the potassium γ lines region is analyzed twice: first in the potassium tracking analysis and then in the full-range fit. Nevertheless, considering that the two analyses exploit different data features (i.e. count rate per detector and total count rate per energy) and the overlap between the two data set is minimal, the overall effect is negligible.

The following criteria are adopted to convert the prior information described in §3.3 into prior probability distributions on the parameters of interest to be used in Bayesian inference: if a measured value with uncertainty is available for a background contamination then a Gaussian distribution with a corresponding centroid and a 1σ width is adopted. In presence of a 90% C.L. upper limit, instead, an exponential prior distribution is constructed with 90% of its area covering parameter values from 0 up to the given 90% C.L. upper limit (i.e. $p \sim e^{-\mu x}$). A uniform prior distribution is assigned to components for which no measured value or upper limit is available. Ranges for uniform priors are initially taken very wide, in order to span a large portion of the allowed parameter space, then optimized to contain at least 99% of the posterior distribution. As mentioned before, in addition to the information from screening measurements, prior distributions for ^{40}K and ^{42}K are constructed considering the posterior inference from their spatial distribution. Moreover, as ^{214}Bi is part of the ^{226}Ra decay chain, we constrain a ^{214}Bi component on the p^+ contact by a Gaussian prior extracted from the obtained ^{226}Ra activity based on the energy estimator in the high-energy α region.

PRIOR
DISTRIBUTIONS

3.5 α -events analysis

Above an energy of 3.5 MeV almost all registered events are due to α -emitting isotopes. The respective part of the full likelihood can be approximately factorized and studied separately. α particles have a very short range in LAr as well as in germanium⁴ and are able to reach a detector's active volume only through the very thin (of the order of 500 nm) p^+ contact surface. Therefore, the α emitter contamination is detector-specific and depends only on the p^+ surface contaminations. For this reason, M1-BEGe and M1-SemiCoax detector data above 3.5 MeV is analyzed independently. The projection in detector space shows no significant correlation between events in different detectors and hence contains no further useful information. Additionally, the number of events in a single detector is not sufficient to further split the data on a detector-by-detector basis. The two data sets are uncorrelated and the statistical analysis can be carried out for each M1 data set separately. As already mentioned, α events in the M2 data are not observed due to the short range of these particles.

All contaminations found are constituents of the ^{238}U decay chain. The main surface contamination observed is ^{210}Po which occurs either as an incident contamination and decays in time with a half-life of 138.3763(17) days [171] or is fed by a ^{210}Pb contamination with a stable rate in time. The spectral form is identical for both cases and can only be disentangled by analyzing the α -event rate in time. The analysis of the evolution of the α -event count rate in time is presented in app. D. Above the ^{210}Po peak very few events are observed. In the M1-BEGe data set we find only four events with an energy larger than 5.3 MeV, while in the M1-SemiCoax data set 22 such events are observed, 14 of which in a single detector ANG2 (see tab. 3.2). These events are due to α decays from ^{222}Rn and subsequent isotopes on the p^+ detector surfaces. ANG2 also shows a higher ^{226}Ra (mother nucleus of ^{222}Rn) contamination which suggests dominantly a surface contamination with ^{226}Ra rather than ^{222}Rn dissolved in LAr. In the latter case the decay chain would be broken, as only the gaseous ^{222}Rn can emanate from the construction materials. Unfortunately, the number of counts is too low to distinguish the spectral shape above 5.3 MeV and disentangle a surface contamination with ^{226}Ra from ^{222}Rn dissolved in LAr.

SOURCES

⁴In the continuous slowing down approximation (CSDA) the range of α particles is estimated to be of 50 μm and 20 μm for LAr and germanium, respectively [170].

Table 3.2: Observed number of counts with energy > 5.3 MeV belonging to the ^{226}Ra decay chain. Detectors with zero counts are not listed.

data set	detector	channel	^{226}Ra chain [cts]
M1-BEGe	GD61C	16	1
	GD79B	32	1
	GD89A	35	2
M1-SemiCoax	ANG1	36	2
	ANG2	27	14
	ANG3	10	1
	ANG4	29	1
	ANG5	8	2
	RG1	9	2

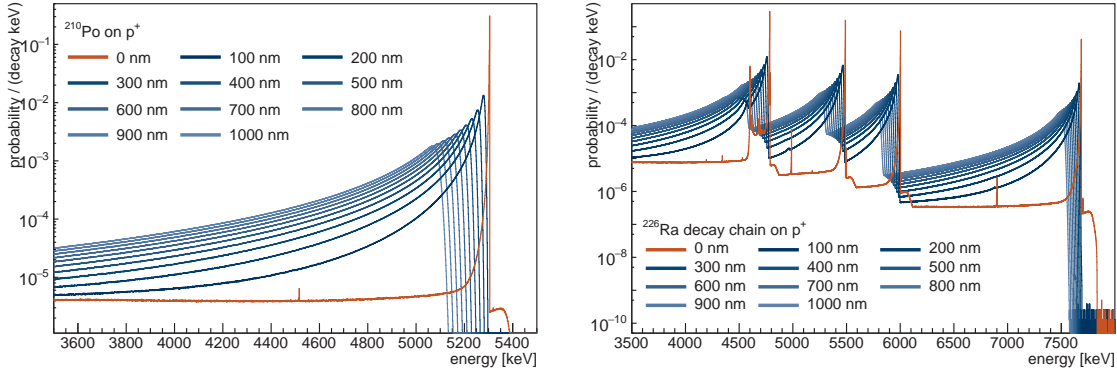
A comparison between the counts observed above 5.3 MeV and the ^{214}Bi 609 keV γ line suggests that α events due to a dissolved ^{222}Rn contamination would not produce observable counts in said energy region. Assuming that all ^{214}Bi observed comes from dissolved ^{222}Rn leads, in fact, to a specific activity smaller than 10 $\mu\text{Bq}/\text{kg}$. Hence, in the following, we will only consider a p^+ surface contamination with ^{226}Ra and all subsequent isotopes to which we refer as the ^{226}Ra decay chain. The ^{210}Po and ^{226}Ra contaminations are not necessarily spatially correlated.

MODEL

Due to the very short range of α particles the energy spectrum of α decays exhibits a line with a pronounced low-energy tail. The tail is formed when the decay occurs under an incident angle with respect to the contact and the α particle loses part of its energy before reaching the detectors active volume. The maximum is shifted with respect to the full emission energy which is due to energy loss inside the electrode and depends on its minimal thickness. The detectors have slightly different contact thicknesses, and the p^+ contact of a single detector may also be intrinsically inhomogeneous. Therefore, the ^{210}Po peak is modeled with a mixture of PDFs obtained from simulations with different contact thicknesses, shown in fig. 3.3. Due to the low number of counts observed in the ^{226}Ra chain it is sufficient to model this component with only one PDF. Furthermore, the isotope contamination is assumed to halve at each decay step. A reduction effect of the subsequent α decays in the ^{222}Rn chain had been observed in Phase I and attributed to possible recoil off the surface into the LAr⁵ [140]. We adopt this explanation in our model although we note that the number of events observed with an energy >5.3 MeV is not sufficient to confirm such an effect.

Dedicated measurements [172] have shown that events originating in the contact separating groove are partly reconstructed with degraded energy. A simulation-based model of these energy-degraded events is not available yet. We approximate this component with an empirical linear distribution truncated below the maximum of the ^{210}Po peak. Such a component accommodates also eventual α decays in the LAr in very close vicinity to the p^+ detector surface. However, the number of events found with

⁵The hypothesis of nuclear recoils caused by α decays might also be supported by the observation that a small suppression of α events (above the level of random coincidences) of about 4% is observed after LAr. Scintillation light could be indeed produced by nuclei recoiling in LAr.



(a) ^{210}Po α decays on p^+ contact surface for different thicknesses of the inactive contact layer. For 0 nm the nuclear recoil energy can be absorbed and some energy can be lost in the LAr.

(b) α decays from the ^{226}Ra decay sub-chain (^{226}Ra , ^{222}Rn , ^{218}Po and ^{214}Po) on the detectors p^+ contact surface for different depths of the inactive contact layer. The isotope contamination is assumed to halve at each decay step, because of the recoil of the nuclei in LAr.

Figure 3.3: α -model PDFs in the full energy domain corresponding to different p^+ contact thicknesses. Contaminants are simulated on the outer contact surface. The red PDF corresponds to the absence of dead layer. All PDFs are normalized to the number of simulated decays.

an energy >5.3 MeV is too low to fully account for the linearly modeled distribution.

The likelihood function for modeling the high-energy region dominated by α decays runs only on single-detector data, namely M1-BEGe and M1-SemiCoax separately, in a range from 3.5 MeV to 5.25 MeV. Events with an energy higher than 5.25 MeV are put in a single overflow bin:

$$\mathcal{L}_\alpha(\lambda_1, \dots, \lambda_m | n) = \prod_{i=1}^{N_{\text{bins}}} \mathcal{P}(n_i; \nu_i) \quad (3.2)$$

where $\mathcal{P}(n; \nu)$ denotes the Poisson probability of observing n counts with mean ν . A flat prior probability is assigned to each of the fit parameters λ_i . Both data sets are fit separately with a fixed bin size of 10 keV⁶ as the α contamination is detector individual and the two single-detector data sets are uncorrelated in the respective energy window.

The fit results are shown in fig. 3.4 and listed in tab. 3.3. The ^{210}Po component is modeled with a combination of p^+ contact thicknesses from 400 to 600 nm for the M1-BEGe data set and from 300 to 700 nm for the M1-SemiCoax data set in steps of 100 nm. Further ^{210}Po components are rejected by a Bayes factor analysis. Impurities belonging to the ^{226}Ra chain are mostly located on ANG2 and thus a fit of the M1-SemiCoax data set using a single p^+ thickness describes this component well. For the M1-BEGe data set we observe a very small number of counts for the ^{226}Ra chain, therefore, also in this case a single component is sufficient. We determine a best-fit value of 100 nm and 500 nm, respectively, consistent with the manufacturer technical specifications. The estimated p -value for M1-BEGe is

⁶The calibration curves are accurate on the sub-keV level up to the highest γ energy of about 2.6 MeV emitted by the ^{228}Th calibration sources. Although no major non-linearity effects were found the same accuracy cannot be guaranteed at 6 MeV. Deviations from linearity at this energy are within 10 keV, hence, we increase the bin size in the higher energy range.

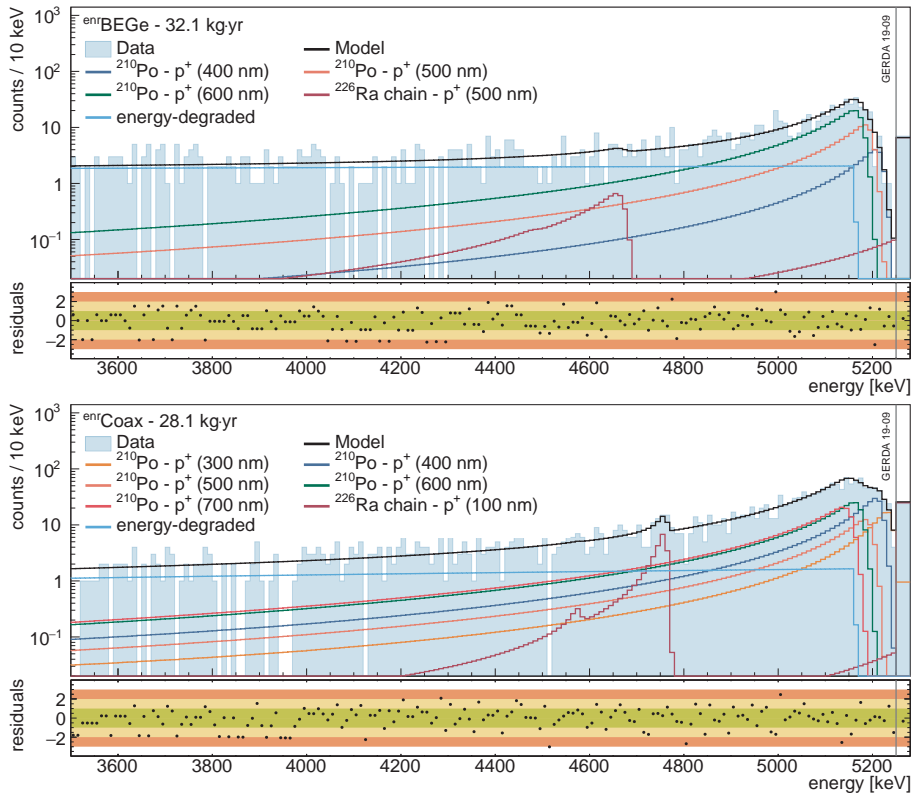


Figure 3.4: Fit results of the α events background analysis for M1-BEGe (top) and M1-SemiCoax (bottom). The last bin contains all events above 5250 keV.

0.2 whereas the p -value for M1-SemiCoax is 0.3. The dominant spectral component below 4.5 MeV is due to degraded α events which extends down to the ROI.

3.6 Potassium tracking analysis

The two full-energy lines of ^{40}K and ^{42}K at 1461 keV and 1525 keV are distinct features of the energy spectrum shown in fig. 3.1. Being a relevant source of background for double-beta decay, the two potassium isotopes play a crucial role in the background modeling process in GERDA. Uncertainties in their origin and distribution propagate directly to searches for exotic physics like Majorons or decay modes to excited states of $2\nu\beta\beta$ decay in which the shape of the $2\nu\beta\beta$ decay spectrum is a unique feature and thus need to be well understood. In the following the focus will be on the characteristics of the events constituting these two intense γ lines. In order to extract information about the spatial distribution of ^{40}K and ^{42}K contamination around the GERDA array, a treatment on a detector-by-detector basis is advantageous. The two γ lines contain enough statistics for such an analysis to be meaningful and constitute samples with a high signal to background ratio.

SOURCES Initial observations in Phase II have shown that the ^{40}K and ^{42}K full-energy line intensities have

Table 3.3: Fit results of the α events background analysis for the M1-BEGe and M1-SemiCoax data sets. Values are given in counts in the full PDF range from 40 keV to 8000 keV.

data set	component	contact [nm]	global mode [cts]	marg. mode 68% C.I. [cts]
M1-BEGe	^{210}Po	400	49	50 [34, 76]
		500	162	165 [107, 222]
		600	346	342 [278, 391]
		comb.	–	555 [523, 586]
M1-SemiCoax	^{226}Ra chain	500	20	20 [15, 29]
	energy-degraded	–	–	845 [698, 948]
	^{210}Po	300	167	165 [140, 208]
		400	363	368 [272, 430]
		500	182	175 [83, 338]
		600	433	420 [233, 582]
	^{226}Ra chain	700	404	410 [295, 537]
		comb.	–	1555 [1511, 1609]
		100	58	59 [49, 70]
		–	–	485 [426, 599]

increased by a factor of 4 and 2, respectively, in the single-detector data compared to Phase I [173]. The ^{42}K increase in activity can be attributed to the exchange of the mini-shrouds material from copper to nylon⁷ during the Phase II upgrade: The electric field generated by the detectors bias high voltage is not screened by the conductive material anymore. The ^{42}K ions can be attracted from a larger LAr volume into the vicinity of the detectors. Moreover, the unshielded high-voltage cables could be an explanation for the higher rate of ^{42}K events seen in the uppermost detectors in the GERDA array. The higher ^{40}K event rate, on the other hand, is possibly attributable to the glue used for the nylon mini-shrouds and other new materials introduced with the LAr veto system. The exact amount, location and radio-purity of the glue is not precisely known. All changes to the setup that have been made during the upgrade to Phase II are described and motivated in exhaustive detail in reference [121].

Data in two energy windows around the potassium γ lines is projected in detector index space, such that, for single-detector data, each data point n_i represents the total counts in detector i in the respective window. For two-detector data the detector space is two-dimensional, and each data point n_{ij} represents the number of events for which energy is deposited in detector i and detector j . The events in the potassium lines (denoted with K40 and K42 in the following) are selected in a $\pm 3\sigma$ energy interval around the respective line, rounded up to an integer number of keV to match the specific energy windows in the energy distributions with 1 keV binning. σ is the energy resolution in the respective energy window. Additionally, three side-bands (SB1, SB2 and SB3 in the following) are used to estimate the

DATA SET

⁷The exchange of material from copper to nylon has been necessary in the presence of a LAr veto system. Copper surfaces would have indeed blocked the scintillation light, instead of letting it propagate and wavelength-shift as with TPB-coated nylon mini-shrouds [126].

Table 3.4: Energy ranges and corresponding number of events for the potassium tracking analysis (visualized in fig. 3.5). Note that the windows for two-detector data are larger as the two single-detector energy resolutions are folded in the summed energy spectrum.

	M1 [keV]	cts.	M2 [keV]	cts.
K40	[1457, 1465]	4472	[1455, 1467]	554
K42	[1521, 1529]	6718	[1519, 1531]	865
SB1	[1405, 1450]	1852	[1405, 1450]	452
SB2	[1470, 1515]	1124	[1470, 1515]	326
SB3	[1535, 1580]	533	[1535, 1580]	41

continuum below and above the γ lines. Considering the further subdivision in single- ($M1-$) and two-detector ($M2-$) data, this leads to the definition of 5×2 energy regions, summarized in tab. 3.4. A visual representation of the selected windows can be found in fig. 3.5. PDFs for ^{214}Bi on the flat cables and detector intrinsic $2\nu\beta\beta$ decays are used to estimate the background. Other components are expected to contribute less in the respective energy windows.

LIKELIHOOD

The statistical approach of factorizing the likelihood is described in §3.4. The part of the likelihood analyzed here runs simultaneously on the 5×2 energy ranges presented above. Following the previously introduced naming convention introduced it reads:

$$\mathcal{L}_K(\lambda_1, \dots, \lambda_{m'} | n) = \prod_{d=1}^{N_{\text{dat}}} \left\{ \prod_{i=1}^{N_{\text{det}}} \mathcal{P}(n_{d,i}^{M1}; \nu_{d,i}^{M1}) \times \prod_{j < k}^{N_{\text{det}}} \mathcal{P}(n_{d,jk}^{M2}; \nu_{d,jk}^{M2}) \right\}, \quad (3.3)$$

where the index i runs over the bins (i.e. detectors) and the index d over the 5 considered energy windows, namely the three side-bands SB1, SB2, SB3 and the two line-bands K40 and K42. The $M2-$ data sets are two-dimensional in detector space and run over the two indices j and k . $\mathcal{P}(n, \nu)$ is the usual Poisson probability.

PRIORS

Gaussian prior probability distributions for the ^{40}K activity are built from radio-purity screening measurements (see app. B). For ^{42}K , for which no screening information is available, uniform priors are adopted, with the exception of the two ^{42}K components located on the n^+ contact surface of BEGE and SEMICOAX detectors. ^{42}K can be attracted to the n^+ surface by the electrical field created by the high voltage potential applied to the detectors. Both components are expected to be correlated by the volume ratio of the mini-shrouds (3:2 BEGE to SEMICOAX) the ^{42}K ions are attracted from. The volume ratio estimate is extracted from the geometric implementation in MAGE. We assume an uncertainty of 0.1 mBq on either activity allowing for a change of their ratio. The correlation is included in the fit via a two-dimensional prior.

BASE MODEL

The analysis flow starts with a construction of a first, preliminary model, which consists only of background contributions that are expected from screening measurements of ^{40}K and known properties of ^{42}K . The resulting model, however, gives a non-satisfactory description of data and the posterior distributions for the ^{40}K components are significantly shifted to higher values with respect to the prior distributions, indicating a surplus of ^{40}K . To find a better agreement with physics data while keeping

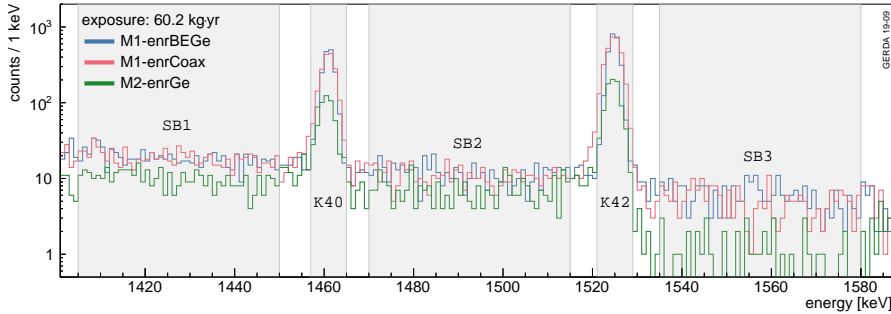


Figure 3.5: Visual representation of the five energy ranges defined for the potassium tracking analysis. The exact intervals and counts are given in tab. 3.4.

the model as simple as possible, additional components using uniform priors are included one at a time in the fitting procedure, and the Bayes factor is calculated between the extended and the preliminary model. The model is iteratively updated by adding the component that results in the highest Bayes factor until no Bayes factor is larger than 10.

In a first iteration a replica of the PDF of ^{40}K in the mini-shrouds is added obtaining a Bayes factor $\gg 10$. ^{40}K in the Tetratex®-coated copper shrouds is added in a second iteration with a Bayes factor of 11. For ^{42}K the only additional component that results in a Bayes factor greater than 1 is ^{42}K on the n^+ detector contacts. Although the fit shows only a slight preference (Bayes factor of 2) the component is added to the model because of its importance in the full-range fit, where the energy region above the 1525 keV γ line is also considered. The results of the base model are shown in tab. 3.5 and a graphic representation showing the counts per detector in both potassium γ lines in M1 and M2 data can be found in fig. 3.6. The complete selection of plots is available in app. E. The analysis yields a p -value of ~ 0.07 , indicating an acceptable description of the data. To further improve the model rotationally asymmetric fit components are needed. The base model is accurate enough to be used as input for the full-range fit, which is insensitive to any rotational inhomogeneity of the location of background sources, as spectra from different detectors are merged into a single data set.

The two components ^{40}K close to the array and ^{42}K in LAr above the array are split into 7 sub-components on a string-by-string basis (for the respective PDFs see app. C). Furthermore, we consider a ^{40}K contamination on top of the central mini-shroud. The results of this extended analysis are listed in tab. 3.6. The reader is referred to app. E for the graphical representation of the background decomposition. Per-string concentrations of ^{40}K and ^{42}K are visualized also in fig. 3.7. An elevated ^{42}K concentration is found above the central string while a lower concentration is observed above the adjacent strings S1 and S6 (string numbers follow the nomenclature used in fig. 2.4). Due to the large number of components the fit yields a high anti-correlation between the ^{42}K concentration above the outer strings and S7. This results in a high uncertainty on the latter fit parameter.

EXTENDED MODEL

The screening measurements do not account for all observed ^{40}K . In general ICP-MS screening of the mini-shrouds with respect to ^{40}K is difficult and yielded only a lower limit. Different measurements seem to indicate different contamination levels of different mini-shrouds. Samples of glued nylon yielded the highest potassium contamination. As the gluing of the nylon mini-shrouds is done manually during installation the amount of glue and its exact location is hard to control. Hence, an

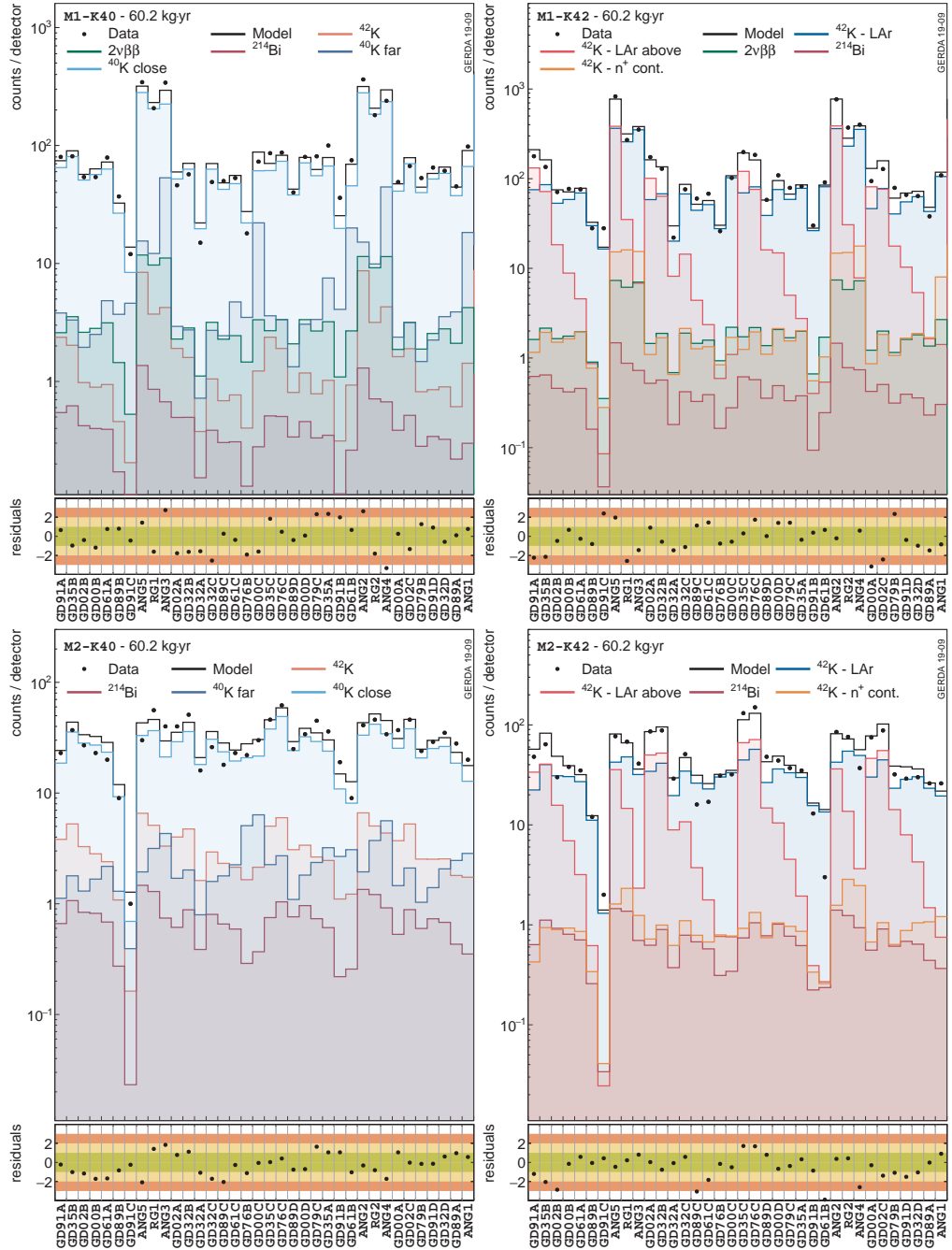


Figure 3.6: Decomposition of the energy windows corresponding to the two potassium lines in detector space: single-detector data (top) one-dimensional representation of two-detector data (bottom). Some components are merged for visualization purposes: in the K40 plots combined components are shown for ^{42}K and ^{214}Bi , while ^{40}K sources are grouped in close (flat cables, holders, mini-shrouds) and far (fibers, SiPMs, copper shrouds, front-end electronics) locations from the detector array. To visualize the two-detector data the sum of the projections on the two domain axes (index i and index j) is shown.

Table 3.5: Summary of the fit parameters estimated with the potassium source tracking analysis (base model). The type of prior distribution is indicated with [f]: flat, [g]: Gaussian. ([†] Tetratex®-coated)

source	[prior] location	units	global mode	marg. mode	68% C.I. or 90% upper C.L.
⁴⁰ K	[g] flat cables	mBq	3.29	3.25	[1.79, 4.72]
	[g] front-end electronics		15.7	15.9	[11.1, 20.1]
	[g] copper shrouds [†]		18.4	18.1	[16.6, 20.0]
	[g] fiber shroud		2.82	2.81	[2.24, 3.38]
	[g] detector holders		1.73	1.73	[1.28, 2.14]
	[g] mini-shrouds		1.70	1.70	[1.60, 1.80]
	[g] SiPM ring		2.50	2.73	[0.83, 4.13]
⁴² K	[f] far from the array		328	322	[232, 416]
	[f] close to the array		10.8	10.8	[9.53, 12.1]
²¹⁴ Bi	[f] n ⁺ (BEGe)	mBq	0	0	< 0.37
	[f] n ⁺ (Coax)		0.22	0.24	[0.12, 0.38]
	[f] LAr – above array		450	454	[436, 470]
	[f] LAr – outside mini-shrouds		2036	2009	[1915, 2080]
²¹⁴ Bi	[g] flat cables	mBq	1.51	1.26	[0.93, 1.51]
$2\nu\beta\beta$	[f] germanium	10^{21} yr	1.91	1.93	[1.86, 2.00]

asymmetric distribution is expected. The ⁴⁰K content of other close components like holders and cables might also be asymmetric. The asymmetric ⁴⁰K contamination is confirmed by the extended potassium tracking analysis. Also, an additional ⁴⁰K distribution on the top-lid of the central mini-shroud is preferred. The surplus in the far ⁴⁰K component instead is possibly explained by setup parts omitted in the model like the PMTs and voltage-dividers of the LAr veto system. An upper limit of their ⁴⁰K content, <330 mBq, was estimated from material screening which is similar to the activity reconstructed for the far ⁴⁰K component. The location of the PMTs with respect to the detector array is very similar to the Tetratex®-coated copper-shrouds and their PDFs are, hence, degenerate.

3.7 Full-range analysis

As described in §3.4 the α -event background and potassium γ lines are studied individually and the results are incorporated in the full-range fit as prior distributions. The latter consists in a simultaneous fit of the M1 and the M2 data sets. For the final combination of parameters, outlined in this section, components with a posterior distribution peaked at zero were removed from the fit. The stability of the results with respect to the bin size and prior distributions was verified. Changing the prior distribution for fit parameters for which no screening measurement is available from a flat to an exponential one does not significantly impact the final posterior distributions. The compatibility of the final model, which includes 34 fit parameters, with data is supported by a p -value of ~ 0.3 .

The estimated activities of individual components and other parameters of interest are listed in

Table 3.6: Summary of the fit parameters estimated with the potassium source tracking analysis (extended model). The type of prior distribution is indicated with [f]: flat, [g]: Gaussian. ([†] Tetratex®-coated)

source	[prior] location	units	global mode	marg. mode	68% C.I. or 90% upper C.L.
⁴⁰ K	[g] flat cables	mBq	2.33	1.08	[0.13, 2.30]
	[g] front-end electronics		14.5	14.4	[10.2, 18.7]
	[g] copper shrouds [†]		18.4	18.5	[16.6, 20.0]
	[g] fiber shroud		2.83	2.77	[2.24, 3.38]
	[g] detector holders		2.57	2.29	[1.75, 2.78]
	[g] mini-shrouds		1.70	1.70	[1.60, 1.79]
	[f] close to S1		0.81	0.83	[0.47, 1.28]
	[f] close to S2		2.35	2.22	[1.83, 2.51]
	[f] close to S3		0	0	< 0.50
	[f] close to S4		2.58	2.55	[2.10, 3.02]
⁴² K	[f] close to S5	mBq	0.97	0.85	[0.56, 1.16]
	[f] close to S6		1.86	1.89	[1.46, 2.30]
	[f] close to S7		0	0	< 2.92
	[f] S7 mini-shroud (top)		2.09	1.83	[1.26, 2.40]
	[g] SiPM ring		2.44	2.32	[0.83, 4.02]
	[f] far from the array		390	374	[280, 468]
	[f] n ⁺ (BEGe)		0.15	0.19	[0.05, 0.37]
	[f] n ⁺ (Coax)		0.22	0.26	[0.12, 0.41]
²¹⁴ Bi	[f] LAr – above S1	mBq	0	0	< 0.80
	[f] LAr – above S2		2.22	2.96	[2.21, 3.63]
	[f] LAr – above S3		1.20	1.57	[1.06, 2.16]
	[f] LAr – above S4		1.43	1.89	[1.33, 2.41]
	[f] LAr – above S5		1.49	1.91	[1.38, 2.73]
	[f] LAr – above S6		0	0	< 1.21
	[f] LAr – above S7		10.4	7.84	[4.95, 9.83]
	[f] LAr – outside mini-shrouds		2083	2058	[1960, 2145]
²¹⁴ Bi	[g] flat cables	mBq	1.60	1.41	[1.14, 1.66]
$2\nu\beta\beta$	[f] germanium	10^{21} yr	1.89	1.89	[1.83, 1.97]

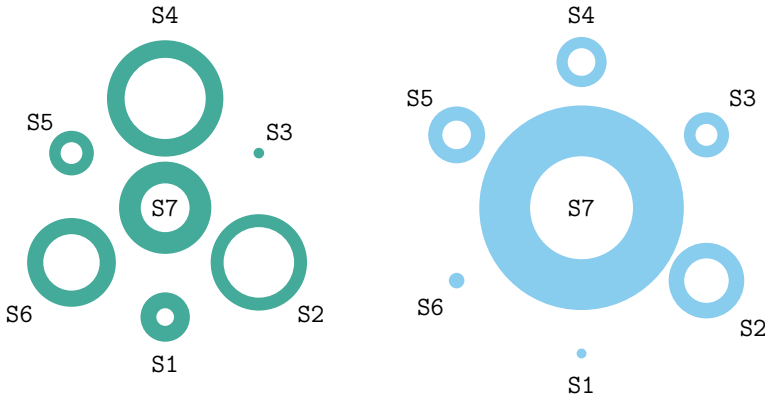


Figure 3.7: Asymmetry of ^{40}K contaminations (left) close to the array strings (for S_7 just on the top-lid) and ^{42}K (right) above the detector strings. The inner and outer radii of each circle are proportional to the edges of the smallest 68% C.I. of the marginalized posterior distributions. The numerical values can be found in tab. 3.6.

tab. 3.7. In particular, for each component we report the global and the marginalized mode of the posterior parameter distribution, along with its smallest 68% C.I. The global mode corresponds to the global best fit value while the marginalized mode is the most probable parameter value when integrating over all other parameters. The original type of prior distribution is marked with [f] for flat, [g] for Gaussian and [e] for exponential; the latter two are used if screening measurements are available. Subsequently, for all ^{40}K and ^{42}K components, the prior distribution is imported from the potassium tracking analysis and for ^{214}Pb and ^{214}Bi on the p^+ contact from the reconstructed ^{226}Ra content from the α events background analysis.

The spectral decomposition of all data sets is shown in fig. 3.8. For each data set the residual distribution as a multiple of the expected 1σ fluctuation in each bin (i.e. the 68% probability interval centered on the mean of the Poisson distribution) is displayed. We find for the M1-BEGe data set 66.4%, 94.5% and 99.6% of points in the 1σ -, 2σ - and 3σ -bands, for the M1-SemiCoax data set 66.0%, 94.7% and 99.8% and for the M2-AllEnr data set 70.0%, 96.1% and 99.7%, respectively. Thus, in all three cases the residuals are normally distributed. No outliers with residuals larger than 3σ are found in a ± 50 keV window around $Q_{\beta\beta}$ and the bins exceeding 3σ do not correspond to any known γ line.

The ^{42}K distribution is optimized to best fit the data. In order to disentangle the ^{42}K γ and β components, the volume inside and outside of the mini-shrouds is separated in the PDF construction. Inside the mini-shrouds a homogeneous distribution is compatible with the data as well as ^{42}K attached to the detectors contact surfaces. In the fit model given here, a possible scenario is chosen where all ^{42}K is located on the n^+ surfaces. However, we note that ^{42}K on the p^+ appears to partly substitute the energy-degraded α component in the M1-SemiCoax data set if introduced in the fit and predicts a higher total background index around $Q_{\beta\beta}$. The extracted ^{42}K activity on the SEMICOAX p^+ contact in this case is $22 \pm 4 \mu\text{Bq}$ corresponding to a contribution to the background index around $Q_{\beta\beta}$ of $(7 \pm 1) \cdot 10^{-3} \text{ cts}/(\text{keV}\cdot\text{kg}\cdot\text{yr})$. For the M1-BEGe data set the posterior distribution of a possible ^{42}K component on the p^+ contact is compatible with zero. Outside the mini-shrouds an inhomogeneous distribution of the ^{42}K decays better explains the observations. Detectors which are located at higher

Table 3.7: Summary of the analysis parameter estimates. Global mode and marginalized mode, along with its smallest 68% C.I., are reported as representatives of the posterior parameter distribution. The number of reconstructed counts in the fit range and the background index at $Q_{\beta\beta}$ prior active background suppression are listed for each component and each analysis data set. The original type of prior distribution is marked with [f] for flat, [g] for Gaussian and [e] for exponential. ([†]Tetrax[®]-coated)

source	[prior] location	units	global mode	marg. mode with 68% CI	screening	counts in fit range Bl at $Q_{\beta\beta}$ units: cts 10^{-3} cts/(keVkg·yr)		
						M1-BEGe	M1-Semi-Coax	M2-AllEnr
$2\nu\beta\beta$	[f] germanium [f] $\delta^{2\nu}$ (Coax)	10^{21} yr cts	2.025 2890	2.030 [2.016, 2.044] 3200 [2600, 3600]	— —	45 272 —	0 1962	37 867 0
$^{212}\text{Bi} + ^{208}\text{Tl}$	[e] flat cables [g] copper shrouds [†] [g] mini-shrouds	μBq	384 194 18.7	380 [355, 408] 197 [175, 213] 17.7 [13.8, 23.8]	<410 194(19) 18(5)	424 3 21	3.52 [3.30, 3.76] [2.03, 2.34]	274 3 21
$^{214}\text{Pb} + ^{214}\text{Bi}$	[f] p ⁺ (BEGe) [f] p ⁺ (Coax) [g] flat cables [g] copper shrouds [†] [g] mini-shrouds [g] SiPM-ring	μBq	0.36 1.053 560 533 45 353	0.35 [0.27, 0.53] 1.07 [0.91, 1.30] 552 [523, 594] 535 [480, 585] 47 [33, 59] 345 [256, 450]	— — 660(210) 532(53) 98 351(97)	6 0 1194 9 98 6	0 26 2.63 [2.50, 2.78] 10 5	2.21 1 750 10 96 3
^{40}K	[g] flat cables [g] front-end electronics [g] copper shrouds [†] [g] fiber shroud [g] detector holders [g] mini-shrouds [g] SiPM ring [f] far from the array [f] close to the array	mBq	2.95 16.6 18.4 2.73 1.64 1.70 1.95 — —	2.9 [2.1, 4.1] 16.0 [11.5, 20.3] 18.2 [16.6, 20.2] 2.83 [2.29, 3.39] 1.75 [1.29, 2.07] 1.69 [1.60, 1.80] 3.0 [1.1, 4.4] — —	6(2) 13(4) 18(2) 2.9(6) 2.8(6) 1.7(6) 2(2) — —	861 104 42 124 886 518 5 784 3469	530 79 45 116 0 468 475 4 847 3182	339 46 17 55 334 216 2 327 1446
^{42}K	[f] n ⁺ (BEGe) [f] n ⁺ (Coax) [f] LAr - above array [f] LAr - outside mini-shrouds	μBq	261.5 490.0 0.451 2.026	295.0 [224.3, 324.7] 415.0 [309.6, 506.0] 0.453 [0.437, 0.468] 2.027 [1.985, 2.068]	— — — —	920 — 5859 10 225	— 5.69 [4.58, 6.29] 9691	162 162 4421 [1.15, 1.40] 4544
^{228}Ac	[g] copper shrouds [†] [e] detector holders [g] mini-shrouds [e] flat cables	μBq	62.0 183 18.0 113	62.5 [56.0, 67.9] 182 [158, 208] 17.8 [12.9, 22.8] 114 [98, 130]	62(6) <250 18(5) 80(21)	1 541 28 382	1 0.36 [0.31, 0.40] 240	0 3.31 [3.12, 3.78] —
^{60}Co	[f] $^{210}\text{Po} + ^{226}\text{Ra}$ chain (BEGe) [f] $^{210}\text{Po} + ^{226}\text{Ra}$ chain (Coax) [f] energy-degraded (BEGe) [f] energy-degraded (Coax)	cts	1173 3320 595 700	1183 [1127, 1253] 3300 [3200, 3400] 628 [583, 680] 698 [641, 747]	— — — —	561 — 587 —	— 1585 [4.40, 5.08] 623	— — — —

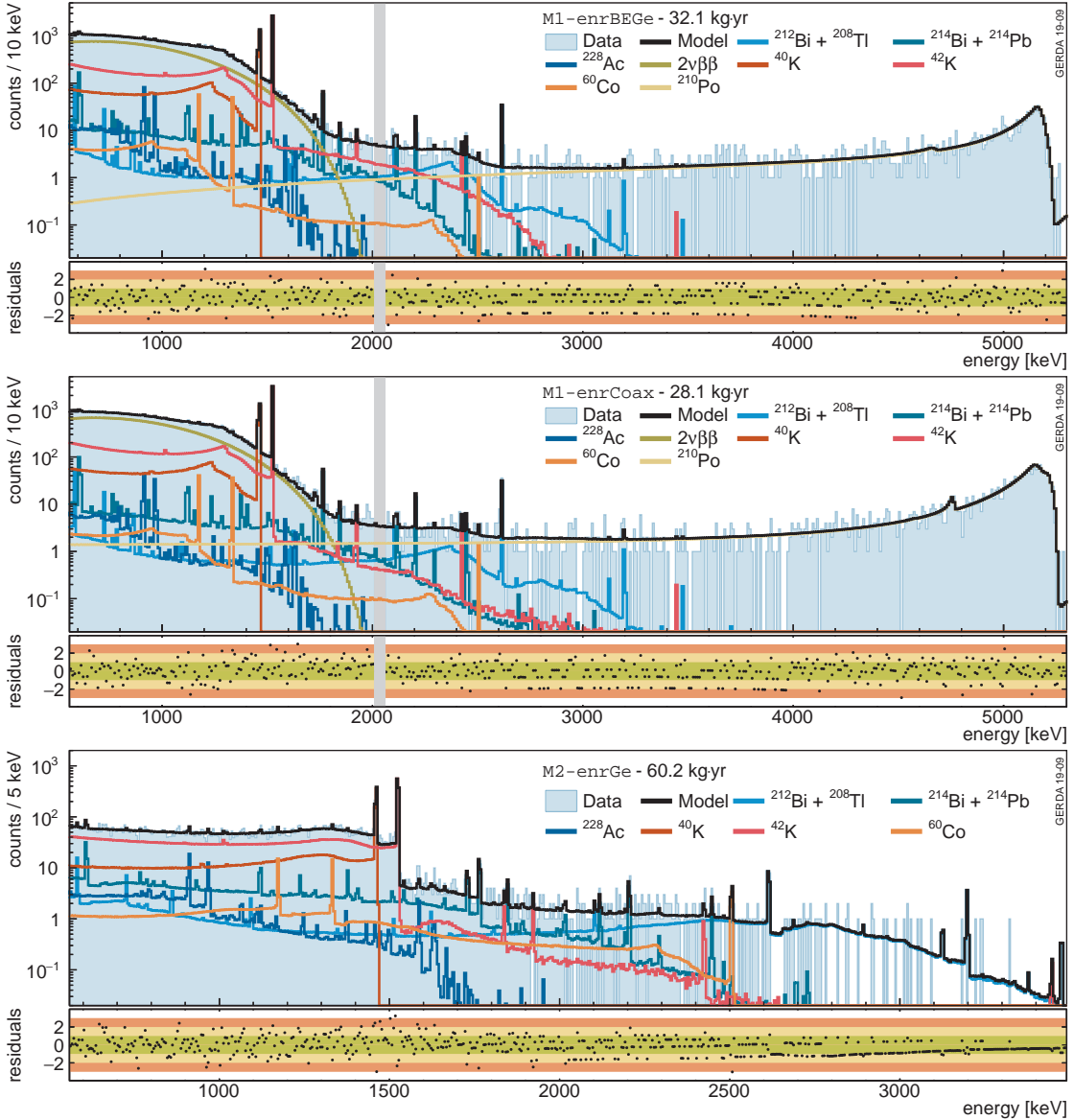


Figure 3.8: Background decomposition of the event energy distributions of the (from top to bottom) M1-BEGe, M1-SemiCoax and M2-AllEnr data sets. Components referring to the same background source in different locations are summed together for visualization convenience. The blinded region $Q_{\beta\beta} \pm 25 \text{ keV}$ is highlighted in gray. In the three lower panels displaying the normalized residual distributions the central 1σ - (green), 2σ - (yellow) and 3σ - (red) bands are marked. Note that for bins with low expected statistics due to the discrete nature of the measured spectrum not all colored bands are meaningful [174].

positions in the strings show an excess of events in the ^{42}K 1525 keV γ line which is compatible with a surplus of ^{42}K located right above the detector array (see §3.6). The full-range fit model contains a homogeneous ^{42}K distribution in LAr, outside the mini-shrouds, which is reconstructed with a specific activity of $186 \pm 39 \mu\text{Bq}/\text{kg}$ plus an additional distribution in the vicinity of the cables (in LAr, above the array).

A large fraction of the contamination with ^{40}K in the setup cannot be accounted for by the screened hardware listed in tab. 3.7. We thus add a close (~ 1 cm) and a far (~ 50 cm) ^{40}K component with respect to the detector array which are in fact replica of the PDFs for the mini-shrouds and the Tetratex®-coated copper shrouds. These additional components absorb the excess indicated by the fit, the largest part of the reconstructed events in the spectra is attributed to impurities close to the array.

The ^{40}K and ^{42}K distributions can be further split into smaller volumes and studied as an extension of the potassium tracking analysis (as described in §3.6) projected in detector space. The additional ^{40}K component close to the array and the ^{42}K component above the array are split into 7 sub-components on a string-by-string basis. The potassium concentration is in general found to be asymmetric among the detector strings. In particular, a more prominent ^{42}K concentration is found above the central string. This is consistent with the electrostatic drift of ^{42}K ions induced by the electric field in the LAr which is generated by the unshielded high-voltage flat cables biased with about 4 kV. The ^{40}K and ^{42}K spatial analysis fitting the potassium γ lines projected in detector space is presented in full detail in §3.6.

α EVENTS

The α distribution is adjusted to best fit the data. The ^{210}Po peak at 5.2 MeV is found to be best described by a mixture of PDFs obtained assuming different p^+ contact thicknesses confirming results of the Phase I background analysis [149]. The empirical linear model which is used to describe α events with degraded energy (see §3.5), extends down to $Q_{\beta\beta}$ and below. For the M1-BEGe data set α events are efficiently isolated using pulse shape discrimination (PSD) techniques (see §2.2). All details about the α events analysis can be found in §3.5.

$2\nu\beta\beta$ DECAY

Most counts in the fit range are attributed to the $2\nu\beta\beta$ decay of ^{76}Ge ; in fact its continuous distribution dominates the spectrum up to almost 1.9 MeV. Here, the $2\nu\beta\beta$ half-life estimate is based on the M1-BEGe data set only. An additional parameter, $\delta^{2\nu}$, parametrizes the observed discrepancy to the value solely derived from the M1-SemiCoax data set. The value of $\delta^{2\nu}$ extracted from the fit amounts to a surplus of 5% of $2\nu\beta\beta$ counts observed in M1-SemiCoax. It mainly quantifies the systematic biases between the active volume determination methods of the two detector types. The BEGe detectors active volume measurements are affected by a smaller systematic uncertainty than the SEMICOAX detectors [122, 149]. Hence, the extracted $2\nu\beta\beta$ half-life, based on the M1-BEGe data set and given here only with statistical uncertainties, amounts to $T_{1/2}^{2\nu} = (2.03 \pm 0.02) \cdot 10^{21}$ yr. A detailed discussion of this result follows in §3.8.

OTHER

Smaller contributions to the background model in the full energy range are attributed to ^{214}Pb and ^{214}Bi from the ^{238}U decay chain, ^{228}Ac , ^{212}Bi and ^{208}Tl from the ^{232}Th decay chains and ^{60}Co . With a total contribution in the fit range of 10^{-3} cts/keV for both the M1-BEGe and M1-SemiCoax data set, ^{234m}Pa gives negligible contribution to the spectra and is therefore dropped from the full-range fit model. The central values preferred in the full-range fit are driven by screening measurements and the spectral contributions are all fully accounted for by the listed hardware components. The only exception is ^{214}Pb and ^{214}Bi where a minor contribution is added on the p^+ contact expected from the observation of α events belonging to the ^{226}Ra decay chain.

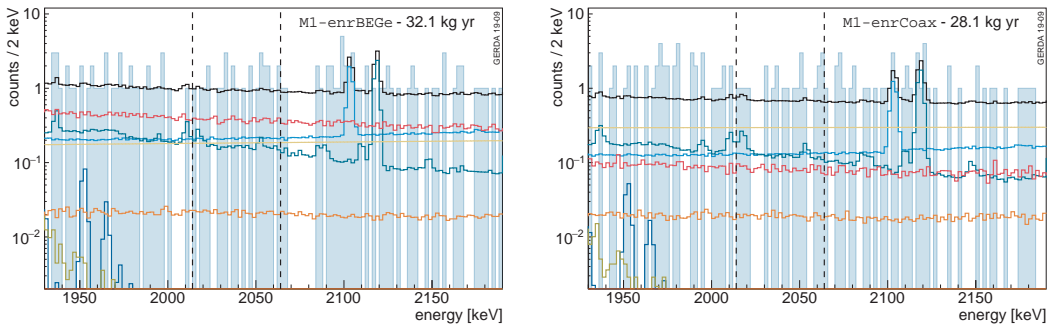


Figure 3.9: Background decomposition for the M1-BEGe (left) and the M1-SemiCoax (right) data sets in the background window between 1930 keV and 2190 keV after data unblinding. The previously blinded window ($Q_{\beta\beta} \pm 25$ keV) is indicated by two dashed lines. The background distribution before active background suppression in the $0\nu\beta\beta$ analysis window can be well approximated with a constant function. For color code see fig. 3.8.

The background model describes the individual contributions to the total background index around $Q_{\beta\beta}$ prior active background suppression (see fig. 3.9). The background index is defined as the number of counts over exposure and energy in the energy window from 1930 keV to 2190 keV excluding the region around $Q_{\beta\beta}$ ($Q_{\beta\beta} \pm 5$ keV) and the intervals 2104 ± 5 keV and 2119 ± 5 keV, which correspond to known γ lines from ^{208}Tl and ^{214}Bi . The dominating background contribution around $Q_{\beta\beta}$ in the M1-BEGe data set come from ^{42}K . Isotopes from the ^{232}Th decay chain, α particles mainly with degraded energy and isotopes from the ^{238}U decay chain contribute about equally. The estimated total background indices extracted from the marginalized posterior distributions are $16.04_{-0.85}^{+0.78} \cdot 10^{-3}$ cts/(keV·kg·yr) for the M1-BEGe data set and $14.68_{-0.52}^{+0.47} \cdot 10^{-3}$ cts/(keV·kg·yr) for the M1-SemiCoax data set.

BACKGROUND
AT $Q_{\beta\beta}$

3.8 Discussion

In general, the marginalized posterior distributions and the results of the material assay measurements are in very good agreement. The only exception is constituted by the ^{40}K activity, which cannot be explained by the available prior information and is fit with the additionally introduced components far and close to the detector array. The ^{42}K and α -event distributions, as already mentioned, cannot be constrained by screening measurements and are adjusted to best fit the data. The background model is not completely free of parameter correlations. As shown in fig. 3.2 several PDFs of the same source of background located in different structural components are very similar and thus generate correlations. Most of them have been resolved by introducing prior distributions based on the screening measurements. However, a few anti-correlations persist which are listed in tab. 3.8.

For what concerns ^{42}K in the LAr volume outside the mini-shrouds, the adoption of an additional PDF for ^{42}K above the detector array is purely motivated by the empirical observation of an excess of background events in the top detectors. The prior knowledge is indeed limited by the fact that the ^{42}K ions undergo drift due to the electrical fields surrounding the detectors and high-voltage cables. Also, due to thermal gradients they can be displaced by convection. With that considered, the presence of

Table 3.8: Correlations between fit components relative to the same background contamination in different locations.

contamination	location 1	location 2	correlation
$^{214}\text{Bi} + ^{214}\text{Pb}$	mini-shrouds	flat cables	-0.43
^{40}K	cabling	detector holders	-0.45
	cabling	close to the array	-0.63
^{42}K	LAr – outside mini-shrouds	n^+ contact	-0.42
	LAr – outside mini-shrouds	LAr – above array	-0.56

unshielded high-voltage cables above the detector array can perhaps explain the excess of ^{42}K observed in this region. A more detailed investigation of the ^{42}K distribution in LAr is not pursued any further, as the full-range fit is inevitably not sensitive to such effects. A more sophisticated Monte Carlo model would in fact not significantly impact the ^{42}K PDFs shape. Nevertheless, some considerations are presented in the contest of the potassium tracking analysis, which is the only analysis presented here that could shed some light on the problem (see §3.6). Systematic uncertainties on the ^{42}K PDF shape can also arise from the model of the partially-active dead layer of the germanium detectors, which is treated as completely dead (the charge-collection efficiency is set to zero throughout all the region between the surface and the full charge-collection depth) in this analysis. The β component of the ^{42}K spectrum above the 1525 keV peak, relevant the in $0\nu\beta\beta$ ROI, is indeed particularly affected by the transition-layer model. It follows that the level of background model contributions from ^{42}K sources particularly close to the n^+ contact might drastically change when considering different active-volume models.

BACKGROUND WINDOW

For each source of background the contribution to the background index at $Q_{\beta\beta}$ prior to active background reduction is listed in tab. 3.7. The statistical uncertainties on the single contributions to the background index are generally of the order of 10% or lower, with the exception of ^{42}K and energy-degraded α events, for which the uncertainty is roughly doubled. The two contributions are affected by a higher uncertainty because they are not bound by screening measurements. In particular, it has been argued how the ^{42}K content in the ROI, arising from β particles reaching the detector active volume, might be strongly affected by the model of the transition region. Because of the amount of systematic effects which might play a significant role in the background decomposition of the ROI, the background indices reported in tab. 3.7 should be taken *cum grano salis*.

The background event distribution in the $0\nu\beta\beta$ analysis window can be well approximated with a constant function (see fig. 3.9). With this assumption, the background indices extracted from data are $16.4_{-1.6}^{+1.7} \cdot 10^{-3}$ cts/(keV·kg·yr) for M1-BEGe and $15.4_{-1.6}^{+1.8} \cdot 10^{-3}$ cts/(keV·kg·yr) for the M1-SemiCoax data set. These values agree well with the background model description presented in §3.7. The background indices prior to further analysis cuts and before the upgrade of the GERDA experiment to Phase II can be found in reference [175]. For the M1-SemiCoax data set the background index prior to the upgrade of $(18 \pm 2) \cdot 10^{-3}$ cts/(keV·kg·yr) is very consistent with the values presented here. The background index of the M1-BEGe data set instead is substantially improved from a Phase I value of $42_{-8}^{+10} \cdot 10^{-3}$ cts/(keV·kg·yr) to a value which is at least 2.5× smaller in Phase II despite a significant increase of inactive hardware mass.⁸ Contributions to the background index from all isotopes have been

⁸Note the slight difference of the M1-BEGe analysis data set presented here and the data set used for $0\nu\beta\beta$ analysis for

improved with respect to Phase I with the exception of background introduced by α surface events. The most drastic improvement is notable for ^{42}K for which the background index contribution for the BEGe detectors appears four times smaller than before the upgrade to Phase II.

As mentioned in §3.7, the extracted $2\nu\beta\beta$ half-life estimate is based on the M1-BEGe data set only. The additional parameter $\delta^{2\nu}$ mainly quantifies the systematic biases between the active volume determination methods of the two detector types. The full charge collection depth (FCCD), which determines the active volume of a detector, has been studied extensively in a detector characterization campaign for the BEGe detectors [120, 122]. The estimate of the FCCD used in this analysis is based on measurements using an ^{241}Am source with characteristic γ lines at 60 keV, 99 keV and 103 keV. However, the FCCD was also measured using a ^{60}Co source with characteristic γ energies of 1173 keV and 1332 keV. The latter FCCD_{Co} is systematically higher (about 3%) with respect to the FCCD_{Am} . The discrepancy could be explained by an energy dependence of the initial charge-carrier cloud size inside the detector but the actual impact on the active volume is still under investigation. For the SEMICOAX detectors only FCCD values determined with a ^{60}Co source are available. Another possible explanation for the observed shift might lie in the correction which is applied to the BEGe FCCD values consequently to the 2–3 year period they were stored at room temperature, after being characterized and before being deployed into liquid argon [122]. The dead-layer growth effect in germanium detector has never been rigorously studied, and therefore the applied correction might be biased. These systematic uncertainties affecting the active volume estimates are investigated in app. A. Considering the systematic uncertainties affecting the determined active ^{76}Ge exposures of the M1-BEGe and M1-SemiCoax data sets (1.8% and 5% respectively, see tab. 3.1), however, $\delta^{2\nu}$ is compatible with zero within 1σ .⁹

Various systematic effects have to be considered when estimating the uncertainty on the $2\nu\beta\beta$ half-life $T_{1/2}^{2\nu}$. Due to the fact that the aim of this analysis is not a precise $2\nu\beta\beta$ half-life measurement, for most of them only a conservative evaluation is provided. Several systematic uncertainties arise from the Monte Carlo simulation framework. Uncertainties due to the GEANT4 model of particle interactions and propagation were estimated to be of the order of 2% in previous publications [27, 149]. Approximations in the implementation of the GERDA setup are conservatively estimated within a 1 – 2% uncertainty range. This accounts for possible spectral shape modifications due to inaccurate charge collection model between the n^+ contact layer and the active detector volume. Uncertainties induced by the theoretical model of $2\nu\beta\beta$ decays implemented in DECAY0, as well as data acquisition and selection methods are considered negligible. A 1.8% contribution accounts for uncertainties in the enrichment and active mass fraction determination (see active ^{76}Ge exposure in tab. 3.1). All the systematic effects considered above sum up to a total systematic uncertainty on $T_{1/2}^{2\nu}$ of 3–4%. In total this leads to $T_{1/2}^{2\nu} = (2.03 \pm 0.09) \cdot 10^{21} \text{ yr}$ compatible with earlier results [27, 149]. A precision measurement of $T_{1/2}^{2\nu}$ after the LAr veto cut, which removes a large fraction of the background, will be presented in chap. 5 together with a careful estimation of the contribution of systematic uncertainty sources.

which the improvement in the background index is slightly higher (3× better background index). This is due to discarded BEGe data for which no PSD can be applied.

⁹The systematic bias between the active volume estimates for the BEGe and SEMICOAX detector types is a sub-dominant contribution in the $0\nu\beta\beta$ analysis with respect to e.g. PSD uncertainties.

3.9 Full Phase II data analysis

The background model presented in the past sections is based on data from the first part of Phase II, for a total exposure of 60.2 kg·yr. In April 2018 the data taking was stopped to permit a hardware upgrade, in which five new detectors of the inverted-coaxial type were deployed together with an improved LAr veto system. For further details about the upgrade the reader is referred to §2.1. The data taking resumed in May 2018 and ended in November 2019 after collecting 44.1 kg·yr of data valid for the background model. In the following, the extension of the full-range energy spectrum analysis to this data set is presented.

DATA AND PDFs The total 44.1 kg·yr of single-detector data is divided according to the detector type, giving three M1 datasets: M1-BEGe⁺, M1-SemiCoax⁺ and M1-InvCoax⁺. Two-detector events are grouped in a single data set: M2-AllEnr⁺. As above, their energy is defined as the sum of the energies reconstructed in the two detectors. The four data sets, their exposures and corresponding detector masses are listed in tab. 3.9. The energy spectra are shown in fig. 3.10. In addition to the list of background contributions in §3.1 that can be identified by eye in the spectra, an event excess is observed at 1124 keV in M1-InvCoax⁺ which is attributed to the decay of ^{65}Zn in germanium¹⁰.

The new experimental setup has been implemented into MAGe. The changes to the software include the implementation of the new INVCOAX detector geometry, the central fiber shroud (see also fig. 2.7, (c) and (d)) the new detector arrangement (each holder unit supports only one detector) and the adaption of the mini-shroud geometry. The updated MAGe version is then used to run simulations of background and signal contaminations and produce the corresponding PDFs, as described in app. C.

BACKGROUND EXPECTATIONS Because of the hardware changes, the expectations about the radio-purity of the setup parts are different than before. In particular, the contribution of the signal and high-voltage cables to the global background budget is expected to be lower, as screening measurements show that the Tecnomec 3 mil cable type is cleaner. Moreover, the introduction of material around the central string might increase the background level. Many of the results of the first screening measurement campaign can be still used as prior information for the Phase II⁺ background model, and part of the new material was screened before deployment in GERDA. The situation is summarized in app. B.

ANALYSIS The full-range analysis of the binned energy spectra has been repeated for the Phase II⁺ data sets. The usual Poissonian likelihood that runs over each single energy bin and each data set is maximized in a Bayesian setting. The C++ BAT-based [148] software routine is publicly available on GitHub¹¹.

¹⁰The ^{65}Zn present in INVCOAX crystals is due to the $^{70}\text{Ge}(\text{n}, \alpha 2\text{n})^{65}\text{Zn}$ reaction, induced by cosmic rays [176, 177]. It disintegrates mainly by electron capture to the 1115 keV excited level of ^{65}Cu with a half-life of 244 days. INVCOAX detectors have been deployed in GERDA short after being produced, so the 1124 keV line (γ de-excitation of ^{65}Cu coincident with K-shell X-rays) can be seen. A first reference to this decay in germanium can be found in a publication from the MILANO $0\nu\beta\beta$ experiment [178].

¹¹The gerda-fitter software, available at <https://github.com/gipert/gerda-fitter>, is a Bayesian histogram fitting program written in C++ and based on the BAT toolkit v1.0.0 [168]. It is specialized and tested on the GERDA data and PDFs format, but any ROOT histogram can be provided as input. The analysis is fully configurable in JSON format (<https://www.json.org>) and does not require writing or compiling C++ code (as one would need to do if using BAT directly). The list of features include: customization of nearly all BAT parameters, computation of the Bayesian evidence, p -value computation, prior distribution configuration by analytical expression or external histogram, variable re-binning and

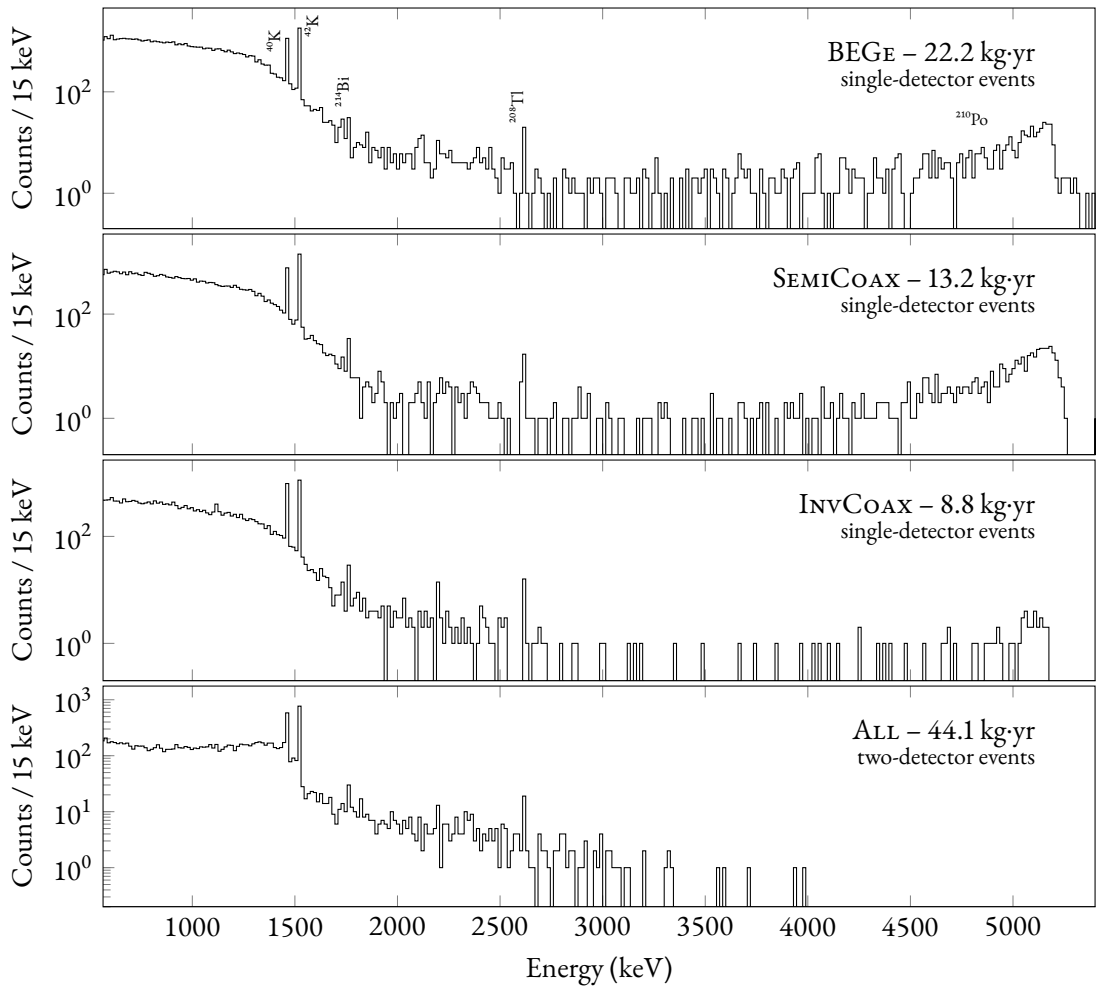


Figure 3.10: The Phase II⁺ data before analysis cuts, divided according to the detector type (only single-detector events). The energy spectrum of two-detector events is shown in the bottom panel.

Table 3.9: Properties of the data sets considered in this analysis. Further details about the GERDA detectors can be found in past publications [121, 123, 149]. Note that the exposures for the BEGe and InvCoax data sets are higher than those reported for the $0\nu\beta\beta$ analysis [57, 58], because of additional data that was discarded due to poor PSD detector performance.

data set	composition	total Ge mass (kg)	active ^{76}Ge mass (kg)	total Ge exposure (kg·yr)	active ^{76}Ge exposure (kg·yr)
M1-BEGe ⁺	29 BEGe ¹²	19.362 ± 0.005	15.11 ± 0.28	22.181 ± 0.006	17.31 ± 0.32
M1-SemiCoax ⁺	6 SEMICOAX	11.827 ± 0.002	9.01 ± 0.38	13.179 ± 0.003	10.00 ± 0.42
M1-InvCoax ⁺	4 InvCoax	7.802 ± 0.002	6.34 ± 0.03	8.775 ± 0.002	7.13 ± 0.03
M2-AllEnr ⁺	all enriched	38.991 ± 0.006	30.46 ± 0.47	44.135 ± 0.007	34.44 ± 0.53

Variable bin sizes are used to represent data and PDFs in the analysis, to speed up the computation and avoid bias from low-statistics PDFs. Dedicated, thin bins (depending on the energy resolution) are used for known γ lines; larger ones (depending on the event rate) for the continuum. The analysis is repeated with fixed-size bins (5 keV) to verify the consistency of the results.

Given the lower α -event rate compared to the first part of Phase II, the α -events analysis has not been repeated. In principle, the ^{210}Po contamination could have changed after being manipulated during the upgrade works (see app. D), resulting in a different shape of the event energy distribution. To avoid using a wrong model of α events in the full-range fit, only two large bins are used in the high-energy region of the single-detector event spectra: [2620, 4500] keV and [4500, 5260] keV. In this way, no potential bias is introduced, and this last part of the energy range is just used to constrain the α event contribution in the $2\nu\beta\beta$ region. The M1-BEGe and M1-SemiCoax α -model PDFs (see §3.5) are re-used for M1-BEGe⁺ and M1-SemiCoax⁺, respectively. The M1-BEGe PDF is also arbitrarily used for M1-InvCoax⁺, since the corresponding detectors have been introduced in Phase II⁺ for the first time. The faithfulness of the PDFs is verified *a posteriori*.

Since also the potassium tracking analysis has not been repeated, no prior information is used to constrain the potassium activity. Priors are extracted from screening measurements results: Gaussian distributions for positive contamination detections and exponential distributions of the form $e^{-2.3\mu x}$ for 90% C.L. upper limits.

RESULTS

A first fit model is constructed including all the background components for which a prior distribution is available from material screening measurements. Additionally, based on the results for the first data of Phase II, two unconstrained ^{40}K fit components are added — one *close*, on the mini-shrouds and *far*, on the outer fiber shroud. As done before, 6 PDFs for ^{42}K are considered: one corresponding to a homogeneous distribution in the LAr volume enclosed by the mini-shrouds, one outside and one in a cylinder above the array (see app. C and §3.7). The other three PDFs correspond to ^{42}K homogeneously distributed on the n^+ surface of the detectors included in the three M1 data sets. A linear function $b_1 + b_2 x$ is also included for each M1 data set separately (6 parameters in total) to account for energy-degraded α events, as also done in §3.7. Given the known discrepancies between the detector active volume determination methods, three independent parameters are used for the $2\nu\beta\beta$ -decay half-

posterior sampling of user-defined observables.

¹²The BEGe detector GD02D is the only detector that does not fully deplete [121]. Hence, events triggered by this detector are not considered in either data set and it is omitted from the mass computation.

lives reconstructed from the three M1 data sets. A uniform prior is set on $1/T_{1/2}^{2\nu}$ ¹³.

The resulting background decomposition of the four analysis data sets is shown in figs. 3.11 to 3.13. Data is presented with the variable binning used in the analysis and a fixed-width 15 keV binning. A close-up in the $0\nu\beta\beta$ region of interest is shown in fig. 3.9. In this fit configuration with many fit parameters, most of the marginalized posteriors are driven by their respective prior distribution. This is expected, given the known correlations between the PDFs and the low count rate of some background sources. All the marginalized posteriors are compatible with the prior information. The additional, special, ${}^{40}\text{K}$ component close to the detector array still reports a non-zero result, while the posterior for ${}^{40}\text{K}$ far from the array is peaked at zero. Differently from what has been previously obtained in §3.7, the ${}^{42}\text{K}$ component on the n^+ contact of the BEGe detectors is now compatible with zero. This is due to the non-null BEGe detectors transition layer model used to obtain the corresponding PDF, which increases the rate of β events above the 1525 keV peak (see fig. 3.2d) and decreases the compatibility with experimental data. A summary of the analysis parameter estimates, including reconstructed counts in the fit range and background indices in the $0\nu\beta\beta$ region of interest, is given in tab. 3.10.

The three marginalized posteriors for the $2\nu\beta\beta$ -decay half-life, coming from the three detector types separately, are shown in fig. 3.15. The distributions have been obtained by re-sampling the Markov chain¹⁴. As it is evident, a systematic discrepancy between the half-life predicted with BEGe detectors and with SEMICOAX detectors is found, at the same level of what observed in the analysis of the M1-BEGe and M1-SemiCoax (see §3.7). The half-life predicted with INVCOAX detectors, on the other hand, seems to give the same results extracted from the SEMICOAX detectors. Again, there is a clear evidence for a systematic underestimation of the SEMICOAX and INVCOAX detector active volume, or overestimation of the BEGe detector active volume, or even a more complex effect. This issue is addressed in detail in app. A, where additional evidence for the presence of systematic biases in the active volume estimate is presented. As remarked before, in the case of BEGe detectors the shift could be largely due to uncertainties on the n^+ dead-layer growth speed at room temperature.

To further investigate the origin of the discrepancy, the full-range analysis is repeated with PDFs (for all background sources and $2\nu\beta\beta$ -decay) that assume the preliminary active and transition layer model extracted from ${}^{39}\text{Ar}$ data, which is described in detail in app. A.3. A comparison between the latter and the official model is given in fig. A.5, and the obtained $T_{1/2}^{2\nu}$ posteriors are shown in fig. 3.16. INVCOAX and SEMICOAX posteriors are shifted up, while the BEGe posterior is shifted down, achieving a better compatibility between the three estimates. These results, however, must be taken with a grain of salt: the ${}^{39}\text{Ar}$ data analysis is still at an early stage and the impact of possible sources of systematic uncertainties has not been evaluated yet. They demonstrate, indeed, the potential of an analysis of ${}^{39}\text{Ar}$ data to obtain unbiased measurements of the detector active volumes in their experimental working conditions. Robust active volume estimates are, in fact, of great interest for the $2\nu\beta\beta$ analysis.

To detect changes of the background level before and after the Phase II⁺ upgrade works, the full-range analysis of the energy spectra presented in §3.7 and in this section has been repeated with a minimal fit configuration. A representative set of background components has been identically selected for

UPGRADE
EFFECT

¹³The detailed fit configuration file is available at https://github.com/gipert/gerda-fitter/config/phaseIIplus/gerda-fitter-phIIp-raw-global_extra_blocks.json.

¹⁴Note that the priors on $T_{1/2}^{2\nu}$ are not exactly flat, as the real uniform priors are set on the number of $2\nu\beta\beta$ counts, which is proportional to $1/T_{1/2}^{2\nu}$. In this range of half-life values, however, they can be well approximated by a flat distribution.

Table 3.10: Summary of the analysis parameter estimates. Global mode and marginalized mode, along with its smallest 68% C.I., are reported as representatives of the posterior parameter distribution. The number of reconstructed counts in the fit range and the background index at $Q_{\beta\beta}$ prior active background suppression are listed for each component and each analysis data set. The original type of prior distribution is marked with [f] for flat, [g] for Gaussian and [e] for exponential.

source	[prior] location	marg. mode with 68% CI	screening	counts in fit range Bl at $Q_{\beta\beta}$ units: cts 10^{-3} cts/(keV kg yr)			
				M1-BEGe ⁺	M1-SemiCoax ⁺	M1-InvCoax ⁺	M2-AllEmr ⁺
$^{2\nu}\beta\beta$ (10^{21} yr)	[f] BEGe detectors	2.09 [2.08, 2.11]	-	31451	-	-	0
	[f] SEMICOAX detectors	1.91 [1.89, 1.93]	-	-	0	19181	0
	[f] InvCoax detectors	1.90 [1.88, 1.92]	-	-	-	13816	0
$^{212}\text{Bi} + ^{208}\text{Tl}$ (μBq)	[f] detector holders	210 [160, 240]	-	248	114	88	415
	[g] mini-shrouds	20 [15, 24]	18(5)	14	3.87	9	25
	[g] inner fiber shroud	25 [18, 31]	24(7)	11	[3.63, 4.16]	6	29
$^{214}\text{Pb} + ^{214}\text{Bi}$ (μBq)	[g] outer fiber shroud	190 [140, 240]	177(53)	32	[2.72, 3.10]	13	21
	[e] cabling	530 [500, 580]	<210	812	312	260	860
	[g] mini-shrouds	51 [34, 61]	46(14)	75	2.78	46	94
^{40}K (mBq)	[g] inner fiber shroud	13 [8.7, 17]	1.2(4)	11	[2.62, 3.00]	6	51
	[g] outer fiber shroud	88 [64, 120]	177(53)	23	[1.88, 2.14]	13	0
	[g] cabling	2.2 [1.4, 2.9]	3.0(8)	462	176	152	252
^{42}K (mBq)	[g] inner fiber shroud	0.49 [0.38, 0.62]	0.4(12)	70	59	73	54
	[g] outer fiber shroud	2.7 [1.8, 3.5]	3.1(9)	91	54	21	51
	[g] detector holders	2.4 [1.9, 3]	2.8(6)	820	0	359	474
	[g] mini-shrouds	1.7 [1.1, 2.3]	1.7(6)	351	205	179	217
	[f] close to the array	13 [11, 14]	-	2640	1542	1347	1628
	[f] n^+ (BEGe)	< 4.8 · 10 ⁻³	-	< 210	< 6	< 5	< 185
^{60}Co (μBq)	[f] n^+ (SEMICOAX)	1.4 [1.1, 1.6]	-	313	1610	188	484
	[f] n^+ (INVCOAX)	0.26 [0.22, 0.31]	-	76	4.75	49	152
	[f] LAr - above array	930 [780, 1000]	-	8527	[3.90, 5.75]	3112	4564
^{228}Ac (μBq)	[f] LAr - inside mini-shrouds	1.2 [0.73, 1.6]	-	999	4.44	338	506
	[f] LAr - outside mini-shrouds	380 [190, 690]	-	1622	957	491	942
	[g] inner fiber shroud	25 [18, 31]	24(7)	16	9	21	24
^{65}Zn (μBq)	[g] mini-shrouds	20 [15, 24]	19(5)	20	0.36	12	20
	[g] detector holders	210 [160, 240]	<250	149	[0.31, 0.40]	66	148
	[e] detector holders	83 [68, 97]	<102	296	133	104	419
α decays (cts)	[f] InvCoax detectors	50 [44, 61]	-	24	16	219	85
	[f] $^{210}\text{Po} + ^{228}\text{Ra}$ chain (BEGe)	1130 [1090, 1180]	-	748	4.36	-	-
	[f] $^{210}\text{Po} + ^{228}\text{Ra}$ chain (SEMICOAX)	1020 [975, 1070]	-	-	[4.19, 4.56]	[1.73, 1.89]	[1.12, 1.46]
	[f] $^{210}\text{Po} + ^{228}\text{Ra}$ chain (INVCOAX)	132 [117, 151]	-	-	-	87	-

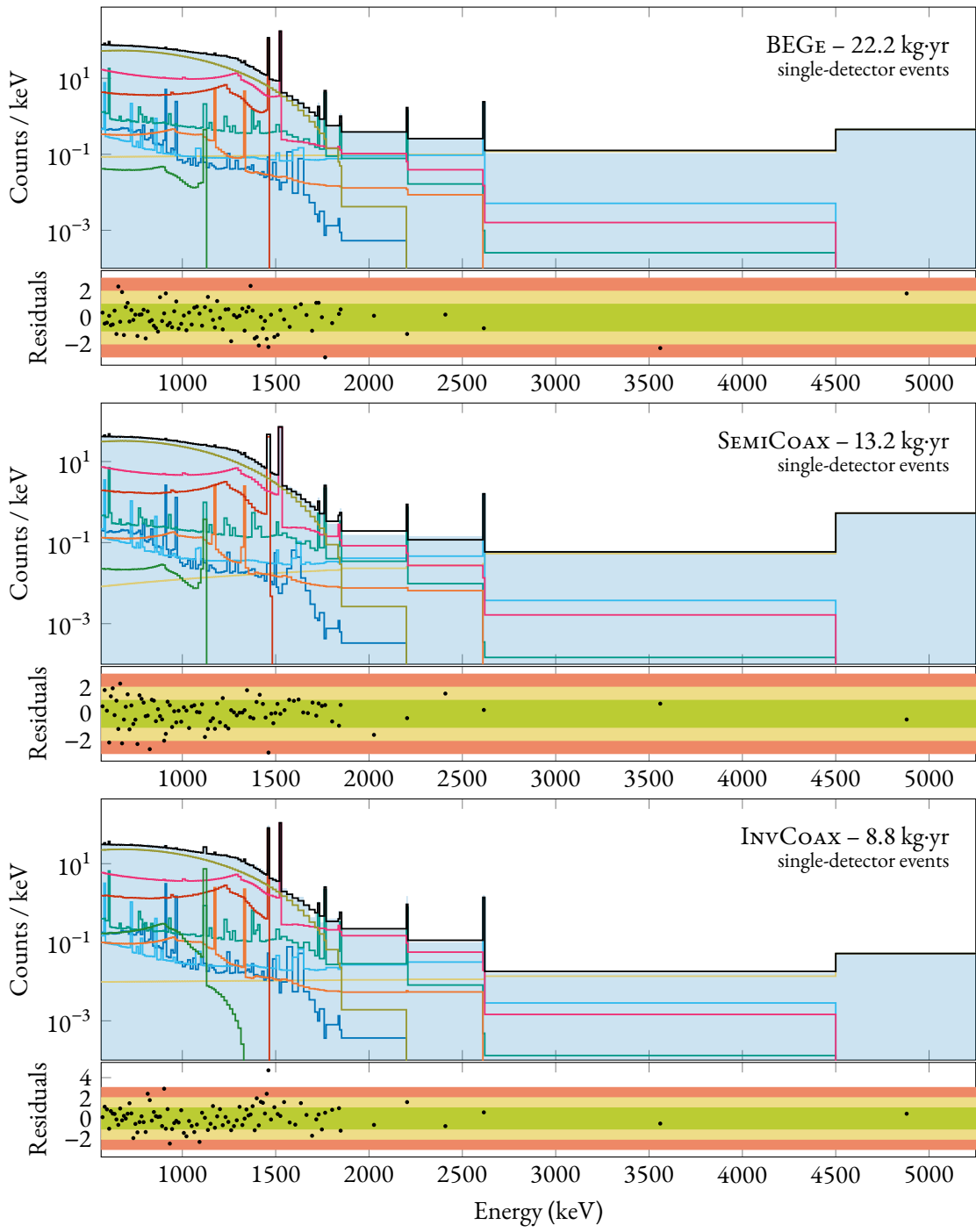


Figure 3.11: The background decomposition of the last 44.1 kg·yr of GERDA Phase II before analysis cuts, single-detector data sets. The binning is the one used in the analysis. Contributions from the same radioactive decay are summed for visualization purposes. The data-to-model ratio is shown in the bottom panels together with the smallest 60%, 95% and 99% confidence intervals.

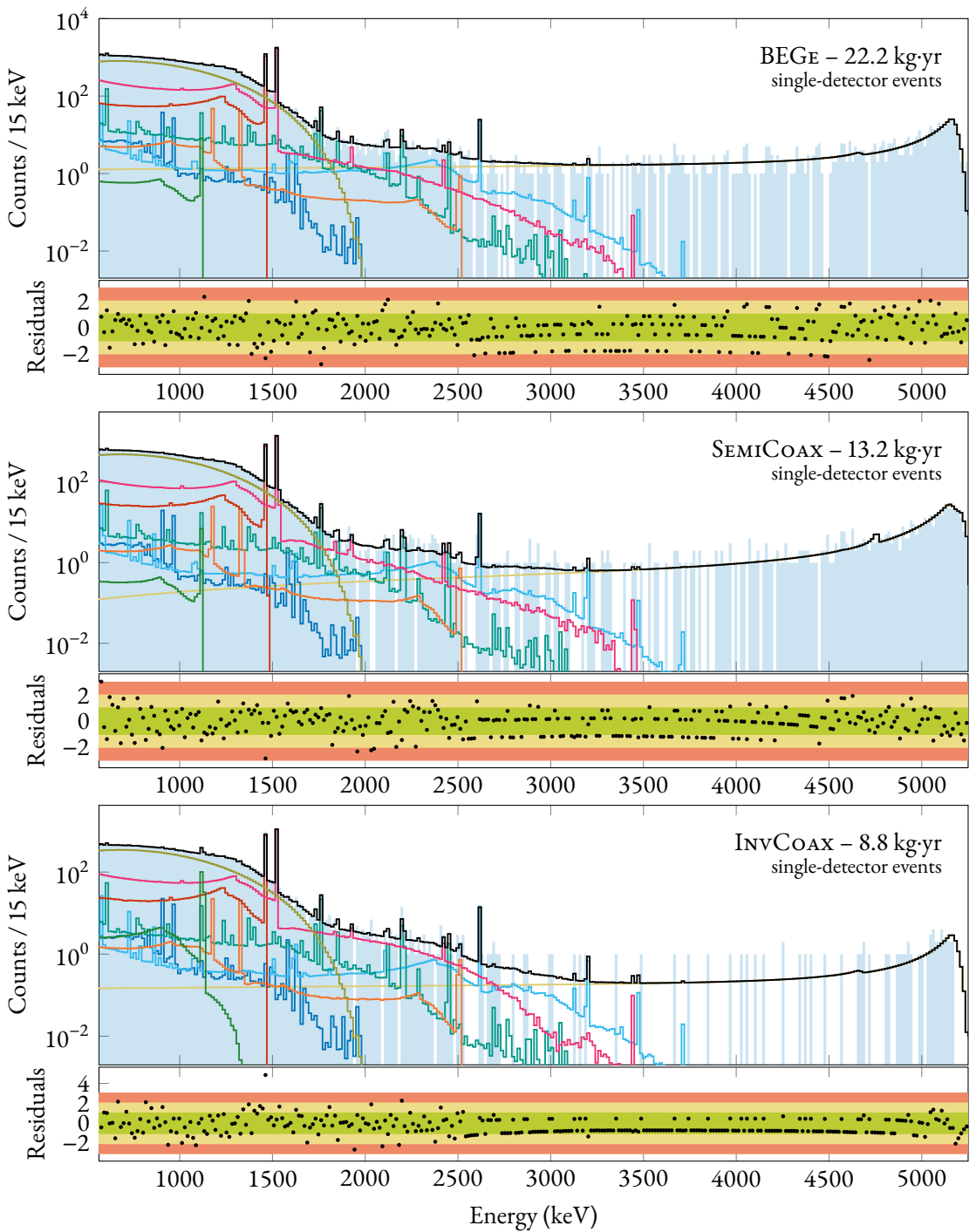


Figure 3.12: The background decomposition of the last 44.1 kg·yr of GERDA Phase II before analysis cuts, single-detector data sets. A fixed-width 15 keV binning is used. Contributions from the same radioactive decay are summed for visualization purposes. The data-to-model ratio is shown in the bottom panels together with the smallest 60%, 95% and 99% confidence intervals.

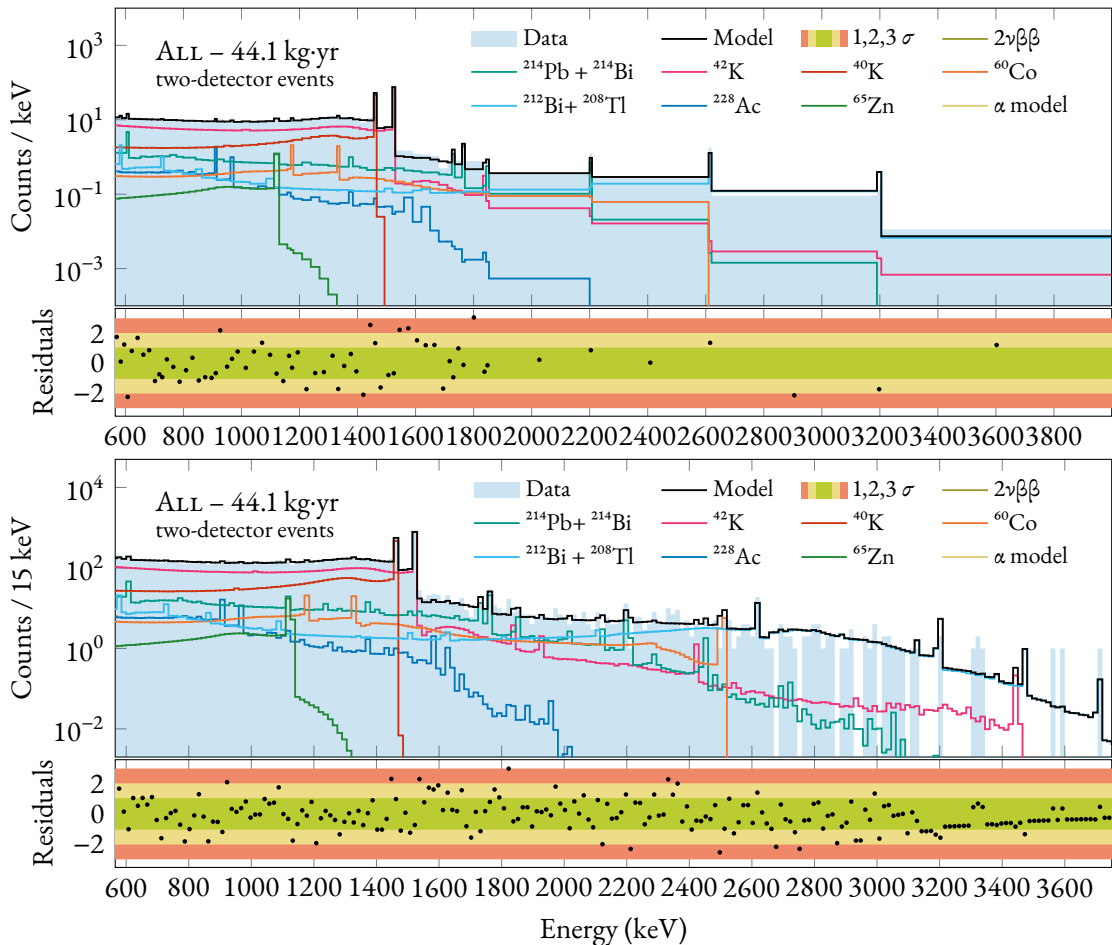


Figure 3.13: The background decomposition of the last 44.1 kg·yr of GERDA Phase II before analysis cuts, M2-AllEnr⁺ data set. The data is shown in its analysis binning (top) and with fixed-width 15 keV bins (bottom). Contributions from the same radioactive decay are summed for visualization purposes. The data-to-model ratio is shown in the bottom panels together with the smallest 60%, 95% and 99% confidence intervals.

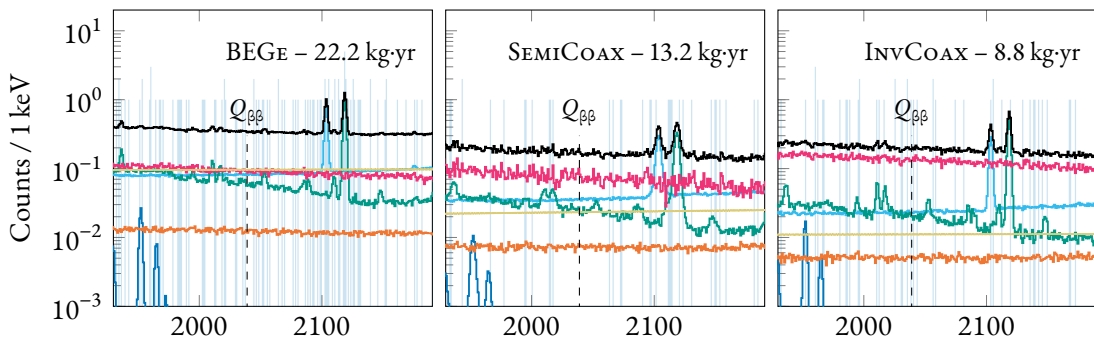


Figure 3.14: The background decomposition of the last 44.1 kg·yr of GERDA Phase II before analysis cuts, in the $0\nu\beta\beta$ analysis window.

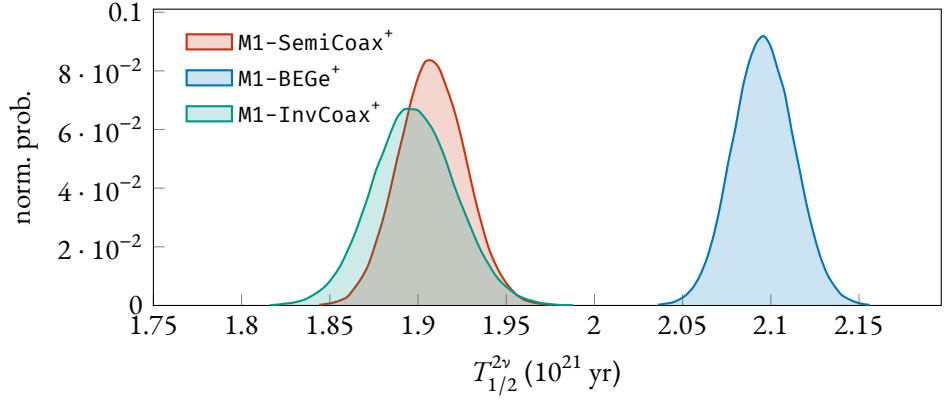


Figure 3.15: Marginalized posterior distributions of the $2\nu\beta\beta$ -decay half-lives reconstructed from the three M1-BEGe⁺, M1-SemiCoax⁺ and M1-InvCoax⁺ data sets separately. The three parameters are independent from each other in the fit and carry a nearly uniform prior distribution (the prior is actually uniform on $1/T_{1/2}^{2\nu}$).

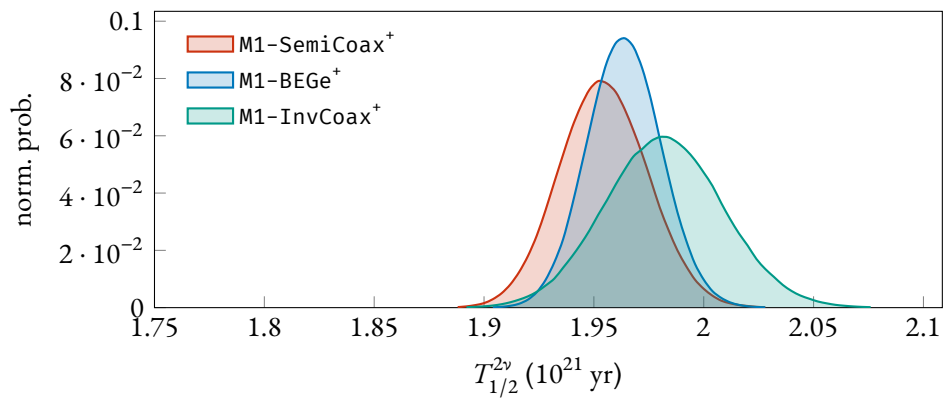


Figure 3.16: Marginalized posterior distributions of the $2\nu\beta\beta$ -decay half-lives reconstructed from the three M1-BEGe⁺, M1-SemiCoax⁺ and M1-InvCoax⁺ data sets separately. The PDFs in the analysis have been computed with the preliminary detector active volume model results obtained from ${}^{39}\text{Ar}$ data in app. A.3. The systematic shifts observed in fig. 3.15 are reduced.

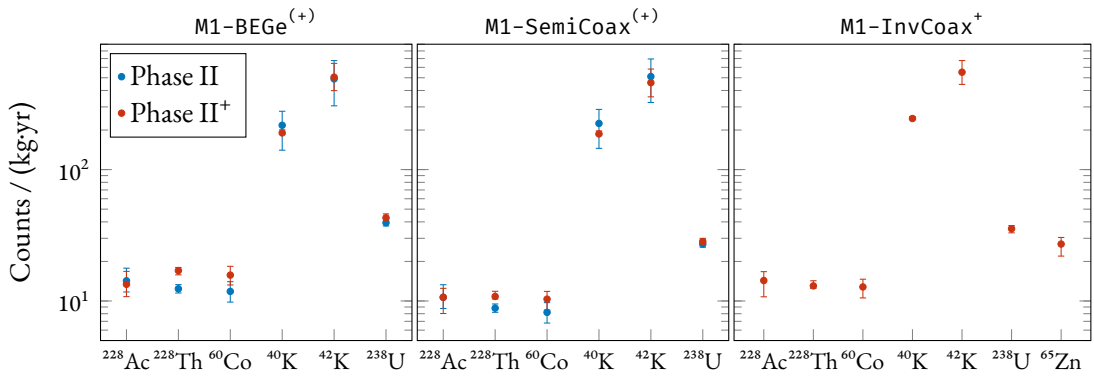


Figure 3.17: Comparison between the single-detector event background counts in units of ^{76}Ge exposure above the ^{39}Ar Q-value (565 keV) reconstructed with the background model analysis before and after the Phase II $^{+}$ hardware upgrade.

the two analyses: $2\nu\beta\beta$ -decay for each detector type, ^{212}Bi , ^{208}Tl , ^{214}Pb , ^{214}Bi , and ^{60}Co on cables, ^{228}Ac on detector holders, ^{40}K close (mini-shrouds) and far (outer fiber shroud) from the array, ^{42}K in LAr outside/inside the mini-shrouds, above the array and on the n $^{+}$ surface for each detector type, the α model PDFs and ^{65}Zn in InvCoax detectors.

In fig. 3.17 the number of reconstructed counts above the ^{39}Ar Q-value (565 keV) for each radioactive source, for each single-detector event data set, before and after the Phase II $^{+}$ upgrade, in units of ^{76}Ge exposure is shown. The extracted count rates before and after the upgrade are consistent within their statistical error, except for ^{228}Th (^{212}Bi and ^{208}Tl) and ^{60}Co contaminations, which seem to have increased after the upgrade.

The results of the background decomposition of the full GERDA Phase II data before the LAr veto and PSD cuts have been combined in fig. 3.18. The single-detector data sets M1-BEGe, M1-SemiCoax, M1-BEGe $^{+}$, M1-SemiCoax $^{+}$ and M1-InvCoax $^{+}$ have been combined in the upper panel; M2-AllEnr and M2-AllEnr $^{+}$ have been combined in the bottom panel.



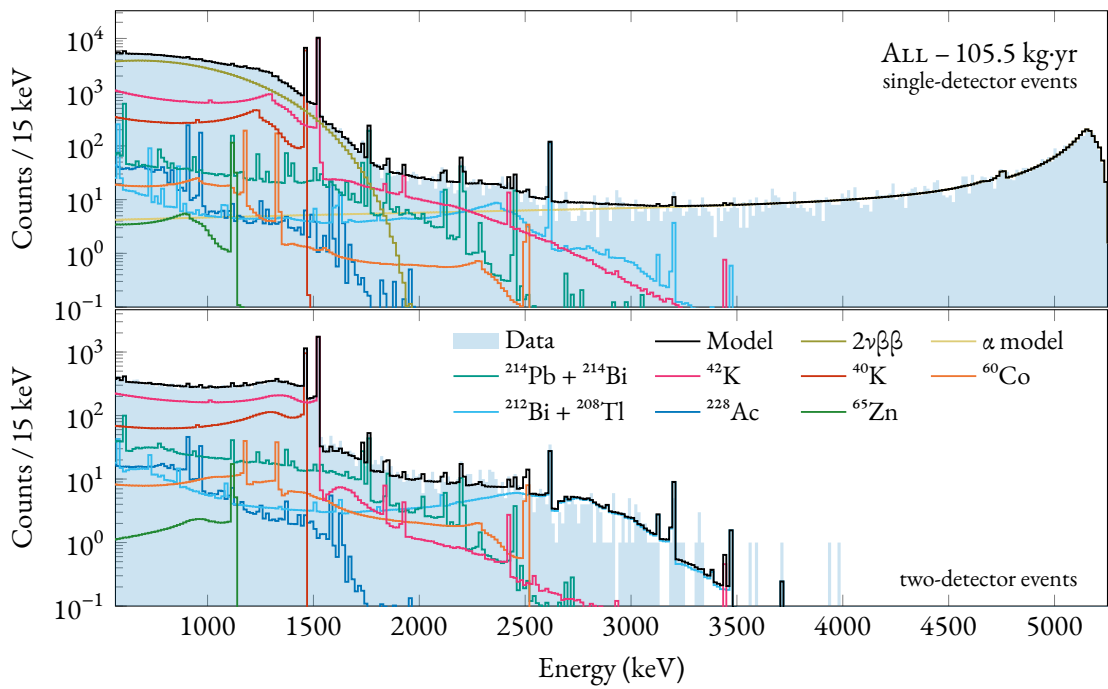


Figure 3.18: Background decomposition of the full GERDA Phase II data set, divided in single- and two- detector events. Background components are grouped per radioactive source for visualization purposes.

IN SHORT

- The development of a careful model of the background in the full energy range of events collected by a neutrinoless double-beta decay experiment is crucial in order to understand the composition of background events in the region of interest. The spatial distribution of the background sources and their effect in the data is useful information in designing future hardware upgrades or experimental efforts. Last but not least, a background model grants access to the two-neutrino double-beta decay event distribution, that can be analyzed to determine the half-life of the process and to constrain the presence of beyond the standard model physics phenomena.
- The energy spectrum of single- and two-detector events before the LAr veto and the PSD cuts, divided by detector type, is decomposed in a Bayesian setting, which includes prior information from material screening measurements. The expected distribution of the various background components is generated starting from a full Monte Carlo simulation chain of the experimental setup. The shape of high-energy events, attributed to α decays on the p^+ detector contacts, is studied separately and incorporated in the final fit. The spatial information enclosed in potassium events from the two intense γ peaks is exploited in a potassium tracking analysis, which considers data from each detector separately and is therefore able to better unravel the origin of the background events. The results are incorporated in the final fit as prior information.
- The obtained model describes the data and reproduces the screening measurement results to a satisfying degree of accuracy. An unexpected higher ^{40}K contamination is found both in locations close to the detector array and far from it. Moreover, an excess of ^{42}K events is seen by detectors at the top of the array, possibly attributed to the electromagnetic attraction of the potassium ions towards the high-voltage cables. The background at the $0\nu\beta\beta$ is found to be flat except for two γ lines from ^{208}Tl and ^{214}Bi . The main contribution is ^{42}K β particles, while α events and isotopes from the ^{232}Th and ^{238}U decay chains contribute equally. However, the composition of the background at the $0\nu\beta\beta$ Q-value must be taken with a grain of salt: many sources of systematic uncertainties have not been taken into account.
- A discrepancy between the $2\nu\beta\beta$ -decay half-life reconstructed with BEGe detectors and the one from SEMICOAX detectors is found, revealing the presence of a systematic bias between the two active volume estimates. This is attributed to the employment of different measurement techniques or the underestimation of the BEGe detectors dead-layer growth at room temperature. Nevertheless, the two results are compatible within the systematic uncertainty attributed to the active volume estimates. The measurement of the $2\nu\beta\beta$ half-life is, however, out of the scope of the analysis of data before the analysis cuts. A more precise determination will be presented in chap. 5, based on data after LAr veto cut.

- The full-range analysis of the energy spectrum has been repeated for data collected after the Phase II⁺ upgrade. The experimental setup implemented in the Monte Carlo has been updated, and new PDFs have been generated. Compared to the first part of Phase II, the background has not significantly changed as a consequence of the upgrade works. A systematic shift between the $2\nu\beta\beta$ -decay half-life estimates from SEMICOAX and INVCOAX detectors, from one side, and BEGE detectors is also observed with the new data. A preliminary re-analysis using the detectors active volume extracted from ^{39}Ar data seems to remove this tension.

The background after the LAr veto cut

All what has been shown until now concerns data before the LAr and PSD cut. In this chapter, instead, a model of the background after the LAr veto cut will be presented, based on a Monte Carlo simulation of the LAr scintillation light propagation. Being able to describe the background after this major event selection is indeed of great interest to study the distribution of two-neutrino double-beta decay events, which are almost never vetoed by the LAr veto system¹. As extensively shown in chap. 1, the presence of several new physics phenomena can be constrained by studying the shape of the $2\nu\beta\beta$ events distribution. Understanding the action of the LAr veto cut on background events from the point of view of the background model requires, however, a full Monte Carlo simulation of the LAr scintillation mechanism as well as a complete implementation of the relevant material and surface optical properties that contribute to light propagation in the setup. Implementing such a simulation, as it will be clear soon, requires an accurate knowledge of many optical parameters, which is, unfortunately, not always available. Nevertheless, it will be shown how special calibration data with low-activity sources and the LAr veto instrumentation turned on can be used to partially overcome the issue. An independent analysis of this special data set is used to tune the unknown optical parameters in the Monte Carlo and reproduce the observed vetoing performance. The obtained parameters are then used to generate a map of the LAr scintillation light detection probability, which is applied to the background model simulations in order to obtain the LAr veto flag. These new background model PDFs are then directly employed in a statistical test of possible deviations of the $2\nu\beta\beta$ distribution from its Standard Model description, an analysis that will be presented in chap. 5.

The chapter is structured as follows: in §4.1 the data after the LAr veto cut, sub-divided in the analysis data sets, is described. Follows a description of the LAr veto system simulation, embedded into the MAGE framework, in §4.2. There it will be also shown how special calibration data is used to tune the simulation model and how the LAr veto flag for synthetic events is evaluated. Finally, the background decomposition of the full-range GERDA energy spectrum after the LAr veto cut (61.4 kg·yr from the first part of Phase II) will be presented in §4.3 and discussed in §4.4.

4.1 Analysis data sets

¹Double-beta decay interactions in germanium release energy in about 1 mm from the interaction vertex, the probability of the emitted electrons to escape the detector and interact with LAr is very small.

²The BEGe detector GD02D is the only detector that does not fully deplete [121]. Hence, events triggered by this detector are not considered in either data set and it is omitted from the mass computation.

Table 4.1: Properties of the data sets considered in this analysis. Further details about the GERDA detectors can be found in past publications [121, 149]. Note that the exposures are slightly higher than those reported in tab. 3.1 because of additional data from the last run of the first part of Phase II (RUN 93) which was not included in the first place.

data set	composition	total Ge mass (kg)	active ^{76}Ge mass (kg)	total Ge exposure (kg·yr)	active ^{76}Ge exposure (kg·yr)
M1-BEGe	29 BEGe ²	19.362 ± 0.005	15.11 ± 0.28	32.748 ± 0.009	25.57 ± 0.48
M1-SemiCoax	7 SEMICOAX	15.576 ± 0.003	11.66 ± 0.46	28.638 ± 0.005	21.43 ± 0.85
M2-AllEnr	all enriched	34.938 ± 0.006	26.76 ± 0.54	61.386 ± 0.011	47.00 ± 0.97

The background model after the LAr veto cut has been developed using data from the first part of GERDA Phase II, as in chap. 3. Single- and two- detector events that survive the LAr veto cut (more in §2.2) have been considered: two data sets from the first category (M1-BEGe and M1-SemiCoax) and a single one for the second (M2-AllEnr). The data set exposures are documented in tab. 4.1. Note that the exposures are slightly higher than those reported in tab. 3.1 because of additional data from the last run of the first part of Phase II (RUN 93) which was not included in the first place. The reader is referred to §3.1 for general details about how these data sets are constructed.

The event energy distributions of the three data sets before and after the LAr veto cut are displayed in fig. 4.1: the sum spectrum of M1-BEGe and M1-SemiCoax in the top panel and M2-AllEnr in the bottom panel. γ peaks and their Compton shoulders are largely suppressed (e.g. 80% of the ^{42}K FEP is cut) with the exception of ^{40}K , which is a pure γ emission (electron capture) and is less likely to deposit coincident energy in the LAr. After the cut, the spectrum is mainly composed by $2\nu\beta\beta$ (the LAr veto survival probability is $> 99\%$) and residual α events. The signal-to-background ratio in the $2\nu\beta\beta$ -dominated region (from 565 keV to 2000 keV excluding the potassium γ lines) improves by a factor 10, jumping from ~ 2 to ~ 20 . This large background reduction motivates the development of a background model after the LAr veto cut to study the $2\nu\beta\beta$ event distribution with a significant sensitivity improvement.

4.2 Monte Carlo simulations and probability density functions

The Monte Carlo simulation of the liquid argon veto requires to enable the GEANT4 optical physics simulation routines, which have been disabled for the production of the background model PDFs before analysis cuts (see §3.2). The relevant material optical properties which are needed to simulate the scintillation of LAr and the propagation of the photons throughout the whole setup have been implemented into MAGE and documented in detail in app. C.1. As reported there, unfortunately, many properties are uncertain or not known at all, especially in the VUV energy regime (~ 128 nm). This uncertainty propagates to the LAr veto model and the background PDFs, and is treated as a systematic contribution in the $2\nu\beta\beta$ distribution analysis presented in chap. 5.

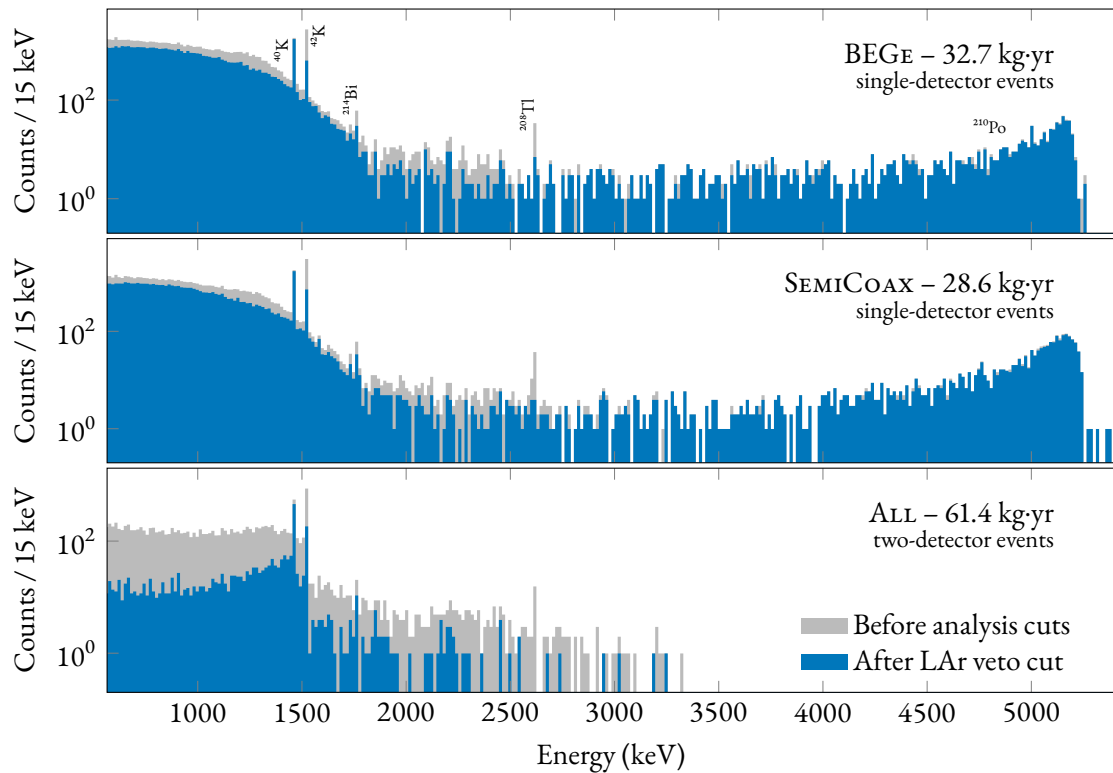


Figure 4.1: The data from the first 61.4 kg·yr of GERDA Phase II before and after the liquid argon veto cut, divided into the three background model data sets: M1–BEGe, M1–SemiCoax and M2–AllEnr.

4.2.1 Simulating the LAr veto system

Simulating optical physics is notoriously a computationally intensive task, as the number of photons that need to be tracked is very high. Enabling optical processes in background model simulations, which already take tens of thousands of CPU hours to complete, is not feasible. To address the problem, an alternative approach to compute the LAr veto flag for already existing simulations has been developed, based on the construction of a detection probability map of scintillation photons in LAr. This object, which is going to be described in this section, will be also be referred to just as “heat map” or “probability map” in the following.

The first step to produce the probability map is to run a full photon-tracking simulation of 128 nm scintillation photons in the whole LAr volume defined in MAGE. An isotropic source of VUV photons, homogeneously distributed in a pre-selected LAr volume, is simulated. MAGE, in fact, allows to restrict the sampling to the volume occupied by LAr only or its intersection with a geometric solid (e.g. a cylinder). The photon initial energy is sampled from a Gaussian distribution with mean 128 nm and variance 2.929 nm [134]. After being propagated in the GERDA setup by the GEANT4 core routines, it may hit a LAr instrumentation sensitive volume (SiPM channel or PMT channel), whose unique identification number is written on disk. After collecting a sufficient amount of simulated events, the simulation output is further processed into the probability map. The three-dimensional LAr volume implemented in MAGE is partitioned in small boxes (or voxels), that define the regions in which the probability is constant. Events generated in a voxel are collected and the ratio between the number of detected photons (in which at least one LAr veto channel fired) over the total is computed:

$$p_k = \frac{n_k}{N_k} \pm \frac{1}{N_k} \sqrt{n_k \left(1 - \frac{n_k}{N_k}\right)}.$$

where n_k and N_k are the total number of detected and simulated photons in voxel k , respectively. The binomial uncertainty estimate assumes $N_k > 0$ and $n_k < N_k$, which is always the case for the voxel size considered in this study. These probability estimates are written on disk as a three-dimensional histogram, or probability map. The GERDA Monte Carlo LAr model is effectively condensed in this object.

The second and last step is to fold the probability map into the usual background model simulation output, for which no information derived from native optical processes is available. Nevertheless, information about energy depositions by γ , β and α particles in LAr is available in the simulation output and provide the starting point to compute the LAr veto flag. For a given single energy deposition the number of generated scintillation photons M is drawn from a Poisson distribution with mean equal to the deposited amount of energy times the LAr scintillation yield times the LAr Fano factor:

$$M \sim \mathcal{P}(E \cdot Y \cdot F).$$

The number of detected photons is then randomly drawn from a binomial distribution with success probability p_k , where k labels the voxel that contains the LAr hit position, and number of trials equal to M :

$$m \sim \mathcal{B}(M, p_k).$$

If $m > 0$ the event is flagged as vetoed by the LAr instrumentation.

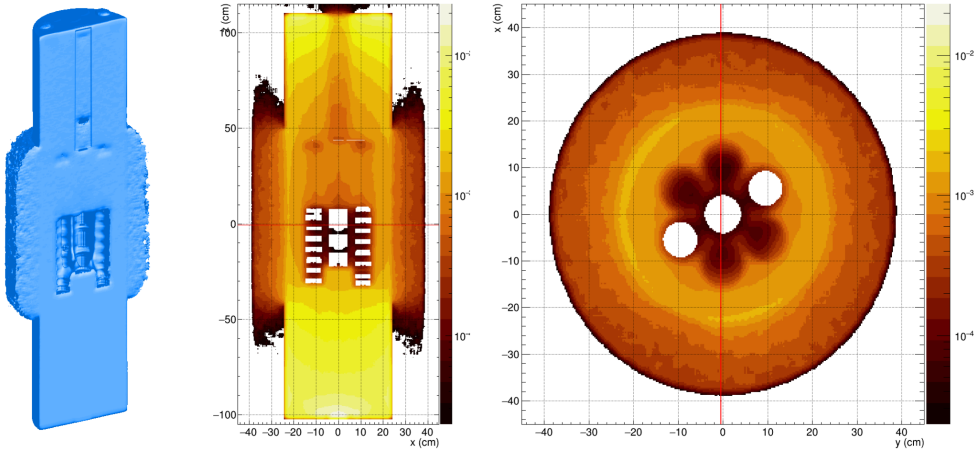


Figure 4.2: The three-dimensional LAr photon detection probability map interactive viewer. Two-dimensional longitudinal and transversal sections are displayed in the second and third pad from the left corresponding to the user pointer position on the 3D rendering in the first pad. Red lines mark the cut positions. A smoothing algorithm is applied to wash out statistical fluctuations and make the map look more homogeneous to the eye.

A visualization of an example probability map is given in fig. 4.2, along with one-voxel wide transversal and longitudinal slices. Voxels are colored according to their probability value: darker areas correspond to regions in which less scintillation photons reach the LAr veto detectors and therefore the vetoing efficiency is worse. The detection probability reaches very low values in the LAr volume enclosed by germanium detectors, as photons get easily trapped in such a complex geometry. On the other hand, the closer to PMTs and fibers the photons are produced, the higher their detection probability is. In the horizontal slice one can also appreciate the effect of the different SiPM channel efficiencies, which break the rotational invariance of the map.

THE LAr HEAT MAP

As remarked in app. C.1, uncertainties on the optical specifications implemented in MAGe can be quite large. Properties like the LAr scintillation yield and attenuation length, the germanium reflectivity and the TPB quantum efficiency have a potentially large impact on the probability map. Other crucial unknowns are the SiPM and PMT channel efficiencies and the coverage of the fiber shroud, defined as the fraction of lateral surface area of the curtain occupied by fiber material. Channel efficiencies extracted from physics data cannot be used, as the simulated efficiencies account for various other effects in the Monte Carlo and can therefore be quite different³. The fiber coverage on the other hand should be around 0.5, but there could be shrinking phenomena or single-fiber twists in LAr which could make the real coverage significantly different.

To understand the systematic impact of these parameters on the LAr probability map, a dedicated Monte Carlo study has been performed. A set of representative voxels has been selected, whose location is documented in fig. 4.3, top panel. For each of these voxels the probability dependence on some

³Suppose, as an example, that a systematic difference between the geometry of an implemented setup part and the experimental reality is present. Suppose also that this impacts systematically on the light seen by sensitive detectors in the Monte Carlo. A very well possible scenario might be that, for example, the trapping efficiency of a fiber module in the simulation largely deviates from reality. In this sense, the efficiency attached to a SiPM or PMT channel in the Monte Carlo in order to reproduce the event suppression seen in data is *effective*, i.e. must include several additional effects arising from an approximate modeling.

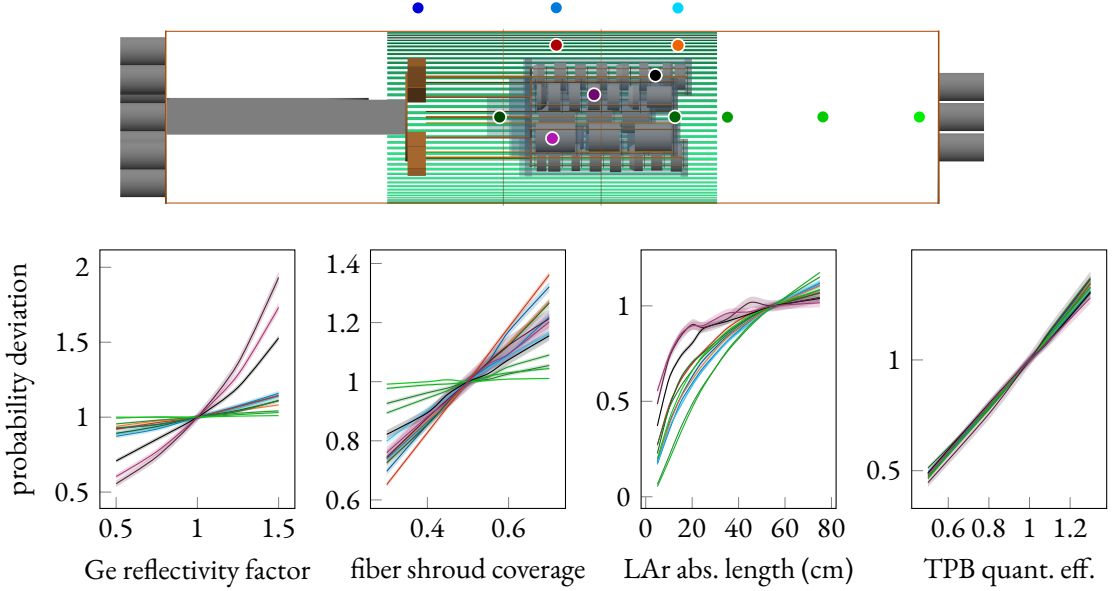


Figure 4.3: Study of the impact of Monte Carlo parameters on LAr light detection probabilities in various spatial points. Each curve shows the dependence of the probability (normalized to the values obtained with the parameter reference value) on germanium reflectivity, fiber shroud coverage and LAr absorption length in the points shown in the top panel, using the same color code. The germanium reflectivity, which is the only quantity that depends on the incident photon energy, is scaled by a global factor, shown on the horizontal axis. A unit value of the scaling factor corresponds to the reference values implemented in MAGE.

Monte Carlo parameters has been investigated with dedicated full photon-tracking simulations. The results are displayed in the remaining plots of fig. 4.3. Voxels have been considered along the central array axis (green), just outside (blue) and inside (red) the fiber shroud. Three additional voxels have been chosen in the low-probability region inside the germanium array (black and violet). Four properties have been taken into consideration for this study: the germanium reflectivity, the fiber shroud coverage, the LAr absorption length and the quantum efficiency of TPB-coated surfaces. Each probability curve is normalized to the value corresponding to reference parameters, such that the vertical axis shows relative changes. Two qualitatively different trends can be noticed: the reflectivity and coverage impact is approximately linear in the considered interval, while the absorption length acts more exponentially on probabilities. This is compatible with the assumption that attenuation in matter generally follows an exponential law. The impact of a parameter depends on the voxel location too. As instance, the probability in the black voxel between GD89B and GD02D changes drastically upon different germanium reflectivity assumptions. On the other hand, the orange and red voxel close to the fibers (where the calibration sources are) are the most sensitive to modifications of the fiber shroud coverage. Acting on the TPB quantum efficiency seems to uniformly scale the detection probability, as one would do by multiplying the heat map by a global factor.

4.2.2 Tuning the LAr veto Monte Carlo model

As mentioned in the previous section, the knowledge of several Monte Carlo optical specifications is unfortunately poor. In particular, PMT and SiPM channel efficiencies, essential to build a predictive LAr veto model, are not known. Efficiencies extracted from physics data cannot be used directly, as the Monte Carlo efficiencies are in reality complex objects that account for other effects³. To overcome these issues, a statistical analysis has been developed to tune the Monte Carlo parameters with physics data. A sample which is independent from the regular GERDA physics data has been identified in the special calibration runs with low-activity sources and the LAr veto instrumentation turned on. A short overview of this analysis will be given in this section; the reader is referred to [179] for an extensive presentation of this broad subject.

The main characteristics of these data sets are documented in tab. 4.2: the first special run carries identification number 68 and has been performed with a ^{228}Th source in July 2016, while the second one is RUN 76 and has been carried through in February 2017 with a ^{226}Ra source. Data has been acquired with sources S2 and S3 at three vertical positions at the top, middle and bottom of the array (seetab. 4.2, right). The lower source activity ($\mathcal{O}(\text{kBq})$) makes it possible to collect data with the LAr veto instrumentation switched on and provide a distinct setting for an accurate data-to-Monte-Carlo comparison. Since the purpose of this special data taking is to study the LAr vetoing performance, the germanium main trigger was maintained during the data taking. Test pulses are also available and are used to estimate the fraction of *random coincidences*. In these particular, false-positive, LAr-vetoed events the physical process generating the coincident scintillation light detected by PMTs and SiPMs is distinct from the one that triggers the germanium detectors. This can happen, for example, if the decay products of a nucleus in the calibration source deposits energy in the germanium while a cosmic ray is ionizing the argon. Similarly, random coincidences can be produced by two nuclei decaying at the same time: one of them triggers the germanium and the other one produces coincident light. A good estimate of the fraction of random coincidences seen in data is crucial when comparing to simulations, in which this background is missing.

The analysis data set is constructed by applying event cuts based on the total energy released in the germanium detectors. The selected energy regions are shown in fig. 4.4: the ^{208}Tl full-energy peak events ($2615 \pm 10 \text{ keV}$) in RUN 68 and the Compton-dominated energy region from the 2204 keV ^{214}Bi line in RUN 76 are considered. The obtained statistics is about $2 \cdot 10^4$ events or more per source position. The data from the LAr instrumentation which is relevant for the comparison with Monte Carlo simulations consists in a set of veto flags (one for each of the 25 LAr veto channels, i.e. 9 top PMTs, 7 bottom PMTs and 9 SiPM modules) for each germanium trigger. The probability that a LAr veto channel is triggered in data can be written as the convolution between a *signal* probability (i.e. the same event is responsible for both the germanium and LAr veto triggers) and a *background* probability (i.e. the false-positive rate from random coincidences). This convolution is simply the logic OR between the two probabilities. The amount of random coincidences is estimated by combining data from test pulses and SiPM traces, as documented in great detail in [179].

The calibration sources are fully implemented in MAGE, with user commands to set their vertical position, the radioactive source and therefore replicate RUN 68 and RUN 76 experimental settings (tab. 4.2). Optical processes are enabled in these special simulation runs, but, since they require high

PCALIB
RUNS

DATA
SELECTION

SIMULATIONS

Table 4.2: Summary of the special calibration data with active LAr veto instrumentation from RUN 68 (July 2016, ^{228}Th source) and RUN 76 (February 2017, ^{226}Ra source). The random coincidences are estimated combining data from test pulses and SiPM traces [179]. Unfortunately, pulser data is partly missing in RUN 68. On the right: a visualization of the source position at three different heights.

isotope	source port	position (mm)	run time (h)	random coincidences (%)
^{228}Th	C2	8168	10.2	–
		8396	3.2	–
		8570	12.5	–
	C3	8220	6.4	7.5 ± 0.6
		8405	4.3	7.2 ± 1.0
		8570	3.6	10.2 ± 1.4
^{226}Ra	C2	8139	8.9	12.2 ± 0.3
		8405	4.3	11.2 ± 0.4
		8570	6.9	12.9 ± 0.3
	C3	8128	8.0	10.8 ± 0.3
		8292	3.6	8.9 ± 0.4
		8570	8.5	10.7 ± 0.3

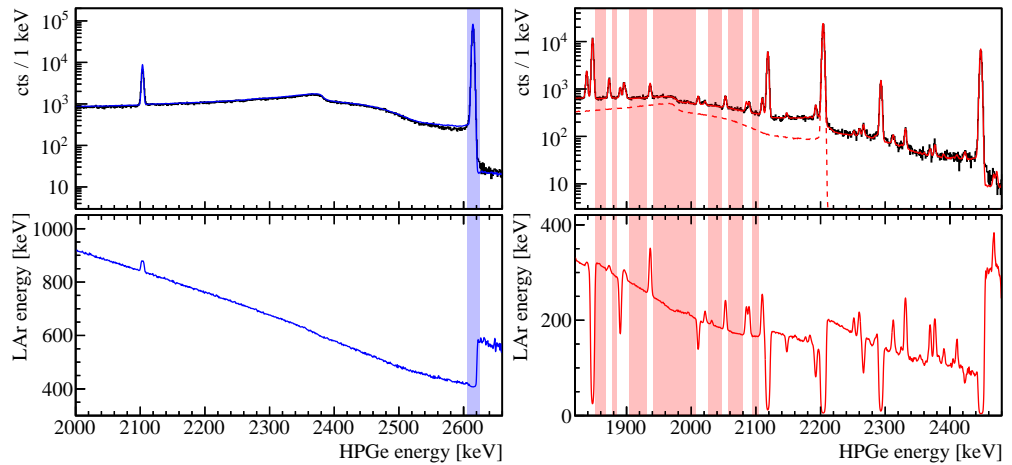
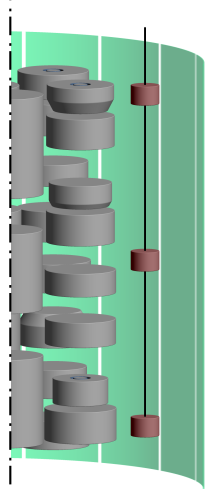


Figure 4.4: The energy spectra of the Phase II special calibration runs. Left: RUN 68 (^{228}Th), Monte Carlo simulation in blue and data in black. The top panel shows the energy distribution of the events while the bottom panel shows the average amount of energy released in LAr by an event with respect to its energy. Right: RUN 76 (^{226}Ra). Colored bands highlight the regions selected for the data analysis.

computational time, photons are fully tracked only if an energy deposition is recorded in germanium as well. The optical properties of the setup are fixed to their best values documented in app. C.1. The two most important Monte Carlo settings for the calibration source physics are the LAr attenuation length and the fiber shroud coverage. As demonstrated in §4.2.1 and in fig. 4.3 in particular, these two parameters induce the largest deviations of the LAr light detection probability in the red and orange points — where the calibration sources are typically deployed (see tab. 4.2). The germanium reflectivity, instead, is crucial when probing the array region. Changes in the LAr light yield or the TPB quantum efficiencies produce almost linear and homogeneous distortions of the probability map and can be absorbed in the PMT and SiPM channel efficiencies.

The probability to detect n LAr scintillation photons with the LAr veto instrumentation includes a signal component (the light is physically correlated to the germanium signal) and a background component from random coincidences:

$$\lambda[n] = \lambda_s[n] * \lambda_b[n] = \lambda_s \vee \lambda_b .$$

A way to introduce an effective detection efficiency ϵ for a LAr veto channel is by the following “binomial repopulation”:

$$\lambda_s[m](\epsilon) = \sum_{n \geq m} \lambda_s[n] \binom{n}{m} \epsilon^m (1 - \epsilon)^{n-m} ,$$

which is the probability, reduced by the efficiency $\epsilon \in [0, 1]$, to observe $m < n$ photons. Since the quantity of interest for this analysis is the LAr veto flag (i.e. an event is seen by the instrumentation or not), the probability to detect $m > 0$ photons can be expressed as

$$\lambda_s(\epsilon) = 1 - \lambda[0](\epsilon) = 1 - \sum_n \lambda_s[n] (1 - \epsilon)^n = 1 - \frac{1}{N_{\text{tot}}} \sum_n N_n (1 - \epsilon)^n ,$$

where the last equality holds for the Monte Carlo simulations, in which $\lambda_s[n]$ is just the ratio between the number of events in which n photons were detected and the total number of events: $\lambda_s[n] = N_n / N_{\text{tot}}$.

A likelihood function is then constructed to match the Monte Carlo simulation output to the special calibration data. Since each single event includes data from 25 LAr veto channels, also the particular detection *pattern* must be taken into account. Given three channels A, B and C , for example, the pattern $\{A, C\}$ represents the occurrence of a signal in channel A, C but not in B . The pattern in the example has probability $p_A \cdot (1 - p_B) \cdot p_C$, i.e. it always probes all the channel detection probabilities p_i . The full likelihood reads

$$\mathcal{L}(\vec{\epsilon}, \dots) = \prod_p \mathcal{B}_{N_{\text{tot}}}^N \left(\sum_G [\lambda_s(\vec{\epsilon}) + \sigma \cdot \Delta \lambda_s(\vec{\epsilon})] \cdot \lambda_b \right) \cdot \prod_G \mathcal{B}_{M_{\text{tot}}}^M (\lambda_b) \cdot \mathcal{G}(\sigma) , \quad (4.1)$$

where the first product runs over all possible $\dim[P] = 2^{N_{\text{ch}}}$ patterns (N_{ch} is the number of considered channels), the summation and the last product run over all the pattern generator pairs $G = \{\{A, B\}, \{B, C\}, \dots\}$. In the first binomial term $\mathcal{B}_{N_{\text{tot}}}^N (\lambda)$, N is the number of events in which light was seen over the total N_{tot} for a certain pattern. The same nomenclature applies for the second binomial term $\mathcal{B}_{M_{\text{tot}}}^M (\lambda)$, but for the random coincidence data set. The probability in the first binomial term is

the product between the signal probability for a given pattern (which is calculated by summing over all possible pattern generators) and the background random coincidence probability λ_b . The signal probability contains an additional contribution $\sigma \Delta \lambda_s(\vec{\epsilon})$ which accounts for the effect of low statistics in the Monte Carlo data sample. The term is regulated by the nuisance parameter σ , which is constrained by the pull term $\mathcal{G}(\sigma)$, a Gaussian distribution with null mean and variance σ . The number of degrees of freedom in this likelihood is $2^{N_{\text{ch}}} - N$.

The likelihood function is then maximized to obtain the best fit values for the parameters of interest, namely the LAr veto channel efficiencies $\vec{\epsilon}$. The same likelihood can also be used to make some inference on other Monte Carlo optical unknowns, e.g. the LAr attenuation length or the fiber shroud coverage. This idea is presented and discussed in [179], but its application is out of the scope of this work, which requires only a rough tuning of the LAr probability map. Indeed, a broad range of systematic map distortions which might be due to uncertain optical specifications is tested in the framework of the $2\nu\beta\beta$ distribution analysis, which will be presented in chap. 5.

RESULTS

Since the tuned LAr probability map will be only used to provide the LAr veto flag for the background model simulations, which are further processed to create the PDFs for the BEGE summed energy spectrum (see chap. 5), an additional simplification can be introduced in the analysis. In principle, the array of channel efficiencies $\vec{\epsilon}$ in eq. (4.1) has dimension 25, but the symmetries of the experimental setup can be exploited to reduce the number of parameters. A cylindrical symmetry is *de facto* present in the arrangement of PMTs and SiPM modules, as shown in the technical drawings in fig. 2.7. This spatial symmetry is evidently broken in the LAr veto channel efficiencies domain, since the measured signal rates are already different one from the other, but the effect has to be evaluated on the analysis data set, i.e. the BEGE summed energy spectrum. Since the BEGE detector arrangement in the array does not significantly deviate from a cylindrical distribution, it is not expected to depend too much on differences between efficiencies of light detectors at the same vertical height. Therefore, only three effective efficiencies are used in eq. (4.1) ($N_{\text{ch}} = 3$): one for all top PMTs, one for all SiPM modules and one for all bottom PMTs. In this simplified setting, the maximization of $\mathcal{L}(\vec{\epsilon})$ yields:

$$\epsilon_{\text{PMTt}} = 0.140 \pm 0.003, \quad \epsilon_{\text{SiPM}} = 0.326 \pm 0.007, \quad \epsilon_{\text{PMTb}} = 0.346 \pm 0.007. \quad (4.2)$$

The magnitude of systematic uncertainty needed to obtain a reasonable goodness-of-fit (p -value ~ 0.3) at the best fit point is around 30%, which already shows how this analysis suffers from the many unknown optical specifications in the Monte Carlo. The impact of this problem on the $2\nu\beta\beta$ distribution analysis is addressed in §5.2 through a dedicated study of the connected systematic uncertainty. Even if these efficiencies are not directly comparable with those extracted from physics data, a qualitative agreement is found. As a matter of fact, the event suppression of top PMTs is generally lower than those observed for bottom PMTs and SiPMs. A possible source of this asymmetry might be the presence of the array instrumentation (i.e. cabling and electronic boards) between the germanium detectors and the top PMTs. These hardware parts, which are absent in the lower side of the LAr veto instrumentation, represent an obstacle to the propagation of optical photons.

PDFs

The background model PDFs after LAr veto cut obtained by applying the probability map to the Monte Carlo simulations are displayed in fig. 4.5. A notable difference with the PDFs constructed for the analysis presented in chap. 3 is that the linear transition layer model obtained from characterization data for BEGE detectors [180] is now taken into account — more information about the germanium

detector transition layer models is found in app. A. A comparison with PDFs before analysis cuts in fig. 3.2 shows large shape deformations, especially for decays from ^{238}U and ^{232}Th chains. In particular, a large suppression of ^{208}Tl full-energy peak at 2614 keV is observed. The effect of the LAr veto cut is also noticeable on the Compton shoulders, e.g. ^{40}K , ^{42}K and ^{60}Co . The only PDF which is practically not affected by the cut is the $2\nu\beta\beta$ PDF. The probability for the two electrons emitted in the decay to escape from the detector and produce scintillation light in LAr is generally very low.

4.3 Full-range analysis

A full-range background analysis of the energy spectra after the LAr veto cut in the same spirit of the one reported in §3.7 has been carried out. The α -event analysis has not been repeated, as they almost completely survive the LAr veto cut; the PDFs extracted from the α model presented in §3.5 can, therefore, be used in the full-range analysis as they are.

The full-energy spectrum has been analyzed in its entire range from 565 keV to 5260 keV and no data sub-sets have been excluded. To speed-up the analysis and exploit all the information brought by data at the same time, a heuristic variable binning has been adopted. Larger bins in the high-energy region, where the event rate is lower, have the additional advantage of avoiding bias from low-statistics PDFs. Dedicated bins have been used for the strongest γ lines: the two ^{40}K and ^{42}K lines, the ^{214}Bi and ^{208}Tl lines. In the rest of the energy spectrum the bin size has been chosen according to the event rate (e.g. 10 keV for M1-BEGe and M1-SemiCoax above the ^{39}Ar Q-value and below the potassium lines, 40 keV for M2-AllEnr). Since above the ^{208}Tl full-energy peak the M1 event spectrum is dominated by α events which are almost completely surviving the LAr veto cut, only two bins [2610, 4500] keV and [4500, 5260] keV have been set. As a cross-check, fit results have been tested to be stable when using this data partitioning scheme or a fixed 5 keV binning.

The statistical analysis to determine the background decomposition consists in the usual Poisson likelihood maximization in a Bayesian setting presented in §3.4. The C++ BAT-based [148] software routine is publicly available on GitHub¹¹. Since just few representative fit parameters are used for each radioactive contamination, no priors from screening measurement data have been used. A uniform prior is assigned to all fit parameters — including the $2\nu\beta\beta$ fit parameter, which is proportional to $1/T_{1/2}^{2\nu}$.

Since the background level (excluding the α events) on the $2\nu\beta\beta$ signal is about an order of magnitude less than before the LAr veto cut, a basic sample of background PDFs has been tested in the fit model. Given the reduced size of the background sample, in fact, no sensitivity to second-order shape distortions between PDFs of the same radioactive decay in different locations (e.g. ^{228}Ac in holders, cables, etc.) is expected. The following set of PDFs has therefore been selected: $2\nu\beta\beta$ in germanium, ^{40}K close (mini-shrouds) and far (fiber shroud) from the detectors, ^{42}K close (on the BEGe and SEMI-Coax n⁺ contact, in the LAr inside the mini-shrouds) and far (in the LAr outside the mini-shrouds, in the LAr above the array), ^{212}Bi and ^{208}Tl on cables, ^{214}Pb and ^{214}Bi on cables, ^{60}Co on cables, ^{228}Ac on detector holders and the α model PDFs for BEGe and SEMICoax detectors from §3.5.

Not all the marginalized posterior distributions of fit parameters report non-zero estimates of background counts in the spectra. Notably, posteriors for ^{42}K above the array and on the BEGe n⁺ contact

STATISTICAL METHODS

RESULTS

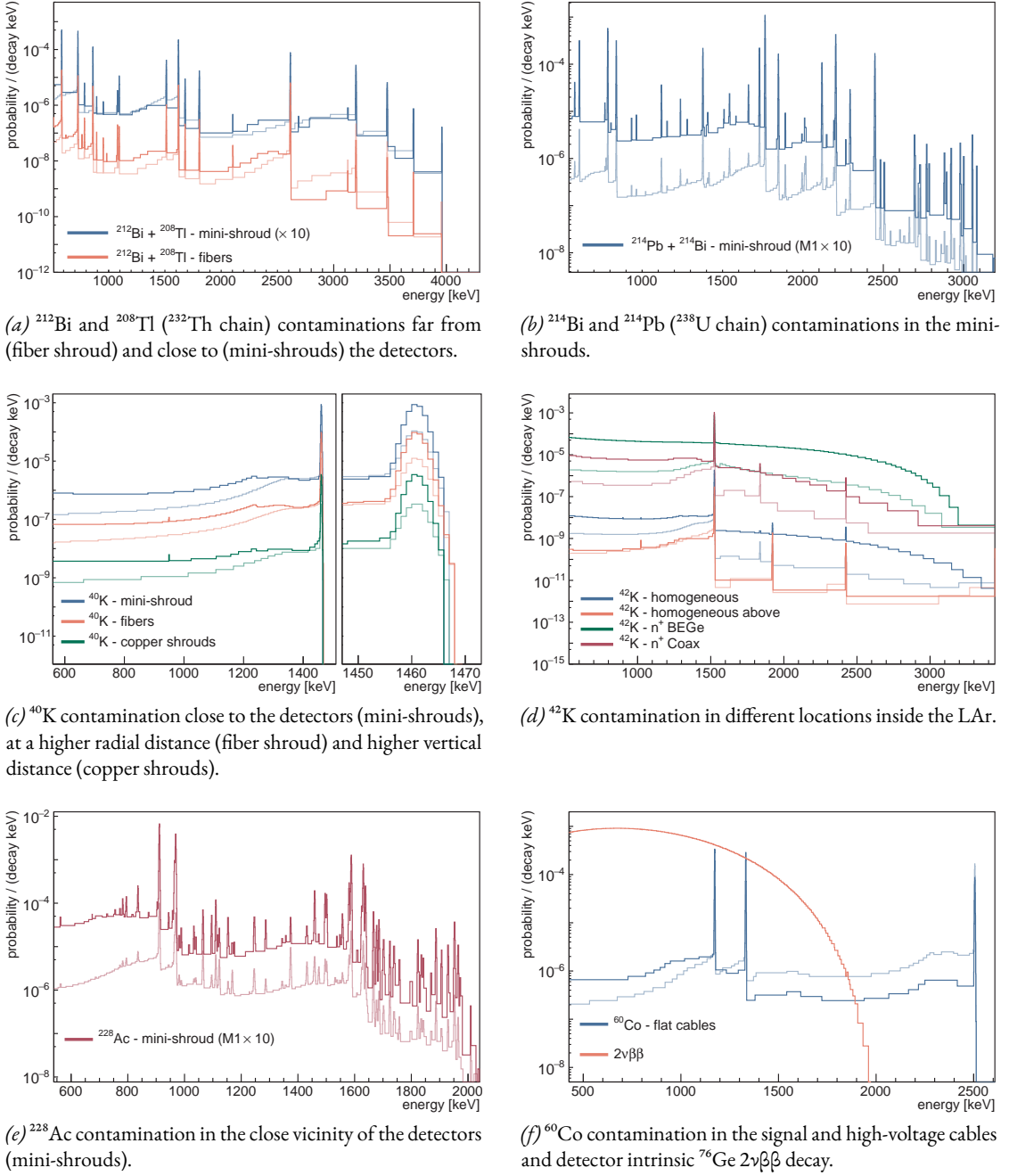
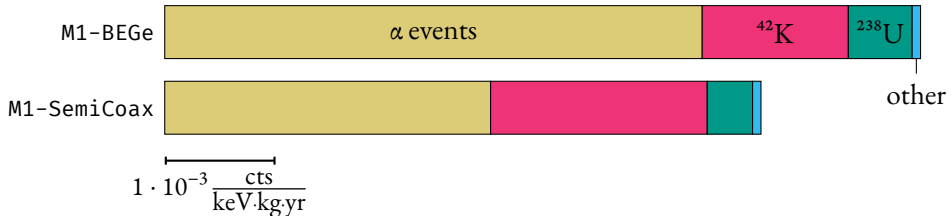


Figure 4.5: The PDFs for the M1-AllEnr (M1-BEGe+M1-SemiCoax) (in fully opaque colors) and the M2-AllEnr (in shaded colors) data sets after the LAr veto cut in the full energy domain and relative to different background sources. Bayesian blocks are used to visualize histograms (see app. F for details. All PDFs are normalized to the number of simulated events. These PDFs should be compared with those before the LAr veto cut in fig. 3.2.

are peaked at zero and are thus removed from the fit. The exclusion of ^{42}K on the BEGe n⁺ contact, which has not been reported in the fit before analysis cuts (chap. 3), is attributed to the novel transition layer model, which significantly affects the PDF shape above the full-energy peak. The β spectrum component above 1525 keV, indeed, is now higher and shows less compatibility with experimental data. The ^{60}Co component is also compatible with zero, possibly because of the high LAr veto efficiency on a background contamination which was already low before the cut (see tab. 3.7). Nevertheless, the component is not removed from the fit because of its clear non-zero mode. Finally, a strong anti-correlation is present between the two ^{40}K sources far and close to the array. The former can be dropped from the model without affecting the fit results.

The results of the analysis are shown in figs. 4.6 to 4.8 and tab. 4.3. A close-up in the $0\nu\beta\beta$ analysis window is shown in fig. 4.9. Since the radioactivity of hardware parts is better constrained within the background model before the analysis cuts (chap. 3), where the background level is higher, and additional uncertainties affect the normalization of the PDFs after the LAr veto cut, only the reconstructed number of counts in the fit range and the background index are given. The background decomposition in fig. 4.6 is presented together with the residuals plot and the 68%, 95% and 99% central Poisson probability intervals of the best fit model. From a visual inspection of the residuals, the goodness of fit is satisfactory through all the spectrum, with a few exceptions. In particular, discrepancies between the best-fit model and the data are visible in M2-AllEnr right below the potassium peaks, in M1-BEGe around the potassium Compton shoulder region (see fig. 4.8).

The background model describes the individual contributions to the total background index around $Q_{\beta\beta}$ after the LAr veto cut. The background index is defined as the number of counts over exposure and energy in the energy window from 1930 keV to 2190 keV excluding the region around $Q_{\beta\beta}$ ($Q_{\beta\beta} \pm 5$ keV) and the intervals 2104 ± 5 keV and 2119 ± 5 keV, which correspond to known γ lines from ^{208}Tl and ^{214}Bi . The values for each background contribution are given in tab. 4.3. The composition of the background around $Q_{\beta\beta}$ is also displayed as fractions of the total background index in the following:



The dominating background contribution in both data sets come from α decays, which are left practically untouched by the LAr veto cut. ^{42}K is the second largest contribution, together with isotopes from the ^{238}U decay chain. The estimated total background indices extracted from the marginalized posterior distributions are $6.78_{-0.42}^{+0.46} \cdot 10^{-3}$ cts/(keV·kg·yr) for the M1-BEGe data set and $5.45_{-0.46}^{+0.28} \cdot 10^{-3}$ cts/(keV·kg·yr) for the M1-SemiCoax data set.

Table 4.3. Summary of the background decomposition after LAr veto cut. The number of reconstructed counts in the fit range and the BI at $Q_{\beta\beta}$ is listed for each component and each analysis data set. Marginalized modes, along with its smallest 68% C.I., are reported as representatives of the marginalized posterior distributions.

source	location	model content in fit range BI at $Q_{\beta\beta}$			
		M1-BEGe	M1-SemiCoax	M2-AllEnr	units: cts 10^{-4} cts/(keV.kg.yr)
${}^{2\nu}\beta\beta$	BEGe detectors SemiCoax detectors	46297 [46070, 46524] -	0 39995 [39809, 40234]	- 0	- -
${}^{42}\text{K}$	n^+ (SemiCoax) LAr – outside mini-shrouds LAr – inside mini-shrouds	19 [11, 26] 1163 [1110, 1212] 13.3 [8.04, 17.2]	284 [169, 399] 1316 [1257, 1373] 19.7 [15.3, 23.8]	30 [18, 43] 669 [639, 697]	669 [639, 697] 27 [16, 36]
${}^{40}\text{K}$	close to the array	2211 [2180, 2250] 0	2472 [2437, 2516] 0	1236 [1219, 1258]	
${}^{212}\text{Bi} + {}^{208}\text{Tl}$	cabling	75 [52, 105] 0.32 [0.22, 0.44]	43 [30, 60] 0.25 [0.17, 0.33]	44 [31, 62]	
${}^{214}\text{Pb} + {}^{214}\text{Bi}$	cabling	184 [167, 204] 5.75 [5.17, 6.31]	117 [106, 129] 4.13 [3.73, 4.56]	128 [116, 142]	
${}^{60}\text{Co}$	cabling	5 [3, 16] 0.14 [0.07, 0.38]	4 [2, 12] 0.18 [0.09, 0.49]	9 [4, 25]	
${}^{228}\text{Ac}$	detector holders	227 [194, 260] 0.30 [0.26, 0.35]	162 [138, 185] 0.30 [0.26, 0.34]	134 [114, 154]	
α decays	${}^{210}\text{Po} + {}^{226}\text{Ra}$ chain (BEGe) ${}^{210}\text{Po} + {}^{226}\text{Ra}$ chain (SemiCoax)	1236 [1199, 1278] -	46.6 [49.7, 50.2]	1935 [1897, 1989] [28.7, 30.1]	- -
TOTAL			67.8 [63.6, 72.4]		54.5 [49.9, 57.3]

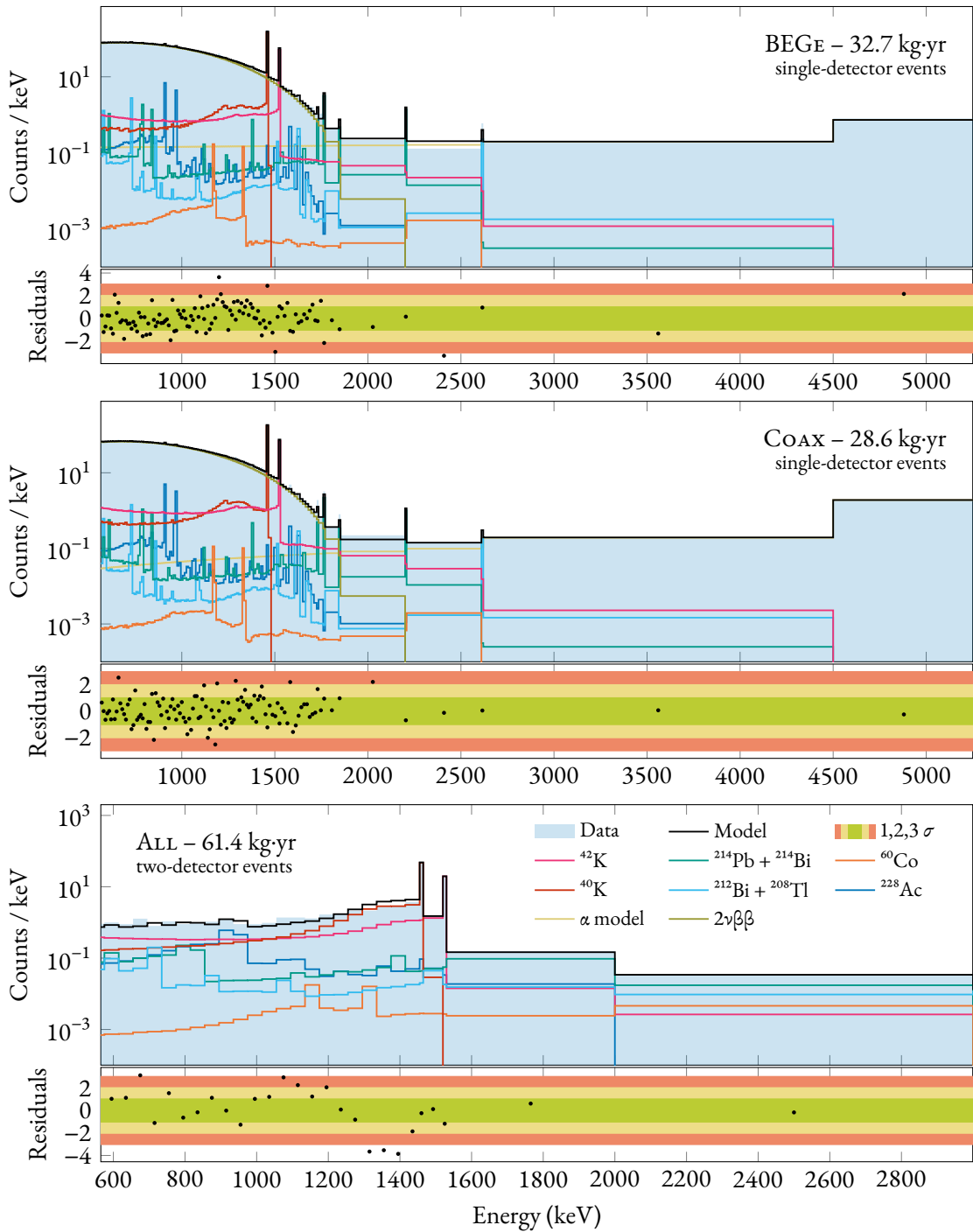


Figure 4.6: The background decomposition of the first 61.4 kg·yr of GERDA Phase II after the liquid argon veto cut. The binning is the one used in the analysis. Contributions from the same radioactive decay are summed for visualization purposes. The data-to-model ratio is shown in the bottom panels together with the smallest 60%, 95% and 99% confidence intervals.

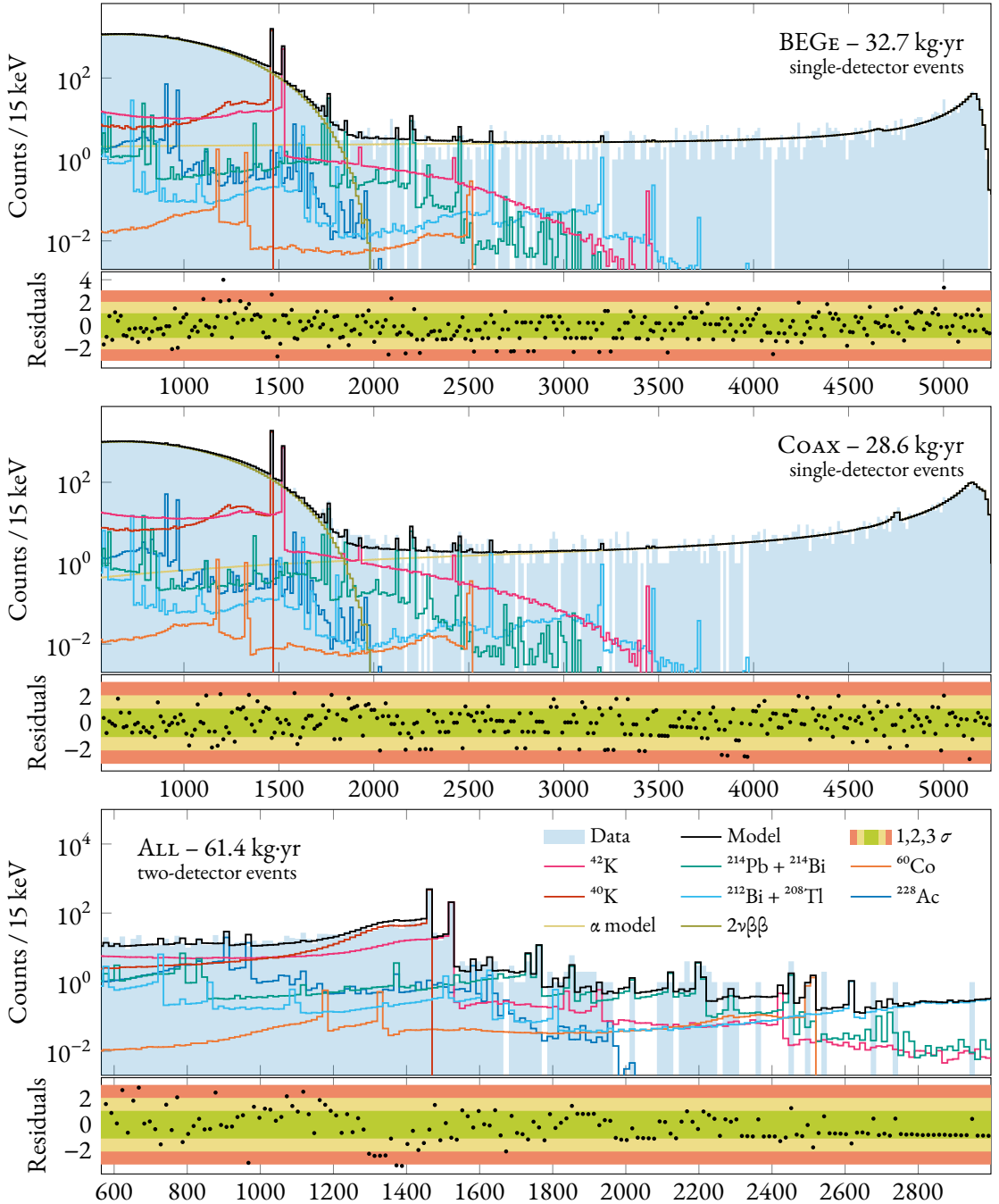


Figure 4.7: The background decomposition of the first 61.4 kg·yr of GERDA Phase II after the liquid argon veto cut with a fixed-width 15 keV binning. Contributions from the same radioactive decay are summed for visualization purposes. The data-to-model ratio is shown in the bottom panels together with the smallest 60%, 95% and 99% confidence intervals.

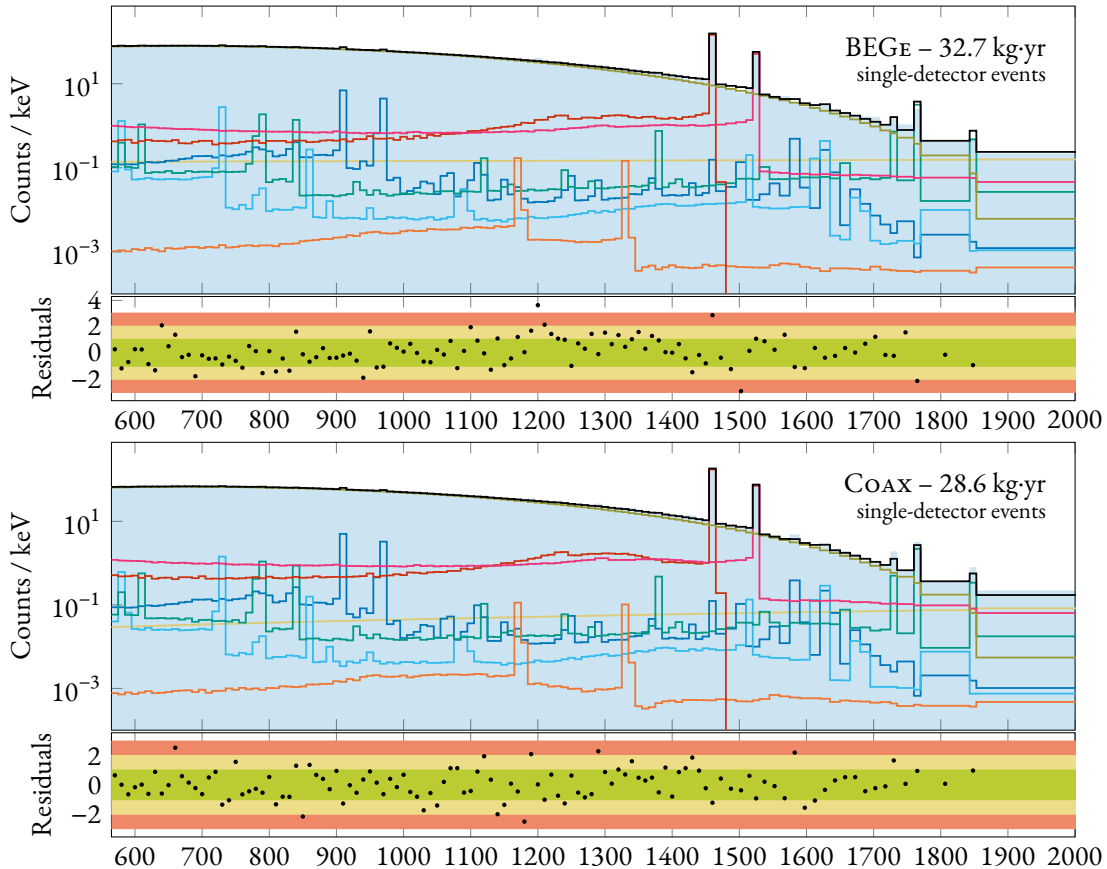


Figure 4.8: The background decomposition of the first 61.4 kg·yr of GERDA Phase II after the liquid argon veto cut in the $2\nu\beta\beta$ region. Contributions from the same radioactive decay are summed for visualization purposes. The data-to-model ratio is shown in the bottom panels together with the smallest 60%, 95% and 99% confidence intervals.

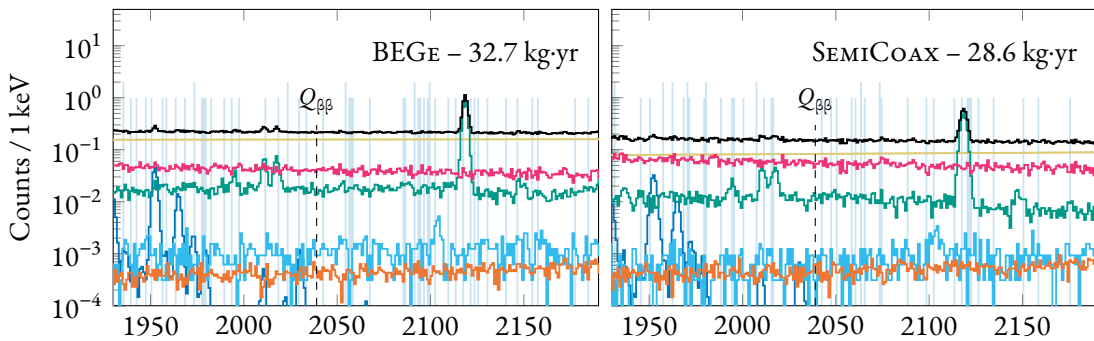


Figure 4.9: The background decomposition of the last 44.1 kg·yr of GERDA Phase II after the LAr veto cut, in the $0\nu\beta\beta$ analysis window.

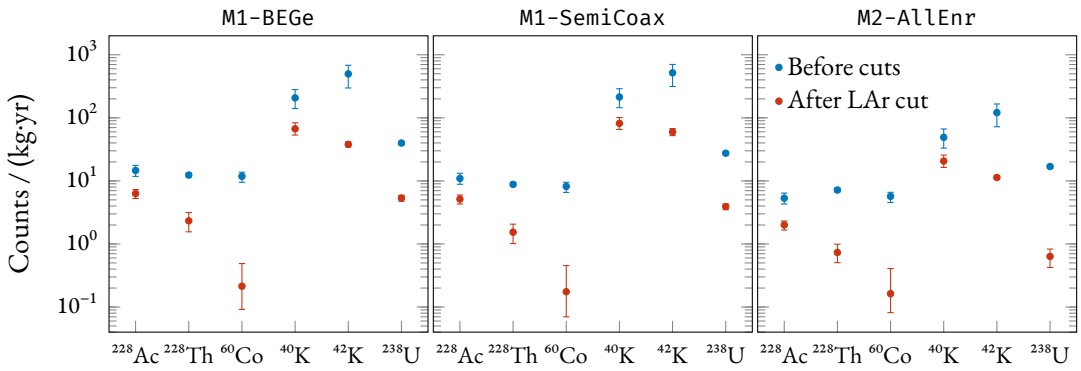


Figure 4.10: Comparison between total counts in the fit range (i.e. above 565 keV) obtained from the background model before analysis cuts and after LAr veto cut. The background decompositions are performed with a reduced set of PDFs, to make a one-to-one comparison possible.

4.4 Discussion

As noted in the plots of the residuals shown in figs. 4.6 to 4.8, the goodness-of-fit is acceptable through nearly all the considered energy range. Few notable discrepancies remain, the most evident being the region below the ⁴⁰K full-energy peak in the M2-AllEnr data set. Since the issue is not present in the analysis before the LAr veto cut (see §3.7), where the statistics is even higher, it could originated from an inaccurate LAr veto system modeling. The same hypothesis might be formulated for the inconsistency between model and data observed in the potassium Compton edge energy region in the M1-BEGe data set and above the ⁴²K line in the M1-SemiCoax data set.

The background indices extracted from data after the LAr veto cut are $6.2_{-0.9}^{+0.9} \cdot 10^{-3}$ cts/(keV·kg·yr) for the M1-BEGe data set and $6.3_{-0.9}^{+1.0} \cdot 10^{-3}$ cts/(keV·kg·yr) for the M1-SemiCoax data set, which agree with the ones predicted by the background model within the statistical uncertainty. The partial contributions to the background index are compared to those found with the background model before analysis cuts (§3.7) in fig. 4.11. The contribution from α decays is not considered as it is left unchanged by the LAr veto cut. The ²²⁸Th (²¹²Bi + ²⁰⁸Tl) and the ⁶⁰Co contributions are the most suppressed, followed by ⁴²K and ²³⁸U (²¹⁴Pb + ²¹⁴Bi). The ²²⁸Ac contribution stays at the same negligible level as before the LAr veto cut. The same picture is observed when comparing the count rates in the analysis energy range (i.e. above the ³⁹Ar Q-value), which are more relevant to the $2\nu\beta\beta$ analysis, in fig. 4.10, with some minor differences.



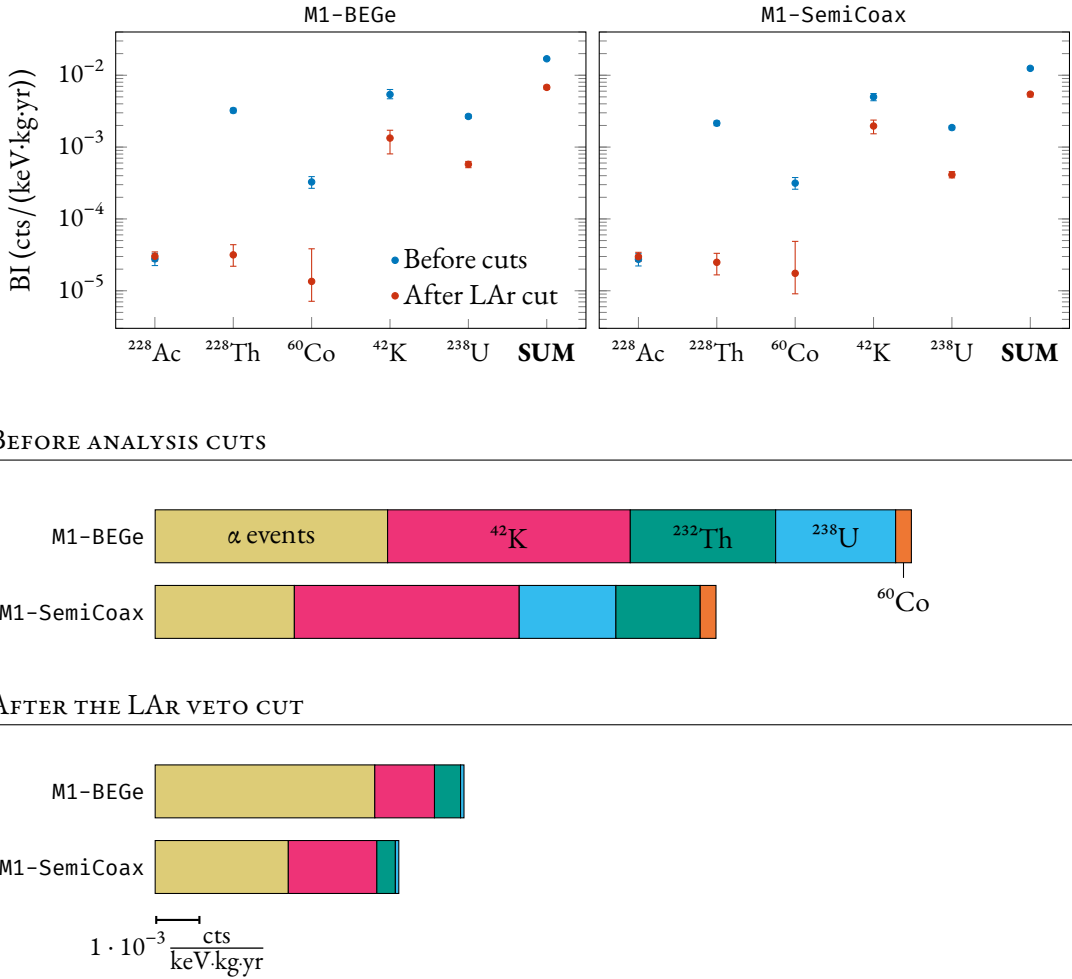


Figure 4.11: Comparison between background indices obtained from the background model before analysis cuts and after LAr veto cut, for the M1-BEGe and M1-SemiCoax data sets. The background decompositions are performed with a reduced set of PDFs, to make a one-to-one comparison possible. On the top, the background index values are reported with statistical uncertainties extracted from the fit. On the bottom, bars are used to represent the fractional composition. The scale in units of 10^{-3} cts/(keV·kg·yr) is reported at the bottom end.

IN SHORT

- The background model PDFs after the LAr veto cut necessitates the implementation of the LAr veto instrumentation as well as the optical properties of all materials involved in the propagation of the scintillation photons into the Monte Carlo framework (MAGE). Many of these properties are unfortunately not precisely known: the LAr absorption length, the channel efficiencies, the germanium reflectivity in the VUV light regime, among the others.
- The high computational time cost of the GEANT4 simulations of optical processes require the implementation of an alternative approach to compute the LAr veto flag for Monte Carlo events, rather than directly enabling the optical physics in the MAGE simulations. A three-dimensional LAr light detection probability map is independently built by means of a dedicated, massive simulation of scintillation photons in the LAr. The map is then convoluted with the existing background model simulations to determine the LAr veto flag.
- Since the shape of the $2\nu\beta\beta$ distribution is nearly not affected by the LAr veto and the background level is low, a qualitative LAr probability map is enough in light of the $2\nu\beta\beta$ energy distribution analysis after the LAr veto cut. Special calibration data with LAr veto discrimination is used to determine three average detection efficiencies for top PMTs, SiPMs and bottom PMTs. The background model PDFs are expected to be negligibly affected by differences between single-channel efficiencies. The impact of other possible systematic uncertainties in the LAr veto modeling is assessed in the context of the $2\nu\beta\beta$ shape analysis.
- The first 61.4 kg·yr of Phase II data after the LAr veto cut is divided into the usual three data sets corresponding to single-detector events in BEGE and SEMICOAX detectors and two-detector events in all enriched detectors. Their energy spectrum is decomposed into background and signal ($2\nu\beta\beta$) components in the same statistical framework presented in chap. 3. The goodness-of-fit is overall acceptable but systematic deviations are present in selected regions of the spectrum. They can be due to uncertainties in the Monte Carlo LAr veto model.

Precision $2\nu\beta\beta$ distribution analysis

As demonstrated in chap. 1, the $2\nu\beta\beta$ event distribution is of great interest for new-physics searches. Many of these exotic processes can indeed generate distortions in the energy spectrum shape predicted by the Standard Model. The most frequently-considered phenomena, namely neutrinoless double-beta decay with Majoron emission ($0\nu\beta\beta\chi$, $0\nu\beta\beta\chi\chi$) has been reviewed in chap. 1. The aim of the research presented in this chapter is to constrain the presence of these distortions in the $2\nu\beta\beta$ event spectrum collected by GERDA in the first part of Phase II, by setting limits on the theoretical model parameters that regulate their magnitude. Moreover, a new estimate of the $2\nu\beta\beta$ half-life $T_{1/2}^{2\nu}$ will be presented with a significantly reduced systematic uncertainty budget compared to previous publications [27]. To improve the sensitivity of the analysis, the data after the liquid argon veto cut is considered for the first time. As already shown in §4.3, in fact, the signal-to-background ratio improves by a factor of 10 in the $2\nu\beta\beta$ energy region after the cut. Furthermore, to reduce the systematic uncertainties connected to the detector active volume model, data from enriched semi-coaxial detectors is discarded. The low background level (signal-to-background ratio of ~ 20 in the $2\nu\beta\beta$ region excluding the potassium γ lines) and the high-statistic signal data sample ($\sim 5 \cdot 10^4$ $2\nu\beta\beta$ events above the ${}^{39}\text{Ar}$ Q-value, see tab. 4.3) motivates the construction of a high-precision fit of the $2\nu\beta\beta$ energy distribution to test the validity of the Standard Model predictions.

This chapter is divided in three sections: the data selection and the statistical methods, which are used to study the signal sensitivity and analyze the data set, are presented in §5.1, while sources of systematic uncertainties and their effect on the analysis are extensively described in §5.2. The results are finally presented and discussed in §5.3.

5.1 Statistical analysis

The M1–BEGe data set after the LAr veto cut (already characterized in §4.1, see fig. 4.1, top panel, for the energy spectrum) has been considered for this analysis both because of the higher signal-to-background ratio in the $2\nu\beta\beta$ region of about 20 (excluding the two potassium γ lines) compared to data before analysis cuts and for the lower uncertainty affecting the BEGe detectors active volume determination, compared to SEMICOAX detectors (see app. A).

DATA AND
PDFs

The theoretical predictions for signal and background event distributions are obtained, as usual, from Monte Carlo simulations through the MAGE software framework. The LAr veto model, which is extensively described in §4.2, is used to compute the LAr veto flag for synthetic events. A selection of

PDFs after the LAr veto cut is shown in fig. 4.5. The same PDF sample considered in the background model presented in §4.3 has been selected to represent the background in this analysis. The choice of a reduced set, compared to the background model before analysis cuts, is motivated by the fact that the description of the shape of such a low background does not benefit from more complex models, from a statistical point of view. The goodness-of-fit for the M1-BEGe data set in the $2\nu\beta\beta$ region is, indeed, satisfactory (see fig. 4.8), and the impact of different PDF shapes (e.g. ^{228}Ac far or close to the detector array) is assessed in the analysis of the systematic uncertainties. Note that the information from the M1-SemiCoax and M2-AllEnr data sets is also not included in the present analysis.

The likelihood function that brings data and expectations together is the usual Poisson likelihood, which runs over the binned M1-BEGe energy spectrum:

$$\mathcal{L}(S, \vec{B} | \vec{n}) = \prod_i^N \frac{\nu_i(S, \vec{B})^{n_i} e^{\nu_i(S, \vec{B})}}{n_i!},$$

where i is the bin index, N is the number of bins, n_i is the number of counts observed in bin i and ν_i is the predicted number of counts in bin i . The latter can be decomposed as

$$\nu_i(S, \vec{B}) = s_i + \sum_k b_{i,k} = S \int_i \text{PDF}_S(E) dE + \sum_k B_k \int_i \text{PDF}_{B_k}(E) dE,$$

where s_i and $b_{i,k}$ are the signal ($2\nu\beta\beta$ or new physics) and background contribution from component k in bin i and the integrals are defined in the energy interval spanned by the bin. S and B_k represent the total number of counts from signal and background events in the analysis range, respectively. The parameter of interest in this analysis is, of course, S , and the B_k are treated as nuisance parameters. The relation between number of signal counts S and the corresponding process half-life can be expressed as:

$$T_{1/2}^{2\nu} = \mathcal{C}_{76} \frac{1}{S}; \quad \text{where } \mathcal{C}_{76} = \frac{\mathcal{N}_A \log 2}{M_{76}} \left(\sum_i m_i^{\text{tot}} f_i^{\text{AV}} t_i \epsilon_{c,i} \right) f_{76} f_R \epsilon_{\text{QC}} \epsilon_{\text{LAr}}, \quad (5.1)$$

\mathcal{N}_A is the Avogadro number, M_{76} is the ^{76}Ge molar mass, m^{tot} is the total detector mass, f_i^{AV} is the active volume fraction, t_i is the detector live-time, $\epsilon_{c,i}$ is the detector containment probability, \sum_i runs over the detectors included in the data set, labeled by index i , f_{76} is the enrichment fraction, f_R is the fraction of $2\nu\beta\beta$ events expected in the analysis range, $\epsilon_{\text{LAr}} = (97.7 \pm 0.1)\%$ is the probability for a signal event to survive the LAr veto cut and $\epsilon_{\text{QC}} = (99.922 \pm 0.002)\%$ is the quality cuts signal efficiency.

TEST STATISTIC

To test a hypothesized value of S the following profile likelihood ratio is defined:

$$\lambda(S) = \frac{\mathcal{L}(S, \hat{\vec{B}})}{\mathcal{L}(\hat{S}, \hat{\vec{B}})}$$

where $\hat{\vec{B}}$ denotes the value of \vec{B} that maximizes \mathcal{L} for the specified S and $\hat{S}, \hat{\vec{B}}$ are maximum likelihood estimators. The test statistic is defined as

$$t_S = -2 \log \lambda(S)$$

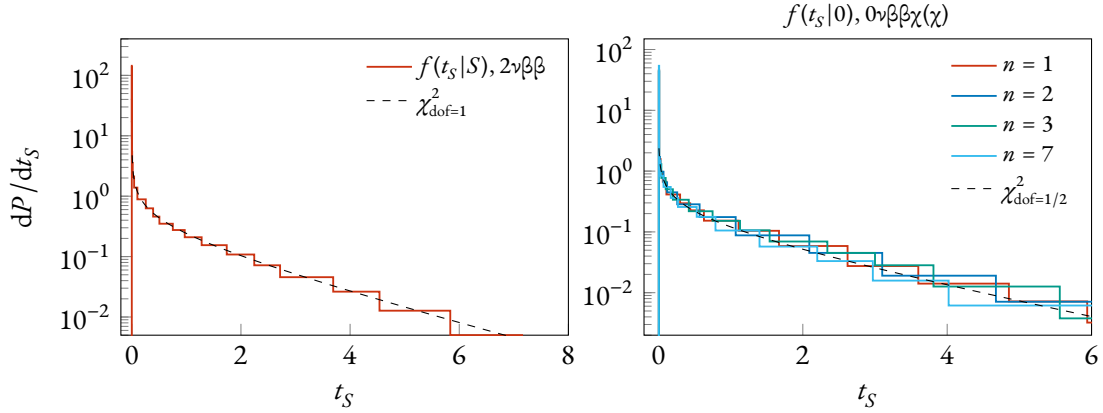


Figure 5.1: Distribution of the test statistic probability P for various signal hypothesis sampled with Monte Carlo methods. On the left: the standard $2\nu\beta\beta$ case, where a signal of $S \sim 4.5 \cdot 10^5$ counts in the analysis range is assumed in the toy experiments. On the right: sampling distributions for the null hypothesis on new-physics signals. Deviations from the Wilks theorem predictions are observed. Bayesian blocks have been used to represent the histograms (see app. F).

where higher values of t_S correspond to increasing incompatibility between the data and the signal hypothesis S . It is a known result of the Wilks theorem that the probability distribution of the test statistic t_S follows, in the large sample limit, a χ^2 distribution with number of degrees of freedom given by the number of parameters of interest [181]. Since, however, not all the regularity conditions of the Wilks theorem [182] are satisfied in this analysis, deviations from the χ^2 distribution are expected. Therefore, the t_S distribution is computed from Monte Carlo toy experiments, in which synthetic energy spectra are generated from the background model results (§4.3). For each signal hypothesis, 10^4 toy data sets are generated and an histogram is filled with the corresponding values of t_S . Examples for the standard $2\nu\beta\beta$ signal hypothesis and new-physics null hypotheses are shown in fig. 5.1. Deviations from the χ^2 distribution for 1 degree of freedom (left panel) are observed for the standard $2\nu\beta\beta$ hypothesis. In the analysis all the fit parameters are constrained to be positive. In the case of new physics hypotheses, where the maximum likelihood estimator of S is close to zero, this assumption modifies the distribution of the test statistic (right panel). In the large sample limit it is expected to be well approximated by a $\frac{1}{2}\chi^2$ distribution — a sum of a delta function at zero and a χ^2 distribution for one degree of freedom [183].

The p -value of an observed value of the test statistic t_S^{obs} under the signal hypothesis S is used to quantify the level of disagreement between data and hypothesis:

$$p = \int_{t_S^{\text{obs}}}^{\infty} f(t_S|S) dt_S .$$

In particular, a map between the observed t_S^{obs} and the signal level S corresponding to a certain confidence region (e.g. 68% C.L. or $p = 0.32$) can be computed using the above equation.

The sensitivity to alternative signal hypotheses can be characterized by the median significance, assuming data generated according to the zero-signal (null) hypothesis, with which one rejects the signal

SENSITIVITY
STUDIES

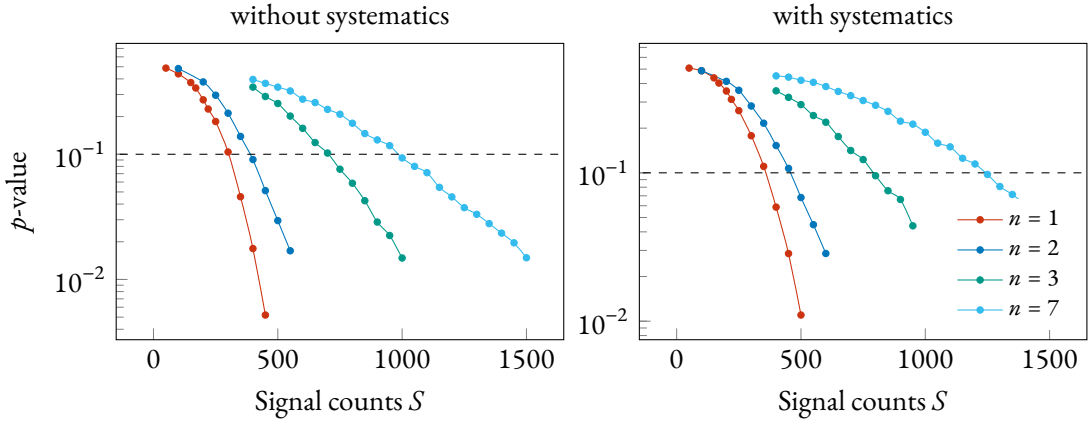


Figure 5.2: Median p -value of the null hypothesis with different signal strength assumption for the new-physics signals, computed with Monte Carlo toy experiments. In the right plot, the effect of systematic uncertainties is included. The p -value corresponding to 90% confidence level is highlighted with a dashed line.

hypothesis [181]. To compute the sensitivity, the distributions $f(t_S|S)$ and $f(t_S|0)$ are needed. For a discrete set of hypotheses on the signal S , the two distributions are obtained with Monte Carlo toy experiments and the median p -value of null hypothesis is computed. In fig. 5.2 the median p -value as a function of S , for all the considered new-physics processes is shown. The sensitivity for 90% C.L. limit setting corresponds to the value of S for which the median p -value is 0.1. The limit-setting sensitivities on the half-lives of the investigated processes are reported in tab. 5.1.

FIT RANGE AND BINNING The fit range is chosen in order to maximize the signal-to-background ratio and the sensitivity. It starts from the ${}^{39}\text{Ar}$ Q-value at 565 keV and stops at the $2\nu\beta\beta$ Q-value (2039 keV). The ${}^{39}\text{Ar}$ background, as a matter of fact, is still dominant after the LAr veto cut and reduces the signal-to-background ratio to less than 1 in its energy domain. On the other hand, extending the fit range above the $2\nu\beta\beta$ Q-value does not improve the signal sensitivity.

A 10 keV binning, given the energy resolution of the M1-BEGe data set, does not remove physical features in the spectrum and is large enough to avoid effects due to energy scale-related systematic uncertainties. Different bin sizes are tested to check that the performance of the fit is not affected by this choice.

5.2 Systematic uncertainties

Besides the purely-statistical effects, a set of uncertainties which might systematically contribute to the final analysis uncertainty (both for $2\nu\beta\beta$ half-life and new-physics limits) must be considered. Until now, the test statistics studies have only been considering the effect of Poisson fluctuations in the bin contents, since the generative model for the toy data sets was fixed. A way to include systematic model uncertainties in the test statistic distribution is to additionally sample the generative PDF from a set of *alternative* models, according to a certain probability distribution. This procedure is conceptually equivalent to fitting the data with “wrong” models, obtained by applying a systematic distortion to

Table 5.1: Sensitivity for 90% C.L. limit setting on the half-lives of new physics processes contributing to the $2\nu\beta\beta$ event distribution, before and after the inclusion of systematic uncertainties. The results are extracted from toy Monte Carlo data sets.

Decay Mode	Spectral index n	Sensitivity			
		Counts	Statistical $T_{1/2} (10^{23} \text{ yr})$	Counts	With systematics $T_{1/2} (10^{23} \text{ yr})$
$0\nu\beta\beta\chi$	1	302	4.5	358	3.8
$0\nu\beta\beta\chi$	2	386	3.3	456	2.8
$0\nu\beta\beta\chi(\chi)$	3	698	1.7	792	1.5
$0\nu\beta\beta\chi\chi$	7	984	0.72	1200	0.59

the reference model. As instance, alternative transition layer or LAr veto heat maps induce coherent distortions in all background and signal PDFs, which must be taken into account when generating the toy data sets.

This way of treating systematic uncertainties is formalized as an *hybrid Bayesian-frequentist* approach [36]. In this setting, the distribution of the test statistic becomes:

$$f(t_s) = \int f(t_s | S, \vec{B}, \nu) \pi(\vec{\nu}) d\vec{\nu},$$

where $\vec{\nu}$ are the parameters representing the sources of systematic uncertainties in the model and $\pi(\vec{\nu})$ the “prior” distribution from which $\vec{\nu}$ is sampled from. The effect introduced by these additional parameters is to smear $f(t_s)$, relaxing the new-physics experimental limits extracted from it. The software that implements this approach for the $2\nu\beta\beta$ analysis is implemented in the `gerda-factory` toolkit, publicly available on GitHub¹. In the following, the main sources of systematic uncertainties impacting the $2\nu\beta\beta$ analysis are discussed.

LAr veto model. The Monte Carlo LAr veto model, as shown in detail in §4.2, suffers from many uncertainties, some of them arising directly from the poor knowledge of LAr channel efficiencies and material optical properties implemented in MAGE (see app. C.1). The systematic effect of variations of some of these Monte Carlo parameters (i.e. the LAr absorption length, the germanium reflectivity, the coverage of the fiber shroud and the TPB quantum efficiency) has been already studied in selected regions of the LAr probability map (the object in which the LAr veto model is encoded) in §4.2.1 and fig. 4.3. Special calibration data can be used to determine the channel efficiencies (§4.2.2),

¹The `gerda-factory` software suite, available at <https://github.com/gipert/gerda-factory>, is implemented in C++ and externally depends only on the ROOT libraries for the histogram utilities. The program input is specified in JSON format. First, a reference model (in the form of a linear combination of histograms, i.e. the signal PDF, the background PDFs etc.) is set, then the program is fed with alternative PDF shapes (histograms) for each of the model components. These are grouped according to the source of systematic uncertainty they represent: they can be provided for all components at the same time (global distortions) or for selected PDFs (specific distortions). The program then computes and stores distortion curves ($\text{pdf}_{\text{orig}} / \text{pdf}_{\text{dist}}$) for each alternative PDF shape. At run time, a distortion curve is randomly selected from each group and applied to the reference model; a random data set is then drawn from the obtained model. The procedure is repeated in order to generate the required number of randomly-distorted synthetic data sets. Optionally, as the alternative PDF shapes are discrete, the program can be instructed to consider intermediate distortion curves by interpolation.

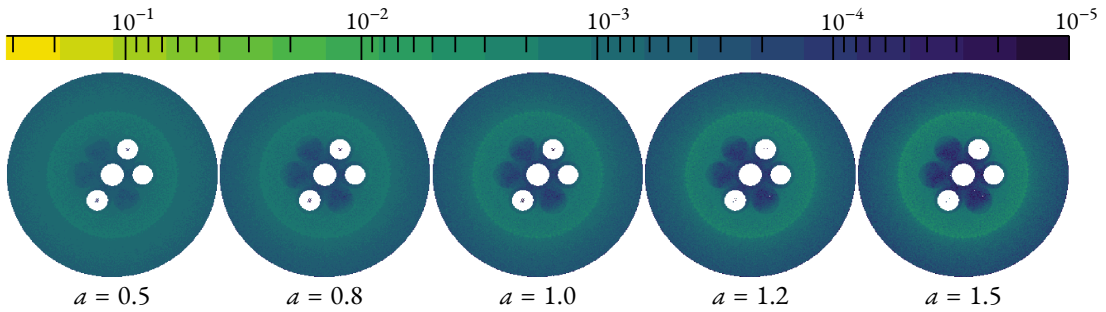


Figure 5.3: Effect of power-law distortions of the LAr probability map in a cross-section parallel to the xy plane. Circular holes correspond to germanium detectors which are crossed by the plane. The value of the exponent α in the $p \rightarrow p^\alpha$ transformation is varied to make the map more or less homogeneous.

but cannot be exploited to reliably constrain other Monte Carlo parameters. This second possibility, which requires a much more complex analysis and a deeper understanding of simulated and physics data, is discussed in [179].

To include the LAr veto model uncertainties in the $2\nu\beta\beta$ distribution analysis, the following approach has been formulated. First, the special calibration data is compared to Monte Carlo simulations to extract three effective channel efficiencies: one for all top PMTs, one for all SiPM modules and one for all bottom PMTs (eq. (4.2)). Considering the cylindrical symmetry of the problem (a set of detectors arranged in a cylindrical array), A more detailed knowledge of efficiencies for each single channel is inessential. In this reference probability map, the other Monte Carlo optical parameters are fixed to the values that better reflect our degree of belief, which are documented in app. C.1.

The second step is to provide alternative LAr veto maps for the determination of the test statistic distribution, generated with different assumptions for the optical parameters. These alternative maps still have to reproduce the special calibration data, i.e. the *control sample*, but they differ from the original map in all other LAr regions, in particular those probed by the background model simulations. Unfortunately, the map generation process is exceptionally expensive from the computational point of view (the required time is on the order of several thousands of CPU hours), therefore obtaining several alternative probability maps from scratch is not feasible. To overcome this issue, the possibility to perform manual distortions of the reference probability map has been investigated.

An alternative presentation of the probability map distortions in fig. 4.3, in which the detection probability in the first calibration source position area is set to unity, is given here in fig. 5.4 for the germanium reflectivity, the fiber shroud coverage and the LAr absorption length (first three panels from left). In this way, the constraint of reproducing the special calibration data set is made visually explicit, as the corresponding probability (in red) is invariant under transformations of the Monte Carlo parameters. TPB quantum efficiency and LAr light yield distortions are not considered because they can be well-approximated with a global scaling of the probability map (i.e. their effect is fully absorbed in the LAr channel efficiencies). The distortions shown in the rightmost panel are obtained in a different way: instead of running the full simulation chain with different Monte Carlo parameters to compute the detection probability in the selected spatial points, the probability map is directly distorted by means

of an analytical transformation. A power-law transformation is used:

$$p_k \rightarrow c \cdot p_k^\alpha, \quad (5.2)$$

in which p_k is the probability value in the LAr voxel k (i.e. the probability map), α is an arbitrary coefficient controlling the magnitude of the distortion and c is a global normalization factor. The latter depends on α and has to be adjusted in order to reproduce the total LAr veto event suppression observed in the special calibration data. In this sense, the volume of LAr probed by the calibration data is a fixed point of the transformation in eq. (5.2), and the magnitude of the distortion in all other regions is regulated by α . The effect of the transformation on a transversal cross-section of the probability map is shown in fig. 5.3.

As it can be stated from fig. 5.4, the power-law distortions shown in the rightmost panel are not radically different from e.g. those generated by the reflectivity changes. Moreover, the latter is arguably the most important source of systematics in the $2\nu\beta\beta$ analysis, since it probes the LAr volume enclosed by the detectors. The power-law map distortion has been therefore judged representative of the class of distortions generated by fundamental Monte Carlo parameters².

A set of alternative background PDF shapes has been generated with power-law distorted maps, varying α from 0.5 to 1.5 in steps of 0.1. The effects on the energy spectra of ^{40}K on cables and ^{42}K in LAr have been reported in fig. 5.5 (left panel), as an example. As it is clear, the distortion strongly depends on the energy and the type (Compton scattering, full absorption) of the event. All these alternative PDFs have been considered in the determination of the distribution of the test statistics, with a flat prior. The uncertainty on the $2\nu\beta\beta$ half-life estimate given by the LAr veto model is about 0.3% of the central value.

^{76}Ge active exposure. The detector active volume and enrichment fraction has been estimated for BEGe detectors up to a certain accuracy during a dedicated characterization campaign [120, 122]. The enriched active volume determines the total amount of detected $2\nu\beta\beta$ counts, and it is therefore not expected to produce distortions in the shape of the PDFs. Its effect must be considered in the conversion of the number of signal counts to the corresponding process half-life, expressed in eq. (5.1). Since three independent estimates of the BEGe enrichment fraction f_{76} are available [120], they are combined into the final estimate of 0.877(13) by evaluating their variance (see tab. 2.1). The estimate of the full charge-collection depth and size of transition region for each detector required a careful analysis of the detector characterization data and is reviewed in app. A [122, 180]. The uncertainty on these values is statistically propagated to the half-life conversion factor \mathcal{C}_{76} by coherently treating with Monte Carlo methods the correlated and un-correlated uncertainties in the linear combination \sum_i of the active volume fraction f^{AV} in eq. (5.1). The resulting uncertainty is about 2% of \mathcal{C}_{76} . Since the distribution of the signal fit parameters (including new physics) is verified to be approximately normal on toy experiments, the uncertainty on \mathcal{C}_{76} can be propagated linearly to the corresponding half-life

²It is not difficult to realize that probability map distortions generated by fundamental Monte Carlo properties cannot be generally reproduced by global map transformations. The effect of these parameters is indeed predominantly local: the germanium reflectivity will affect the array region, the fiber shroud coverage the region close to the shroud etc. Also the LAr absorption length effect might be localized, depending on the scintillation photon mean free path in a certain LAr region. Based on this observation, more complex direct distortions of the map limited to certain locations could be also considered. Nevertheless, given the expected low impact of LAr veto model uncertainties on the $2\nu\beta\beta$ analysis, this option has not been further explored.

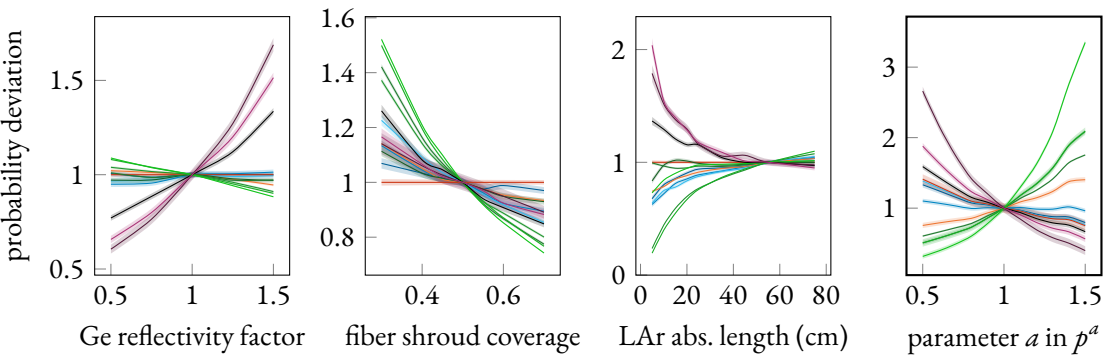


Figure 5.4: Study of the impact of Monte Carlo parameters on LAr light detection probabilities in various spatial points, normalized to unity at the best value and such to leave the probability at the uppermost calibration source position (red point) unchanged. In the rightmost panel the effect of a direct, power-law transformation of the probability map is shown (no normalization to the red point applied, see text for details). The color code and other details are described in fig. 4.3.

estimate and summed in quadrature with the other contributions. Since the latter contribute at the sub-percent level, the ^{76}Ge active exposure estimation results to be the major source of uncertainty in the standard $2\nu\beta\beta$ half-life determination. In contrast, it is a second-order contribution to new-physics limits, as the systematic uncertainty is typically about 10% or higher.

Transition layer model. As already discussed in several occasions (see in particular app. A), the transition region from the n^+ electrode to the fully-active detector volume is not completely dead (i.e. the charge-collection efficiency is not zero). Since events interacting within this special region are reconstructed with a smaller effective energy, a shape effect on the energy distribution is expected. Distortions induced by variations of the transition layer size are particularly noticeable in the ^{39}Ar event distribution (fig. A.4) and in the lower tail of intense γ peaks (fig. A.2). A first estimate of the transition region size for BEGEs has been extracted from detector characterization data [180], using a simplified linear model for the charge-collection efficiency profile (fig. A.1). This estimate, however, has been obtained before a significant amount of storage time at room temperature (2–3 years before deployment in LAr), in which n^+ lithium profile growing effects took place. The effect of this dead-layer growing process on the size of the transition region is unfortunately unknown. The assumption of a fixed proportion between the size of the transition region and the size of the dead region during the growing process leads to results which are clearly incompatible with experimental data (see e.g. fig. A.2 and fig. A.5).

To provide a more reliable BEGE detector transition layer model for the $2\nu\beta\beta$ analysis, an independent analysis of the ^{228}Th full-energy-peak lower tail from calibration data has been performed and documented in detail in app. A.2. A best-fit value of the dead-layer fraction with statistical uncertainty has been obtained for each detector. PDFs for signal and background sources corresponding to the best-fit values $\pm 1\sigma$, $\pm 2\sigma$ and $\pm 5\sigma$ (σ denotes the standard deviation) have been produced and reported in fig. 5.5 (right panel) for ^{40}K , ^{42}K and $2\nu\beta\beta$ in the M1-BEGe data set. The PDF distortions are noticeably lower than those induced by the LAr veto model uncertainties, and are found to be negligible in the total $T_{1/2}^{2\nu}$ systematic uncertainty count.

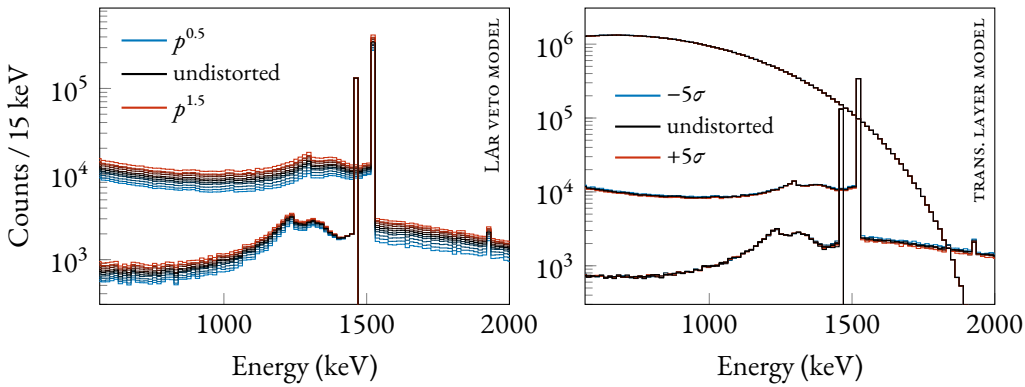


Figure 5.5: Effect of alternative LAr veto models (right) and transition layer models (left) on ^{40}K (signal and high-voltage cables), ^{42}K (homogeneous in the LAr) and $2\nu\beta\beta$ PDFs for the M1-BEGe data set after the LAr veto cut. See text for details on how the alternative models have been constructed.

Background model. The uncertainty on the location of the main background sources is treated as a systematic uncertainty source in the analysis. PDFs for the same radioactive contamination in different locations are provided as an alternative to the reference model PDF. In the following table the alternative locations selected for the evaluation of the systematic contribution are listed for each fit model component (the reference location in *italic*):

Component	Location
^{40}K	<i>mini-shrouds</i> , cabling, holder mounting, front-end electronics, copper shroud
^{42}K (close)	<i>inside mini-shrouds</i> , n^+ contact, p^+ contact
^{42}K (far)	<i>outside mini-shrouds</i> , above the array
^{228}Ac	<i>holder mounting</i> , fiber shroud
$^{212}\text{Bi} + ^{208}\text{Tl}$	<i>cabling</i> , outer fibers

Some of these PDFs are shown in fig. 4.5. The contribution of background modeling-related uncertainties to the total $2\nu\beta\beta$ half-life uncertainty amounts to 0.4% of the central value.

Theoretical $2\nu\beta\beta$ decay model. The theoretical calculations of the $2\nu\beta\beta$ distribution shape are not exact and are based on approximations and assumptions (chap. 1). $2\nu\beta\beta$ primary vertices are generated in MAGE through the DECAY0 program, whose theoretical formulae are documented in [155] and references therein. In similar works in the past [27, 184] the systematic uncertainty contribution arising from the decay theoretical description has been evaluated by considering the $2\nu\beta\beta$ distribution obtained with the Primakoff-Rosen approximation [24] as an alternative. The comparison resulted in a < 1% effect, which was negligible in the total uncertainty budget. There is, however, no guarantee that the impact on the current analysis is at the same, second-order, level. The lower background and higher statistics compared to the Phase I data set makes a re-evaluation of this systematic contribution necessary. Calculations in the Primakoff-Rosen approximation, however, are known to yield results which are inexact (see fig. 5.6). Results from recent calculations, e.g. phase space factors calculated with exact Dirac wave functions with finite nuclear size and electron screening effects [15], are more suitable

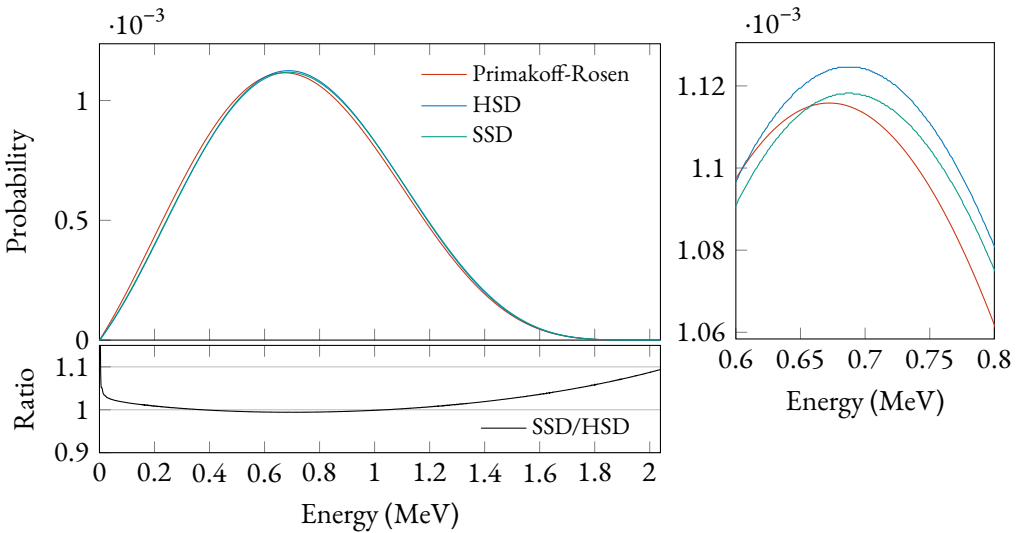


Figure 5.6: Comparison between different theoretical assumption in the calculation of the phase space factor for the standard $2\nu\beta\beta$ decay. Results of the calculations with the Primakoff-rosen approximation, the higher-state dominance (HSD) and single-state dominance (SSD) are shown, normalized to unit area. The HSD curve is implemented in DECAY0 and used as the reference spectrum in the $2\nu\beta\beta$ analysis.

to this comparison. As a matter of fact, the calculations implemented in DECAY0 and those presented in [15] yield nearly identical results. Therefore, no contribution to the systematic uncertainty is expected, from this side.

Another source of theoretical uncertainty which has recently turned out to be relevant [29, 83] is the assumption on the nuclear state configuration of the intermediate nucleus in the decay (${}^{76}\text{As}$ for $2\nu\beta\beta$ decay of ${}^{76}\text{Ge}$). In ${}^{76}\text{Ge}$ a higher-state dominance (HSD) is usually assumed, but a single-state dominance (SSD) scenario cannot be excluded. Summed-energy spectra obtained with the two hypotheses, using exact Dirac wave functions with finite nuclear size and electron screening effects [15], are compared in fig. 5.6. Once the distributions are normalized to unit area, the difference is mostly visible above ~ 1.3 MeV, where it reaches 5% and more. In this region, however, the event statistics is also low. Detailed studies are ongoing to assess whether the $2\nu\beta\beta$ shape analysis is sensitive to this discrepancy. For now, a conservative $< 0.1\%$ contribution to the total uncertainty budget is assumed.

MAGE and GEANT4. Another possible source of systematic biases in the analysis is the implementation of the experimental setup into the Monte Carlo software stack (MAGE) and the implementation of the physics processes (particle generation and propagation) in GEANT4. Starting from the first point, uncertainties in the dimension and position of the implemented setup components are potentially present in MAGE, and could in principle affect the shape of the signal and background PDFs. Because of the point-like topology of the $2\nu\beta\beta$ decay and uniformity of the ${}^{76}\text{Ge}$ isotopic fraction, its PDF is expected to depend on the total detector volume and active volume model, rather than the exact dimensions or location. The effect of this type of uncertainty source has been already described above. On the other hand, the shape of the background PDFs is expected to depend more on the details of the geometrical implementation. This kind of effect, however, is partly similar to (and certainly less in-

tense than) the one produced by background model-related uncertainties (see above). Moreover, given the modest size of the background sample, it is expected to contribute with less than 0.1%. Past evaluations showed a \sim 1% impact on the $2\nu\beta\beta$ half-life estimate [27, 184]. The size of the background sample after the LAr veto cut, a factor \sim 10 less than before the cut, and the correlation with the background modeling uncertainties, motivates the reduction of this contribution by one order of magnitude.

GEANT4 is a broadly-used and heavily-tested software suite in the high-energy physics community. No systematic biases due to the implementation of particle creation and propagation routines in the code are expected, however there could be some originating from uncertainties in the experimental data on which **GEANT4** relies on (i.e. cross sections and decay widths). To test this eventuality, the full simulation chain has been re-run with different electromagnetic low-energy process models available in **GEANT4** (Livermore is the default, alternatives are Penelope and Standard_opt3). The PDFs are observed to change at the sub-percent level, and the associated contribution to the systematic uncertainty is negligible³. A drastic reduction of the impact of this systematic uncertainty compared to previous estimates [184] is also motivated by the lower background level. In this particular application, as a matter of fact, the Monte Carlo uncertainty is mainly due to the propagation of the external γ rays: the $2\nu\beta\beta$ -decay electrons generated in the germanium detectors have a sub-cm range and they usually deposit their entire kinetic energy, apart from small losses due to the escape of *bremstrahlung* or fluorescence photons.

Other sources. The energy scale and resolution is another potential source of bias in the analysis. Given, however, the excellent resolution of germanium detectors and the remarkably precise knowledge of the energy calibration parameters (see e.g. fig. 2.11), this contribution is negligible. The uncertainty on the other quantities appearing in the conversion factor between the reconstructed number of counts and the process half-life C_{76} in eq. (5.1) is also negligible.

The effect of the inclusion of systematic uncertainties in the test-statistic sampling distribution is shown in fig. 5.7. Compared to fig. 5.1, broader tails are observed at higher values of the test statistic, resulting in larger confidence intervals on the signal strength. p -value curves, shown in the right-hand side of fig. 5.2, are consequently shifted to higher values of the assumed signal strength S . The effect on the $2\nu\beta\beta$ half-life estimate of all sources of systematic uncertainty combined is about 2.1% of the central value. In contrast, the statistical uncertainty (or fit error) is only 0.5%. For limits on exotic-physics signals the situation is the opposite: the effect of systematic uncertainties is to relax the 90% C.L. interval by 10% or more (specifically, about 30% for spectral index $n = 1$, 10% for $n = 2, 3$ and 20% for $n = 7$), but the estimate is dominated by the statistical error. The limit-setting sensitivities on new-signal searches after the inclusion of the systematic uncertainties are reported in tab. 5.1.

5.3 Results and discussion

Once the analysis procedure has been fixed and the distribution of the test statistic is determined, its value is computed on physics data to extract the $2\nu\beta\beta$ half-life estimate and 90% C.L. lower limits for new-physics processes.

³In support of this conclusion, the reader is referred to the official **GEANT4** validation portal at <https://geant-val.cern.ch>, that shows how precise the software is in reproducing the experimental cross-section data in the energy domain of the typical GERDA backgrounds.

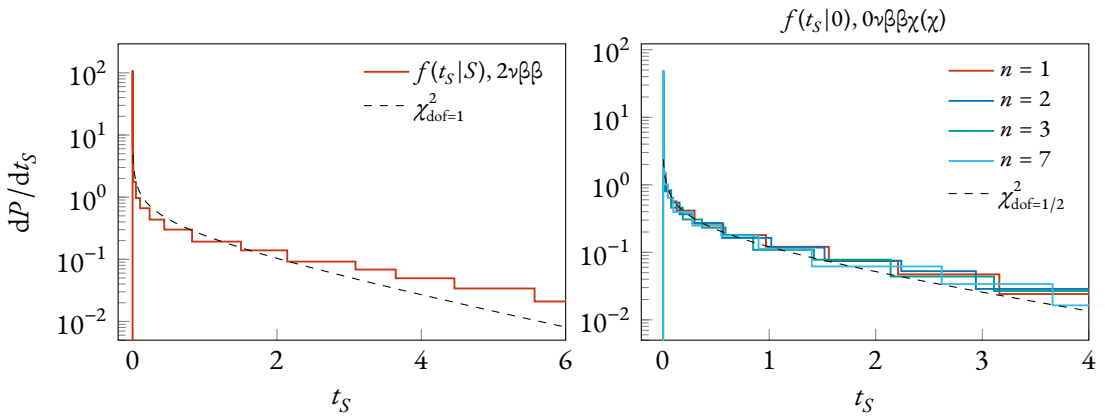


Figure 5.7: Distribution of the test statistic probability P for various signal hypothesis sampled with Monte Carlo methods, including the effect of systematic uncertainties. On the left: the standard $2\nu\beta\beta$ case, in which a signal of $S \sim 4.5 \cdot 10^5$ counts in the analysis range is assumed in the toy experiments. On the right: sampling distributions for the null hypothesis on new-physics signals. Deviations from the Wilks theorem predictions are observed. Bayesian blocks have been used to represent the histograms (see app. F).

$2\nu\beta\beta$ DECAY The obtained best-fit value of the standard $2\nu\beta\beta$ -decay half-life with its 68% C.L. interval is

$$T_{1/2}^{2\nu} = (2.050 \pm 0.011_{\text{stat}} \pm 0.042_{\text{sys}}) \cdot 10^{21} \text{ yr}.$$

The statistical and systematic uncertainty is remarkably reduced compared to the estimate extracted from Phase I data before analysis cuts [27]. The improvement in statistical uncertainty does not only follow from the higher data set exposure, which is roughly doubled with respect to Phase I, but also from the higher signal-to-background ratio — more than a factor 10 better. The level of systematic uncertainty also benefits from the substantial cut of background events obtained with the application of the LAr veto. As shown in §5.2, the effect of most sources of systematic uncertainty is found in the shape of background PDFs. Uncertainties on the signal shape, from e.g. nuclear theory or from the model of the detector dead layer, are found to be sub-leading. The dominant contribution is the uncertainty on the size of the detectors active volume and on the enrichment fraction. With a total uncertainty of 2.1% on the $2\nu\beta\beta$ half-life, the measurement presented here is one of the most precise ever obtained, on the same footing of recent results from CUPID-Mo (2.9%) [28], CUPID-0 (2.2%) [29], CUORE (2.8%) [30], EXO-200 (2.8%) [31] and KAMLAND-ZEN (3.4%) [23] (compare also with tab. 1.1).

The uncertainty on the BEGe detectors active volume deserves a dedicated discussion. As a matter of fact, evidence of a systematic underestimation of the detectors dead layer has emerged from different sources. From one side, a significant discrepancy between the $2\nu\beta\beta$ half-life obtained from SEMICOAX and BEGe detectors independently has been observed in background model studies presented in §3.7. The bias is confirmed by an analysis of the background data after the Phase II⁺ upgrade, where the same bias is observed between half-lives from BEGe and InvCOAX detectors. On the other side, the situation seems confirmed by a preliminary analysis of the low-energy ${}^{39}\text{Ar}$ data (see app. A, fig. A.5 in particular). A re-analysis of the data after the Phase II⁺ upgrade with an ${}^{39}\text{Ar}$ -corrected active volume model restores the compatibility between the three half-life predictions (see fig. 3.16). A careful ex-

Table 5.2: 90% C.L. lower limits for Majoron-emitting $0\nu\beta\beta$ modes contributing to the $2\nu\beta\beta$ event distribution. Half-life lower limits are converted to coupling constant upper limits, depending on the considered model, using nuclear matrix elements and phase space factors available in the literature. Nuclear matrix elements for spectral index $n = 1$ are the same as the standard $0\nu\beta\beta$, and have been therefore selected from the most recent nuclear calculations. Matrix elements for the other decay modes computed in the IBM-2 theoretical framework [185] have been kindly provided by F. Iachello and J. Kotila, and will be the subject of a future publication. Phase space factors have been taken from [79]. Results for g_α for two-Majoron modes include the uncertainty on the nuclear matrix elements.

Model	Mode	n	$(g_A = 1.27)$	$(10^{-18} \text{ yr}^{-1})$	90% C.L. limits		
			$\mathcal{M}^{0\nu\chi(\chi)}$	$G^{0\nu\chi(\chi)}$	Counts	$T_{1/2} (10^{23} \text{ yr})$	g_α
IB, IC, IIB	$0\nu\beta\beta\chi$	1	2.66–6.04	44.2	197	6.8	$(1.9–4.3) \cdot 10^{-5}$
IF (bulk)	$0\nu\beta\beta\chi$	2	–	–	405	3.2	–
ID, IE, IID	$0\nu\beta\beta\chi\chi$	3	$4.04 \cdot 10^{-3}$	0.22	917	1.3	0.95
IIC, IIF	$0\nu\beta\beta\chi$	3	0.485	0.073	917	1.3	$1.3 \cdot 10^{-2}$
IIE	$0\nu\beta\beta\chi\chi$	7	$4.04 \cdot 10^{-3}$	0.42	705	1.0	0.87

traction of detector active volumes from ${}^{39}\text{Ar}$ data is envisioned to obtain a non-biased measurement of the $2\nu\beta\beta$ half-life. Since the systematic uncertainty on the half-life is currently dominated by the uncertainty on the dead-layer growth speed at room temperature, a further, substantial precision improvement is expected using corrected active volumes.

Lower limits at 90% C.L. on the half-lives of various Majoron-emitting $0\nu\beta\beta$ modes are reported in tab. 5.2. Majoron signals corresponding to the obtained constraints are visualized over the M1–BEGe energy spectrum in fig. 5.8. An improvement of about a factor two is obtained with respect to previous determinations [27]. For spectral index $n = 7$, the improvement is of more than a factor three. Despite the significant reduction of the background compared to Phase I, this degree of enhancement is expected, since the limits are dominated by the statistical uncertainty and the exposure is less than doubled. The achieved sensitivities are comparable to those obtained by ${}^{136}\text{Xe}$ experiments⁴ [80, 81], depending on the spectral index n (see also tab. 1.3). GERDA is, in fact, setting significantly more stringent limits only on the $n = 7$ mode, by a factor ten.

NEW
PHYSICS

Using phase space factors from [79] and the most recent set of nuclear matrix elements it is possible to convert the half-life limit into an upper limit on the g_α coupling constant⁵. Also here, the improvement with respect to the Phase I result is a factor ~ 2 . Similar constraints have been obtained with ${}^{136}\text{Xe}$ (see tab. 1.3).

⁴Note, however, that no sensitivity estimates are reported for ${}^{136}\text{Xe}$ analyses. An exhaustive comparison with other experimental results should indeed be based on both sensitivity and observed limits, to bypass the effect of possibly extreme statistical realizations in data.

⁵The nuclear matrix elements for spectral index $n = 1$ are the same as the standard $0\nu\beta\beta$ -decay, and are therefore affected by the usual uncertainty range [17]. The only calculation of nuclear matrix elements for $0\nu\beta\beta\chi$ -decay modes with spectral indices $n = 3, 7$ available in the literature is found in [186]. Unfortunately, these are very old and rough calculations (published in 1995) that do not take into account the last 25 years of nuclear theory developments. The nuclear matrix elements, obtained within the IBM-2 theoretical framework [185], used in this work have been kindly provided by F. Iachello and J. Kotila. A dedicated publication by the authors is currently under development.

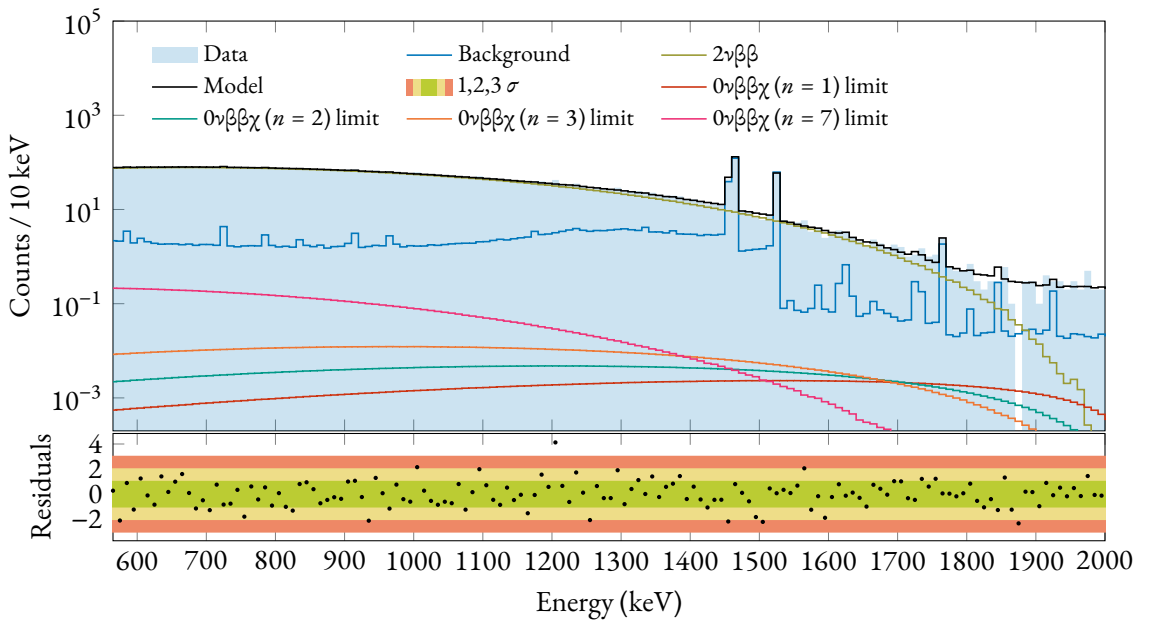


Figure 5.8: Best-fit model and data for the M1-BEGe data set. The 90% C.L. upper limits on the Majoron-emitting $0\nu\beta\beta$ modes are visualized. In the bottom panel the residuals are shown, together with normalized 68%, 95% and 99% C.L. intervals. The fit model does not include new-physics contributions.



IN SHORT

- The development of a Monte Carlo model of the GERDA LAr veto system (described in chap. 4) makes it possible to obtain predictions on the distribution of background and $2\nu\beta\beta$ events in the energy spectrum of data after the LAr veto cut. The high statistics of the $2\nu\beta\beta$ data sample ($\sim 5 \cdot 10^4$ events in BEGE detectors above the ${}^{39}\text{Ar}$ Q-value from the first part of Phase II) and the excellent signal-to-background ratio after the LAr veto cut (~ 20 , a factor ~ 10 better than before the cut) motivates a high-precision analysis of its distribution to extract the $2\nu\beta\beta$ half-life and constrain the existence of new-physics phenomena (see chap. 1).
- The data from BEGE detectors from the first 61.4 kg·yr of Phase II is analyzed with a hybrid Bayesian-frequentist approach. Data from semi-coaxial detectors is discarded due to the large active volume uncertainties. A test statistic based on the profile likelihood ratio is defined, and its distribution with respect to the considered (new-)physics signal is studied with Monte Carlo methods. The analysis is optimized in order to maximize the sensitivity for limit setting to new-physics signals. Sensitivities to Majoron-emitting $0\nu\beta\beta$ modes are obtained in the 10^{22} – 10^{23} yr range. The statistical error on the $2\nu\beta\beta$ half-life estimate is about 0.6%.
- Various sources of systematic uncertainties are considered in the computation of the test statistic distribution by introducing distortions of the reference model of the Monte Carlo toy data sets. Various alternative LAr veto models and detector transition layer models are used to produce the background and signal PDFs, but their effect on the test statistic distribution for the standard $2\nu\beta\beta$ signal is of the order of 1% or less. The main source of systematic uncertainty on $T_{1/2}^{2\nu}$ remains the detector ${}^{76}\text{Ge}$ active volume estimation, which contributes with 1.3% to the total uncertainty count. Systematic uncertainties relax new-physics lower limits by 10–30%, depending on the considered process.
- The extracted $T_{1/2}^{2\nu} = (2.050 \pm 0.044) \cdot 10^{21}$ yr is one of the most precise measurements of double-beta decay half-life ever reported, together with recent estimates with ${}^{136}\text{Xe}$, ${}^{130}\text{Te}$ and ${}^{100}\text{Mo}$. The central value, however, is potentially biased by an incorrect estimate of the BEGE detectors active volume fraction. A proposed solution to the issue involves the analysis of the ${}^{39}\text{Ar}$ energy spectrum collected by GERDA, which is sensitive to the active volume model of germanium detectors. Limits on Majoron-emitting neutrinoless double-beta decay modes are placed at the 10^{23} yr level, improving the Phase I results by a factor two, roughly. The constraints are competitive with analogous results with ${}^{136}\text{Xe}$ data from the KAMLAND-ZEN and EXO-200 collaborations.

Conclusions and outlook

In the course of this thesis work, a path has been drawn from the origins of the GERDA background model to a full study of the spectral shape of two-neutrino double-beta decay events. In chap. 3, the background model of GERDA Phase II data before analysis cuts has been presented to the reader, to demonstrate the accuracy of the Monte Carlo predictions in reproducing the experimental data. The distribution of the background in the region of interest for neutrinoless double-beta decay is shown to be uniform, excluding two γ peaks, which are far enough from the Q-value. The largest part of these results has been published on a scientific journal [150]. In chap. 4, it has been shown how propagation of optical photons is implemented into the Monte Carlo framework in order to simulate the liquid argon veto system. Thanks to this capability, the LAr veto flag has been computed for simulated background events, and a background model of events after the LAr veto cut has been developed. This last achievement allowed for a precision analysis of the two-neutrino double-beta decay energy spectrum, both to measure the process half-life and to search for new-physics phenomena. The experimental estimate of the two-neutrino double-beta decay half-life $T_{1/2}^{2\nu} = (2.050 \pm 0.044) \cdot 10^{21}$ yr is one of the most precise measurements ever reported in the double-beta decay research field. Limits on Majoron-emitting neutrinoless double-beta decay modes are set at the 10^{23} yr level, competitive with recent experimental estimates by KamLAND-ZEN and EXO-200. The most stringent half-life lower limit of $6.8 \cdot 10^{23}$ yr at 90% C.L. is set on the Majoron-emitting double-beta decay modes with spectral index $n = 1$. The latter converts to an upper limit on the coupling constant g_α of $1.9\text{--}4.3 \cdot 10^{-5}$ GeV, depending on the nuclear matrix elements. A scientific publication with the results of the two-neutrino double-beta decay spectral analysis is currently in preparation.

In conclusion of this research work, I would like to spend few words on learned lessons and possible ideas on how to improve the quality of the science program in future experimental efforts — the LEGEND program, in particular. Building a Monte Carlo model of the liquid argon veto has proven to be a challenging task. From one side, optical specifications of materials commonly used in low-background cryogenic experiments are poorly known in the vacuum ultra-violet regime. A particularly serious problem is posed by the lack of a precise measurement of the germanium reflectivity at the LAr scintillation light typical wavelengths. Dedicated measurements campaigns commissioned by the LEGEND collaboration are ongoing. Properties of liquid argon, e.g. the attenuation length, should be also determined with dedicated devices and monitored during data taking. Ideas on how to put this in practice are being developed for the LEGEND experiment. From the other side, optical simulations are exceptionally demanding from the computational point of view, on average CPUs. The issue has been partly overcome by generating a light-detection probability map, that effectively encap-

sulates the LAr veto model and can be applied to existing background simulations obtained without photon tracking. Nevertheless, generating a single map requires tens of thousands of CPU hours, and its characterization is therefore problematic. Experiments in which massive simulations of optical processes are imperative usually make use of Graphical Processing Units (GPUs) [187, 188] — a possibility that could be considered by the LEGEND collaboration. A more efficient way to simulate light propagation in liquid argon would speed up the development of a reliable background model after the LAr veto cut and the subsequent analysis of the $2\nu\beta\beta$ distribution.

The second issue regards the active volume of germanium detectors. A precise knowledge of this detector parameter is mandatory to extract an unbiased measure of the $2\nu\beta\beta$ -decay half-life. Evidence for unreliable active volume fractions of BEGe detectors has emerged from the study of the $2\nu\beta\beta$ distribution in different detector types and a preliminary analysis of ^{39}Ar data. The detectors have been indeed precisely characterized after being fabricated, but were then stored at room temperature for a long period before deployment in liquid argon. At room temperature, the detector dead layer grows at a rate which has never been rigorously determined. The ^{39}Ar data set offers the unique opportunity to calibrate the detector active volume at the same experimental conditions in which the physics data is recorded. A careful analysis of the ^{39}Ar energy spectrum is strongly advised to correct and reduce the uncertainty of the $2\nu\beta\beta$ half-life estimate presented in this work and to measure the dead-layer growth rate.

The ultimate achievement for a ^{76}Ge neutrinoless double-beta decay experiment would be to build a model of the background after the pulse-shape discrimination cut. The results would be extremely relevant for the neutrinoless signal search, which is performed after this cut, and the two-neutrino double-beta decay distribution analysis. As a matter of fact, the GERDA energy spectrum after PSD consists of a nearly-pure double-beta decay event sample. Unfortunately, computing the PSD flag for Monte Carlo events is currently a challenging task, as pulse-shape simulations are still under heavy development. Heuristic PSD cuts based on the width of the distribution of interaction centers in germanium detectors show only a qualitative agreement. An intense pulse-shape simulation program, started in the GERDA and MAJORANA collaborations, is ongoing for the LEGEND project.



Acknowledgements

I would like to express all my gratitude to my mentors Riccardo Brugnera and Alberto Garfagnini, for welcoming me in their research group and providing me with everything I needed to successfully carry on my research project. Thank you for the time you dedicated to me, especially when things were going wrong. Thank you for the intellectual honesty of your advices, thank you for the opportunities you offered me and for helping me designing my future as a researcher. I believe not so often a Ph.D. student has the luck to receive this kind of support and motivation from its research group.

A Ph.D. research project is never a one-man effort. This thesis would not have been successfully completed without the guidance and the collaboration of several people. Before everyone, I would like to thank Katharina von Sturm for being the great person she is, both as a physicist and as a human being. Thank you for being always and unconditionally there to help, I wish everyone could have the possibility to work side to side with a friend. I would like to thank all friends from the München TUM group too, for collaborating to the work presented in this thesis and for the many fruitful discussions. Special thanks to Matteo Agostini, Christoph Wiesinger and Elisabetta Bossio.

Finally, I would like to acknowledge the help from Prof. Francesco Iachello and Dr. Jenny Kotila, who kindly provided me with up-to-date theoretical calculations for two-neutrino double-beta decay.



A. Germanium detector models

As a result of the presence of the n^+ contact on the outer surface of the germanium detectors, the charge-collection efficiency (CCE) differs from unity in the region of the crystal close to the contact. As a matter of fact, lithium impurities diffused inside the crystal during the n^+ contact fabrication process act as recombination centers for charge carriers, and thus the CCE curve strongly depends on the lithium concentration profile. Since part of the charge is lost, events depositing energy in this region are typically characterized by a lower reconstructed energy, depending on the local CCE. Since the p^+ contact is boron-implanted, it is expected to have a thin dead layer, on the order of $1\ \mu\text{m}$, and it will not be considered in the following. The interested reader is referred to [180] for an extensive discussion of the charge-collection mechanism in germanium detectors and CCE models.

A.1 Recommended model from characterization data

The full charge-collection depth (FCCD), defined as the depth at which the CCE reaches unity, has been estimated for each germanium detector deployed in GERDA at the n^+ contact during dedicated characterization campaigns. In these measurements, a radioactive source (e.g. ^{241}Am , ^{133}Ba , ^{60}Co) is positioned close to the detector surface, and a data sample is acquired. A comparison between data and Monte Carlo simulations is then performed to find the FCCD value that best describes data. The recommended FCCD values obtained from this characterization data are reported in tab. A.1 and are briefly described in the following. The SEMICOAX values are extracted from ^{60}Co data as documented in [189], while the BEGE values are obtained combining ^{241}Am and ^{133}Ba data [122]. INVCOAX values are extracted from ^{241}Am measurements [123]. The BEGE detectors have been stored at room temperature in the time interval between their characterization to the deployment in liquid argon, and must be therefore corrected for the dead-layer growing effect. The growth speed at room temperature has never been determined rigorously, and the best available estimate is of about $\sim 0.1\ \text{mm/yr}$, with a standard deviation of $0.04\ \text{mm/yr}$ ([122] and references therein). The correction is therefore applied considering the exact time spent by each detector at room temperature together with an additional systematic uncertainty of 50%.

The region enclosed by the detector surface and the FCCD is, of course, not completely dead, and regions with reduced CCE are expected. The CCE curve in this region strongly depends on the lithium concentration profile, which is in turn strongly dependent on the diode fabrication process (initial lithium concentration at the surface, thermal annealing cycles etc.) and is *a priori* different for

FULLY
ACTIVE
VOLUME

TRANSITION
LAYER

Table A.1: Recommended full charge-collection depth (FCCD) and dead layer fraction (DLF) values for each detector deployed in GERDA Phase II, calculated from detector characterization data. The BEGE FCCD values are obtained combining ^{241}Am and ^{133}Ba data [122] while SEMICOAX values are extracted from ^{60}Co data [189]. The INVCOAX values are obtained from ^{241}Am data [123]. The BEGE FCCDs are corrected for the dead-layer growing effect at room temperature experienced before deployment in GERDA [122]. The BEGE uncertainties are split into correlated and uncorrelated contributions ($\text{FCCD}_{-\text{corr}-\text{uncorr}}^{\text{corr}+\text{uncorr}}$). The DLF values have been estimated in [180] and do not include any growing effect at room temperature. Detector GD02D does not fully deplete and is therefore excluded from any physics analysis [122].

Detector	FCCD (mm)	DLF	Detector	FCCD (μm)	DLF
ANG1	1.80 ± 0.5	–	GD35C	$0.79_{-0.13}^{+0.12 \pm 0.02}$	$0.34_{-0.02}^{+0.02}$
ANG2	2.30 ± 0.7	–	GD61A	$1.00_{-0.15}^{+0.15 \pm 0.05}$	$0.15_{-0.05}^{+0.04}$
ANG3	1.90 ± 0.8	–	GD61B	$1.00_{-0.15}^{+0.14 \pm 0.04}$	$0.37_{-0.03}^{+0.03}$
ANG4	1.40 ± 0.7	–	GD61C	$0.93_{-0.14}^{+0.12 \pm 0.04}$	$0.44_{-0.03}^{+0.03}$
ANG5	2.60 ± 0.6	–	GD76B	$1.14_{-0.16}^{+0.14 \pm 0.04}$	$0.32_{-0.03}^{+0.03}$
RG1	1.50 ± 0.7	–	GD76C	$1.15_{-0.16}^{+0.15 \pm 0.03}$	$0.45_{-0.02}^{+0.02}$
RG2	2.30 ± 0.7	–	GD79B	$1.03_{-0.17}^{+0.16 \pm 0.03}$	$0.25_{-0.03}^{+0.02}$
GD00A	$0.91_{-0.15}^{+0.14 \pm 0.04}$	$0.13_{-0.04}^{+0.05}$	GD79C	$1.09_{-0.14}^{+0.13 \pm 0.03}$	$0.45_{-0.02}^{+0.02}$
GD00B	$1.04_{-0.15}^{+0.14 \pm 0.04}$	$0.20_{-0.04}^{+0.03}$	GD89A	$1.00_{-0.17}^{+0.16 \pm 0.04}$	$0.19_{-0.04}^{+0.02}$
GD00C	$1.01_{-0.17}^{+0.16 \pm 0.02}$	$0.17_{-0.03}^{+0.03}$	GD89B	$1.12_{-0.17}^{+0.16 \pm 0.02}$	$0.28_{-0.02}^{+0.02}$
GD00D	$1.03_{-0.16}^{+0.15 \pm 0.02}$	$0.37_{-0.02}^{+0.02}$	GD89C	$0.99_{-0.17}^{+0.15 \pm 0.03}$	$0.33_{-0.03}^{+0.03}$
GD02A	$0.88_{-0.13}^{+0.12 \pm 0.03}$	$0.02_{-0.04}^{+0.03}$	GD89D	$1.03_{-0.15}^{+0.14 \pm 0.03}$	$0.36_{-0.03}^{+0.02}$
GD02B	$0.97_{-0.15}^{+0.14 \pm 0.04}$	$0.24_{-0.04}^{+0.04}$	GD91A	$1.00_{-0.16}^{+0.15 \pm 0.04}$	$0.14_{-0.04}^{+0.02}$
GD02C	$1.03_{-0.15}^{+0.14 \pm 0.04}$	$0.49_{-0.03}^{+0.03}$	GD91B	$0.95_{-0.15}^{+0.14 \pm 0.03}$	$0.19_{-0.03}^{+0.02}$
GD02D [†]	–	–	GD91C	$0.95_{-0.15}^{+0.14 \pm 0.04}$	$0.13_{-0.05}^{+0.03}$
GD32A	$0.91_{-0.18}^{+0.17 \pm 0.02}$	$0.17_{-0.03}^{+0.03}$	GD91D	$0.99_{-0.17}^{+0.16 \pm 0.04}$	$0.36_{-0.03}^{+0.04}$
GD32B	$1.05_{-0.14}^{+0.13 \pm 0.02}$	$0.21_{-0.02}^{+0.03}$	IC48A	$0.82 \pm 0.05_{\text{stat}} \pm 0.05_{\text{sys}}$	–
GD32C	$0.97_{-0.14}^{+0.13 \pm 0.02}$	$0.28_{-0.03}^{+0.02}$	IC48B	$0.80 \pm 0.03_{\text{stat}} \pm 0.05_{\text{sys}}$	–
GD32D	$0.77_{-0.14}^{+0.13 \pm 0.03}$	$0.31_{-0.04}^{+0.04}$	IC50A	$1.03 \pm 0.06_{\text{stat}} \pm 0.06_{\text{sys}}$	–
GD35A	$0.95_{-0.17}^{+0.17 \pm 0.01}$	$0.13_{-0.02}^{+0.03}$	IC50B	$0.79 \pm 0.03_{\text{stat}} \pm 0.05_{\text{sys}}$	–
GD35B	$0.78_{-0.13}^{+0.12 \pm 0.06}$	$0.16_{-0.07}^{+0.09}$	IC74A	$1.14 \pm 0.06_{\text{stat}} \pm 0.05_{\text{sys}}$	–

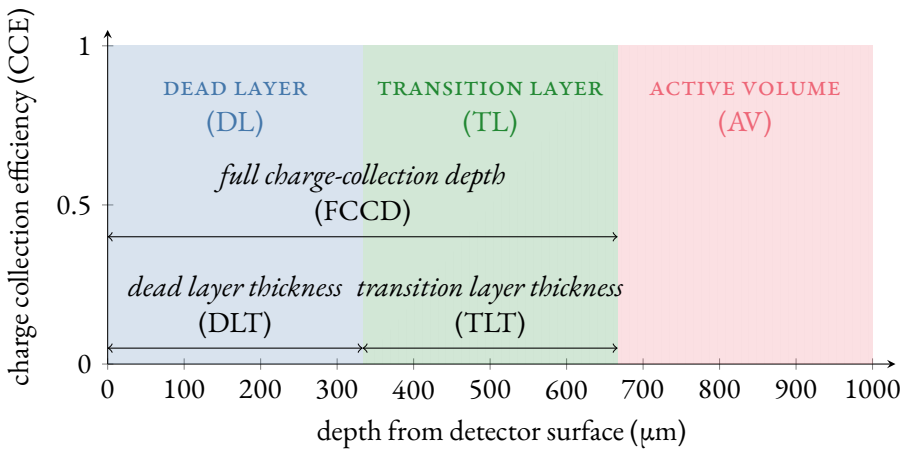


Figure A.1: Germanium detector active volume model. The charge-collection efficiency is zero by definition at the outer surface and remains such through all the “dead layer”. The detector is partially active in the “transition layer” region, where the CCE gradually increases until reaching its maximal value in the fully active volume.

each detector. As a consequence, the transition region must be characterized for each detector individually, i.e. in a similar way as FCCD is determined from external source data.

It is important to stress here that a precise characterization of the transition layer is not needed for the $0\nu\beta\beta$ analysis, as the introduction of a partially-active region above the FCCD results in hypothetical, new $0\nu\beta\beta$ events below the $Q_{\beta\beta}$. $0\nu\beta\beta$ events originating in this transition region would in fact be detected with an effectively lower energy and therefore “get out” of the gaussian peak at $Q_{\beta\beta}$, which is what the experiment looks for. In other words, the presence of a non-null transition layer would have no impact on the signal detection efficiency defined for the $0\nu\beta\beta$ analysis. Constraining the CCE curve is instead important for the $2\nu\beta\beta$ analysis. Different transition layer models result in shape distortions of the $2\nu\beta\beta$ energy distribution that can potentially mimic the presence of new-physics phenomena (e.g. those considered in chap. 1)¹. The potential systematic effect due to the uncertainties in the CCE curve determination is investigated in §5.2.

An attempt to determine the CCE curve for GERDA’s BEGe detectors has been carried on in [180]. A simple linear model (the one shown in fig. A.1) has been considered at first. Once the FCCD is fixed, as it is clear from the formulation of the model, the only parameter that needs to be constrained is the starting point of the transition region, i.e. the dead layer thickness (DLT). Monte Carlo simulations performed with different DLTs have been compared to ^{241}Am data in order to determine the dead-layer fraction (DLF), defined as

$$\text{DLF} = \frac{\text{DLT}}{\text{FCCD}} \in [0, 1],$$

For each BEGe detector. The results are reproduced in tab. A.1. Since the effect of the lithium concentration profile evolution at room temperature on the transition region is not known, these values have not been corrected. A more complex transition layer model has been also derived from first principles

¹Technically, the size of the transition region marginally affects also the $T_{1/2}^{2\nu}$ estimate, since it depends on the total number of detected $2\nu\beta\beta$ events, which increases with the size of the transition region. This effect, however, is negligible compared to the uncertainty induced by the FCCD estimates.

in [180], but it requires special PSD data from other radioactive sources (i.e. A/E from ^{90}Sr in [180]) that is available just for GD91C.

KNOWN ISSUES Unfortunately, the active volume model presented above suffers from many uncertainties and cannot be fully trusted. A systematic discrepancy between FCCD values obtained from different radioactive sources (^{241}Am , ^{133}Ba and ^{60}Co) has been highlighted and discussed [180], but no convincing explanation of its origin has been formulated yet. Moreover, the fact that BEGE detectors were stored at room temperature for a significant amount of time after being carefully characterized poses an additional question mark on these FCCD values, as the growing effect has never been studied in detail. In particular, the size of the transition region extracted from the characterization data must also be affected by the evolution of the lithium concentration profile in some way, and cannot be left uncorrected when considering data collected in the GERDA cryostat. Finally, the linear transition layer model could be a bad approximation in some detectors. An evidence for the presence of these systematic biases lies in the results of the background model presented in chap. 3, which yields incompatible $T_{1/2}^{2\nu}$ estimates from different detector types. More evidence in support of this discrepancy and possible solutions will be presented in the following sections.

A.2 Tuning the BEGE model on calibration data

The effect of the transition region size on the event energy spectrum is particularly strong in the lower tail of intense γ peaks. Full-energy events interacting in the transition region are reconstructed with a smaller effective energy, and are therefore shifted out of the peak. The high-statistics ^{208}Tl 2615 keV line from calibration data is an interesting sample that can be used to determine the size of the transition region. Data from the special ^{228}Th calibration run 68² collected by the GD02A detector is shown in the left-hand side of fig. A.2, in red. PDFs corresponding to different sizes of the transition region (DLF) are overlaid to demonstrate the effect on the low side of the full-energy peak.

To determine the optimum transition region size the observable V/P is defined, where V (valley) and P (peak) are the total number of counts in the [2500, 2600] keV and [2610, 2620] keV regions, respectively (the two energy ranges are highlighted in grey in fig. A.2, left). The uncertainty on V/P is obtained by error propagation of the Poisson uncertainties on V and P . PDFs with dead-layer fractions from 0 to 0.9 in steps of 0.1 and the FCCDs fixed to the official values in tab. A.1 have been produced for each detector, in order to obtain the predicted V/P values. Since V/P is observed to change linearly upon the dead-layer fraction, a linear interpolation is performed between the simulated values. The result is depicted in fig. A.2, on the right, for detector GD02A. Finally, the value of the observable is calculated from data (grey lines) and compared against the interpolation result in order to find the optimum dead-layer fraction value (red lines). The results are reported in tab. A.2 for each detector and in fig. A.3, where they are compared with the dead-layer fractions extracted from detector characterization data. The latter look clearly underestimated, possibly because of the effect of the n^+ contact growth at room temperature, which has never been studied in the transition region.

Unfortunately, not all detectors were active during run 68. Some of them were switched off be-

²As documented in §4.2.2, data from run 68 has been collected with low-activity $\mathcal{O}(1)$ kBq ^{228}Th sources, to study the performance of the liquid argon veto system. Since in these experimental conditions the rate of pile-up events is much lower than in regular calibrations, this data set is more suited to a comparison with Monte Carlo simulations.

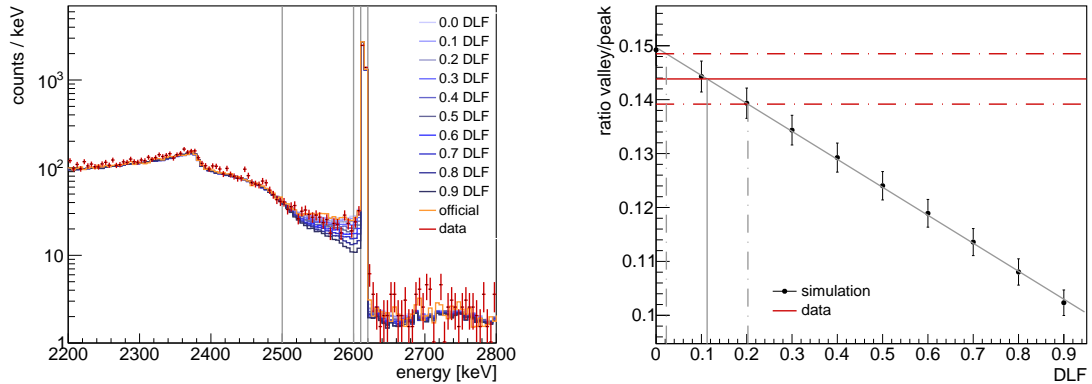


Figure A.2: Example optimization of the dead-layer fraction for detector GD02A. Left: close-up of the energy spectrum in the ^{208}Tl FEP region. The data (red) is compared against simulations with different DLF values, from 0 to 0.9 in steps of 0.1. The PDF corresponding to the recommended DLF value (tab. A.1) is highlighted in orange. The energy regions used to compute the V/P observable are shown in grey. Right: extraction of the optimal DLF value by interpolating the simulation results. The statistical uncertainties are plotted in dashed lines.

Table A.2: BEGe dead-layer fractions obtained from special ^{228}Th calibration data (run 68). Detector GD02D does not fully deplete [122] and is excluded from the analysis. Detectors marked with an asterisk (*) are switched off or unusable in run 68.

Detector	DLF	Detector	DLF	Detector	DLF
GD00A	$0.28^{+0.08}_{-0.07}$	GD32C	$0.51^{+0.09}_{-0.09}$	GD79B*	–
GD00B	$0.08^{+0.20}_{-0.08}$	GD32D	$0.38^{+0.10}_{-0.11}$	GD79C*	–
GD00C	$0.56^{+0.05}_{-0.04}$	GD35A	$0.34^{+0.07}_{-0.07}$	GD89A	$0.31^{+0.09}_{-0.10}$
GD00D	$0.76^{+0.07}_{-0.08}$	GD35B	$0.81^{+0.19}_{-0.21}$	GD89B	$0.45^{+0.17}_{-0.17}$
GD02A	$0.11^{+0.09}_{-0.09}$	GD35C	$0.53^{+0.08}_{-0.09}$	GD89C	$0.60^{+0.07}_{-0.07}$
GD02B	$0.44^{+0.21}_{-0.21}$	GD61A	$0.35^{+0.18}_{-0.18}$	GD89D	$0.48^{+0.09}_{-0.09}$
GD02C	$0.67^{+0.05}_{-0.06}$	GD61B	$0.68^{+0.04}_{-0.05}$	GD91A	$0.43^{+0.18}_{-0.19}$
GD02D [†]	–	GD61C	$0.73^{+0.06}_{-0.07}$	GD91B*	–
GD32A	$0.24^{+0.12}_{-0.13}$	GD76B	$0.58^{+0.09}_{-0.08}$	GD91C	$0.24^{+0.15}_{-0.15}$
GD32B	$0.48^{+0.05}_{-0.06}$	GD76C	$0.79^{+0.05}_{-0.04}$	GD91D	$0.00^{+0.00}_{-0.00}$

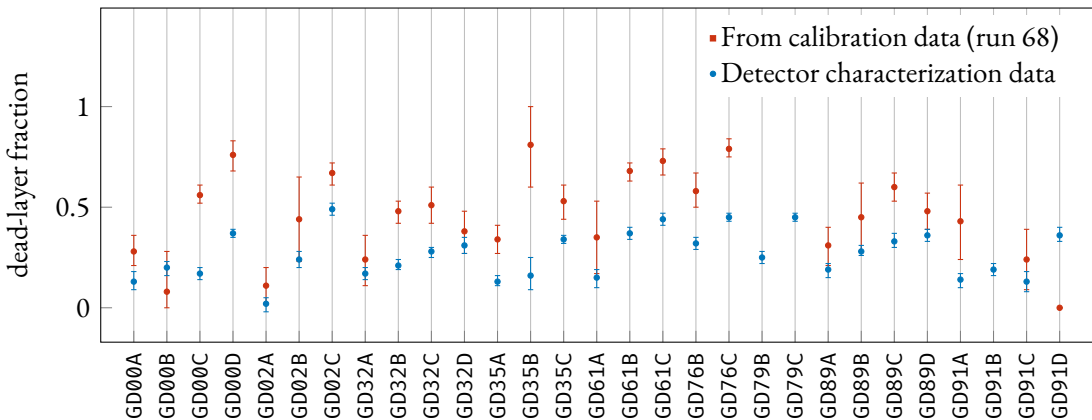


Figure A.3: Comparison between the recommended DLF values (extracted from detector characterization data) and the ones extracted by analyzing the low energy tail of the ^{208}Tl full-energy peak in calibration data. Some values are missing because of detectors for which no data is available.

cause of hardware instabilities and some of them were not usable because of unstable energy calibration. Since no data is available for these detectors, an educated guess is made by assuming a dead-layer fraction equal to an average value. This average value is calculated by repeating the V/P analysis on the BEGe summed energy spectrum, and by varying the simulated dead-layer fraction consistently in all detectors (i.e. all BEGe dead-layer fractions set to 0.0, 0.1, ..., 0.9). The obtained effective dead-layer fraction is

$$0.529 \pm 0.016 ,$$

which carries a smaller uncertainty because of the higher statistics in the data sample³.

A.3 Insights from low-energy data

The GERDA event spectrum is dominated, at low energies, by ^{39}Ar -decay events. This unstable nucleus is naturally present in the atmosphere and is cosmogenically activated. It decays to the ground state of ^{39}K via β^- decay with a half-life of 269(3) yr and Q-value of 656(5) keV [190]. Being commercial liquid argon distilled from air, it naturally contains a fraction of ^{39}Ar , whose activity has been estimated to be of about 1 Bq/kg by various experiments [191–194]. The ^{39}Ar energy spectrum of events collected by GERDA in the first part of Phase II has been partly published in [195].

The β particle emitted in the ^{39}Ar decay can be detected directly or indirectly in GERDA. In the first case the electron has to directly reach the detector active volume. Since a β particle of that energy has a mean range in germanium of less than 100 μm and the n^+ contact is typically several hundreds of μm thick, the only way is through the p^+ electrode. For the same reason, the mother ^{39}Ar nucleus must

³This effective dead-layer fraction value is used as an educated guess for detectors in the $2\nu\beta\beta$ analysis (chap. 5) that were inactive in run 68. This assumption holds well if only the combined BEGe energy spectrum is considered in the analysis. Moreover, the obtained effective uncertainty is adopted in the estimation of the systematic uncertainty contribution from the transition layer model, as it represents the average potential distortion seen in the combined energy spectrum.

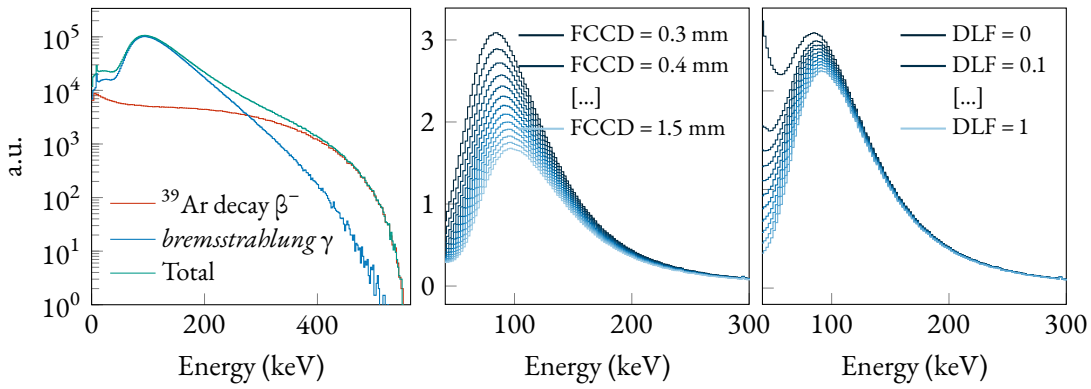


Figure A.4: Left: decomposition of the ^{39}Ar energy spectrum as seen by all GERDA detectors into β and γ components. Center and right: Impact of different linear transition layer model (fig. A.1) parameters on the ^{39}Ar energy spectrum shape, keeping the ^{39}Ar activity in LAr fixed. Center: the dead layer fraction (DLF) is fixed to 1 (i.e. hard step model) and the full charge-collection depth (FCCD) is varied between 0.3 mm and 1.5 mm in steps of 0.1 mm. Right: the FCCD is fixed to 0.9 mm and the DLF is varied between 0 (i.e. no dead layer) and 1 (i.e. no transition layer).

decay very close to the detector surface, i.e. less than 1 mm far from it. Being the p^+ contact a small fraction of the total detector surface, the β component of the ^{39}Ar spectrum is expected to be sub-dominant or even negligible for point-like contact detectors such as BEGeS or InvCoaxs (c.f.r fig. A.4, left).

^{39}Ar electrons typically emit *bremssstrahlung* radiation in LAr that can reach the detector active volume: this is referred as the “indirect” detection method. Since the photon absorption length in germanium and liquid argon is much longer than the electron absorption length, ^{39}Ar decays originating much further from the detector surface can be detected. Moreover, *bremssstrahlung* photons can interact with the whole detector volume, and thus constitute a “volume probe”. It follows from what stated above that the γ component largely dominates the ^{39}Ar event spectrum (c.f.r. fig. A.4, left).

The ^{39}Ar spectral shape is strongly affected by the germanium detector’s active volume model, as it will be demonstrated in the following. This high-statistics data sample collected by GERDA offers the interesting possibility to tune the active volume model on a detector-by-detector basis. Let’s consider, for the sake of simplicity, the simple linear transition layer model depicted in fig. A.1 for the n^+ contact. The effects of variations of its two parameters (the FCCD and the DLF) are shown in fig. A.4. Varying the FCCD (and keeping the DLF fixed at 1, i.e. no transition layer) has of course the effect of changing the number of detected ^{39}Ar events, but introduces a shape distortion too. The effect of the DLF seems to be more localized in the low side of the distribution. Clearly, the more the transition layer extends closer to the surface, the more events with incomplete charge collection appear at lower energies. Remarkably, both parameters seems to shift the position of the maximum of the distribution.

An attempt to fit the ^{39}Ar energy spectrum and extract FCCD and DLF values for each detector has been carried on, whose preliminary results are presented here. The Phase II $^+$ data set (44.1 kg·yr) has been considered, as the germanium detectors energy threshold has been kept low enough (about 40 keV) for the whole data taking. No LAr veto cut or PSD cut has been applied, as the corresponding Monte Carlo model is not known in sufficient detail yet or is completely missing. Each detector

ACTIVE
VOLUME
MODEL

TUNING THE
MODEL

collected more than $5 \cdot 10^4$ events below 200 keV, where the bulk of the ^{39}Ar events is located.

A set of ^{39}Ar PDFs has been generated for each detector separately and considering different combinations of FCCD and DLF values. In this preliminary setting, FCCDs and DLFs have been sampled in discrete steps of 0.1 mm and 0.1, respectively. Together with the signal PDF (^{39}Ar), the most prominent background PDFs in the considered energy region have been generated. Specifically, ^{214}Pb and ^{214}Bi in the detector cabling, $2\nu\beta\beta$ in germanium, ^{42}K in liquid argon and ^{40}K in the mini-shrouds. ^{42}Ar , which decays into ^{42}K by emitting a β particle with a Q-value of 599(6) keV [190] which is very close to the ^{39}Ar Q-value, has not been considered as its activity in LAr is negligible, compared to ^{39}Ar (about 40 $\mu\text{Bq}/\text{kg}$ [191]). The ^{85}Kr contribution has also been discarded because it is highly localized at 514 keV, in correspondence with its only γ line, and does not contribute significantly to the rest of the energy spectrum⁴. To find the combination of FCCD and DLF that best describes the data, first the background of the ^{39}Ar event distribution is fixed at the results of the background model presented in chap. 3. Then, for each detector separately, the ^{39}Ar activity, the FCCD and DLF values are adjusted in order to reproduce the shape of the energy spectrum and the total number of counts. Since activities in the 1.3–1.4 Bq/kg range seem to reasonably describe data from all detectors, the same value of 1.35 Bq/kg is preliminary set for all of them. The results of this manual optimization are shown in figs. A.6 to A.9, including the 68%, 95% and 99% confidence intervals that highlight the magnitude of statistical fluctuations in data. The obtained FCCD and DLF values are compared to the official values from detector characterization data (where available) in fig. A.5. It is stressed here that these results are preliminary and qualitative, as they have not been extracted by means of a careful analysis, which includes the evaluation of the systematic uncertainties. Note that data is not available for some detectors that have not been deployed in Phase II⁺ (ANG1) or were switched off because of hardware instabilities (ANG5 and IC48B).

RESULTS

Starting from the FCCD values, it is interesting to note the high compatibility between the characterization data and the ^{39}Ar data for INVCOAX detectors. Indeed, these are the most precisely characterized and newly-produced detectors deployed in GERDA. In contrast, the ^{39}Ar data analysis reports quite different FCCDs for some SEMICOAX detectors, but the uncertainty on their official estimate is large enough to account for such a deviation. The situation changes again for BEGe detectors, in which the new values are almost always higher than the official estimates and incompatible with them. This discrepancy could be motivated by the observation that these detectors have been stored at room temperature, after being characterized, for 2–3 years, a time in which the lithium concentration profile in the n⁺ contact could have grown at a different rate than what has been suggested in the past ([122] and references therein). For what concerns the BEGe dead-layer fraction values, the ^{39}Ar analysis results are systematically higher than the old estimates. This finding is in agreement with what already seen in calibration data (app. A.2), and could again be motivated by the fact that the dead-layer growth model has never been studied in detail with experimental data.

As already mentioned, an ^{39}Ar activity in the 1.3–1.4 Bq/kg range is needed to reproduce the ob-

⁴ ^{85}Kr disintegrates by β emission mainly to the ground state of ^{85}Rb . Its activity in the atmosphere is of the order of 1 Bq/m³, with a half-life of nearly 11 yr. Its energy spectrum is characterized by a strong γ line at 514 keV, compared to the Compton and β components. The distillation procedure for the production of liquid argon substantially reduces the ^{85}Kr fraction, and the residual ^{85}Kr in liquid argon may vary in different batches of liquid [193]. A rough estimate of its activity in the liquid argon in the GERDA cryostat obtained by comparing the simulated ^{85}Kr PDF to the 514 keV line count rate yields 2.3(3) mBq/kg.

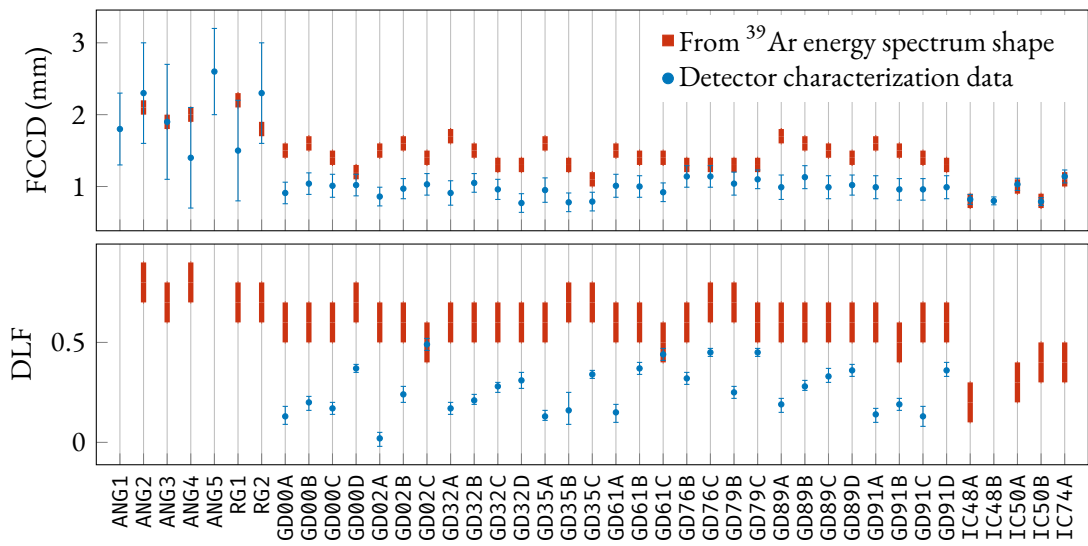


Figure A.5: Comparison between the recommended FCCD and DLF values (extracted from detector characterization data and used for the $0\nu\beta\beta$ analysis) and the ones extracted by analyzing the shape of the ^{39}Ar energy spectrum. The width of the red bars does not represent an uncertainty (see text). Note that DLFs have not been estimated for SEMICOAXs and INVCOAXs and that some FCCD values from ^{39}Ar are missing because of detectors for which no data is available.

served count rate, given the transition layer model that best reproduces the energy spectrum shape. This result is in contrast with what reported by other experimental efforts [191–194], which quote an activity of about 1 Bq/kg. Considering that an independent analysis of GERDA Phase I data (private communications) seems to obtain the same result and there is no reason to hypothesize that the argon deployed in GERDA has a naturally-higher ^{39}Ar activity, the explanation might lie in the different experimental conditions in which GERDA operates, compared to other experiments. However, no convincing hypothesis have been formulated nor tested yet.

There are systematic effects that might play a significant role in this analysis and that could not be studied with the attention they deserve. These results are indeed preliminary and should be taken with a grain of salt. Nevertheless, a tentative list of the main sources of systematic biases is given here for completeness.

SYSTEMATIC UNCERTAINTIES

Transition layer model. A linear model for the CCE in the transition region has been used to keep the analysis simple. However, as it can be easily noticed by observing data close to the energy threshold, the approximation does not hold perfectly throughout the whole ^{39}Ar energy spectrum. More realistic models should be studied in order to asses whether the linear model introduces a severe bias in the results.

Background model. systematic effects arising from an incomplete or inexact background model in the low energy region cannot be excluded. As instance, a ^{85}Kr contribution is known to be present in LAr (γ line at 514 keV) but is ignored in the present analysis. A fit of the ^{85}Kr PDF to the γ line visible in data, however, suggests a negligible contribution.

³⁹Ar spectrum theoretical shape. The dynamics of the first-forbidden unique β^- decay of ³⁹Ar are not known in great detail, from a theoretical point of view [196]. The impact of different numerical calculations should be considered when performing such a shape analysis on its energy spectrum. However, judging from the order of magnitude of the distortions shown in [196], this theoretical uncertainty should have a negligible impact.

These qualitative results, despite not being obtained within a robust statistical framework and despite the lack of a careful study of potential sources of systematic uncertainties, show all the potential of an ³⁹Ar data analysis. This decaying nucleus offers the unique possibility to characterize the active volume of germanium detectors *in situ* and in a clear way, without recurring to dedicated characterization campaigns prior deployment in the experimental apparatus.

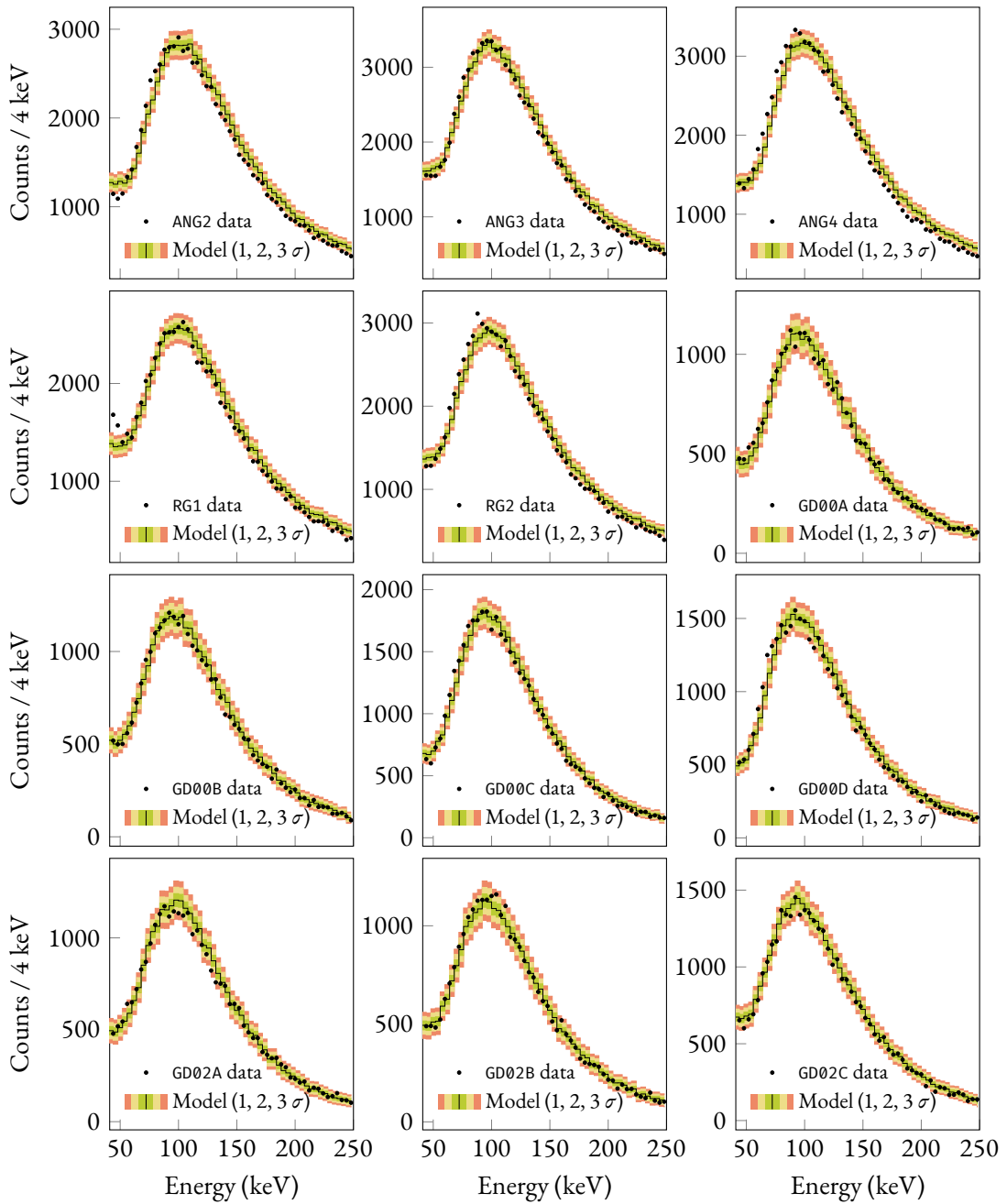


Figure A.6: GERDA Phase II⁺ data (44.1 kg·yr) in the [40, 250] keV energy range and best-matching Monte Carlo model determined by adjusting the transition layer model. The corresponding FCCD and DLF values are shown in fig. A.5.

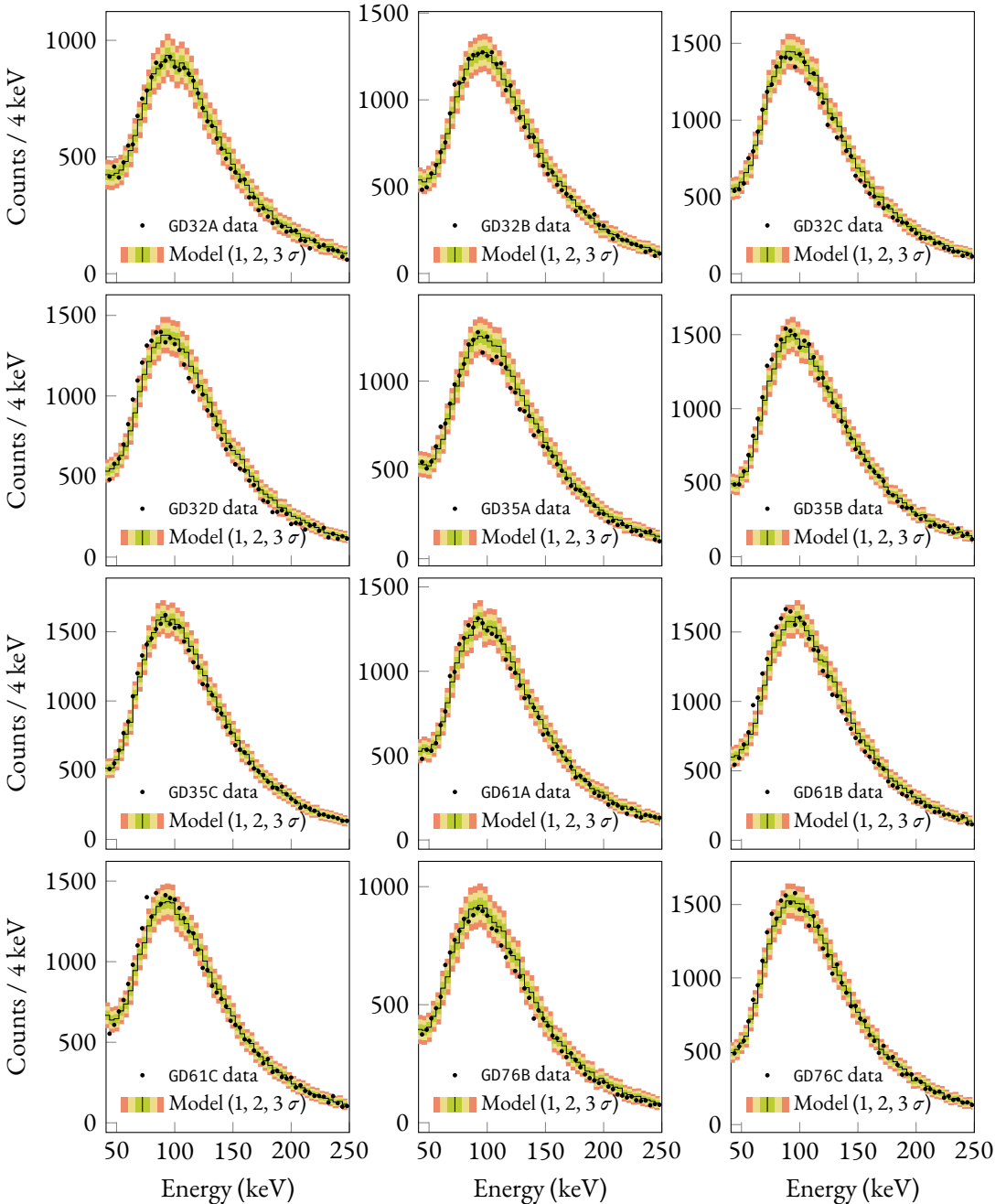


Figure A.7: GERDA Phase II⁺ data (44.1 kg·yr) in the [40, 250] keV energy range and best-matching Monte Carlo model determined by adjusting the transition layer model. The corresponding FCCD and DLF values are shown in fig. A.5.

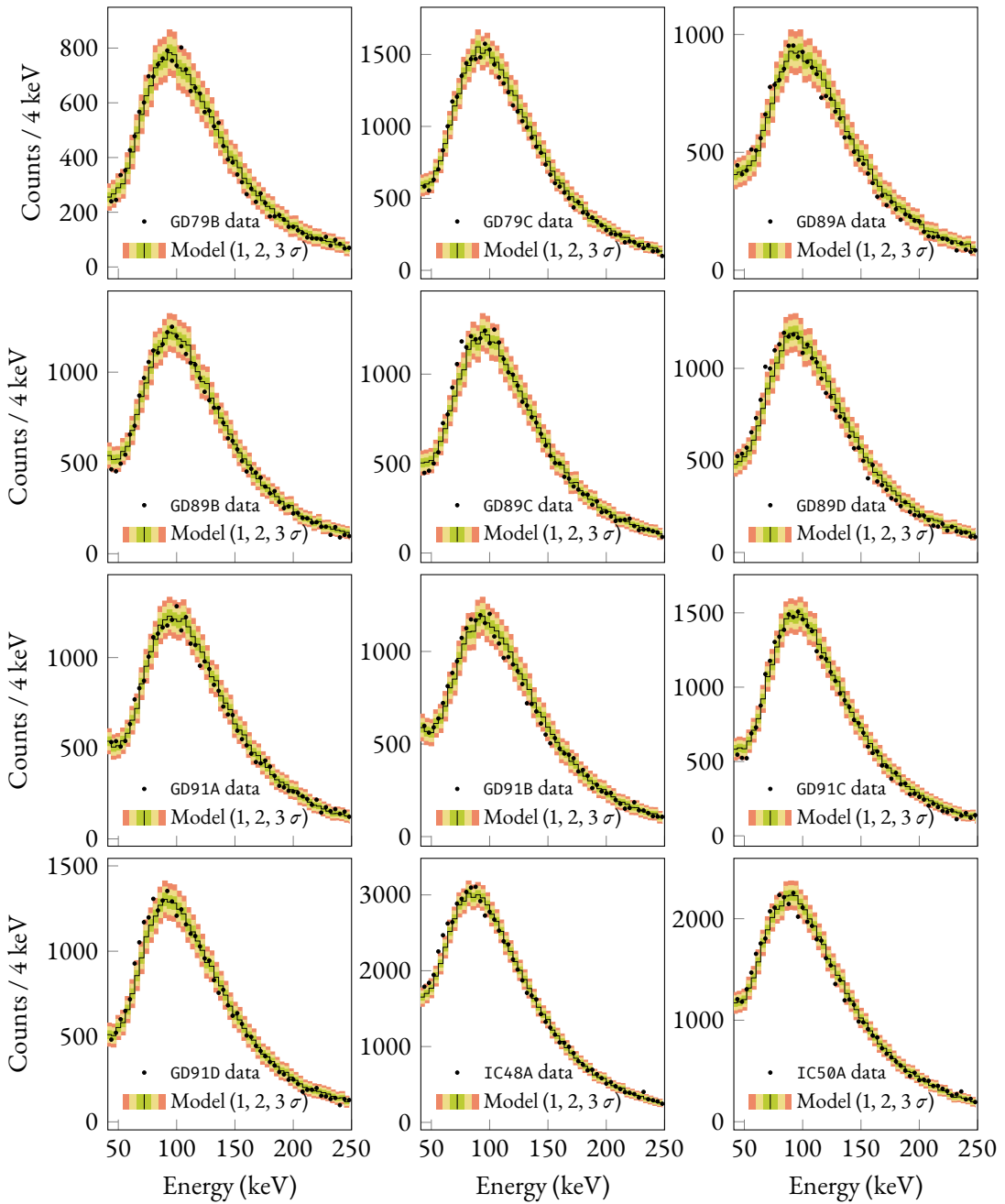


Figure A.8: GERDA Phase II⁺ data (44.1 kg·yr) in the [40, 250] keV energy range and best-matching Monte Carlo model determined by adjusting the transition layer model. The corresponding FCCD and DLF values are shown in fig. A.5.

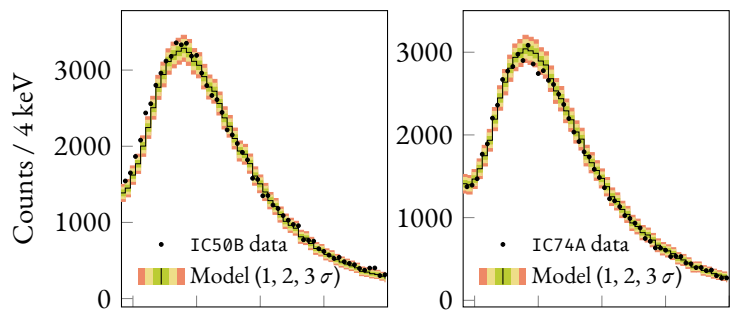


Figure A.9: GERDA Phase II⁺ data (44.1 kg·yr) in the [40, 250] keV energy range and best-matching Monte Carlo model determined by adjusting the transition layer model. The corresponding FCCD and DLF values are shown in fig. A.5.

IN SHORT

- A transition region in which the charge-collection efficiency is reduced is present between the n^+ contact surface of a germanium detector and the fully-active volume (defined as the region in which the efficiency is maximal). The full charge-collection depth and the size of the transition region have been measured during dedicated detector characterization campaigns.
- The SEMICOAX detectors inherited from the HDM and IGEX experiments have not been characterized very precisely, and the uncertainty on their active volume is large. BEGE and INVCOAX detectors have been instead precisely characterized. BEGE detectors, however, have been stored at room temperature for 2–3 years after their characterization and before being deployed in liquid argon. This fact poses a large systematic uncertainty on the dead-layer thickness, which is known to grow at that temperature due to the diffusion of the lithium dopant. The dynamics of the lithium diffusion in a germanium detector, unfortunately, have never been studied in detail in an experimental setting. Moreover, systematic discrepancies are noticed between results obtained with different characterization methods, which are not fully explained.
- To estimate the size of the transition region in BEGE detectors, an important parameter for the $2\nu\beta\beta$ shape analysis (chap. 5), the full-energy ^{208}Tl peak from ^{228}Th calibration data is modeled via Monte Carlo simulations. Energy spectrum shapes are generated considering different sizes of the transition region and compared to data to find the best-matching values on a detector-by-detector basis. The obtained values suggest that the fully-dead layer (the region between the outer surface and the starting point of the transition region) is thicker than what predicted by characterization data.
- The high-statistics, low-energy ^{39}Ar data sample is also qualitatively analyzed to characterize the fully-active volume and the transition region. Preliminary results confirm the discrepancy between data and official active-volume parameters for BEGE detectors, while INVCOAX characteristics seem to be well reproduced. These preliminary investigations show the potential of an analysis of the ^{39}Ar data to precisely constrain the active volume model of a germanium detector without the need of dedicated characterization campaigns preceding deployment in the experimental apparatus.

B. Assay measurements

To assess whether construction materials meet the GERDA radio-purity requirements, screening measurement campaigns have been carried out before the Phase II and Phase II⁺ upgrades. The extracted radioactive decay activities constitute an important set of prior information that guides the construction of the background model presented in chap. 3 and following chapters. The results of the measurements are converted to useful units for the characterisation of prior distributions in the background model and other analyses. Part of these measurements are published also in [121].

Radio-purity was measured with three techniques: γ spectroscopy, ICP-MS and neutron activation analysis (NAA), which main characteristics are summarized below.

γ spectroscopy. is performed with photon-counting apparatus (usually germanium detectors). The radio-activity of a material sample is determined by measuring the intensity of known γ lines from various decaying isotopes. γ spectroscopy is well suited to constrain ^{40}K contaminations.

ICP-MS. (Inductively Coupled Plasma Mass Spectrometry) is a technique that ionizes the material samples and counts the resulting ions after separating them according to their charge-to-mass ratio. It is applicable to materials which can be easily put in liquid form. Statistical uncertainties on ICP-MS measurements are usually small, but systematic effects can bias the results.

NAA. (Neutron Activation Analysis) essentially exposes the target material sample to a flux of neutrons. The γ radiation emitted by the activated nuclei in the sample is analyzed to determine the initial isotopic composition. Light atomic nuclei (e.g. potassium) which are not activated by neutrons cannot be detected by this method.

The results of all screening measurements available for GERDA Phase II materials are summarized in tables B.1 and B.2. Recommendations on how to properly use the values as prior information in the background model are included. Note that the following groups of isotopes are assumed to be in secular equilibrium:

$$^{238}\text{U} > ^{234\text{m}}\text{Pa} \parallel ^{226}\text{Ra} > ^{214}\text{Pb} > ^{214}\text{Bi} \parallel ^{228}\text{Ra} > ^{228}\text{Ac} \parallel ^{228}\text{Th} > ^{212}\text{Bi} > ^{208}\text{Tl} .$$

Table B.1: Activity of GERDA Phase II setup components calculated from radio-purity screening measurements. Values in gray can be used as priors for Phase II background modeling as they are; values in green are (partly) derived from ICP-MS/NAA measurements under the assumption of secular equilibrium in the U/Th decay chains; values in light blue have to be multiplied by 2/3. The latter is an approximation for the shortening of the cables before deployment in GERDA.

Part	Material	Method	^{228}Ra (μBq)	^{226}Ra (μBq)	^{228}Th (μBq)	^{60}Co (μBq)	^{40}K (mBq)	^{238}U (mBq)
holders	Si V IKZ	γ spec.	< 250	< 130	< 96	< 100	2.75 ± 0.58	< 6.2
Si		NAA	< $6.4 \cdot 10^{-4}$	< $6.4 \cdot 10^{-5}$	< $6.4 \cdot 10^{-4}$	–	–	< $6.4 \cdot 10^{-8}$
cables	Haefele 10 mil	γ spec.	< 230	210 ± 60	< 150	60 ± 30	3.00 ± 0.60	< 10
	Haefele 2 mil	γ spec.	< 320	780 ± 170	< 380	< 270	3.5 ± 1.7	< 35
	Tecnomec 3 mil	γ spec.	< 73	< 49	< 60	< 10	1.43 ± 0.39	< 5.7
	Tecnomec 2 mil	γ spec.	< 42	< 29	< 35	< 6	0.83 ± 0.23	< 3.3
<i>4 above</i>		< 660	990 ± 310	< 620	60 ± 310	8.7 ± 3.0	–	< 54
electronics	CC3	γ spec.	760 ± 380	2670 ± 380	< 1300	< 300	13.3 ± 3.8	< 21
mini-shroud	coated	ICP-MS	10.8 ± 3.2	20.1 ± 6	10.8 ± 3.2	–	< 0.11	0.0201 ± 0.0060
	glued	ICP-MS	7.2 ± 2.2	21.4 ± 6.4	7.2 ± 2.2	–	> 1.7	0.0214 ± 0.0064
<i>2 above</i>		18 ± 5	43 ± 13	18 ± 5	–	> 1.7	0.043 ± 0.013	–
LAr veto	BCF-91A fibers	ICP-MS	44 ± 4	32 ± 3	44 ± 4	–	0.350 ± 0.070	0.032 ± 0.003
	copper supports		130 ± 130	520 ± 520	130 ± 130	–	–	–
	SAMI RG178 cables	γ spec.	–	< 340	< 440	–	2.49 ± 0.49	–
<i>3 above</i>		180 ± 140	520 ± 870	180 ± 560	–	2.85 ± 0.56	0.550 ± 0.52	–
SiPM		ICP-MS	< 1.3	< 3.9	< 1.3	–	–	< 0.0039
plastic opt. coupling	γ spec.	–	< 6.1	4.8 ± 0.08	–	0.0960 ± 0.0096	–	–
Cufflon	γ spec.	–	19.5 ± 6	12 ± 0.5	–	0.270 ± 0.027	–	–
pins	γ spec.	–	141 ± 28	< 55	–	2.07 ± 0.20	–	–
screws	γ spec.	–	191 ± 51	< 74	–	< 1.5	–	–
glue EP601	γ spec.	< 6	< 2.2	< 6	–	< 0.052	–	–
<i>6 above</i>		< 7.3	351 ± 97	16.8 ± 140	–	2.4 ± 1.8	< 0.0039	–
PMT top	γ spec.	–	< 15 · 10 ³	< 18 · 10 ³	–	< 82	–	–
PMT bottom	γ spec.	–	< 12 · 10 ³	< 14 · 10 ³	–	< 64	–	–
voltage dividers (VD)	γ spec.	–	< 18 · 10 ³	< 8 · 10 ³	–	< 180	–	–
PMT bottom + 7 _x VD		–	< 20 · 10 ³	< 17 · 10 ³	–	< 140	–	–
PMT top + 9 _x VD		–	< 26 · 10 ³	< 22 · 10 ³	–	< 190	–	–
copper shrouds	ICP-MS	62 ± 6	250 ± 25	62 ± 6	–	–	0.250 ± 0.025	–
Tetratex [®]	γ spec.	–	282 ± 28	132 ± 13	–	18.4 ± 1.8	–	–
<i>2 above</i>		62 ± 6	532 ± 53	194 ± 19	–	18.4 ± 1.8	0.250 ± 0.025	–

Table B.2. Activity of additional setup components deployed during the GERDA Phase II⁺ upgrade calculated from radio-purity screening measurements. Values in gray can be used as priors for Phase II background modeling as they are; values in green are (partly) derived from ICP-MS/NAA measurements under the assumption of secular equilibrium in the U/Th decay chains; values in light blue have to be multiplied by 2/3. The latter is an approximation for the shortening of the cables before deployment in GERDA.

Part	Material	Method	^{228}Ra (μBq)	^{226}Ra (μBq)	^{228}Th (μBq)	^{60}Co (μBq)	^{40}K (mBq)	^{238}U (mBq)
cables	Tecnomec 3 mil	γ spec.	< 153	< 203	< 126	< 21	3.01 ± 0.82	< 18.0
LAr veto	outer BCF-91A fibers	ICP-MS	177 ± 53	93 ± 28	177 ± 53	—	3.1 ± 0.9	0.093 ± 0.028
	inner BCF-91A fibers	ICP-MS	24 ± 7	12 ± 4	24 ± 7	—	0.41 ± 0.01	0.012 ± 0.004
mini-shroud	coated + glued	ICP-MS	19 ± 5	46 ± 14	19 ± 5	—	> 1.8	0.046 ± 0.014

C. Monte Carlo simulations and probability density functions

Background components that were identified in the energy spectra or in radio-purity screening measurements (see app. B) are simulated using the MAGE software [151] based on GEANT4 [152–154]. The GERDA Phase II detectors, their arrangement in seven strings as well as the LAr instrumentation are implemented into MAGE. A graphic rendering of the relevant implemented hardware components is presented in fig. 2.7.

Simulations of radioactive decays and full tracking of the decay products are performed in all the hardware components close enough to the detector. Relevant event data like energy depositions in sensitive detectors (germanium, LAr, SiPMs and PMTs), hit location in germanium and LAr is written on disk. Propagation of optical photons (e.g. resulting from the LAr scintillation) is disabled by default to save computing time. It is only enabled during special simulations of the LAr veto system. The built-in GEANT4 generators and databases are used to simulate all radioactive decays except for double-beta decay in germanium, for which more details about the decay dynamics (e.g. angular correlations between the emitted electrons) are needed. The primary spectrum of the two electrons is indeed sampled separately according to the distribution implemented in DECAY0 [155].

The ^{42}K decays (except for surface contaminations) are simulated homogeneously distributed in the relevant LAr volume. The following LAr volumes are chosen for the background model: the first is a cylinder centered on the detector array ($b = 250 \text{ cm}$, $r = 100 \text{ cm}$) subsequently divided into the volume enclosed by the mini-shrouds and the remaining one (outside the mini-shrouds); the second is a cylinder ($b = 100 \text{ cm}$, $r = 25 \text{ cm}$) positioned just above the array and the remaining seven are smaller cylinders ($b = 20 \text{ cm}$, $r = 5 \text{ cm}$), each one positioned just above each of the seven detector strings. The obtained PDFs are used in the full energy range background model and in the potassium tracking analysis

The output of MAGE simulations is further processed to compute the probability density functions (pdfs) used to model the GERDA data in the statistical analysis. This procedure includes folding in run-time dependent information, i.e. the detector status in each physics run, the finite energy resolution and threshold of each detector. The detector dead-layer model is also applied in this post-processing step, by re-weighting energy positions according to their distance from the nearest surface. All PDFs presented in this work are computed using the run-time parameters of the data sets they refer to. A selection of the PDFs projected in energy space and normalized to the number of simulated

events, is displayed in fig. 3.2.

For the potassium tracking analysis PDFs binned in detector space are used to model the data. The rotationally symmetric single-detector PDFs for the ^{40}K and ^{42}K energy windows are shown in fig. C.2 and fig. C.1. For two-detector events the following representation style is used: projections of the two-dimensional histograms on their axis are summed, such that each two-detector event enters the final histogram twice, in the two bins associated to the respective detectors. They can be found in fig. C.1 together with the single-detector PDFs of the rotationally asymmetric components.

Common features can be noticed across the multitude of histogram shapes. The event rate in single-detector data is generally higher in coaxial detectors, due to their larger mass compared to BEGe detectors — maximal correlation between event rate and detector-by-detector exposure can be found in the $2\nu\beta\beta$ PDF in fig. C.2. This feature is generally lost in the two-detector data: the coaxial detectors larger volume allows to stop more efficiently γ particles that would otherwise escape and eventually deposit energy in a second detector. Other similarities between different PDFs can be attributed to detectors live-times, like in the case of GD91C, which was inactive for a large fraction of the Phase II exposure and thus generally registers a low number of counts. The effects of asymmetrically distributed background contaminations are easily recognizable in the shape of the PDFs. Impurities located above the detector array are mostly seen by the uppermost detectors in each string as can be seen for ^{40}K in the front-end electronics in fig. C.1a and in fig. C.1c and for ^{42}K above each mini-shroud (see fig. C.2b and fig. C.1d). Rotationally asymmetric components are mostly evident in a single string, see for example ^{40}K in single mini-shrouds in fig. C.1b and fig. C.1d.

All α decays in the ^{226}Ra to ^{210}Pb sub-chain and from ^{210}Po are simulated on the p^+ detector surface separately and for different thicknesses of the p^+ electrode. The ^{226}Ra chain is simulated together under the assumption that in each α decay half of the contamination is lost due to the recoil of the nucleus into the LAr. The resulting PDFs are displayed in fig. 3.3a and fig. 3.3b. The spectra exhibit a peak like structure with a pronounced low-energy tail. The maximum is shifted with respect to the full emission energy due to the thickness of the p^+ contact. The low-energy tail is characteristic for α decays; the α particle is susceptible to the change in the contact thickness when penetrating the detector surface under an incident angle and loses part of its energy before reaching the active detector volume.

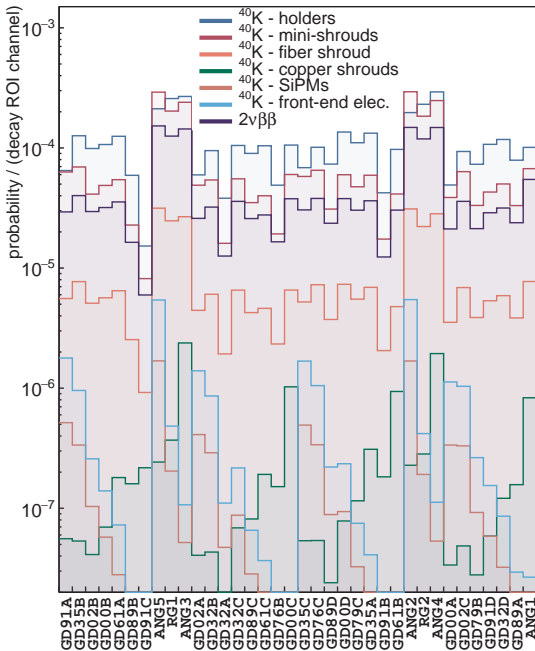
MANAGEMENT TOOLS

The MAGE simulations are performed at the high-performance computing cluster of the Max Planck Institut für Kernphysik in Heidelberg (Germany), where access to a job queue (for a maximum of 200 concurrent jobs per user) and several PB of disk space is granted. Managing simulations and their post-processing queue is not a simple task when scaling up significantly their number and size. As a reference, the GERDA simulation output saved on disk which is used to produce the background model PDFs amounts to about 30 TB of data. Moreover, simulations are split up in small chunks to allow for parallelization of the workload and to not exceed the maximum run time per job allowed by the job scheduler¹, resulting in about $\sim 10^5$ files that need to be managed.

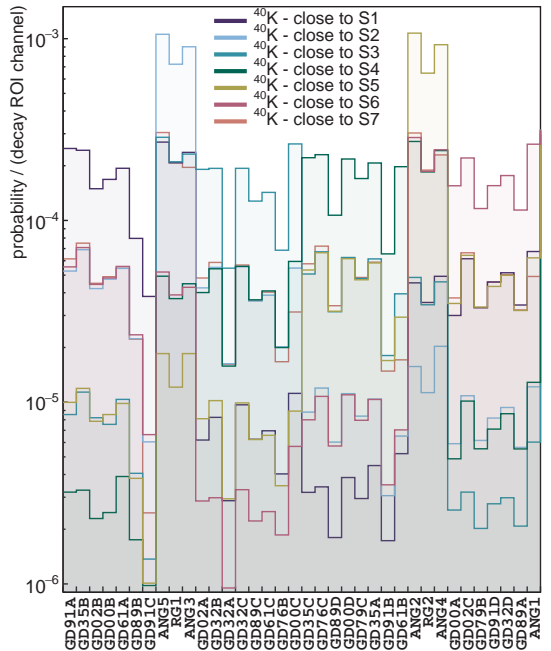
The MAGE simulations are stored in databases, which contain macro files (that configure a simulation job and are directly fed into MAGE), output files and log files organized in a specific directory structure (i.e. group1/group2/isotope/subtype). Multiple separate databases can be managed at the same time (e.g. to keep Phase II and Phase II⁺ simulations separate). A library of code utilities² has

¹The Son of Grid Engine (<https://arc.liv.ac.uk/trac/SGE>), a community project to continue Sun's old grid engine previously used on the cluster, is used for allocating computing resources to users and running batch jobs.

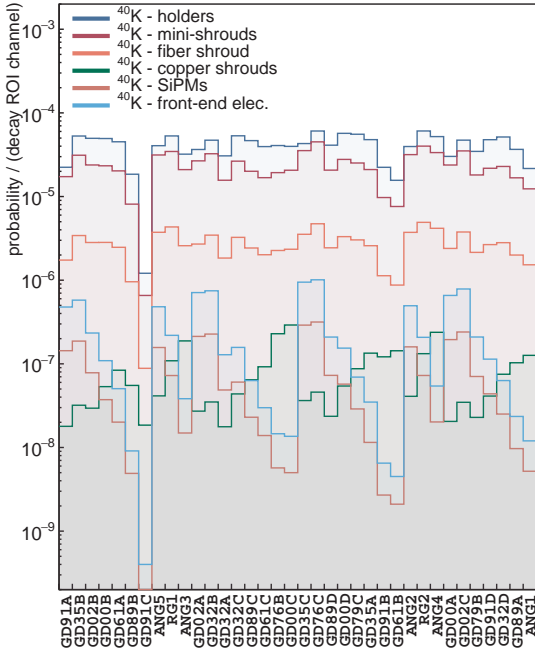
²The GeMS.jl (GERDA MAGE Simulations) library is a Julia-based [197] toolkit with functions to analyze JSON simula-



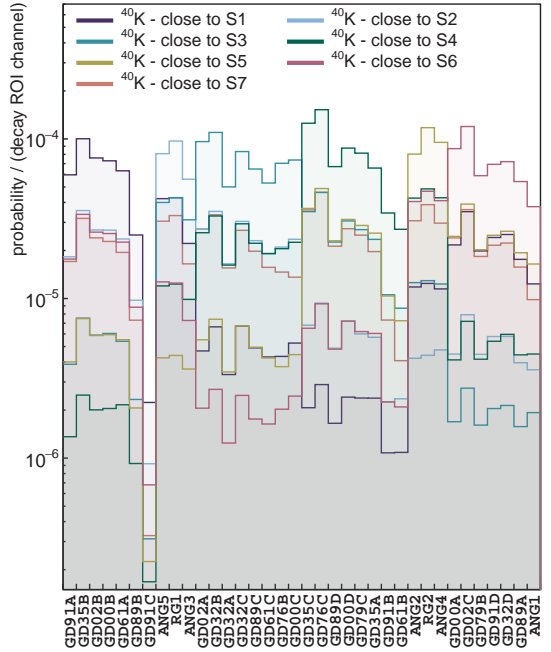
(a) ^{40}K in different setup locations and $2\nu\beta\beta$ in Ge, M1-K40 data set.



(b) ^{40}K located close to each single mini-shroud, M1-K40 data set.

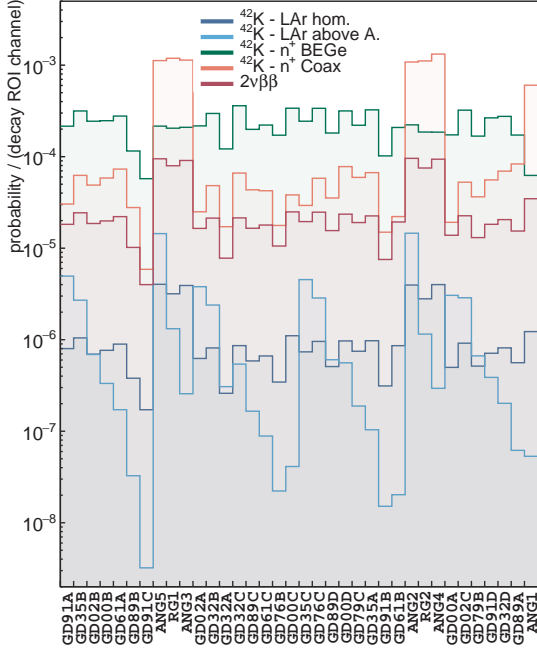


(c) ^{40}K in different setup locations, M2-K40 data set.

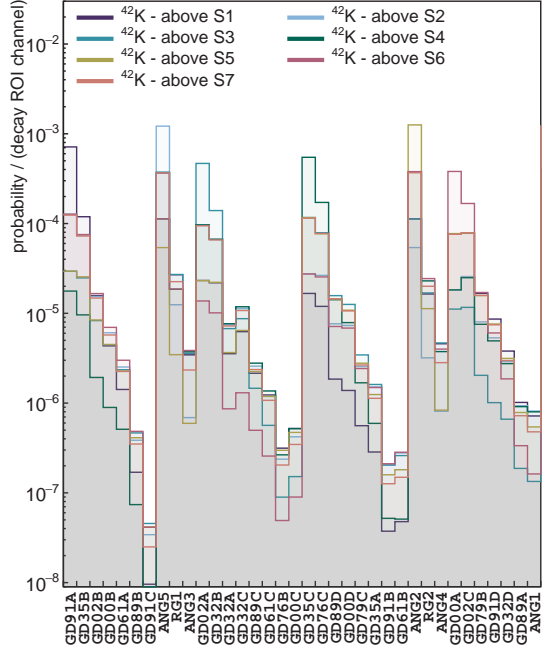


(d) ^{40}K located close to each single mini-shroud, M2-K40 data set.

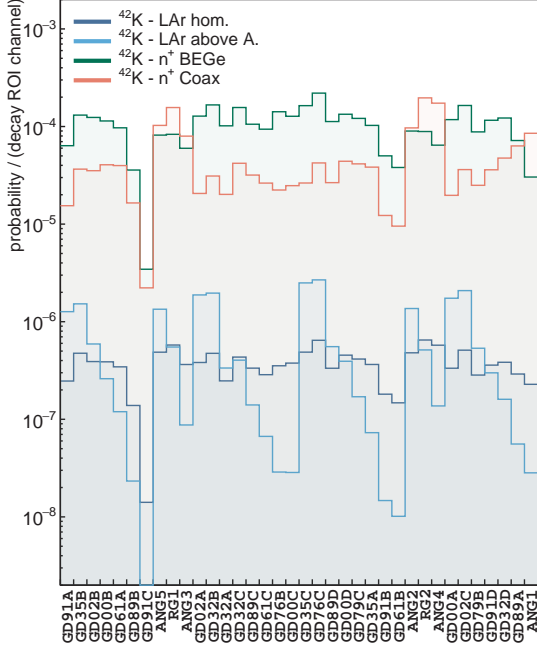
Figure C.1: PDFs binned in detector space for the ^{40}K tracking analysis. All PDFs are normalized to the number of simulated primary decays.



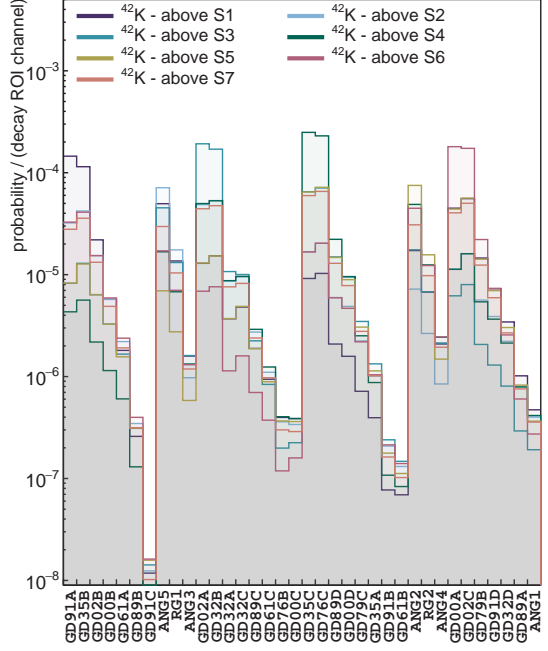
(a) ^{42}K in different setup locations and $2\nu\beta\beta$ in Ge, M1-K42 data set.



(b) ^{42}K in LAr above each single mini-shroud, M1-K42 data set.



(c) ^{42}K in different setup locations, M2-K42 data set.



(d) ^{42}K in different setup locations, M2-K42 data set.

Figure C.2: PDFs binned in detector space for the ^{42}K tracking analysis. All PDFs are normalized to the number of simulated primary decays.

been developed to automate the interaction with the job scheduler and populate the database with simulation output. The database is built through a JSON-based metadata interface. The user is required to specify the simulation parameters (including the MAGE volume in which the primaries should be confined, the number of simulated events, the number of parallel jobs, the commands required to define the physics of the simulation, the software version, etc.) by filling `metadata.json` files, which are subsequently parsed by the `GeMS.jl` software when populating the database with macro configuration files. The following part of metadata file, for example, defines the volume used to simulate radioactive contaminations in the cabling (`cables/cables_all`):

```
{
  "cables": {
    "template": "gerda-ph2",
    "cables_all": {
      "description": "All the cables parts together, HV, signal and the cable patches",
      "simulated-properties": {
        "mass-g": 31.01,
        "volume-cm3": 20.26,
        "density-gcm3": 1.53
      },
      "image-volumes": [
        "HVCableAtHolder_Phase2_[0-39]",
        "SignalCableAtHolder_Phase2_[0-39]",
        "HVCableFromHolderToElectronicsPlate_Phase2_[0-39]",
        "SignalCableFromHolderToElectronicsPlate_Phase2_[0-39]"
      ]
    },
    // ...
  }
}
```

The following excerpt configures a ^{40}K simulation in the cables.

```
{
  "cables": {
    "cables_all": {
      "K40": {
        "additional-commands": {
          "generator": [
            "/MG/generator/select G4gun",
            "/MG/generator/g4gun/cone_on true",
            "/gun/particle ion",
            "/gun/ion 19 40",
            "/gun/energy 0 eV"
          ]
        },
        "edep": {
          "mage-version": {
            "revision": "gerda-v2.0.0-rc3",
            "gerda-sw-all": "gerda-sw-all_v6.1.1-mage@gerda-v2.0.0-rc3"
          },
          "total-events": 1.0e9,
          "number-of-files": 100,
          "contact": "L.Pertoldi"
        }
      }
    }
  }
}
```

tion databases, populate them with MAGE macros and interact with a SGE job scheduler. Management of large databases is efficiently automated, providing a simple user interface to check whether macros should be written or updated or outdated simulations should be re-run. Support for parallel processing is available. GeMS.jl is part of the gerda-gems-sw software stack available on GitHub at <https://github.com/mppmu/gerda-gems-sw>.

```
        }
    },
    // other isotope...
}
```

In this way, the user is absolved from having to deal with thousands of files and the database can be versioned with Git³. Databases for background model simulations are uploaded to GitHub⁴.

The simulation post-processing to obtain the background PDFs is also managed with the cluster job scheduler and dedicated automation software tools⁵. Each single simulation has to undergo a process pipeline to fold detector parameters and run-dependent information into the raw MAGE output, before being parsed by histogram generation routines that write the PDFs to disk. The software utilities interact with the job scheduler and add the requested or outdated jobs to the queue, based on the set of simulations selected by the user. The latter is required to provide a list of simulations as input; the software then builds a local replica of the database with symbolic links to the corresponding directories in the simulation database and inspects it. The PDF production is also configured with JSON files; the detector active volume parameters, the energy calibration and all other settings can then be modified by the user without any need to recompile the software. The ROOT files with the output PDFs are then distributed to the collaboration.

The reproducibility of the results is guaranteed in various ways. First, the simulation databases and the software are versioned with Git. Once a new PDF release is ready, it is distributed with a progressive version number, and the software revision is tagged. The PDF production configuration files are shipped as part of the PDF release. Lastly, all the simulation and PDF production pipeline is run within Singularity [198, 199] containers.

C.I Optical physics in MAGE

The computation of the LAr veto flag for Monte Carlo events is described in §4.2.1. Here, a reference list of the optical properties implemented in **MAGE** that regulate the propagation of light in the **GERDA** cryostat is given.

Optical materials and surfaces are implemented in MAGE through the relevant GEANT4 libraries. Once properties like reflectivity, wavelength-shifting capabilities, attenuation lengths, scintillation yields etc. are defined, the GEANT4 core routines take care of simulating light propagation accordingly. When defining optical parameters in the Monte Carlo, one must keep in mind what are the typical photon wavelengths that come to play in the GERDA setup. The most important wavelength is 128 nm, in the so-called vacuum-ultra-violet (VUV) regime, which defines the energy of the photon emitted by the LAr scintillation process. The second interesting regime is in the 400–600 nm range, typical of photons which are wavelength-shifted (WLS) in the fiber curtain or by Tetraphenil-Butadiene (TPB) coatings to match the absorption range of the light detectors (PMTs, SiPMs). As it will be clear in the next sections, many optical parameters are poorly known in the VUV regime or depend on the de-

³<https://git-scm.com>

⁴<https://github.com/mppmu/gerda-gems-db>

⁵ Available on GitHub at <https://github.com/mppmu/gerda-pdfs>.

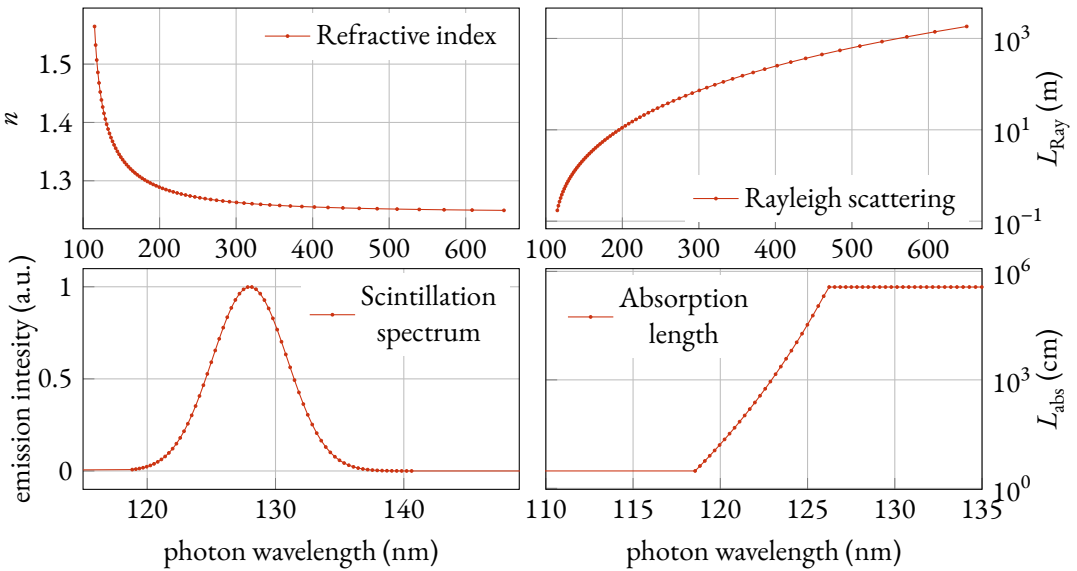


Figure C.3: LAr optical properties as implemented in MAGE. Top left: the refractive index, top right: the Rayleigh absorption length, bottom left: the scintillation spectrum, bottom right: the absorption length. Taken from [134, 200, 201].

tails of the experimental setup (LAr purity, WLS coating thickness etc.), and a dedicated measurement should be therefore performed. In the following a reference list of the optical properties implemented in MAGE is provided, with references to the literature.

Key properties of the liquid argon from the point of view of the vetoing performance in GERDA are the scintillation mechanism, the refractive index and the attenuation length. The first two are relatively well known, while the latter strongly depends on the LAr purity, which has not been measured for GERDA. We recall here that the deployed LAr has not been subject to any purification process, and is therefore expected to meet the purity specifications of natural argon.

LIQUID
ARGON

Refractive index. Its implementation depends on the photon energy (shown in fig. C.3). Formulas are taken from [200] and give about 1.41 at 128 nm. A more recent measurement, similarly based on an extrapolation of measured data to lower wavelengths, suggests a lower value of about 1.37 [202].

Rayleigh scattering length. Depends on the refractive index and therefore the photon energy (shown in fig. C.3). Formulas are taken from [201]. The already implemented refractive index values are used. The obtained scattering length value at 128 nm is about 60 cm. The value suggested in [202] is 91 cm, 50% higher.

Scintillation spectrum. Taken from [134], which reports an experimental measurement (figs. 1 and 2). Only the (gaussian) peak is implemented in MAGE, as the non-gaussian contributions are of several orders of magnitude lower and are therefore negligible. A normal distribution ($\mu = 128$ nm, $\sigma = 2.929$ nm) is implemented (fig. C.3).

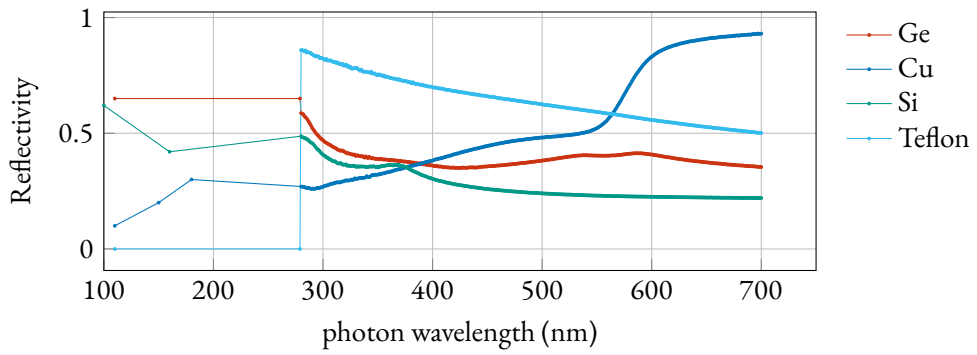


Figure C.4: Reflectivity of germanium, copper, silicon and Teflon as implemented in MAGE.

Scintillation yield. Different scintillation processes are defined in the MAGE physics list for different ionizing particles, that in general have different scintillation yields in LAr. A nominal value of $51 \gamma/\text{keV}$ is recommended for *flat-top* particles [137, 203] (see references for the definition of flat-top particles), which reduces to $40 \gamma/\text{keV}$ for β and γ particles. This value does certainly not represent the reality of GERDA, as the yield strongly depends on the electric field configuration and the quencher impurity level. Unfortunately a reliable direct measure of the scintillation yield of the GERDA LAr is not available. Indirect measurements were performed within the LArGE setup [180] and with a dedicated setup deployed inside the GERDA cryostat [204], but they both yield incompatible results. A tentative, default value of $28 \gamma/\text{keV}$ for β and γ particles is implemented in MAGE, which is the maximum achievable scintillation yield corresponding to $1 \mu\text{s}$ triplet lifetime⁶. As shown in [203], some particles (in particular α particles and nuclei) can be characterized by lower yields. Therefore, the photon yield is reduced for α particles and nuclei by a factor of 0.875 and 0.375 respectively in the physics list. These numbers are extracted from [203]. In this way β and γ particles will be affected by the nominal (maximum) photon yield, while α particles and nuclei will produce less light by a factor 0.875 and 0.375 (0.7/0.8 and 0.3/0.8 according to [203]), respectively.

Singlet and triplet lifetime. The implemented triplet lifetime is the one measured during GERDA Phase II, before the Phase II⁺ upgrade (fig. 2.10), the singlet lifetime is about 6 ns. The relative occurrence of the two de-excitation processes is also specified in terms of scintillation yield. The GEANT4 YIELDRATIO property, which is defined as the relative strength of the fast component as a fraction of total scintillation yield, is set to 0.23 for all particles (β and γ particles), 0.75 for nuclei and 1.0 for α particles (the latter is a rough guess).

Attenuation length. As the absorption length is strongly dependent on the LAr purity, no literature values can be used. It is known to depend on the wavelength of the photon in general, but this dependence is poorly known in the VUV regime. What is most important in MAGE is its value

⁶in first order, only the long-lived triplet state is affected by contaminant-induced non-radiative de-excitation. Electromagnetic interactions have a singlet-to-triplet ratio of 0.3 [203]. The integral over the triplet decay for nominal $1.6 \mu\text{s}$ [203], compared to the $1 \mu\text{s}$ measured in GERDA (see fig. 2.10), gives a reduction of the light yield of $(0.3 + 1/1.6)/1.3 = 71\%$. This estimate neglects impurities that affect the primary excimer production.

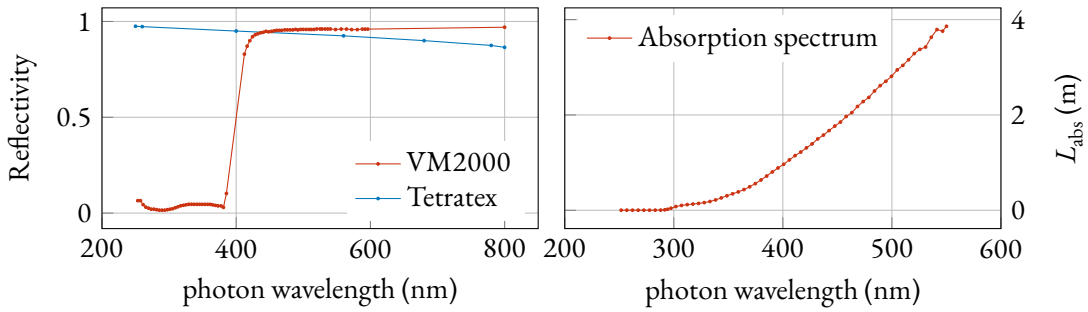


Figure C.5: Reflectivity of VM2000 and Tetratex® reflectors (right) and absorption length of the nylon mini-shrouds (left), as implemented in MAGE.

at 128 nm, i.e. the wavelength of the LAr scintillation light. The following, heuristic implementation is adopted: an exponential function is used to make sure that the LAr is opaque to VUV photons ($\lambda \leq 128$ nm) but transparent to wavelength-shifted photons ($\lambda \geq 400$ nm), see fig. C.3. A measurement of the attenuation length in the GERDA LAr was performed [204], yielding ~ 15 cm as a result, but the performance of the LAr veto as well as recent measurements point towards larger absorption length. A default, reasonable value of 55 cm is thus implemented in MAGE and used in the LAr veto system simulation as best guess.

Fano factor. A Fano factor of 0.11 is set, taken from [205].

Reflectivity is another key property in optical simulations, as it can be different for VUV scintillation photons and wavelength-shifted photons. Unfortunately, the available literature about material reflectivity in the VUV regime is often very scarce. Surfaces in the GERDA setup for which knowing the reflectivity is crucial are certainly germanium, silicon holder plates and the VM2000 and Tetratex® reflectors that cover the internal copper surface of the LAr veto instrumentation.

REFLECTIVITY

Ge, Si, Cu and Teflon. Measurements performed for GERDA are available in [206]. A reflectometer at room temperature and in air was used to measure the reflectivity in the wavelength range [280, 700] nm, therefore values in the VUV region must be taken from other sources. For germanium it seems to strongly depend upon the radiation incident angle [207], but it's not possible to implement angle-dependent reflectivities in GEANT4 yet. A rough, average value of 0.65 is therefore set for wavelengths smaller than 280 nm. The reflectivity values for all materials mentioned above are plot in fig. C.4.

Polymeric reflectors. Tetratex® values are taken from [208]. The author reports measurements of the reflectivity of 2 and 4 superimposed layers of 160 μm thick Tetratex®. As the thickness of the foils used in GERDA is 254 μm , the results for the two superimposed foils (320 μm) are implemented in MAGE. In reality, the reflectivity of the GERDA foils should be (negligibly) smaller. The TPB layer has some effect on the reflectivity, but there's no measurement available in literature. VM2000 values are taken from [209]. The authors report measurements of TPB-coated VM2000, as in the GERDA setup, which then take into account the effect of the TPB emission spectrum. The measurement seems to be independent on the TPB layer thickness.

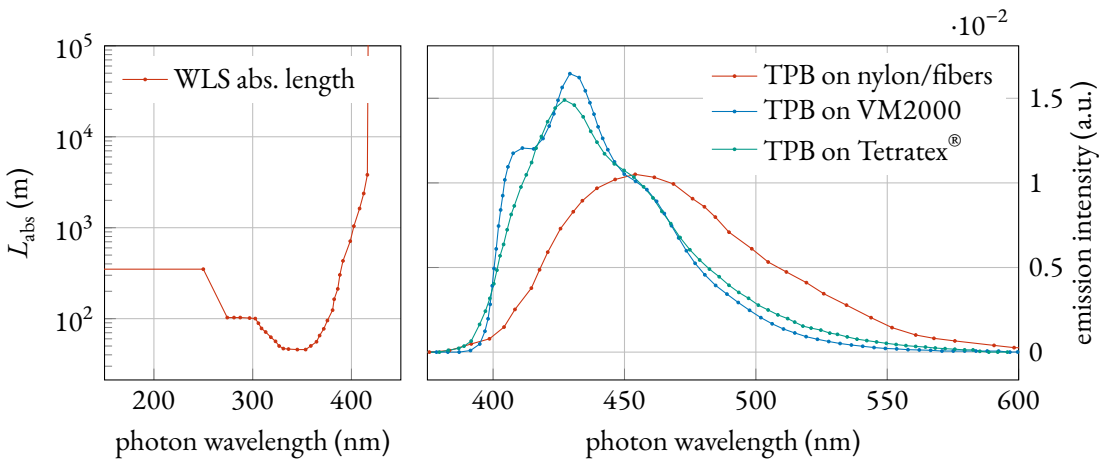


Figure C.6: Optical properties of Tetraphenyl-Butadiene (TPB) implemented in MAGE. On the left: the attenuation length of the wavelength-shifted light. On the right: emission spectrum.

The values are plot in fig. C.5, left.

WAVELENGTH SHIFTERS

Various surfaces in the GERDA setup are coated with a wavelength-shifting material in order to enhance the light collection efficiency and therefore the LAr veto cut efficiency. Tetraphenyl-Butadiene (TPB) is either evaporated on the surface pure or embedded in a polystyrene matrix. The concerned surfaces are the nylon mini-shrouds, the light-guiding fibers, the VM2000 and Tetratex® reflectors on the copper components of the LAr veto instrumentation (or simply copper shrouds in the following) and the PMTs glass window. The physical properties that define the wavelength-shifting process are the quantum efficiencies (average number of WLS photons emitted), the emission spectrum of the emitted WLS photons and their absorption length in the material. Since these properties depend on the substrate and other characteristics like the thickness or the deposition technique, multiple definitions of TPB are present in MAGE. The quantum efficiency depends on the layer thickness, so it should be measured for the specific sample. Since these measurements are not available, an arbitrary but realistic value of 1.2 is set. The WLS absorption length is another property for which no good data seems to be available in the literature. The implemented values are taken from [210] (fig. C.6, left). Other TPB properties which are common to all instances are the WLS emission time constant, which is set to an arbitrarily small value of 0.01 ns and the reflectivity which should be small but not zero (set to 0.2). The WLS emission spectrum changes upon the specific layer

TPB on nylon mini-shrouds. This WLS coating consists of TPB embedded in a polystyrene matrix (3:7 ratio TPB:polystyrene) and diluted in toluene (1:10). The solution is then brushed on the nylon. The emission spectrum has been measured [211] (see fig. C.6, right) and is similar to the one in reported [209] (fig. 14) for TPB in polystyrene matrix on glass.

TPB on VM2000. The copper shroud internal reflective surface is coated with evaporated TPB. The emission spectrum is taken from [209] (fig. C.6, right). The authors report the measurement of a ~ 160 μm thick TPB layer on VM2000 at an excitation wavelength of 128 nm and at 87 K, the same GERDA experimental conditions. The major differences brought in by the LAr

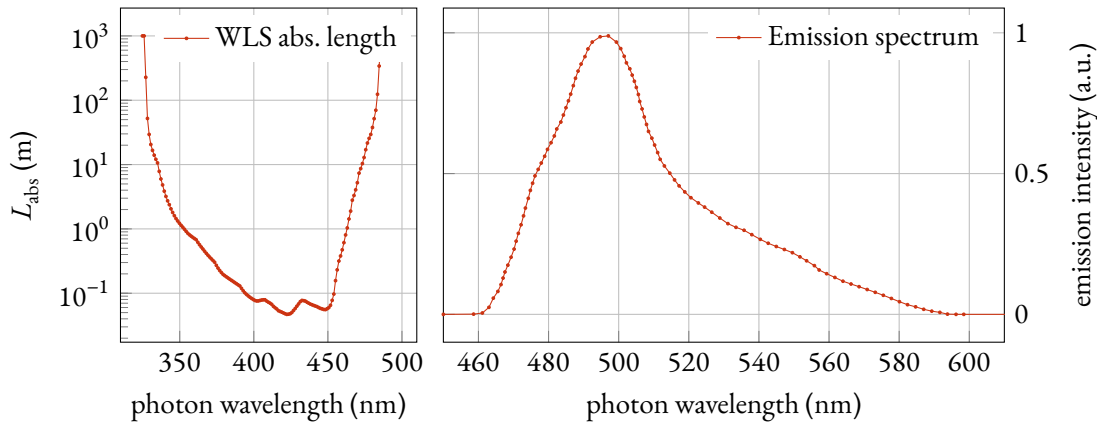


Figure C.7: Absorption length and emission spectrum of the wavelength-shifted light in the light-guiding fibers, as implemented in MAGE.

temperature are the vibronic structures that modify the shape of the spectrum.

TPB on fibers. No measurement is available here so the same emission spectrum defined for TPB on VM2000 is used. The TPB is evaporated.

TPB on Tetratex®. The Tetratex® is dip-coated (0.9 mg/cm^2 , $8 \mu\text{m}$ thickness) with TPB. The emission spectrum has been measured for GERDA [212] and is reported in fig. C.6, right. The measured sample has a TPB surface density of 0.17 mg/cm^2 . In principle the thickness affects the shape of the emission spectrum, as the efficiency of the reabsorption effect increases with the thickness of the layer. However, no relative measurements could be found at the time.

An essential part of the LAr veto system is the wavelength-shifting light-guiding fiber curtain. The fibers themselves are a Saint Gobain product (BCF-91A polystyrene fibers [213]), and consist of a core and two cladding layers with different refraction indices, to increase the light trapping efficiency, which is of about 3%. Photons interacting in the fiber are shifted to the green band of the optical spectrum, guided to the endpoints and collected by the SiPMs at the top. The fibers are coated with TPB, that shifts the VUV light to match the fiber absorption range.

The nylon mini-shrouds have the triple role of keeping ${}^{42}\text{K}$ ions out, being transparent to optical photons and eventually shift VUV photons to higher wavelengths. This capability is achieved by coating them with TPB.

BCF-91A polystyrene. Material of the fiber core. The data sheet from Saint Gobain [213] reports the absorption spectrum, knowing that the fibers are 1 mm thick one can extract the absorption length. Starting from the trivial relation:

$$1 - P(E) = e^{-x/l(E)}$$

where $P(E)$ is the probability (thus proportional to the absorption spectrum) for a photon travelling a distance x to be absorbed in the material. Given the attenuation length $l(E)$, one can

FIBER SHROUD
MINI-SHROUDS

extract $l(E)$ from $P(E)$. By integrating over the thickness of the material L one obtains:

$$L \cdot (1 - P(E)) = l(E) \cdot (1 - e^{-L/l(E)})$$

The problem now is that $l(E)$ cannot be extracted analytically (the expression is inhomogeneous). It can however be solved numerically. Since the units are arbitrary because the original absorption spectrum has arbitrary units, the spectrum has been then rescaled to match a measurement performed at 400 nm, which yielded 0.7 mm [214]. The result is shown in fig. C.7, left. The emission spectrum is taken again from [213] and shown in fig. C.7, right. The absorption length has been measured [214] and is set to 3.5 m. The WLS time constant, the refractive index have also been taken from [213]. The quantum efficiency is set to 1. The two cladding layers are made of PMMA. As only the refractive index is important, it is set to 1.49 for the inner cladding layer and to 1.42 for the outer layer [213].

Nylon mini-shrouds. The refraction index is set to 1.54, constant over incident photon wavelength. The attenuation length values are taken from [215], since GERDA is using the same material used for the BOREXINO balloon (fig. C.5, right).



D. Time distribution of α events

The time distribution of ^{210}Po decays is well known to be exponential. In the presence of a ^{210}Pb contamination, however, an additional constant contribution can also be observed. ^{210}Pb , decaying to ^{210}Po , feeds a constant ^{210}Po component once their decay rates stabilize in a secular equilibrium. To disentangle the two, a fit of the time distribution of events with energies between 3.5 MeV and 5.3 MeV observed in the GERDA data is performed, with a constant C and an exponential function:

$$f(t) = C + N \exp\left(-\frac{\log 2}{T_{1/2}} t\right),$$

where $T_{1/2} = (138.4 \pm 0.2)$ days is the half-life of ^{210}Po . A Poisson likelihood function corrected for data acquisition dead time [216] is used, in which the bin contents are modeled as follows:

$$\nu_i = f_i^{\text{LT}} \left\{ C \delta t + N \tau \left[\exp\left(-\frac{t_0 + i \delta t}{\tau}\right) - \exp\left(-\frac{t_0 + (i+1) \delta t}{\tau}\right) \right] \right\},$$

where C and N are the amplitudes of the constant and the exponentially-decaying components respectively and are the only two free fit parameters. f_i^{LT} is the live-time fraction in time-bin i which is estimated from injected test pulser events, δt is the time-bin width and $\tau = T_{1/2} / \log 2$.

The log-likelihood can be expressed as a sum:

$$\log \mathcal{L}_\alpha^{\text{time}}(C, N | n) = \sum_{i=1}^{N_{\text{bins}}} n_i \cdot \log \nu_i - \nu_i - \log n_i!.$$

Only detectors that were ON or in anti-coincidence mode¹ in the full data taking period have been selected. 27 BEGES, 5 SEMICoAXs and 4 InvCoAXs result eligible. In this way, bias due to selection or de-selection of particularly contaminated detectors is avoided. Furthermore, the initial data-taking period between December 2015 to January 2016 is excluded from the present analysis because of detector instabilities after the Phase II upgrade works. The analyzed data spans the period between the end of January 2016 to the end of November 2019 and is split into five data sets according to detector type (BEGE, SEMICoAX and InvCoAX) and experimental phase (Phase I and Phase II⁺).

¹Detectors in anti-coincidence mode are not well energy-calibrated and generally discarded in data analysis. Here, we are not interested in the precise energy of an event because the selected energy window is large with respect to a possible mis-calibration.

The fit results are shown in Figure D.1. For the BEGE data set, about half of the initial contamination decays exponentially, while for the SEMICOAX data set the ratio of N to C is about 5 to 1. After several ^{210}Po half-lives a stable rate of $\sim 1 \alpha/\text{day}$ is expected in either data set. A comparison between the fit results before and after the Phase II $^+$ upgrade demonstrates the achievement in detector handling techniques during the upgrade works. As a matter of fact, the constant fit component, representing the long-lived ^{210}Po contamination, is not affected by the manual intervention in 2018. Moreover, the initial level of ^{210}Pb is lower at the beginning of Phase II $^+$, compared to the beginning of Phase II. The α -emitter contamination at the InvCOAX surface, as one may notice also in fig. 3.10, is observed to be particularly low.



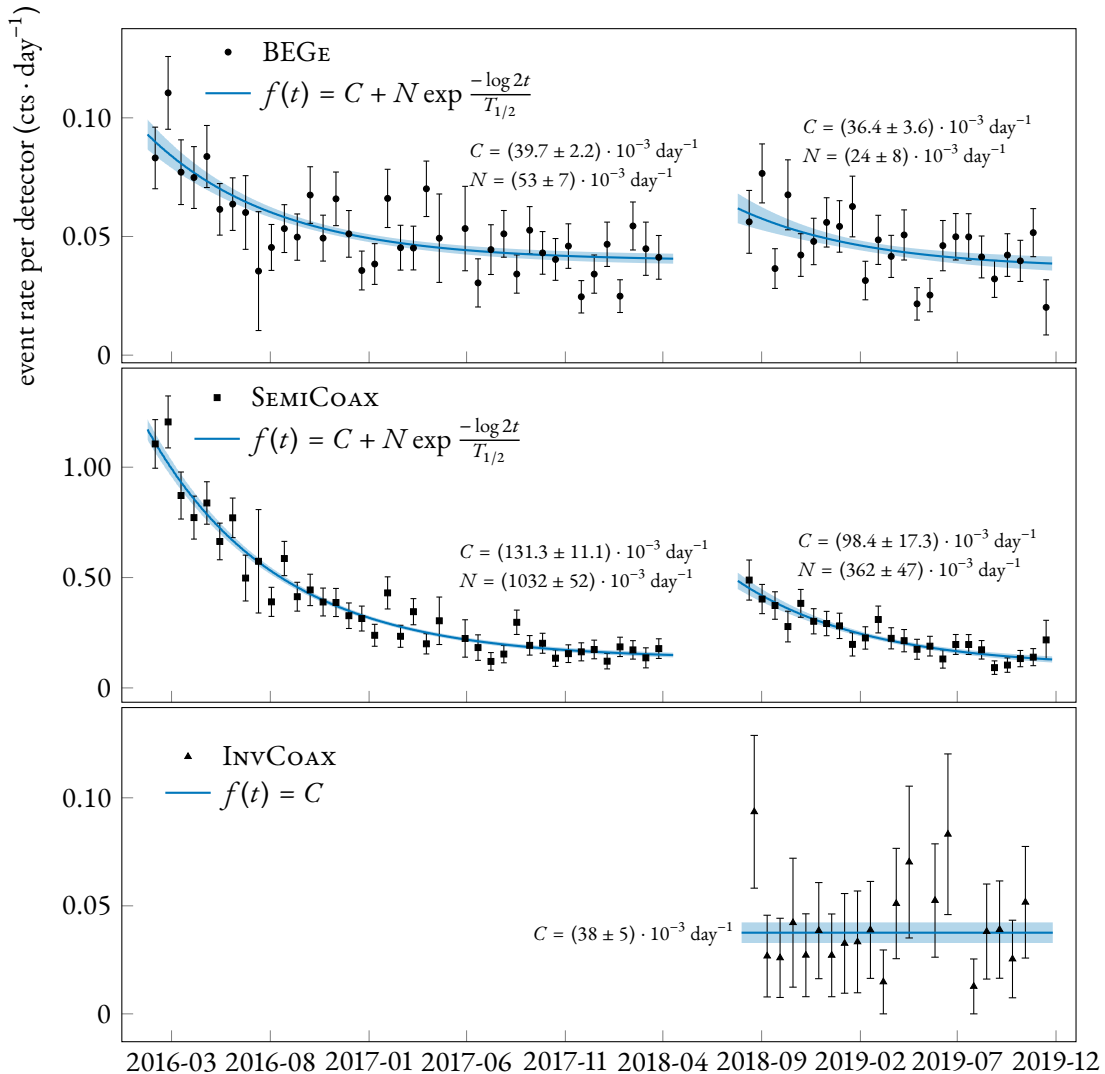


Figure D.1: α events time distribution in the [3.5, 5.4] MeV energy range during the whole Phase II data taking. Each data point correspond to events cumulated in 20 days of effective run time. Five data sets are considered: 27 BEGE detectors in Phase II and Phase II⁺ (top panel), 5 SEMICOAX detectors in Phase II and Phase II⁺, and 4 INVCOAX detectors in Phase II⁺ (bottom panel). An exponential model is fit to each data set and the results are overlaid on the plot.

E. Potassium tracking analysis plots

The results of the potassium tracking analysis of GERDA Phase II data described in §3.6 are reported here. The four series of plots that follow represent the background decomposition of potassium events classified according to the detectors in which an energy deposition was registered. Two models have been developed: a base model and an extended model including PDFs for each separate detector string. In figs. E.1 and E.2 the first two series of plots the results for single-detector and two-detector events in the base model are given. The two last series in figs. E.3 and E.4 refer to the extended model.

Some components are merged together to improve the readability: in the K40 plots combined components are shown for ^{42}K and ^{214}Bi , while ^{40}K sources are grouped in close (flat cables, holders, mini-shrouds) and far (fibers, SiPMs, copper shrouds, front-end electronics) locations from the detector array. To visualize the two-detector data a one-dimensional histogram has been obtained by summing together the projections on the two domain axes (index i and index j in eq. (3.3)) of the original two-dimensional histogram.



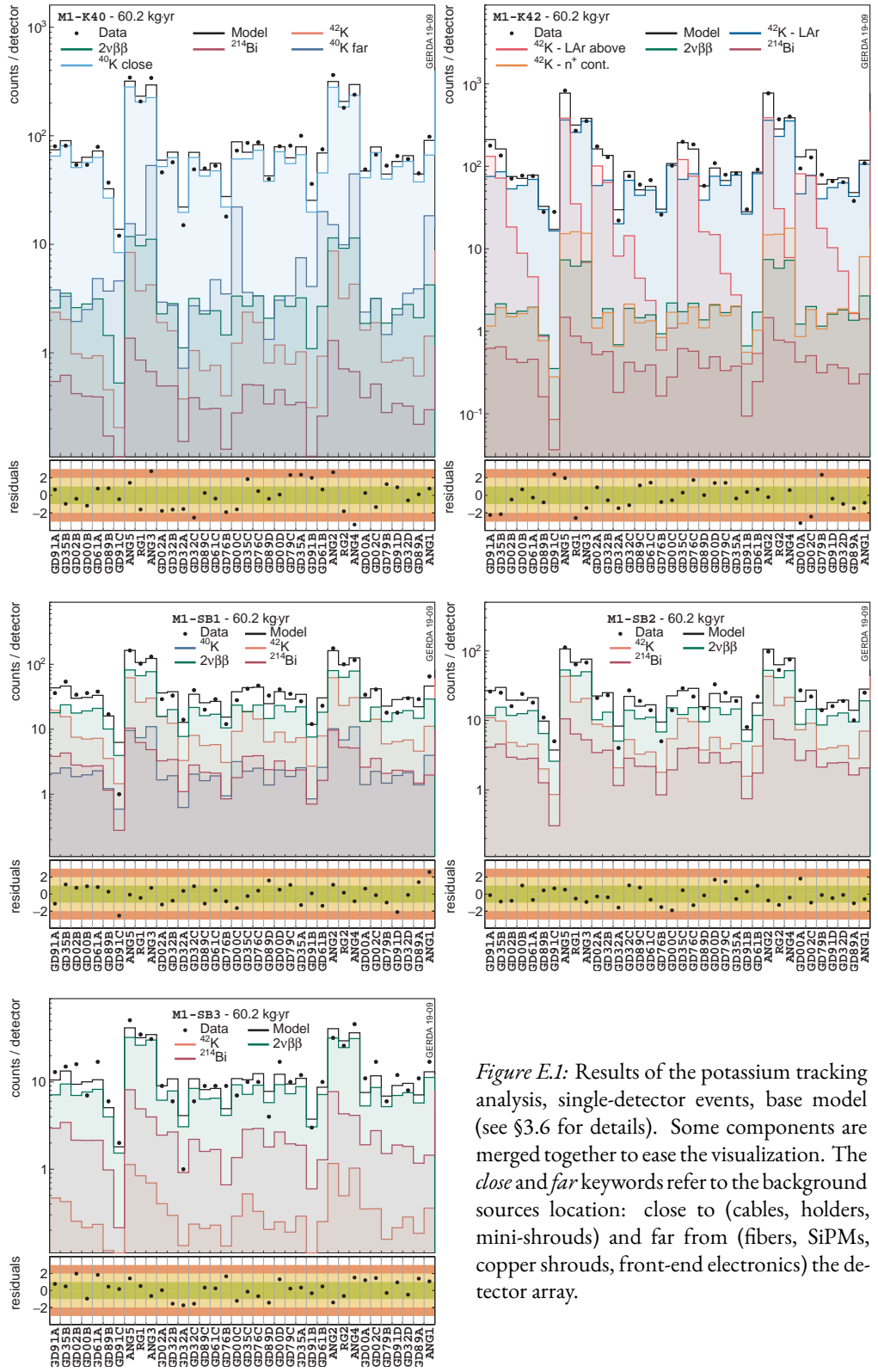


Figure E.1: Results of the potassium tracking analysis, single-detector events, base model (see §3.6 for details). Some components are merged together to ease the visualization. The *close* and *far* keywords refer to the background sources location: close to (cables, holders, mini-shrouds) and far from (fibers, SiPMs, copper shrouds, front-end electronics) the detector array.

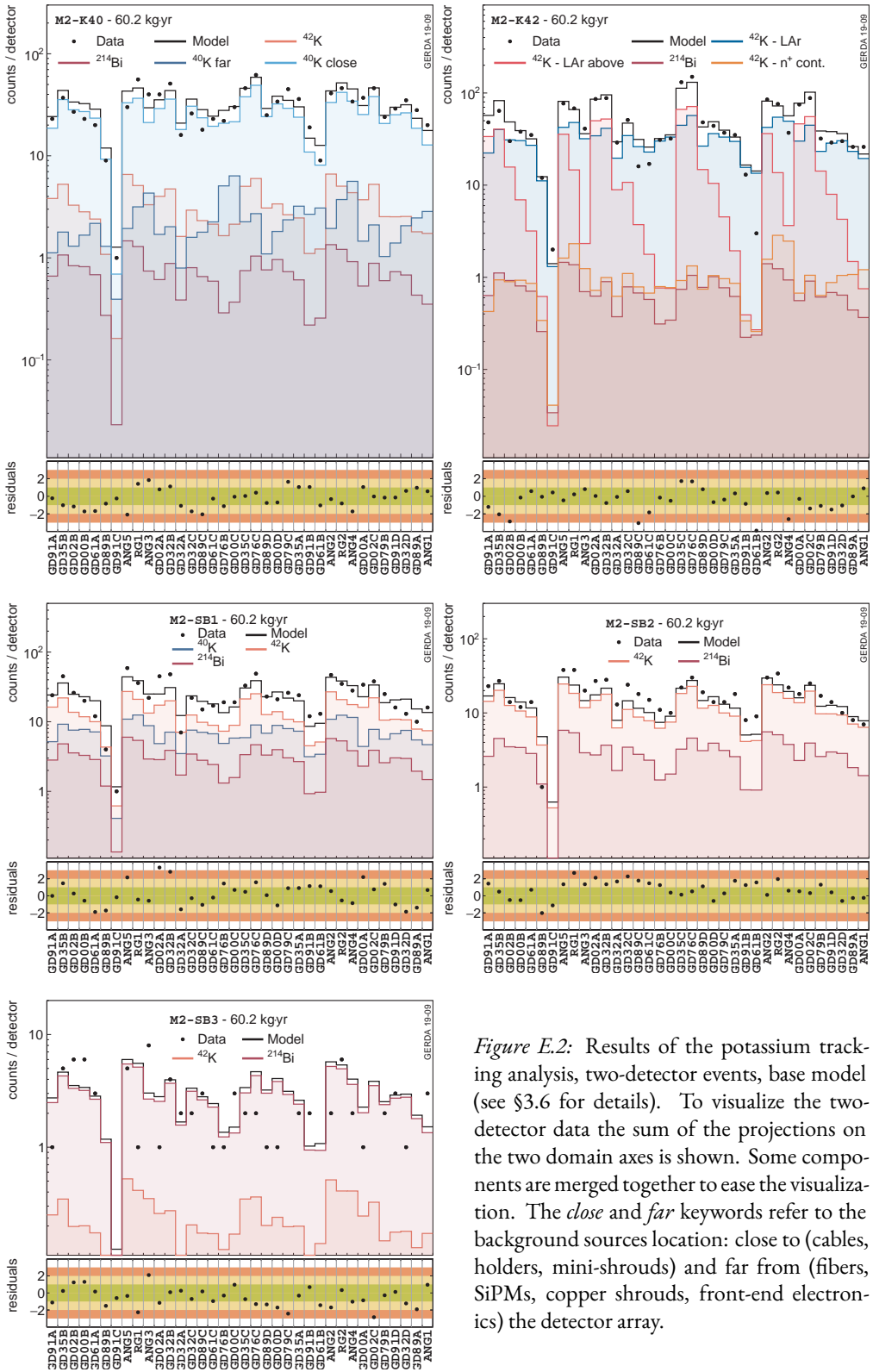


Figure E.2: Results of the potassium tracking analysis, two-detector events, base model (see §3.6 for details). To visualize the two-detector data the sum of the projections on the two domain axes is shown. Some components are merged together to ease the visualization. The *close* and *far* keywords refer to the background sources location: close to (cables, holders, mini-shrouds) and far from (fibers, SiPMs, copper shrouds, front-end electronics) the detector array.

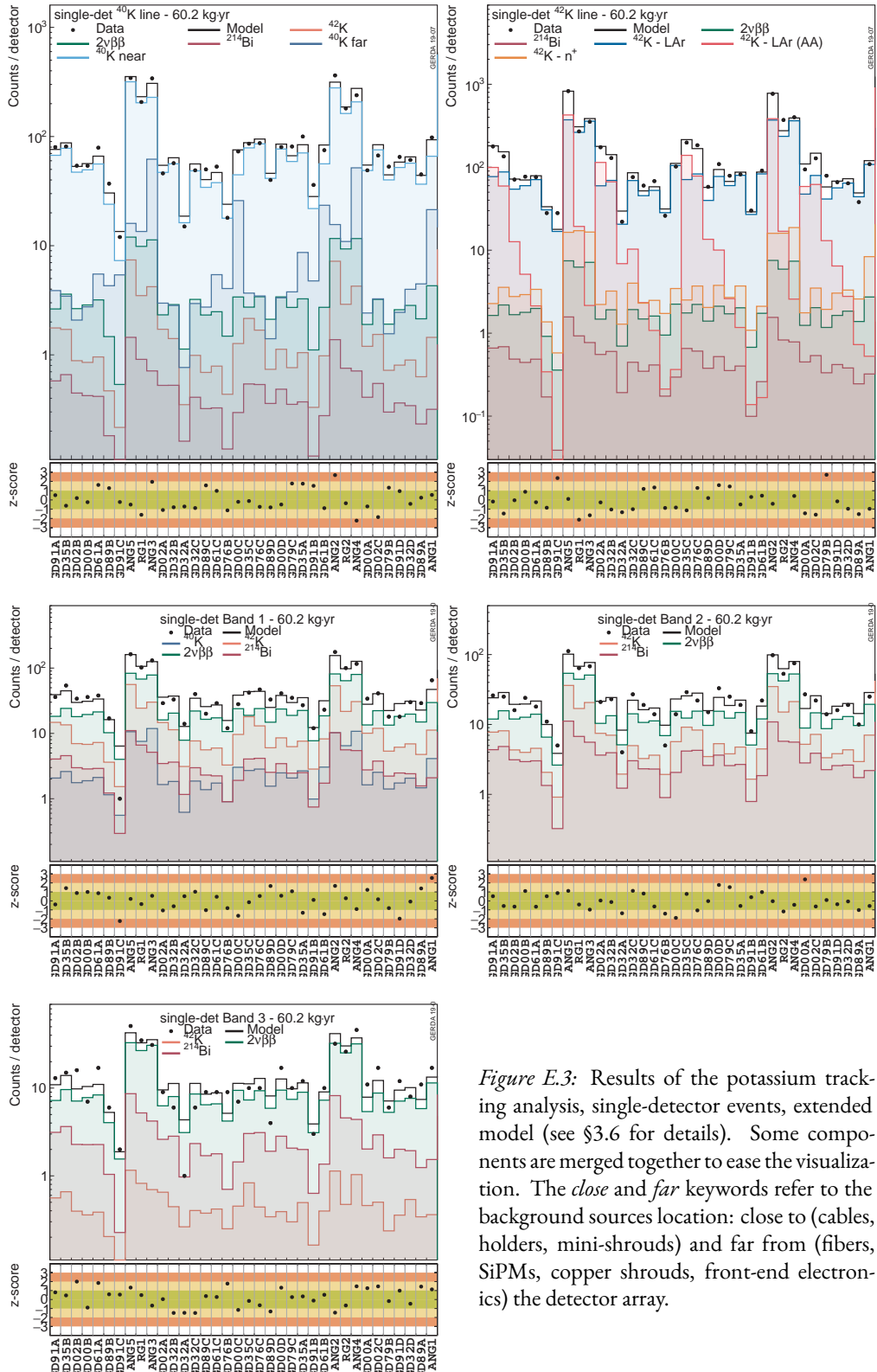


Figure E.3: Results of the potassium tracking analysis, single-detector events, extended model (see §3.6 for details). Some components are merged together to ease the visualization. The *close* and *far* keywords refer to the background sources location: close to (cables, holders, mini-shrouds) and far from (fibers, SiPMs, copper shrouds, front-end electronics) the detector array.

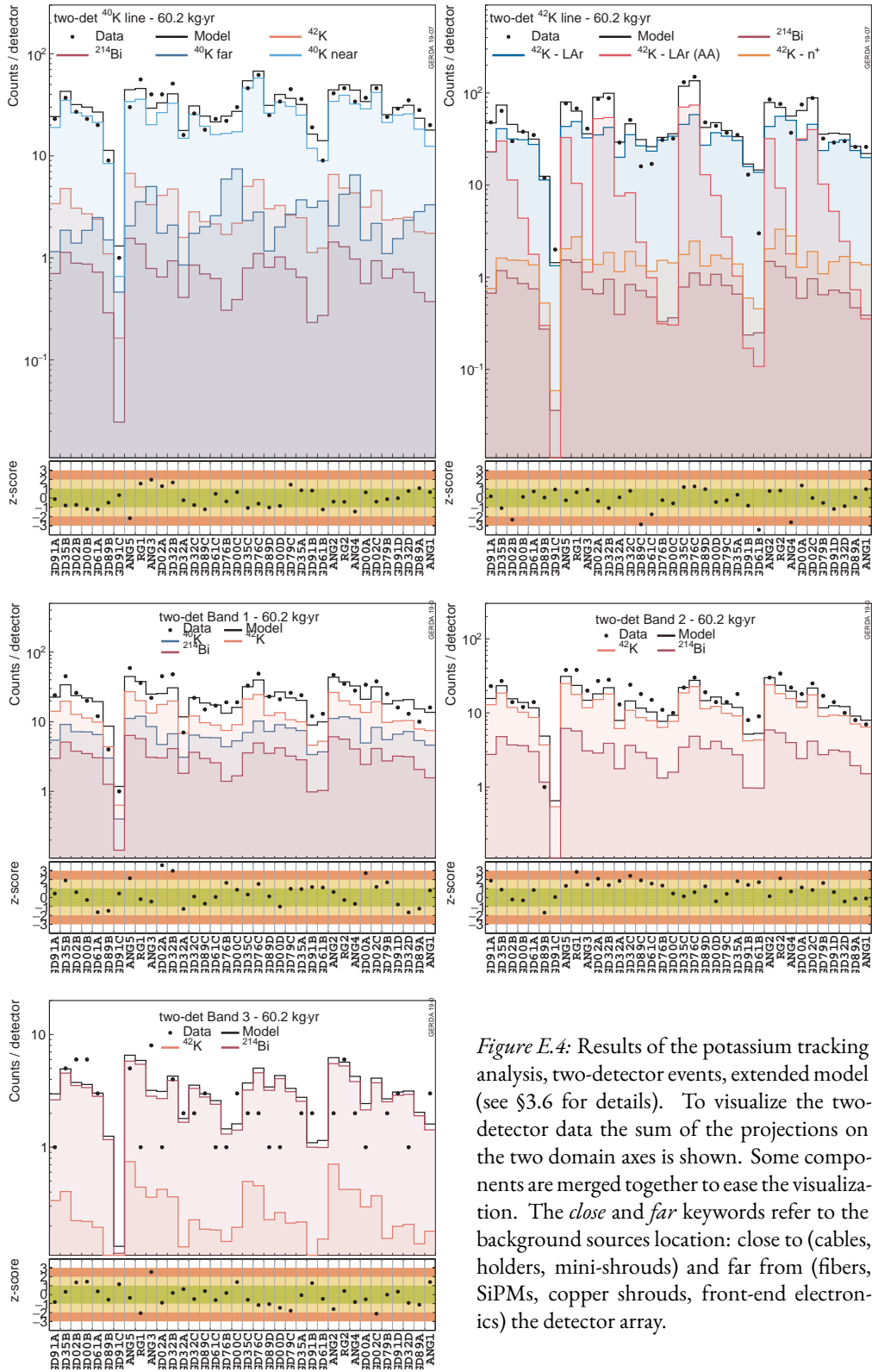


Figure E.4: Results of the potassium tracking analysis, two-detector events, extended model (see §3.6 for details). To visualize the two-detector data the sum of the projections on the two domain axes is shown. Some components are merged together to ease the visualization. The *close* and *far* keywords refer to the background sources location: close to (cables, holders, mini-shrouds) and far from (fibers, SiPMs, copper shrouds, front-end electronics) the detector array.

F. Bayesian blocks

The Bayesian block representation is a non-parametric representation of data derived with a Bayesian statistical procedure. The idea has been introduced by Jeffrey D. Scargle and applied in the context of astronomical time series analysis [217, 218]. As a generic (non-parametric) way to present data, the algorithm can be efficiently employed to discover local structures in background data by exploiting the full information brought in by the data itself and imposing few preconditions as possible on signal and background shapes. As it will be shown later, the algorithm is also able to handle arbitrary sampling and dynamic ranges of data. But perhaps the most appealing characteristic of the algorithm is that it operates in a Bayesian framework and therefore works with posterior probabilities.

The purpose of the Bayesian blocks algorithm is to construct a segmentation of a certain data interval into variable-sized blocks, each block containing consecutive data elements satisfying some well-defined criterion. Among all the possible segmentations, the *optimal* segmentation is defined as the one that maximizes some quantification of this criterion. The latter is represented by a likelihood (or fitness) function, which acts on a block k and depends exclusively on the data contained by the block. The fitness of the entire partition is then calculated as the product of each block fitness. The chosen fitness function will then depend on a certain set of parameters, in particular, the length spanned by the block (considering, for simplicity, one-dimensional data). Once the fitness function is defined, the algorithm will marginalize it with respect to all the other (nuisance) parameters, therefore obtaining the length of each single block, or the final data segmentation.

There is a considerable freedom in choosing the fitness function, relying on the concept of *sufficient statistics*. One of the simplest block model is perhaps the *piecewise constant model*, i.e. a constant representation of data within a block. In this example the fitness of a block depends on two parameters: the length and the height (nuisance parameter) of the block. The Cash statistics can be then employed to build the likelihood function. With a model $M(t, \theta)$ (the variable t represents the data, which is often time in applications of the Bayesian blocks), the unbinned log-likelihood \mathcal{L} reads:

$$\log \mathcal{L}(\theta) = \sum_n \log M(t_n, \theta) - \int M(t, \theta) dt$$

which, considering the piecewise constant model $M(t, \lambda) = \lambda$, becomes for block k :

$$\log \mathcal{L}^{(k)}(\lambda) = N^{(k)} \log \lambda - \lambda T^{(k)} .$$

When maximizing the expression with respect to the nuisance parameter λ (the height of the block), it

becomes

$$\log \mathcal{L}_{\max}^{(k)} = N^{(k)} (\log N^{(k)} - \log T^{(k)}) + N^{(k)}$$

The $N^{(k)}$ term sums up to N so it can be dropped because it's independent of the partition:

$$\log \mathcal{L}_{\max}^{(k)} = N^{(k)} (\log N^{(k)} - \log T^{(k)}) + \mathcal{N}^{(k)}.$$

The obtained fitness function has the appealing properties of being relatively simple and scale invariant. The fitness of the entire partition will then be the sum over the total number of blocks:

$$\log \mathcal{L} = \sum_k \log \mathcal{L}_{\max}^{(k)}$$

The next essential item in Bayesian statistics is the prior distribution, which must be chosen for each model parameter, in this case the total number of blocks N_{blocks} . A uniform prior on the number of blocks looks unreasonable, as most of the times one looks for a data segmentation where $N_{\text{blocks}} \ll N$, the total number of data points, rather than $N_{\text{blocks}} \approx N$. For example the *geometric* prior:

$$P(N_{\text{blocks}}) = \begin{cases} P_0 \gamma^{N_{\text{blocks}}} & 0 \leq N_{\text{blocks}} \leq N \\ 0 & \text{else} \end{cases}$$

has well-understood properties ($\gamma < 1$) and is simply implemented in the algorithm. The value of γ affects the representation but note that, however, sharply defined structures are retained. Objective procedures can be used to select the desired value of γ , which express the trade-off between conservative and liberal positions in letting faint data features emerge in the partition. In general, running the algorithm with a few different values of γ can be enough because the number of change-points in the partition is generally insensitive to a large range of reasonable values of the prior “steepness” parameter. This approach can be made rigorous by calibrating the prior as a function of the number of data points N and the false-positive (type-I error) rate p_0 on pure-noise toy experiments, as suggested in [218]. A calibration of this type performed there yields:

$$\log P(N, p_0) = \log(73.53 p_0 N^{-0.478}) - 4.$$

BINNING HISTOGRAMS

The Bayesian blocks algorithm was developed to be mainly applied to time series analyses (e.g. to spot light flux changes from astrophysical objects), but has advantages also in binning histograms, as shown in [219]. Compared to fixed-size bins, whose width is often *ad hoc*, Bayesian blocks surely are a more objective way to present data and to reveal shape features that could be hid by certain fixed-width binnings. Using Bayesian blocks to represent data in a statistical analysis could as instance avoid testing for systematics effects arising from the choice of the bin size. Compared to other optimal segmentation search rules (Knuth's rule, Scott's rule etc.), it has the feature of using variable-width blocks, and is therefore attractive when representing not homogeneously distributed data. An exhaustive comparison between this and similar segmentation schemes is presented in [219]. An example application of Bayesian blocks to Z_0 boson resonance data is reported here in fig. F.1.

IMPLEMENTATION

Sorting the optimality of 2^N data partitions is definitely not a quick task for a computer, when N is big. The central point of implementing an algorithm to compute Bayesian blocks is to follow

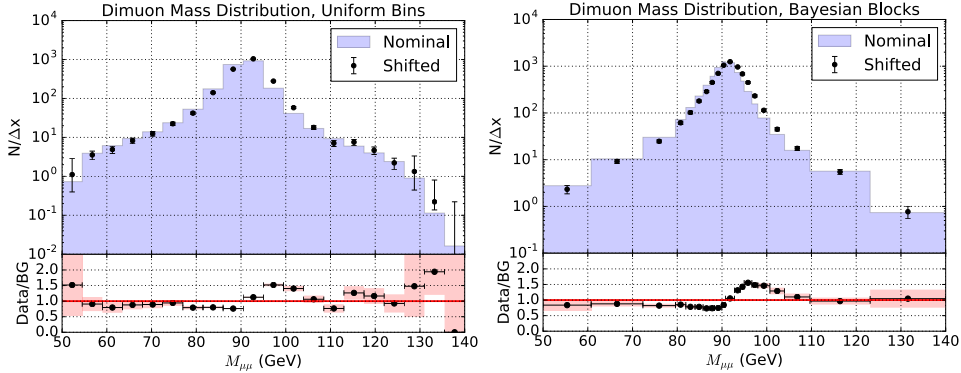


Figure F.1: Comparison of fixed-width binning and Bayesian blocks applied to the distribution of the invariant mass $M_{\mu\mu}$ of muon pairs produced at a hadron collider. A shift in the peak position between two data sets is clearly visible with Bayesian blocks. Taken from [219].

a *dynamic programming* approach, in the spirit of mathematical induction. In practice the data is first sorted in ascending order and the algorithm, starting from the first point, updates the optimal data partition at each added point using only the information from the previous steps. In this way, the algorithm complexity is reduced from $\mathcal{O}(2^N)$ to $\mathcal{O}(N^2)$. A possible pseudo code for the main iteration is the following:

```

for k in 1:N
    # define the (log) fitness function + (log) prior for a block
    # N(k,r) is the number of data points between point r and point k
    # T(k,r) is the distance between point r and point k
    F(r) = logfitness(N(k,r), T(k,r)) + log_prior
    # compute all possible configurations
    A = [F(r) + best[r-1] for r in 1:k]
    # save change-point with maximum fitness
    push!(last, indmax(A))
    # save maximum fitness value
    push!(best, maximum(A))
end

```

What the algorithm does when adding a given data point k is to check whether a new change-point should be added by considering a partition in which the last block contains data points from r to k , where $0 < r < k$. The total fitness is calculated for all data points up to k by adding the fitness of the last block $[r, k]$, to the best fitness calculated at step r . The maximum is saved (`last`), along with the fitness value (`best`). At the end of the iteration, the change-points can be reconstructed from the `last` array.

The GERDA data, which has a highly non-homogeneous event rate, benefits from being represented by Bayesian blocks. The following figure shows the invariant mass distribution $M_{\mu\mu}$ for the GERDA data, comparing uniform binning (left) and Bayesian blocks (right).

sented with Bayesian blocks, rather than fixed-width bins which are used by default. The results of the application of the algorithm to event energy data are displayed in fig. F.2. Since the algorithm naturally assigns wider blocks to less-populated regions, one can see how the binning is finer in the left part of the spectrum, dominated by ^{39}Ar and $2\nu\beta\beta$ events, and it gets more coarse in the α event-dominated region. Even finer binning is used for the high-statistics ^{40}K and ^{42}K lines. Bayesian blocks are also used to plot background model PDFs and calibration data, see e.g. figs. 2.11 and 3.2.



Julia code

The implementation of a routine that computes change points in an array of data applying the Bayesian blocks algorithm is available in C++ and Julia [197], at the following link:

<https://github.com/gipert/bayesian-blocks>

The C++ library ships with `bblocks`, a command line utility to re-bin ROOT [146] histograms. The Julia code is reported also in the following.

```

1 # bayesian_blocks.jl
2 #
3 # Author: Luigi Pertoldi - pertoldi@pd.infn.it
4 # Created: 29 Jun 2018
5 #
6 # The following software is distributed under the MIT licence
7 # http://www.opensource.org/licenses/mit-license.php
8 # Copyright (c) 2018 Luigi Pertoldi
9 #
10 # Use Julia >= v0.7!
11
12 using StatsBase, ProgressMeter
13
14 """
15     bayesian_blocks(data, logfitness=:cash, logprior=:p0, [gamma=0.01, p0=0.01])
16
17 Return an array of optimal change points for a set of one-dimensional data. This
18 is the implementation of the bayesian blocks algorithm, as outlined in [^1].
19
20 ## Arguments
21 * `data`: numeric array or a `StatsBase.Histogram`
22 * `logfitness`: log of the block fitness function to be used, choose between
23     [:cash]
24 * `logprior`: log of the prior distribution on the number of blocks to be used,
25     choose between [:gamma, :p0]
```

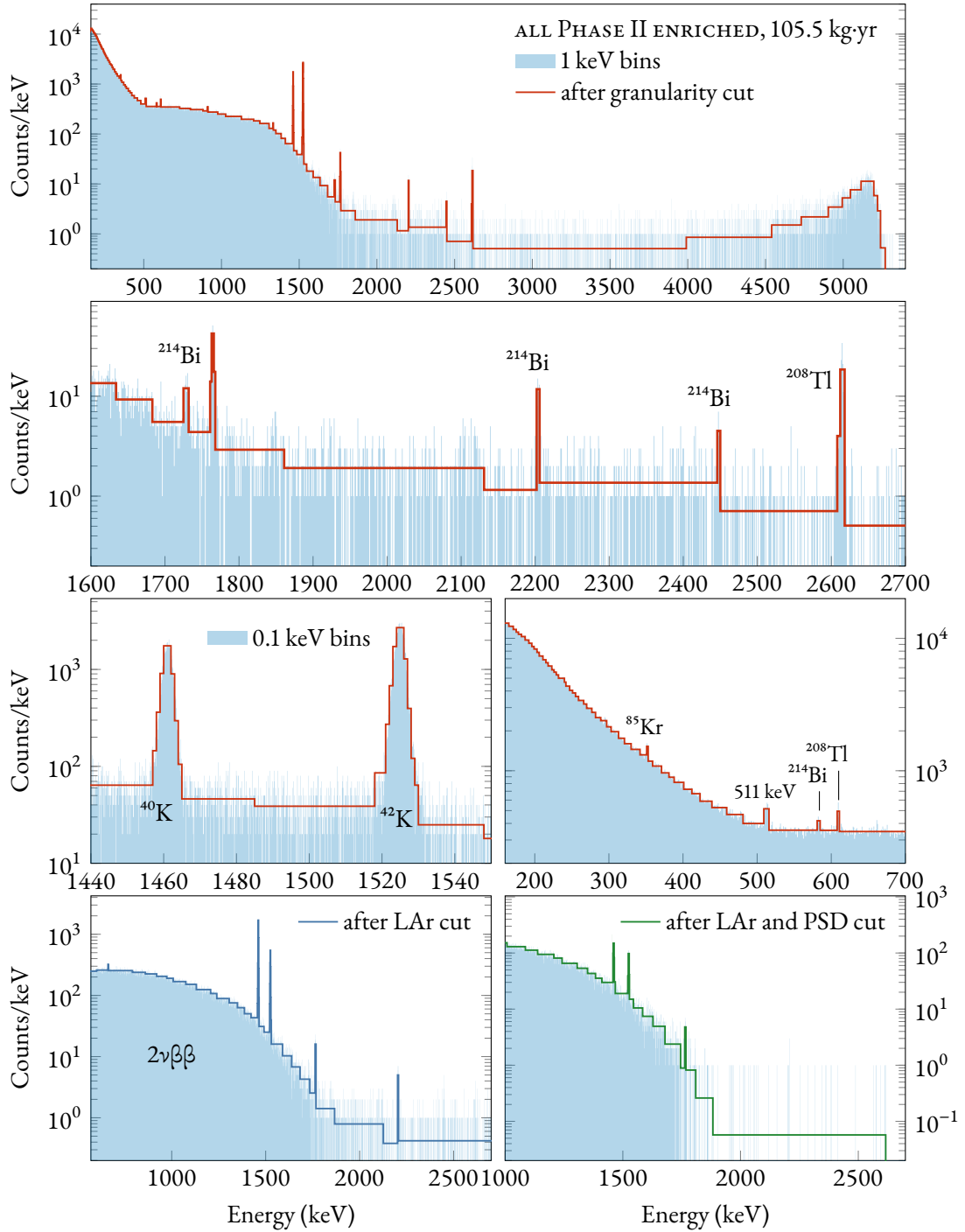


Figure F.2: Histograms of GERDA data with Bayesian blocks. Histograms binned with 0.1 keV-wide bins are provided as input to the algorithm with the prior calibration parameter $p_0 = 0.05$. In the three first rows, data after granularity cut. In the last row, data after LAr and PSD cut.

```

26 * `gamma`, `p0` ... : set the parameter value for the specified prior distribution
27
28 ## Example
29 ````julia
30 using Distributions, StatsBase, Plots, LinearAlgebra
31
32 data = vcat(rand(Normal(0),1000),rand(Cauchy(5),1000))
33 data = data[(data .> -5) .& (data .< 10)]
34
35 h = fit(Histogram, gerda, -5:100:10, closed = :left)
36
37 # choose to use all data or an histogram of it!
38 hb = normalize(fit(Histogram, data, bayesian_blocks(data), closed = :left))
39 hb = normalize(fit(Histogram, data, bayesian_blocks(h), closed = :left))
40
41 plot(data, st = :stephist, normalized = true, nbins=1000)
42 plot!(hb, st = :step, w = 3)
43 ````

44
45 ### Performance tips
46 You can convert your data container to a less precise representation to improve
47 the performance a bit, e.g.
48 ````julia
49 x::Array{Float32} = [1.1, π, √(5-1)/2]
50 ````

51
52 [^1]: Scargle, J et al. (2012) [https://arxiv.org/abs/1207.5578]
53 """
54 function bayesian_blocks(x;
55     logfitness::Symbol=:cash, logprior::Symbol=:p0,
56     gamma=0.01, p0=0.01)
57
58     if typeof(x) <: Array{<:Real,1}
59         # take care of repeated data
60         x_sorted = sort(x)
61         x_unique = [x_sorted[1]]
62         x_weight::Array{Int32} = [1]
63         for i in 2:length(x_sorted)
64             if x_sorted[i] == x_sorted[i-1]
65                 x_weight[end] += 1
66             else
67                 push!(x_unique, x_sorted[i])
68                 push!(x_weight, 1)
69             end
70         end
71     elseif typeof(x) <: Histogram{<:Integer,1}
72         v = collect(x.edges[1])
73         x_unique = [0.5 * (v[i] + v[i + 1]) for i = 1:length(v) - 1]
74         x_weight = x.weights

```

```

75
76      # delete empty bins
77      deleteat!(x_unique, findall(iszero, x_weight))
78      deleteat!(x_weight, findall(iszero, x_weight))
79  else
80      error("Unsupported input type: $(typeof(x))")
81  end
82
83  # final number of data points
84  N = length(x_unique)
85
86  # pre-defined (log)fitness functions
87  logf_dict = Dict(
88      :cash => (N_k, T_k) -> N_k * log(N_k/T_k)
89  )
90
91  # pre-defined (log)prior distributions on Nblocks
92  logp_dict = Dict(
93      # simple  $\gamma^{N\text{blocks}}$  prior
94      :gamma => (γ=gamma) -> log(γ),
95      # Note that there is a mistake in this equation in the original Scargle
96      # paper (the "log" was missing). The following corrected form is taken
97      # from https://arxiv.org/abs/1304.2818
98      :p0 => (Np=N, p=p0) -> log(73.53 * p * Np^(-0.478)) - 4
99  )
100
101 # check input
102 !haskey(logf_dict, logfitness) && error("$logfitness function not defined!")
103 !haskey(logp_dict, logprior) && error("$logprior function not defined!")
104
105 # save prior value for later computation
106 ncp_prior = logp_dict[logprior]()
107
108 # array of (all possible) block edges
109 edges = vcat(x_unique[1],
110               0.5f0(x_unique[1:end-1]+x_unique[2:end]),
111               x_unique[end])
112
113 # see Sec. 2.6 in [^1]
114 best = Number[]
115 last = Number[]
116
117 # display progress bar for long computations
118 # total number of steps:  $\Sigma n(n-1) = N(N^2-1)/3$ 
119 p = Progress(Integer(N*(N^2-1)/3), 2); m = 0
120
121 for k in 1:N
122     # define nice alias to mimic the notation used in [^1]
123     F(r) = logf_dict[logfitness](cumsum(x_weight[r:k])[end], edges[k+1] -

```

```

edges[r]) + ncp_prior
124
125      # compute all possible configurations (Eq. (8) in [^1])
126      A = [F(r) + (r == 1 ? 0 : best[r-1]) for r in 1:k]
127
128      # save best configuration
129      push!(last, argmax(A))
130      push!(best, maximum(A))
131
132      update!(p, m += k*(k-1))
133 end
134
135 # extract changepoints by iteratively peeling off the last block
136 cp = Number[]
137 i = N+1
138 while i != 0
139     push!(cp, i)
140     i = (i == 1 ? 0 : last[i-1])
141 end
142
143 return [edges[j] for j in cp[end:-1:1]]
144 end

```

Bibliography

- [1] C. L. Cowan et al. *Science* 124.3212 (1956), pp. 103–104. doi: [10.1126/science.124.3212.103](https://doi.org/10.1126/science.124.3212.103)
- [2] E. Majorana. *Il Nuovo Cimento* 9.10 (1932), pp. 335–344. doi: [10.1007/BF02959557](https://doi.org/10.1007/BF02959557)
- [3] E. Fiorini et al. (MILANO Collaboration). *Phys. Lett.* 25B (1967). [,662(1967)], pp. 602–603. doi: [10.1016/0370-2693\(67\)90127-X](https://doi.org/10.1016/0370-2693(67)90127-X)
- [4] L. M. Brown. *Physics Today* 31.9 (1978), pp. 23–28. doi: [10.1063/1.2995181](https://doi.org/10.1063/1.2995181)
- [5] Y. Fukuda et al. (SUPER-KAMIOKANDE Collaboration). *Phys. Rev. Lett.* 81.8 (1998), pp. 1562–1567. doi: [10.1103/physrevlett.81.1562](https://doi.org/10.1103/physrevlett.81.1562). ARXIV: [hep-ex/9807003 \[hep-ex\]](https://arxiv.org/abs/hep-ex/9807003)
- [6] Q. R. Ahmad et al. (SNO Collaboration). *Phys. Rev. Lett.* 89.1 (2002). doi: [10.1103/physrevlett.89.011301](https://doi.org/10.1103/physrevlett.89.011301). ARXIV: [nucl-ex/0204008 \[nucl-ex\]](https://arxiv.org/abs/nucl-ex/0204008)
- [7] K. Eguchi et al. (KAMLAND Collaboration). *Phys. Rev. Lett.* 90.2 (2003). doi: [10.1103/physrevlett.90.021802](https://doi.org/10.1103/physrevlett.90.021802). ARXIV: [hep-ex/0212021 \[hep-ex\]](https://arxiv.org/abs/hep-ex/0212021)
- [8] T. Kajita. *Rev. Mod. Phys.* 88.3 (2016). doi: [10.1103/revmodphys.88.030501](https://doi.org/10.1103/revmodphys.88.030501)
- [9] A. B. McDonald. *Rev. Mod. Phys.* 88.3 (2016). doi: [10.1103/revmodphys.88.030502](https://doi.org/10.1103/revmodphys.88.030502)
- [10] J. Schechter and J. W. F. Valle. *Phys. Rev. D* 25 (1982), pp. 2951–2954. doi: [10.1103/PhysRevD.25.2951](https://doi.org/10.1103/PhysRevD.25.2951)
- [11] M. Goeppert-Mayer. *Phys. Rev.* 48 (1935), pp. 512–516. doi: [10.1103/PhysRev.48.512](https://doi.org/10.1103/PhysRev.48.512)
- [12] C. Giunti and Chung W. Kim. Oxford University Press, 2007
- [13] T. Tomoda. *Rep. Prog. Phys.* 54.1 (1991), p. 53. doi: [10.1088/0034-4885/54/1/002](https://doi.org/10.1088/0034-4885/54/1/002)
- [14] W. C. Haxton and G. J. Stephenson. *Prog. Part. Nucle. Phys.* 12 (1984), pp. 409–479. doi: [10.1016/0146-6410\(84\)90006-1](https://doi.org/10.1016/0146-6410(84)90006-1)
- [15] J. Kotila and F. Iachello. *Phys. Rev. C* 85.3 (2012). doi: [10.1103/physrevc.85.034316](https://doi.org/10.1103/physrevc.85.034316). ARXIV: [1209.5722 \[nucl-th\]](https://arxiv.org/abs/1209.5722)
- [16] S. Stoica and M. Mirea. *Phys. Rev. C* 88.3 (2013). doi: [10.1103/physrevc.88.037303](https://doi.org/10.1103/physrevc.88.037303). ARXIV: [1307.0290 \[nucl-th\]](https://arxiv.org/abs/1307.0290)
- [17] J. Engel and J. Menéndez. *Rep. Prog. Phys.* 80.4 (2017), p. 046301. doi: [10.1088/1361-6633/aa5bc5](https://doi.org/10.1088/1361-6633/aa5bc5). ARXIV: [1610.06548 \[nucl-th\]](https://arxiv.org/abs/1610.06548)
- [18] J. M. Yao et al. *Phys. Rev. Lett.* 124.23 (2020), p. 232501. doi: [10.1103/PhysRevLett.124.232501](https://doi.org/10.1103/PhysRevLett.124.232501). ARXIV: [1908.05424 \[nucl-th\]](https://arxiv.org/abs/1908.05424)
- [19] Jouni T. Suhonen. *Front. in Phys.* 5 (2017), p. 55. doi: [10.3389/fphy.2017.00055](https://doi.org/10.3389/fphy.2017.00055). ARXIV: [1712.01565 \[nucl-th\]](https://arxiv.org/abs/1712.01565)

- [20] J. Menendez, D. Gazit, and A. Schwenk. *Phys. Rev. Lett.* 107 (2011), p. 062501. doi: [10.1103/PhysRevLett.107.062501](https://doi.org/10.1103/PhysRevLett.107.062501). ARXIV: [1103.3622 \[nucl-th\]](https://arxiv.org/abs/1103.3622)
- [21] J. Engel, F. Simkovic, and P. Vogel. *Phys. Rev. C* 89.6 (2014), p. 064308. doi: [10.1103/PhysRevC.89.064308](https://doi.org/10.1103/PhysRevC.89.064308). ARXIV: [1403.7860 \[nucl-th\]](https://arxiv.org/abs/1403.7860)
- [22] A. Ekström et al. *Phys. Rev. Lett.* 113.26 (2014), p. 262504. doi: [10.1103/PhysRevLett.113.262504](https://doi.org/10.1103/PhysRevLett.113.262504). ARXIV: [1406.4696 \[nucl-th\]](https://arxiv.org/abs/1406.4696)
- [23] A. Gando et al. *Phys. Rev. Lett.* 122.19 (2019). doi: [10.1103/physrevlett.122.192501](https://doi.org/10.1103/physrevlett.122.192501). ARXIV: [1901.03871 \[hep-ex\]](https://arxiv.org/abs/1901.03871)
- [24] H. Primakoff and S. P. Rosen. *Rep. Prog. Phys.* 22.1 (1959), p. 121. doi: [10.1088/0034-4885/22/1/305](https://doi.org/10.1088/0034-4885/22/1/305)
- [25] V.I. Tretyak and Yu. G. Zdesenko. *Atom. Data Nucl. Data* 61.1 (1995), pp. 43–90. doi: [10.1016/S0092-640X\(95\)90011-X](https://doi.org/10.1016/S0092-640X(95)90011-X)
- [26] V. I. Tretyak and Yu. G. Zdesenko. *Atom. Data Nucl. Data* 80.1 (2002), pp. 83–116. doi: [10.1006/adnd.2001.0873](https://doi.org/10.1006/adnd.2001.0873)
- [27] M. Agostini et al. (GERDA Collaboration). *Eur. Phys. J. C* 75.9 (2015), p. 416. doi: [10.1140/epjc/s10052-015-3627-y](https://doi.org/10.1140/epjc/s10052-015-3627-y). ARXIV: [1501.02345 \[nucl-ex\]](https://arxiv.org/abs/1501.02345)
- [28] E. Armengaud et al. *Eur. Phys. J. C* 80.7 (2020), p. 674. doi: [10.1140/epjc/s10052-020-8203-4](https://doi.org/10.1140/epjc/s10052-020-8203-4). ARXIV: [1912.07272 \[nucl-ex\]](https://arxiv.org/abs/1912.07272)
- [29] O. Azzolini et al. *Phys. Rev. Lett.* 123.26 (2019), p. 262501. doi: [10.1103/PhysRevLett.123.262501](https://doi.org/10.1103/PhysRevLett.123.262501). ARXIV: [1909.03397 \[nucl-ex\]](https://arxiv.org/abs/1909.03397)
- [30] A. Caminata. *Universe* 5.1 (2019), p. 10. doi: [10.3390/universe5010010](https://doi.org/10.3390/universe5010010)
- [31] J.B. Albert et al. (EXO-200 Collaboration). *Phys. Rev. C* 89.1 (2014), p. 015502. doi: [10.1103/PhysRevC.89.015502](https://doi.org/10.1103/PhysRevC.89.015502). ARXIV: [1306.6106 \[nucl-ex\]](https://arxiv.org/abs/1306.6106)
- [32] W. H. Furry. *Phys. Rev.* 56 (1939), pp. 1184–1193. doi: [10.1103/PhysRev.56.1184](https://doi.org/10.1103/PhysRev.56.1184)
- [33] S. Weinberg. *Phys. Rev. Lett.* 43 (1979), pp. 1566–1570. doi: [10.1103/PhysRevLett.43.1566](https://doi.org/10.1103/PhysRevLett.43.1566)
- [34] A. D. Sakharov. *Sov. Phys. Uspekhi* 34.5 (1991), pp. 392–393. doi: [10.1070/pu1991v034n05abeh002497](https://doi.org/10.1070/pu1991v034n05abeh002497)
- [35] W. Buchmuller, R. D. Peccei, and T. Yanagida. *Ann. Rev. Nucl. Part. Sci.* 55 (2005), pp. 311–355. doi: [10.1146/annurev.nucl.55.090704.151558](https://doi.org/10.1146/annurev.nucl.55.090704.151558). ARXIV: [hep-ph/0502169](https://arxiv.org/abs/hep-ph/0502169)
- [36] P.A. Zyla et al. (PARTICLE DATA GROUP Collaboration). *PTEP* 2020.8 (2020), p. 083C01. doi: [10.1093/ptep/ptaa104](https://doi.org/10.1093/ptep/ptaa104)
- [37] N. Aghanim et al. (PLANCK Collaboration). *arXiv e-prints* (2018). ARXIV: [1807.06209 \[astro-ph.CO\]](https://arxiv.org/abs/1807.06209)
- [38] M. Fukugita and T. Yanagida. *Phys. Lett. B* 174.1 (1986), pp. 45–47. doi: [10.1016/0370-2693\(86\)91126-3](https://doi.org/10.1016/0370-2693(86)91126-3)
- [39] W. Rodejohann. *Int. J. Mod. Phys. E* 20 (2011), pp. 1833–1930. doi: [10.1142/S0218301311020186](https://doi.org/10.1142/S0218301311020186). ARXIV: [1106.1334 \[hep-ph\]](https://arxiv.org/abs/1106.1334)
- [40] E. Ma. *Phys. Rev. Lett.* 81 (1998), pp. 1171–1174. doi: [10.1103/PhysRevLett.81.1171](https://doi.org/10.1103/PhysRevLett.81.1171). ARXIV: [hep-ph/9805219](https://arxiv.org/abs/hep-ph/9805219)
- [41] R. N. Mohapatra and G. Senjanovic. *Phys. Rev. Lett.* 44 (1980), p. 912. doi: [10.1103/PhysRevLett.44.912](https://doi.org/10.1103/PhysRevLett.44.912)

- [42] I. Esteban et al. (NuFIT Collaboration). *J. High Energy Phys.* 2019.1 (2019). doi: [10.1007/JHEP01\(2019\)106](https://doi.org/10.1007/JHEP01(2019)106). ARXIV: [1811.05487 \[hep-ph\]](https://arxiv.org/abs/1811.05487)
- [43] S. Hannestad and T. Schwetz. *J. Cosmol. Astropart. P.* 2016.11 (2016), pp. 035–035. doi: [10.1088/1475-7516/2016/11/035](https://doi.org/10.1088/1475-7516/2016/11/035). ARXIV: [1606.04691 \[astro-ph.CO\]](https://arxiv.org/abs/1606.04691)
- [44] T. Schwetz et al. *arXiv e-prints* (2017). ARXIV: [1703.04585 \[astro-ph.CO\]](https://arxiv.org/abs/1703.04585)
- [45] S. Gariazzo et al. *J. Cosmol. Astropart. P.* 2018.03 (2018), pp. 011–011. doi: [10.1088/1475-7516/2018/03/011](https://doi.org/10.1088/1475-7516/2018/03/011). ARXIV: [1801.04946 \[hep-ph\]](https://arxiv.org/abs/1801.04946)
- [46] K. J. Kelly et al. (2020). ARXIV: [2007.08526 \[hep-ph\]](https://arxiv.org/abs/2007.08526)
- [47] I. Esteban et al. (2020). ARXIV: [2007.14792 \[hep-ph\]](https://arxiv.org/abs/2007.14792)
- [48] M. Gerbino and M. Lattanzi. *Front. Phys.* 5 (2018). doi: [10.3389/fphy.2017.00070](https://doi.org/10.3389/fphy.2017.00070)
- [49] M. Aker et al. (KATRIN Collaboration). *Phys. Rev. Lett.* 123 (2019), p. 221802. doi: [10.1103/PhysRevLett.123.221802](https://doi.org/10.1103/PhysRevLett.123.221802). ARXIV: [1909.06048 \[hep-ex\]](https://arxiv.org/abs/1909.06048)
- [50] L. Gastaldo. 2018. doi: [10.5281/zenodo.1286950](https://doi.org/10.5281/zenodo.1286950)
- [51] B. Alpert et al. (HOLMES Collaboration). *Eur. Phys. J. C* 75.3 (2015), p. 112. doi: [10.1140/epjc/s10052-015-3329-5](https://doi.org/10.1140/epjc/s10052-015-3329-5). ARXIV: [1412.5060 \[physics.ins-det\]](https://arxiv.org/abs/1412.5060)
- [52] A. Caldwell et al. *Phys. Rev. D* 96.7 (2017). doi: [10.1103/physrevd.96.073001](https://doi.org/10.1103/physrevd.96.073001). ARXIV: [1705.01945 \[hep-ph\]](https://arxiv.org/abs/1705.01945)
- [53] M. Agostini, G. Benato, and J.A. Detwiler. *Phys. Rev. D* 96.5 (2017). doi: [10.1103/physrevd.96.053001](https://doi.org/10.1103/physrevd.96.053001). ARXIV: [1705.02996 \[hep-ex\]](https://arxiv.org/abs/1705.02996)
- [54] S. Ge, W. Rodejohann, and K. Zuber. *Phys. Rev. D* 96.5 (2017). doi: [10.1103/physrevd.96.055019](https://doi.org/10.1103/physrevd.96.055019). ARXIV: [1707.07904 \[hep-ph\]](https://arxiv.org/abs/1707.07904)
- [55] M. J. Dolinski, A. W. P. Poon, and W. Rodejohann. *Annu. Rev. Nucl. Part. S.* 69.1 (2019), pp. 219–251. doi: [10.1146/annurev-nucl-101918-023407](https://doi.org/10.1146/annurev-nucl-101918-023407). ARXIV: [1902.04097 \[nucl-ex\]](https://arxiv.org/abs/1902.04097)
- [56] J.M. Yao. 2020. ARXIV: [2008.13249 \[nucl-th\]](https://arxiv.org/abs/2008.13249)
- [57] Y. Kermaidić. 2020. doi: [10.5281/zenodo.3959593](https://doi.org/10.5281/zenodo.3959593)
- [58] M. Agostini et al. (GERDA Collaboration). *Phys. Rev. Lett.* (2020). To appear. ARXIV: [2009.06079 \[nucl-ex\]](https://arxiv.org/abs/2009.06079)
- [59] S. I. Alvis et al. (MAJORANA Collaboration). *Phys. Rev. C* 100.2 (2019), p. 025501. doi: [10.1103/PhysRevC.100.025501](https://doi.org/10.1103/PhysRevC.100.025501). ARXIV: [1902.02299 \[nucl-ex\]](https://arxiv.org/abs/1902.02299)
- [60] E. Andreotti et al. *Astropart. Phys.* 34 (2011), pp. 822–831. doi: [10.1016/j.astropartphys.2011.02.002](https://doi.org/10.1016/j.astropartphys.2011.02.002). ARXIV: [1012.3266 \[nucl-ex\]](https://arxiv.org/abs/1012.3266)
- [61] K. Alfonso et al. (CUORE Collaboration). *Phys. Rev. Lett.* 115.10 (2015), p. 102502. doi: [10.1103/PhysRevLett.115.102502](https://doi.org/10.1103/PhysRevLett.115.102502). ARXIV: [1504.02454 \[nucl-ex\]](https://arxiv.org/abs/1504.02454)
- [62] D. Q. Adams et al. (CUORE Collaboration). *Phys. Rev. Lett.* 124.12 (2020), p. 122501. doi: [10.1103/PhysRevLett.124.122501](https://doi.org/10.1103/PhysRevLett.124.122501). ARXIV: [1912.10966 \[nucl-ex\]](https://arxiv.org/abs/1912.10966)
- [63] G. Anton et al. (EXO-200 Collaboration). *Phys. Rev. Lett.* 123.16 (2019), p. 161802. doi: [10.1103/PhysRevLett.123.161802](https://doi.org/10.1103/PhysRevLett.123.161802). ARXIV: [1906.02723 \[hep-ex\]](https://arxiv.org/abs/1906.02723)
- [64] A. Gando et al. (KAMLAND-ZEN Collaboration). *Phys. Rev. Lett.* 117.8 (2016). [Addendum: *Phys. Rev. Lett.* 117, no.10, 109903(2016)], p. 082503. doi: [10.1103/PhysRevLett.117.082503](https://doi.org/10.1103/PhysRevLett.117.082503). ARXIV: [1605.02889 \[hep-ex\]](https://arxiv.org/abs/1605.02889)
- [65] Y. Chikashige, R. N. Mohapatra, and R. D. Peccei. *Phys. Lett. B* 98.4 (1981), pp. 265–268. doi: [10.1016/0370-2693\(81\)90011-3](https://doi.org/10.1016/0370-2693(81)90011-3)

- [66] J. Schechter and J. W. F. Valle. *Phys. Rev. D* 25 (1982), pp. 774–783. doi: [10.1103/PhysRevD.25.774](https://doi.org/10.1103/PhysRevD.25.774)
- [67] G. B. Gelmini and M. Roncadelli. *Phys. Lett. B* 99.5 (1981), pp. 411–415. doi: [10.1016/0370-2693\(81\)90559-1](https://doi.org/10.1016/0370-2693(81)90559-1)
- [68] H. M. Georgi, S. L. Glashow, and S. Nussinov. *Nucl. Phys. B* 193.2 (1981), pp. 297–316. doi: [10.1016/0550-3213\(81\)90336-9](https://doi.org/10.1016/0550-3213(81)90336-9)
- [69] R. N. Mohapatra and P. B Pal. 3rd. World Scientific, 2004. doi: [10.1142/5024](https://doi.org/10.1142/5024)
- [70] Z. G. Berezhiani, A.Yu. Smirnov, and J. W. F. Valle. *Phys. Lett. B* 291.1 (1992), pp. 99–105. doi: [10.1016/0370-2693\(92\)90126-0](https://doi.org/10.1016/0370-2693(92)90126-0). ARXIV: [hep-ph/9207209 \[hep-ph\]](https://arxiv.org/abs/hep-ph/9207209)
- [71] C. P. Burgess and J. M. Cline. *Phys. Lett. B* 298.1 (1993), pp. 141–148. doi: [10.1016/0370-2693\(93\)91720-8](https://doi.org/10.1016/0370-2693(93)91720-8). ARXIV: [hep-ph/9209299 \[hep-ph\]](https://arxiv.org/abs/hep-ph/9209299)
- [72] C. P. Burgess and J. M. Cline. *Phys. Rev. D* 49 (1994), pp. 5925–5944. doi: [10.1103/PhysRevD.49.5925](https://doi.org/10.1103/PhysRevD.49.5925). ARXIV: [hep-ph/9307316 \[hep-ph\]](https://arxiv.org/abs/hep-ph/9307316)
- [73] A. Masiero and J. W. F. Valle. *Phys. Lett. B* 251.2 (1990), pp. 273–278. doi: [10.1016/0370-2693\(90\)90935-Y](https://doi.org/10.1016/0370-2693(90)90935-Y)
- [74] R. N. Mohapatra and E. Takasugi. *Phys. Lett. B* 211.1 (1988), pp. 192–196. doi: [10.1016/0370-2693\(88\)90832-5](https://doi.org/10.1016/0370-2693(88)90832-5)
- [75] C. D. Carone. *Phys. Lett. B* 308.1 (1993), pp. 85–88. doi: [10.1016/0370-2693\(93\)90605-H](https://doi.org/10.1016/0370-2693(93)90605-H). ARXIV: [hep-ph/9302290 \[hep-ph\]](https://arxiv.org/abs/hep-ph/9302290)
- [76] P. Bamert, C. P. Burgess, and R. N. Mohapatra. *Nucl. Phys. B* 449.1 (1995), pp. 25–48. doi: [10.1016/0550-3213\(95\)00273-U](https://doi.org/10.1016/0550-3213(95)00273-U). ARXIV: [hep-ph/9412365 \[hep-ph\]](https://arxiv.org/abs/hep-ph/9412365)
- [77] R. N. Mohapatra, A. Pérez-Lorenzana, and C. A. de S. Pires. *Phys. Lett. B* 491.1 (2000), pp. 143–147. doi: [10.1016/S0370-2693\(00\)01031-5](https://doi.org/10.1016/S0370-2693(00)01031-5). ARXIV: [hep-ph/0008158 \[hep-ph\]](https://arxiv.org/abs/hep-ph/0008158)
- [78] K. Blum and M. Nir Y. and Shavit. *Phys. Lett. B* 785 (2018), pp. 354–361. doi: [10.1016/j.physletb.2018.08.022](https://doi.org/10.1016/j.physletb.2018.08.022). ARXIV: [1802.08019 \[hep-ph\]](https://arxiv.org/abs/1802.08019)
- [79] J. Kotila, J. Barea, and F. Iachello. *Phys. Rev. C* 91.6 (2015). Erratum: *Phys. Rev. C* 92, 029903 (2015), p. 064310. doi: [10.1103/PhysRevC.91.064310](https://doi.org/10.1103/PhysRevC.91.064310). ARXIV: [1509.05154 \[nucl-th\]](https://arxiv.org/abs/1509.05154)
- [80] J. B. Albert et al. (EXO-200 Collaboration). *Phys. Rev. D* 90.9 (2014), p. 092004. doi: [10.1103/PhysRevD.90.092004](https://doi.org/10.1103/PhysRevD.90.092004). ARXIV: [1409.6829 \[hep-ex\]](https://arxiv.org/abs/1409.6829)
- [81] A. Gando et al. (KAMLAND-ZEN Collaboration). *Phys. Rev. C* 86 (2012), p. 021601. doi: [10.1103/PhysRevC.86.021601](https://doi.org/10.1103/PhysRevC.86.021601). ARXIV: [1205.6372 \[hep-ex\]](https://arxiv.org/abs/1205.6372)
- [82] R. Arnold et al. (NEMO-3 Collaboration). *Phys. Rev. D* 89.11 (2014), p. 111101. doi: [10.1103/PhysRevD.89.111101](https://doi.org/10.1103/PhysRevD.89.111101). ARXIV: [1311.5695 \[hep-ex\]](https://arxiv.org/abs/1311.5695)
- [83] R. Arnold et al. (NEMO-3 Collaboration). *Eur. Phys. J. C* 79.5 (2019), p. 440. doi: [10.1140/epjc/s10052-019-6948-4](https://doi.org/10.1140/epjc/s10052-019-6948-4). ARXIV: [1903.08084 \[nucl-ex\]](https://arxiv.org/abs/1903.08084)
- [84] R. Arnold et al. (NEMO-3 Collaboration). *Eur. Phys. J. C* 78.10 (2018), p. 821. doi: [10.1140/epjc/s10052-018-6295-x](https://doi.org/10.1140/epjc/s10052-018-6295-x). ARXIV: [1806.05553 \[hep-ex\]](https://arxiv.org/abs/1806.05553)
- [85] R. Arnold et al. (NEMO-3 Collaboration). *Phys. Rev. D* 95.1 (2017), p. 012007. doi: [10.1103/PhysRevD.95.012007](https://doi.org/10.1103/PhysRevD.95.012007). ARXIV: [1610.03226 \[hep-ex\]](https://arxiv.org/abs/1610.03226)
- [86] R. Arnold et al. (NEMO-3 Collaboration). *Phys. Rev. D* 93.11 (2016), p. 112008. doi: [10.1103/PhysRevD.93.112008](https://doi.org/10.1103/PhysRevD.93.112008). ARXIV: [1604.01710 \[hep-ex\]](https://arxiv.org/abs/1604.01710)

- [87] R. Arnold et al. (NEMO-3 Collaboration). *Phys. Rev.* D94.7 (2016), p. 072003. doi: [10.1103/PhysRevD.94.072003](https://doi.org/10.1103/PhysRevD.94.072003). ARXIV: [1606.08494 \[hep-ex\]](https://arxiv.org/abs/1606.08494)
- [88] Roger Arnold et al. (NEMO-3 Collaboration). *Phys. Rev. Lett.* 107 (2011), p. 062504. doi: [10.1103/PhysRevLett.107.062504](https://doi.org/10.1103/PhysRevLett.107.062504). ARXIV: [1104.3716 \[nucl-ex\]](https://arxiv.org/abs/1104.3716)
- [89] J. Argyriades et al. (NEMO-3 Collaboration). *Nucl. Phys.* A847 (2010), pp. 168–179. doi: [10.1016/j.nuclphysa.2010.07.009](https://doi.org/10.1016/j.nuclphysa.2010.07.009). ARXIV: [0906.2694 \[nucl-ex\]](https://arxiv.org/abs/0906.2694)
- [90] C. Alduino et al. (CUORE Collaboration). *Phys. Rev. Lett.* 120.13 (2018), p. 132501. doi: [10.1103/PhysRevLett.120.132501](https://doi.org/10.1103/PhysRevLett.120.132501). ARXIV: [1710.07988 \[nucl-ex\]](https://arxiv.org/abs/1710.07988)
- [91] D. Budjas et al. (GERDA Collaboration). *JINST* 8 (2013), P04018. doi: [10.1088/1748-0221/8/04/P04018](https://doi.org/10.1088/1748-0221/8/04/P04018). ARXIV: [1303.6768 \[physics.ins-det\]](https://arxiv.org/abs/1303.6768)
- [92] N. Abgrall et al. (MAJORANA Collaboration). *Adv. High Energy Phys.* 2014 (2014), pp. 1–18. doi: [10.1155/2014/365432](https://doi.org/10.1155/2014/365432). ARXIV: [1308.1633 \[physics\]](https://arxiv.org/abs/1308.1633)
- [93] N. Abgrall et al. (LEGEND Collaboration). *AIP Conf. Proc.* 1894.1 (2017), p. 020027. doi: [10.1063/1.5007652](https://doi.org/10.1063/1.5007652). ARXIV: [1709.01980 \[physics.ins-det\]](https://arxiv.org/abs/1709.01980)
- [94] C. Arnaboldi et al. (CUORE Collaboration). *Nucl. Instrum. Meth.* A518 (2004), pp. 775–798. doi: [10.1016/j.nima.2003.07.067](https://doi.org/10.1016/j.nima.2003.07.067). ARXIV: [hep-ex/0212053 \[hep-ex\]](https://arxiv.org/abs/hep-ex/0212053)
- [95] D. R. Artusa et al. (CUORE Collaboration). *Adv. High Energy Phys.* 2015 (2015), p. 879871. doi: [10.1155/2015/879871](https://doi.org/10.1155/2015/879871). ARXIV: [1402.6072 \[physics.ins-det\]](https://arxiv.org/abs/1402.6072)
- [96] G. Wang et al. (CUPID Collaboration) (2015). ARXIV: [1504.03599 \[physics.ins-det\]](https://arxiv.org/abs/1504.03599)
- [97] G. B. Kim et al. *Adv. High Energy Phys.* 2015 (2015), p. 817530. doi: [10.1155/2015/817530](https://doi.org/10.1155/2015/817530). ARXIV: [1602.07401 \[physics.ins-det\]](https://arxiv.org/abs/1602.07401)
- [98] M. Auger et al. (EXO-200 Collaboration). *JINST* 7 (2012), P05010. doi: [10.1088/1748-0221/7/05/P05010](https://doi.org/10.1088/1748-0221/7/05/P05010). ARXIV: [1202.2192 \[physics.ins-det\]](https://arxiv.org/abs/1202.2192)
- [99] S. Al Kharusi et al. (NEXO Collaboration) (2018). ARXIV: [1805.11142 \[physics.ins-det\]](https://arxiv.org/abs/1805.11142)
- [100] N. Lopez-March (NEXT Collaboration). *J. Phys. Conf. Ser.* 888.1 (2017), p. 012243. doi: [10.1088/1742-6596/888/1/012243](https://doi.org/10.1088/1742-6596/888/1/012243). ARXIV: [1701.02697 \[physics.ins-det\]](https://arxiv.org/abs/1701.02697)
- [101] X. Chen et al. *Sci. China Phys. Mech. Astron.* 60.6 (2017), p. 061011. doi: [10.1007/s11433-017-9028-0](https://doi.org/10.1007/s11433-017-9028-0). ARXIV: [1610.08883 \[physics.ins-det\]](https://arxiv.org/abs/1610.08883)
- [102] D. S. Akerib et al. (LZ Collaboration) (2015). ARXIV: [1509.02910 \[physics.ins-det\]](https://arxiv.org/abs/1509.02910)
- [103] E. Aprile. APS April Meeting Abstracts. 2017
- [104] J. Aalbers et al. (DARWIN Collaboration). *JCAP* 1611 (2016), p. 017. doi: [10.1088/1475-7516/2016/11/017](https://doi.org/10.1088/1475-7516/2016/11/017). ARXIV: [1606.07001 \[astro-ph.IM\]](https://arxiv.org/abs/1606.07001)
- [105] S. Andringa et al. (SNO+ Collaboration). *Adv. High Energy Phys.* 2016 (2016), p. 6194250. doi: [10.1155/2016/6194250](https://doi.org/10.1155/2016/6194250). ARXIV: [1508.05759 \[physics.ins-det\]](https://arxiv.org/abs/1508.05759)
- [106] Josephine Paton (SNO+ Collaboration). *Prospects in Neutrino Physics (NuPhys2018) London, United Kingdom, December 19-21, 2018*. 2019. ARXIV: [1904.01418 \[hep-ex\]](https://arxiv.org/abs/1904.01418)
- [107] S. Umehara et al. *Phys. Procedia* 61 (2015), pp. 283–288. doi: [10.1016/j.phpro.2014.12.046](https://doi.org/10.1016/j.phpro.2014.12.046)
- [108] R. Arnold et al. (SUPERNEMO Collaboration). *Eur. Phys. J.* C70 (2010), pp. 927–943. doi: [10.1140/epjc/s10052-010-1481-5](https://doi.org/10.1140/epjc/s10052-010-1481-5). ARXIV: [1005.1241 \[hep-ex\]](https://arxiv.org/abs/1005.1241)
- [109] R. Arnold et al. (NEMO-3 Collaboration). *Nucl. Instrum. Meth.* A536 (2005), pp. 79–122. doi: [10.1016/j.nima.2004.07.194](https://doi.org/10.1016/j.nima.2004.07.194). ARXIV: [physics/0402115 \[physics\]](https://arxiv.org/abs/physics/0402115)

- [110] J. Detwiler. 2020. doi: [10.5281/zenodo.3959552](https://doi.org/10.5281/zenodo.3959552)
- [111] I. Abt et al. 2004. URL: <https://www.mpi-hd.mpg.de/gerda/proposal.pdf>
- [112] H. V. Klapdor-Kleingrothaus et al. (HdM Collaboration). *Eur. Phys. J.* A12 (2001), pp. 147–154. doi: [10.1007/s100500170022](https://doi.org/10.1007/s100500170022). ARXIV: [hep-ph/0103062 \[hep-ph\]](https://arxiv.org/abs/hep-ph/0103062)
- [113] C. E. Aalseth et al. (IGEX Collaboration). *Phys. Rev. D* 65 (2002), p. 092007. doi: [10.1103/PhysRevD.65.092007](https://doi.org/10.1103/PhysRevD.65.092007). ARXIV: [hep-ex/0202026 \[hep-ex\]](https://arxiv.org/abs/hep-ex/0202026)
- [114] G Heusser. *Annu. Rev. Nucl. Part. S.* 45.1 (1995), p. 543. doi: [10.1146/annurev.ns.45.120195.002551](https://doi.org/10.1146/annurev.ns.45.120195.002551)
- [115] M. Agostini et al. *Nucl. Part. Phys. Proc.* 273–275 (2016), pp. 1876–1882. doi: [10.1016/j.nuclphysbps.2015.09.303](https://doi.org/10.1016/j.nuclphysbps.2015.09.303)
- [116] M. Agostini et al. (GERDA Collaboration). *Science* 365 (2019), p. 1445. doi: [10.1126/science.aav8613](https://doi.org/10.1126/science.aav8613). ARXIV: [1909.02726 \[hep-ex\]](https://arxiv.org/abs/1909.02726)
- [117] C. Wiesinger, L. Pandola, and S. Schönert. *Eur. Phys. J.* C78.7 (2018), p. 597. doi: [10.1140/epjc/s10052-018-6079-3](https://doi.org/10.1140/epjc/s10052-018-6079-3). ARXIV: [1802.05040 \[hep-ex\]](https://arxiv.org/abs/1802.05040)
- [118] K. Freund et al. *Eur. Phys. J.* C76.5 (2016), p. 298. doi: [10.1140/epjc/s10052-016-4140-7](https://doi.org/10.1140/epjc/s10052-016-4140-7). ARXIV: [1601.05935 \[physics.ins-det\]](https://arxiv.org/abs/1601.05935)
- [119] I. Yonenaga. *Single Crystals of Electronic Materials*. Ed. by Roberto Fornari. Woodhead Publishing Series in Electronic and Optical Materials. Woodhead Publishing, 2019, pp. 89–127. doi: [10.1016/B978-0-08-102096-8.00004-5](https://doi.org/10.1016/B978-0-08-102096-8.00004-5)
- [120] M. Agostini et al. (GERDA Collaboration). *Eur. Phys. J.* C75.2 (2015), p. 39. doi: [10.1140/epjc/s10052-014-3253-0](https://doi.org/10.1140/epjc/s10052-014-3253-0). ARXIV: [1410.0853 \[physics.ins-det\]](https://arxiv.org/abs/1410.0853)
- [121] M. Agostini et al. (GERDA Collaboration). *Eur. Phys. J.* C78.5 (2018), p. 388. doi: [10.1140/epjc/s10052-018-5812-2](https://doi.org/10.1140/epjc/s10052-018-5812-2). eprint: [1711.01452](https://arxiv.org/abs/1711.01452)
- [122] M. Agostini et al. (GERDA Collaboration). *Eur. Phys. J.* C79.11 (2019), p. 978. doi: [10.1140/epjc/s10052-019-7353-8](https://doi.org/10.1140/epjc/s10052-019-7353-8). ARXIV: [1901.06590 \[physics.ins-det\]](https://arxiv.org/abs/1901.06590)
- [123] M. Miloradovic. PhD thesis. Zürich U., 2020. URL: https://www.physik.uzh.ch/dam/jcr:94fa6df0-e441-413a-a31d-59f89e375970/miloradovic_thesis.pdf
- [124] M. Agostini et al. (GERDA Collaboration). *Eur. Phys. J. C* (2021). To appear
- [125] S. Riboldi et al. *2015 4th International Conference on Advancements in Nuclear Instrumentation Measurement Methods and their Applications (ANIMMA)*. 2015, pp. 1–6. doi: [10.1109/ANIMMA.2015.7465549](https://doi.org/10.1109/ANIMMA.2015.7465549)
- [126] A. Lubashevskiy et al. *Eur. Phys. J. C* 78.1 (2018), p. 15. doi: [10.1140/epjc/s10052-017-5499-9](https://doi.org/10.1140/epjc/s10052-017-5499-9). ARXIV: [1708.00226 \[physics.ins-det\]](https://arxiv.org/abs/1708.00226)
- [127] L. Baudis et al. *JINST* 10.12 (2015), P12005. doi: [10.1088/1748-0221/10/12/P12005](https://doi.org/10.1088/1748-0221/10/12/P12005). ARXIV: [1508.05731 \[physics.ins-det\]](https://arxiv.org/abs/1508.05731)
- [128] R. Mingazheva. PhD thesis. Zürich U., 2019. URL: <https://www.physik.uzh.ch/dam/jcr:1c037fcf-eee7-487d-9336-4b8cc88f6710/MingazhevaThesis.pdf>
- [129] M. Agostini et al. (GERDA Collaboration). *Eur. Phys. J. C* (2021). To appear
- [130] M. Agostini et al. (GERDA Collaboration). *Eur. Phys. J.* C75.6 (2015), p. 255. doi: [10.1140/epjc/s10052-015-3409-6](https://doi.org/10.1140/epjc/s10052-015-3409-6). ARXIV: [1502.04392 \[physics.ins-det\]](https://arxiv.org/abs/1502.04392)
- [131] M. Agostini et al. *JINST* 6 (2011), P08013. doi: [10.1088/1748-0221/6/08/P08013](https://doi.org/10.1088/1748-0221/6/08/P08013). ARXIV: [1106.1780 \[physics.data-an\]](https://arxiv.org/abs/1106.1780)

- [132] M. Agostini et al. (GERDA Collaboration). *Nature* 544 (2017), p. 47. doi: [10 . 1038 / nature21717](https://doi.org/10.1038/nature21717). ARXIV: [1703.00570 \[nucl-ex\]](https://arxiv.org/abs/1703.00570)
- [133] M. Agostini et al. (GERDA Collaboration). *Phys. Rev. Lett.* 120.13 (2018), p. 132503. doi: [10 . 1103/PhysRevLett.120.132503](https://doi.org/10.1103/PhysRevLett.120.132503). ARXIV: [1803.11100 \[nucl-ex\]](https://arxiv.org/abs/1803.11100)
- [134] T. Heindl et al. *EPL* 91.6 (2010), p. 62002. doi: [10 . 1209/0295-5075/91/62002](https://doi.org/10.1209/0295-5075/91/62002). ARXIV: [1511.07718 \[physics.ins-det\]](https://arxiv.org/abs/1511.07718)
- [135] J. Jortner et al. *J. Chem. Phys.* 42.12 (1965), pp. 4250–4253. doi: [10 . 1063/1.1695927](https://doi.org/10.1063/1.1695927)
- [136] M. V. McCusker. Ed. by Ch. K. Rhodes. Vol. 30. Topics in Applied Physics. Springer-Verlag Berlin Heidelberg, 1984. Chap. 3. doi: [10 . 1007/3-540-13013-6](https://doi.org/10.1007/3-540-13013-6)
- [137] T. Doke et al. *Nucl. Instrum. Meth.* A269 (1988), pp. 291–296. doi: [10 . 1016 / 0168 - 9002\(88\)90892-3](https://doi.org/10.1016/0168-9002(88)90892-3)
- [138] Claude Amsler et al. *JINST* 3 (2008), P02001. doi: [10 . 1088/1748-0221/3/02/P02001](https://doi.org/10.1088/1748-0221/3/02/P02001). ARXIV: [0708.2621 \[physics.ins-det\]](https://arxiv.org/abs/0708.2621)
- [139] M. Agostini et al. (GERDA Collaboration). *Eur. Phys. J. C* (2021). To appear
- [140] M. Agostini et al. *Eur. Phys. J. C* 73.10 (2013), p. 2583. doi: [10 . 1140/epjc/s10052-013-2583-7](https://doi.org/10.1140/epjc/s10052-013-2583-7). ARXIV: [1307.2610 \[physics.ins-det\]](https://arxiv.org/abs/1307.2610)
- [141] M. Agostini et al. *JINST* 6 (2011), P03005. doi: [10 . 1088/1748-0221/6/03/P03005](https://doi.org/10.1088/1748-0221/6/03/P03005). ARXIV: [1012.4300 \[physics.ins-det\]](https://arxiv.org/abs/1012.4300)
- [142] D. Budjas et al. *2008 IEEE Nuclear Science Symposium and Medical Imaging Conference and 16th International Workshop on Room-Temperature Semiconductor X-Ray and Gamma-Ray Detectors*. 2008, pp. 2513–2515. doi: [10 . 1109 / NSSMIC . 2008 . 4774866](https://doi.org/10.1109/NSSMIC.2008.4774866). ARXIV: [0812.1735 \[nucl-ex\]](https://arxiv.org/abs/0812.1735)
- [143] D. Budjas, O. Chkvorets, and S. Schonert. *AIP Conf. Proc.* 1182.1 (2009), pp. 96–99. doi: [10 . 1063/1.3293966](https://doi.org/10.1063/1.3293966)
- [144] D. Budjas et al. *JINST* 4 (2009), P10007. doi: [10 . 1088/1748-0221/4/10/P10007](https://doi.org/10.1088/1748-0221/4/10/P10007). ARXIV: [0909.4044 \[nucl-ex\]](https://arxiv.org/abs/0909.4044)
- [145] M. Agostini et al. *JINST* 6 (2011), P04005. doi: [10 . 1088/1748-0221/6/04/P04005](https://doi.org/10.1088/1748-0221/6/04/P04005). ARXIV: [1012.5200 \[physics.ins-det\]](https://arxiv.org/abs/1012.5200)
- [146] R. Brun and F. Rademakers. *Nucl. Instrum. Meth. A* 389 (1997), pp. 81–86. doi: [10 . 1016 / S0168-9002\(97\)00048-X](https://doi.org/10.1016/S0168-9002(97)00048-X)
- [147] A. Lazzaro. PhD thesis. Munich, Tech. U., 2019
- [148] A. Caldwell, D. Kollar, and K. Kroninger. *Comput. Phys. Commun.* 180 (2009), pp. 2197–2209. doi: [10 . 1016 / j.cpc.2009.06.026](https://doi.org/10.1016/j.cpc.2009.06.026). ARXIV: [0808.2552 \[physics.data-an\]](https://arxiv.org/abs/0808.2552)
- [149] M. Agostini et al. (GERDA Collaboration). *Eur. Phys. J. C* 74.4 (2014), p. 2764. doi: [10 . 1140/epjc/s10052-014-2764-z](https://doi.org/10.1140/epjc/s10052-014-2764-z). ARXIV: [1306.5084 \[physics.ins-det\]](https://arxiv.org/abs/1306.5084)
- [150] M. Agostini et al. (GERDA Collaboration). *JHEP* 03 (2020), p. 139. doi: [10 . 1007 / JHEP03\(2020\)139](https://doi.org/10.1007/JHEP03(2020)139). ARXIV: [1909.02522 \[nucl-ex\]](https://arxiv.org/abs/1909.02522)
- [151] M. Boswell et al. *IEEE Trans. Nud. Sci.* 58 (2011), pp. 1212–1220. doi: [10 . 1109/TNS . 2011 . 2144619](https://doi.org/10.1109/TNS.2011.2144619). ARXIV: [1011.3827 \[nucl-ex\]](https://arxiv.org/abs/1011.3827)
- [152] S. Agostinelli et al. (GEANT4 Collaboration). *Nucl. Instrum. Meth. A* 506 (2003), pp. 250–303. doi: [10 . 1016 / S0168-9002\(03\)01368-8](https://doi.org/10.1016/S0168-9002(03)01368-8)
- [153] J. Allison et al. *IEEE T. Nud. Sci.* 53.1 (2006), pp. 270–278. doi: [10 . 1109 / TNS . 2006 . 869826](https://doi.org/10.1109/TNS . 2006 . 869826)

- [154] J. Allison et al. *Nucl. Instrum. Meth. A* 835 (2016), pp. 186–225. doi: [10.1016/j.nima.2016.06.125](https://doi.org/10.1016/j.nima.2016.06.125)
- [155] O.A. Ponkratenko, V.I. Tretyak, and Yu.G. Zdesenko. *Phys. Atom. Nuc.* 63 (2000), pp. 1282–1287. doi: [10.1134/1.855784](https://doi.org/10.1134/1.855784). ARXIV: [nucl-ex/0104018](https://arxiv.org/abs/nucl-ex/0104018)
- [156] K.H. Ackermann et al. (GERDA Collaboration). *Eur. Phys. J. C* 73.3 (2013), p. 2330. doi: [10.1140/epjc/s10052-013-2330-0](https://doi.org/10.1140/epjc/s10052-013-2330-0). ARXIV: [1212.4067 \[physics.ins-det\]](https://arxiv.org/abs/1212.4067)
- [157] M. L. di Vacri et al. *AIP Conf. Proc.* 1672.1 (2015), p. 150001. doi: [10.1063/1.4928024](https://doi.org/10.1063/1.4928024)
- [158] K. Pelczar. PhD thesis. Jagiellonian U. (main), 2016
- [159] G. Meierhofer et al. *Eur. Phys. J. A* 40.1 (2009), pp. 61–64. doi: [10.1140/epja/i2008-10741-0](https://doi.org/10.1140/epja/i2008-10741-0)
- [160] G. Meierhofer et al. *Phys. Rev. C* 81.2 (2010), p. 027603. doi: [10.1103/PhysRevC.81.027603](https://doi.org/10.1103/PhysRevC.81.027603)
- [161] G. Meierhofer et al. *Eur. Phys. J. A* 48.2 (2012), p. 20. doi: [10.1140/epja/i2012-12020-y](https://doi.org/10.1140/epja/i2012-12020-y)
- [162] M. Agostini et al. (GERDA Collaboration). *Astropart. Phys.* 91 (2017), pp. 15–21. doi: [10.1016/j.astropartphys.2017.03.003](https://doi.org/10.1016/j.astropartphys.2017.03.003). ARXIV: [1611.06884 \[physics.ins-det\]](https://arxiv.org/abs/1611.06884)
- [163] K. Freund. PhD thesis. Eberhard Karls Universität Tübingen, 2014
- [164] I. Barabanov et al. *Nucl. Instrum. Meth. A* 606 (2009), pp. 790–794. doi: [10.1016/j.nima.2009.04.006](https://doi.org/10.1016/j.nima.2009.04.006)
- [165] L. Vanhoefer. PhD thesis. Technischen Universität München, 2018
- [166] D. M. Mei et al. *Phys. Rev. C* 77 (2008), p. 054614. doi: [10.1103/PhysRevC.77.054614](https://doi.org/10.1103/PhysRevC.77.054614). ARXIV: [0704.0306 \[nucl-ex\]](https://arxiv.org/abs/0704.0306)
- [167] K. Winger et al. *J. Environ. Radioactiv.* 80.2 (2005), pp. 183–215. doi: [10.1016/j.jenvrad.2004.09.005](https://doi.org/10.1016/j.jenvrad.2004.09.005)
- [168] F. Beaujean et al. 2018. doi: [10.5281/ZENODO.1322675](https://doi.org/10.5281/ZENODO.1322675)
- [169] F. Beaujean et al. *Phys. Rev. D* 83 (2011), p. 012004. doi: [10.1103/PhysRevD.83.012004](https://doi.org/10.1103/PhysRevD.83.012004). ARXIV: [1011.1674 \[physics.data-an\]](https://arxiv.org/abs/1011.1674)
- [170] M. J. Berger et al. *NIST Standard Reference Database* 124 (2017). doi: [10.18434/T4NC7P](https://doi.org/10.18434/T4NC7P)
- [171] M.-M. Bé et al. Vol. 4. Monographie BIPM-5. Pavillon de Breteuil, F-92310 Sèvres, France: Bureau International des Poids et Mesures, 2008. URL: http://www.bipm.org/utils/common/pdf/monographieRI/Monographie_BIPM-5_Tables_Vol4.pdf
- [172] M. Agostini. PhD thesis. Technischen Universität München, 2013
- [173] V. D’Andrea. PhD thesis. Gran Sasso Science Institute (GSSI), 2017
- [174] R. Aggarwal and A. Caldwell. *Eur. Phys. J. Plus* 127 (2012), p. 24. doi: [10.1140/epjp/i2012-12024-0](https://doi.org/10.1140/epjp/i2012-12024-0). ARXIV: [1112.2593 \[physics.data-an\]](https://arxiv.org/abs/1112.2593)
- [175] M. Agostini et al. (GERDA Collaboration). *Phys. Rev. Lett.* 111.12 (2013), p. 122503. doi: [10.1103/PhysRevLett.111.122503](https://doi.org/10.1103/PhysRevLett.111.122503). ARXIV: [1307.4720 \[nucl-ex\]](https://arxiv.org/abs/1307.4720)
- [176] S. Cebrian et al. *Astropart. Phys.* 33 (2010), pp. 316–329. doi: [10.1016/j.astropartphys.2010.03.002](https://doi.org/10.1016/j.astropartphys.2010.03.002)
- [177] T. Horiguchi et al. *The International Journal of Applied Radiation and Isotopes* 34.11 (1983), pp. 1531–1535. doi: [https://doi.org/10.1016/0020-708X\(83\)90288-0](https://doi.org/10.1016/0020-708X(83)90288-0)
- [178] E. Bellotti et al. *Nuovo Cim. A* 95 (1986), pp. 1–46. doi: [10.1007/BF02768738](https://doi.org/10.1007/BF02768738)
- [179] C. Wiesinger. To appear. PhD thesis. Munich, Tech. U., 2020
- [180] B. Lehnert. PhD thesis. Technischen Universität Dresden, 2016

- [181] G. Cowan et al. *Eur. Phys. J. C* 71 (2011). [Erratum: Eur.Phys.J.C 73, 2501 (2013)], p. 1554. doi: [10.1140/epjc/s10052-011-1554-0](https://doi.org/10.1140/epjc/s10052-011-1554-0). ARXIV: [1007.1727 \[physics.data-an\]](https://arxiv.org/abs/1007.1727)
- [182] S. Algeri et al. *Nature Rev. Phys.* 2.5 (2020), pp. 245–252. doi: [10.1038/s42254-020-0169-5](https://doi.org/10.1038/s42254-020-0169-5)
- [183] H. Chernoff. *Ann. Math. Stat.* 25 (1954), pp. 573–578. doi: [10.1214/aoms/1177728725](https://doi.org/10.1214/aoms/1177728725)
- [184] M. Agostini et al. (GERDA Collaboration). *J. Phys. G* 40 (2013), p. 035110. doi: [10.1088/0954-3899/40/3/035110](https://doi.org/10.1088/0954-3899/40/3/035110). ARXIV: [1212.3210 \[nucl-ex\]](https://arxiv.org/abs/1212.3210)
- [185] J. Barea, J. Kotila, and F. Iachello. *Phys. Rev. C* 91.3 (2015), p. 034304. doi: [10.1103/PhysRevC.91.034304](https://doi.org/10.1103/PhysRevC.91.034304). ARXIV: [1506.08530 \[nucl-th\]](https://arxiv.org/abs/1506.08530)
- [186] M. Hirsch et al. *Phys. Lett. B* 372 (1996), pp. 8–14. doi: [10.1016/0370-2693\(96\)00038-X](https://doi.org/10.1016/0370-2693(96)00038-X). ARXIV: [hep-ph/9511227](https://arxiv.org/abs/hep-ph/9511227)
- [187] M. Merck et al. *J. Phys. Conf. Ser.* 396 (2012). Ed. by Michael Ernst et al., p. 022046. doi: [10.1088/1742-6596/396/2/022046](https://doi.org/10.1088/1742-6596/396/2/022046)
- [188] S. Blyth. *EPJ Web Conf.* 214 (2019). Ed. by A. Forti et al., p. 02027. doi: [10.1051/epjconf/201921402027](https://doi.org/10.1051/epjconf/201921402027)
- [189] M. B. Heider. PhD thesis. Max-Planck-Institut für Kernphysik, Heidelberg, Germany, 2009. doi: [10.11588/heidok.00009551](https://doi.org/10.11588/heidok.00009551)
- [190] M. Wang et al. *Chin. Phys. C* 41.3 (2017), p. 030003. doi: [10.1088/1674-1137/41/3/030003](https://doi.org/10.1088/1674-1137/41/3/030003)
- [191] R. Ajaj et al. (DEAP Collaboration). *Phys. Rev. D* 100.7 (2019), p. 072009. doi: [10.1103/PhysRevD.100.072009](https://doi.org/10.1103/PhysRevD.100.072009). ARXIV: [1905.05811 \[nucl-ex\]](https://arxiv.org/abs/1905.05811)
- [192] J. Calvo et al. (ARDM Collaboration). *JCAP* 12 (2018), p. 011. doi: [10.1088/1475-7516/2018/12/011](https://doi.org/10.1088/1475-7516/2018/12/011). ARXIV: [1712.01932 \[physics.ins-det\]](https://arxiv.org/abs/1712.01932)
- [193] P. Benetti et al. (WARP Collaboration). *Nucl. Instrum. Meth. A* 574 (2007), pp. 83–88. doi: [10.1016/j.nima.2007.01.106](https://doi.org/10.1016/j.nima.2007.01.106). ARXIV: [astro-ph/0603131](https://arxiv.org/abs/astro-ph/0603131)
- [194] H. H. Loosli. *Earth and Planetary Science Letters* 63.1 (1983), pp. 51–62. doi: [10.1016/0012-821X\(83\)90021-3](https://doi.org/10.1016/0012-821X(83)90021-3)
- [195] M. Agostini et al. (GERDA Collaboration). *Phys. Rev. Lett.* 125.1 (2020), p. 011801. doi: [10.1103/PhysRevLett.125.011801](https://doi.org/10.1103/PhysRevLett.125.011801). ARXIV: [2005.14184 \[hep-ex\]](https://arxiv.org/abs/2005.14184)
- [196] J. Kostensalo, J. Suhonen, and K. Zuber. *J. Phys. G* 45.2 (2018), p. 025202. doi: [10.1088/1361-6471/aa958e](https://doi.org/10.1088/1361-6471/aa958e). ARXIV: [1705.05726 \[nucl-th\]](https://arxiv.org/abs/1705.05726)
- [197] J. Bezanson et al. *SIAM Review* 59.1 (2017), pp. 65–98. doi: [10.1137/141000671](https://doi.org/10.1137/141000671). ARXIV: [1411.1607 \[cs.MS\]](https://arxiv.org/abs/1411.1607)
- [198] G. M. Kurtzer, V. Sochat, and M. W. Bauer. *PLOS ONE* 12.5 (2017), pp. 1–20. doi: [10.1371/journal.pone.0177459](https://doi.org/10.1371/journal.pone.0177459)
- [199] 2020. doi: [10.5281/zenodo.4001185](https://doi.org/10.5281/zenodo.4001185)
- [200] A. Bideau-Mehu et al. *J. Quant. Spectrosc. Radiat. Transf.* 25 (1981), pp. 395–402. doi: [10.1016/0022-4073\(81\)90057-1](https://doi.org/10.1016/0022-4073(81)90057-1)
- [201] G. M. Seidel, R. E. Lanou, and W. Yao. *Nucl. Instrum. Meth. A* 489 (2002), pp. 189–194. doi: [10.1016/S0168-9002\(02\)00890-2](https://doi.org/10.1016/S0168-9002(02)00890-2). ARXIV: [hep-ex/0111054](https://arxiv.org/abs/hep-ex/0111054)
- [202] M. Babicz et al. *Nucl. Instrum. Meth. A* 936 (2019). Ed. by G. Batignani et al., pp. 178–179. doi: [10.1016/j.nima.2018.10.082](https://doi.org/10.1016/j.nima.2018.10.082)
- [203] T. Doke et al. *Jap. J. Appl. Phys.* 41 (2002), pp. 1538–1545. doi: [10.1143/JJAP.41.1538](https://doi.org/10.1143/JJAP.41.1538)

- [204] N. Barros et al. *Nucl. Instrum. Meth. A* 953 (2020), p. 163059. doi: [10.1016/j.nima.2019.163059](https://doi.org/10.1016/j.nima.2019.163059). ARXIV: [1906.11589 \[physics.ins-det\]](https://arxiv.org/abs/1906.11589)
- [205] T. Doke et al. *Nucl. Instrum. Meth.* 134 (1976), pp. 353–357. doi: [10.1016/0029-554X\(76\)90292-5](https://doi.org/10.1016/0029-554X(76)90292-5)
- [206] A. C. Wegmann. PhD thesis. U. Heidelberg (main), 2017. doi: [10.11588/heidok.00022568](https://doi.org/10.11588/heidok.00022568)
- [207] L. Marton and J. Toots. *Phys. Rev.* 160 (1967), pp. 602–606. doi: [10.1103/physrev.160.602](https://doi.org/10.1103/physrev.160.602)
- [208] M. Janecek. *IEEE Trans. Nucl. Sci.* 59 (2012), pp. 490–497. doi: [10.1109/tns.2012.2183385](https://doi.org/10.1109/tns.2012.2183385)
- [209] R. Francini et al. (2013). doi: [10.1088/1748-0221/8/09/P09006](https://doi.org/10.1088/1748-0221/8/09/P09006). ARXIV: [1304.6117 \[physics.ins-det\]](https://arxiv.org/abs/1304.6117)
- [210] C. Benson et al. *Eur. Phys. J. C* 78.4 (2018), p. 329. doi: [10.1140/epjc/s10052-018-5807-z](https://doi.org/10.1140/epjc/s10052-018-5807-z), [10.1140/s10052-018-5807-z](https://doi.org/10.1140/s10052-018-5807-z). ARXIV: [1709.05002 \[physics.ins-det\]](https://arxiv.org/abs/1709.05002)
- [211] M. Walter. PhD thesis. University of Zurich, 2015. doi: [10.5167/uzh-113939](https://doi.org/10.5167/uzh-113939)
- [212] L. Baudis et al. *JINST* 10.09 (2015), P09009. doi: [10.1088/1748-0221/10/09/P09009](https://doi.org/10.1088/1748-0221/10/09/P09009). ARXIV: [1503.05349 \[physics.ins-det\]](https://arxiv.org/abs/1503.05349)
- [213] URL: <https://www.crystals.saint-gobain.com/sites/imdf.crystals.com/files/documents/fiber-brochure.pdf>
- [214] Kneißl, R. BA thesis. Technischen Universität München, 2012
- [215] M. Agostini et al. (BOREXINO Collaboration). *Astropart. Phys.* 97 (2018), pp. 136–159. doi: [10.1016/j.astropartphys.2017.10.003](https://doi.org/10.1016/j.astropartphys.2017.10.003). ARXIV: [1704.02291 \[physics.ins-det\]](https://arxiv.org/abs/1704.02291)
- [216] B. T. Cleveland. *Nucl. Instrum. Meth.* 214 (1983), pp. 451–458. doi: [10.1016/0167-5087\(83\)90616-6](https://doi.org/10.1016/0167-5087(83)90616-6)
- [217] J. D. Scargle. *Astrophys. J.* 504 (1998), p. 405. doi: [10.1086/306064](https://doi.org/10.1086/306064). ARXIV: [astro-ph/9711233](https://arxiv.org/abs/astro-ph/9711233)
- [218] J. D. Scargle et al. *Astrophys. J.* 764 (2013), p. 167. doi: [10.1088/0004-637X/764/2/167](https://doi.org/10.1088/0004-637X/764/2/167). ARXIV: [1207.5578 \[astro-ph.IM\]](https://arxiv.org/abs/1207.5578)
- [219] B. Pollack, S. Bhattacharya, and M. Schmitt (2017). ARXIV: [1708.00810 \[physics.data-an\]](https://arxiv.org/abs/1708.00810)